# Tailored Mesoporous Silica Microspheres as HPLC Column Materials by a Hard-Templating Method

**Dissertation**

der Mathematisch-Naturwissenschaftlichen Fakultät

der Eberhard Karls Universität Tübingen

zur Erlangung des Grades eines

Doktors der Naturwissenschaften

(Dr. rer. nat.)

vorgelegt von

Julia Catherine Uli Steinbach

aus Stuttgart

Tübingen

2023

Gedruckt mit Genehmigung der Mathematisch-Naturwissenschaftlichen Fakultät der Eberhard Karls Universität Tübingen.

| | |
|---|---|
| Tag der mündlichen Qualifikation: | 29.09.2023 |
| Dekan: | Prof. Dr. Thilo Stehle |
| 1. Berichterstatter: | Prof. Dr. Hermann A. Mayer |
| 2. Berichterstatter: | Prof. Dr. Thomas Chassé |
| 3. Berichterstatter: | Prof. Dr. Andreas Kandelbauer |

# Preface

The following doctoral dissertation provides a comprehensive overview of the preparation of monodisperse, mesoporous silica microspheres via a hard template assisted synthesis method. It includes a summary and disocurse of the key results, and original scientific publications. This work arises from a cooperation project between the Eberhard Karls University Tübingen, the Reutlingen University and Dr. Maisch GmbH. Funding for this project has been gratefully received from the Bundesministerium für Bildung und Forschung BMBF (grant number 13FH647IX6). The work has been carried out at the Institute Process Analysis & Technology of the Reutlingen University and at the Institute for Inorganic Chemistry of the Eberhard Karls University Tübingen from April 2020 to April 2023 under the supervision of Prof. Dr. Hermann A. Mayer and Prof. Dr. Andreas Kandelbauer.

# Danksagung

An dieser Stelle möchte ich mich herzlich bei allen bedanken, die zum Gelingen dieser Doktorarbeit beigetragen haben.

Ein besonderer Dank gilt meinen beiden Betreuern Prof. Dr. Hermann A. Mayer und Prof. Dr. Andreas Kandelbauer, welche mich in Ihre Arbeitsgruppen aufgenommen und mir ermöglicht haben in diesem spannenden Thema zu promovieren. Durch zahlreiche Anregungen und Diskussionen haben Sie mich stets aufs Neue motiviert und inspiriert. Ich habe das Vertrauen und die wissenschaftliche Freiheit, die mir gegeben wurden, stets sehr geschätzt.

Ich möchte mich auch sehr herzlich bei Herrn Prof. Dr. Thomas Chassé bedanken, der das Zweitgutachten für diese Arbeit erstellt hat, sowie bei Herrn Prof. Dr. Reiner Anwander, der sich mit meiner Arbeit für die Disputation befasst hat.

Diese Arbeit ist in Kooperation mit der Firma Dr. Maisch GmbH entstanden. Herrn Dr. Johannes Maisch und Herrn Dr. Jürgen Maier-Rosenkranz danke ich für ihre wertvolle Unterstützung bei chromatografischen Fragestellungen.

Bedanken möchte ich mich bei allen, die zu dieser Arbeit durch analytische Messungen oder den Zugang zu Messgeräten und die entsprechende Einweisung beigetragen haben: Elke Nadler und Prof. Dr. Thomas Chassé (Rasterelektronenmikroskopie), Hannelore Nonnenmacher, Catalina Szerbakowski, und Prof. Dr. Thorsten Textor (Rasterelektronenmikroskopie, Hochschule Reutlingen), sowie Wolfgang Bock (Elementaranalyse). Frau Dr. Kutuzova danke ich für die Einweisung in die Thermoanalytik (TGA und DSC), sowie die Einführung in die modellfreie Kinetik.

Dr. Fabio Fait, Dr. Stefanie Wagner und Dr. Björn Brodbeck gebührt ein großes Dankeschön für die Aufnahme in die Arbeitsgruppe und Einarbeitung in meiner Anfangszeit. Insbesondere möchte ich Fabio für die großartige gegenseitige Unterstützung, die produktiven Diskussionen und das effektive Teamwork danken, welche diese Arbeit sehr bereichert haben.

Ich möchte meinen Dank an alle Kolleginnen und Kollegen aus dem PA&T-Team und der Fakultät Life Science richten, die mich auf meinem Weg begleitet haben, einschließlich der ehemaligen Kollegen. Ein Dankeschön gilt Mohammad Al Ktash, Dr. Miriam Bassler, Tim Bäuerle, Natalia Behring, Tobias Drieschner, Max Eberle, Otto Hauler, Mona Knoblich, Ralf Koslik, Ashutosh Mukherjee, Dr. Steffen Ulitzsch, Dr. Frank Wackenhut und Alexandra Wagner.

Den beiden von mir betreuten POL-Gruppen, namentlich Katrin Markus, Patrick Wahrendorff und Mark Wolf (poröse Polymerpartikel), sowie Leonie Loritz, Lars Nölle,

Christian Schietinger und Marius Virtatci (Polystyrolpartikel), gilt ein großer Dank für ihre zuverlässige Arbeitsweise und den regen Gedankenaustausch. Zeki Atila und Ramona Seeger danke ich für die schöne gemeinsame Zeit während ihren jeweiligen Abschlussarbeiten. Ich danke Leon Rösch für die Zuarbeit im Labor.

Dr. Miriam Bassler, Fabio Fait, Sabrina Müller und Philipp Steinbach danke ich von Herzen, dass sie sich die Zeit genommen haben meine Arbeit Korrektur zu lesen.

Zuletzt möchte ich mich bei meiner Familie bedanken. Meiner Mutter, meinem Vater, Stefan, Sven und meinem Mann Philipp danke ich für den Rückhalt und die bedingungslose Unterstützung die sie mir in jeder Lebenssituation geben.

# Table of Content

**List of Abbreviations** ..... **VIII**

**Summary** ..... **XI**

**Zusammenfassung** ..... **XII**

**List of manuscripts included in this thesis** ..... **XIV**

**List of manuscripts not included in this thesis** ..... **XV**

**Contributions to the manuscripts included in this thesis** ..... **XVI**

**1. Introduction and objectives** ..... **1**

1.1. Introduction ..... 1

1.2. Objectives ..... 3

1.3. Mesoporous silica microspheres by a hard template assisted method – from monomers to packing materials ..... 4

*1.3.1. Reaction procedure for the preparation of MPSMs* ..... *4*

*1.3.2. Seed particle synthesis – Dispersion polymerization* ..... *5*

*1.3.3. Porous polymeric template – Seed-swelling polymerization* ..... *6*

*1.3.4. Porous silica particles – Sol-gel process on hard templates* ..... *7*

**2. Summary of the main results** ..... **12**

2.1. Preparation of monodisperse PS seeds ..... 12

2.2. Designing the pore properties of *p*(GMA-*co*-EDMA) templates ..... 14

2.3. Effect of the template pore properties on the MPSMs ..... 17

2.4. Effect of catalyst concentration and water-to-TEOS ratio on the incorporation of silica into the porous polymeric template ..... 21

2.5. Effect of sol-gel process factor settings on MPSMs ..... 27

**3. Conclusion** ..... **33**

**4. Paper I** ..... **35**

**Rational Design of Pore Parameters in Monodisperse Porous Poly(glycidyl methacrylate-co-ethylene glycol dimethacrylate) Particles Based on Response Surface Methodology** ..... **35**

Abstract ..... 36

4.1. Introduction ..... 36

4.2. Materials and methods ..... 38

*4.2.1. Chemicals* ..... *38*

*4.2.2. Instrumentation* ..... *38*

*4.2.3. Seeded suspension polymerization of porous p(GMA-co-EDMA) particles* ..... *39*

*4.2.4. Experimental design* ..... *39*

*4.2.5. Pore characterization using inverse size exclusion chromatography (iSEC)* ..... *41*

*4.2.6. Scanning electron microscopy images (SEM)* ..... *41*

4.3. Results and discussion ..... 42

*4.3.1. Particle size and dispersity* ..... *42*

*4.3.2. Morphology* ..... *43*

*4.3.3. Multivariate calibration model for epoxy functionalization* ..... *45*

*4.3.4. Pore volume* ..... *46*

*4.3.5. Pore size* ..... *48*
*4.3.6. Specific surface area* ..... *51*
*4.3.7. Model validation* ..... *53*
4.4. Conclusions ..... 54
4.5. Appendix ..... 56
*4.5.1. Synthesis of polystyrene (PS) seed particles* ..... *56*
*4.5.2. Explained variance of multivariate calibration model for epoxy functionalization* ..... *56*

**5. Paper II ..... 58**

**Impact of Porosity and Surface Functionalization of Hard Templates on the Preparation of Mesoporous Silica Microspheres ..... 58**
Abstract ..... 59
5.1. Introduction ..... 59
5.2. Materials and methods ..... 61
*5.2.1. Chemicals* ..... *61*
*5.2.2. Characterizations* ..... *61*
*5.2.3. Synthesis* ..... *63*
5.3. Results and discussion ..... 64
*5.3.1. Modification of p(GMA-co-EDMA) microspheres with different GMA and EDMA ratios* ..... *64*
*5.3.2. Spectral analysis of p(GMA-co-EDMA) and **P@TEPA** microspheres* ..... *66*
*5.3.3. Preparation of mesoporous silica microspheres (**MPSM1–6**)* ..... *68*
*5.3.4. Protein separation using $C_{18}$-functionalized **MPSM1–4** as stationary phases* ..... *71*
5.4. Conclusion ..... 73
5.5. Supplementary Information ..... 74
*5.5.1. Chemicals* ..... *74*
*5.5.2. Synthesis of polystyrene* ..... *74*

**6. Paper III ..... 80**

**Monodisperse Porous Silica/Polymer Nanocomposite Microspheres with Tunable Silica Loading, Morphology and Porosity ..... 80**
Abstract ..... 81
6.1. Introduction ..... 81
6.2. Results ..... 84
*6.2.1. Size and dispersity* ..... *86*
*6.2.2. $SiO_2$ content* ..... *87*
*6.2.3. Pore size* ..... *89*
*6.2.4. Specific surface area* ..... *91*
*6.2.5. Pore volume* ..... *91*
*6.2.6. Morphology and silica nanoparticle size* ..... *92*
6.3. Discussion ..... 93
6.4. Materials and methods ..... 99
*6.4.1. Chemicals* ..... *99*
*6.4.2. Preparation of HBs* ..... *100*
*6.4.3. Nitrogen adsorption measurements* ..... *100*
*6.4.4. Scanning electron microscopy images (SEM)* ..... *101*

*6.4.5. Thermogravimetric (TGA) determination of $SiO_2$ content* ... *101*
*6.4.6. Experimental design* ... *101*
6.5. Conclusion ... 102
6.6. Appendix ... 103
*6.6.1. Preparation of amino-functionalized porous polymer template* ... *103*
*6.6.2. Supplementary SEM images* ... *103*
*6.6.3. ANOVA Tables for the RSMs* ... *104*

**7. Paper IV ... 107**

**Sol-Gel-Controlled Size and Morphology of Mesoporous Silica Microspheres Using Hard Templates ... 107**
Abstract ... 108
7.1. Introduction ... 108
7.2. Materials and methods ... 110
*7.2.1. Chemicals* ... *110*
*7.2.2. Preparation of MPSMs* ... *111*
*7.2.3. Preparation of reversed-phase HPLC column materials* ... *112*
*7.2.4. Nitrogen sorption measurements* ... *113*
*7.2.5. Scanning electron microscopy images (SEM)* ... *113*
*7.2.6. Experimental design* ... *113*
*7.2.7. HPLC analyses* ... *114*
7.3. Results and discussion ... 114
*7.3.1. Particle size and morphology* ... *115*
*7.3.2. Effect of incorporated silica content on MPSMs pore volume* ... *119*
*7.3.3. Pore size* ... *121*
*7.3.4. Specific surface area* ... *123*
*7.3.5. HPLC separations of biomolecules* ... *124*
7.4. Conclusions ... 127
7.5. Supplementary Information ... 128
*7.5.1. Preparation of Hybrid Beads* ... *128*
*7.5.2. pH Values after 24 h* ... *129*
*7.5.3. ANOVA Tables* ... *129*
*7.5.4. Appendix Figures* ... *131*
*7.5.5. Inverse Size Exclusion Chromatography Characterization of Columns **MPSM-C18-1** and **MPSM-C18-2*** ... *133*

**8. Paper V ... 134**

**Incorporation of Silica Nanoparticles into Porous Templates to Fabricate Mesoporous Silica Microspheres for High Performance Liquid Chromatography Applications ... 134**
Abstract ... 135
8.1. Introduction ... 135
8.2. Materials and methods ... 137
*8.2.1. Chemicals* ... *137*
*8.2.2. Characterization* ... *138*
*8.2.3. Synthesis* ... *139*
8.3. Results and discussion ... 140

8.4. Conclusion ..... 147
8.5. Supplementary Information ..... 149
*8.5.1. Chemicals ..... 149*
*8.5.2. Synthesis of polystyrene ..... 149*
*8.5.3. Synthesis of p(GMA-co-EDMA) ..... 150*
*8.5.4. Characterization of HBs ..... 151*
*8.5.5. $^{13}C$ CP/MAS solid state NMR spectroscopy of p(GMA-co-EDMA) and P@APTES ..... 152*
*8.5.6. DRIFT IR spectroscopy of p(GMA-co-EDMA), P@APTES, HBs and MPSMs ..... 153*

**9. Paper VI ..... 155**

**Tailoring the Morphology of Monodisperse Mesoporous Silica Particles Using Different Alkoxysilanes as Silica Precursors ..... 155**
Abstract ..... 156
Keywords ..... 156
9.1. Introduction ..... 156
9.2. Materials and methods ..... 158
*9.2.1. Chemicals ..... 158*
*9.2.2. Characterization ..... 158*
*9.2.3. Synthesis ..... 159*
9.3. Results and discussion ..... 160
*9.3.1. Preparation and characterization of **MPSM1a–d** and **MPSM2a–d** ..... 161*
*9.3.2. Preparation and characterization of **MPSM1e** and **MPSM1f** ..... 164*
*9.3.3. Chromatographic measurements of **MPSM1b** ..... 165*
9.4. Conclusions ..... 167
9.5. Supplementary Information ..... 169
*9.5.1. Chemicals ..... 169*
*9.5.2. Synthesis of polystyrene ..... 169*
*9.5.3. Synthesis of P@TEPA ..... 169*

**10. Unpublished Results ..... 173**
10.1. Polystyrene – Effects of syntheses conditions on size, dispersity and yield ..... 173
*10.1.1. Material and methods ..... 173*
*10.1.2. Results and discussion ..... 174*
*10.1.3. Conclusion ..... 180*
10.2. Optimization of the separation method for reversed-phase HPLC protein separation ..... 181
*10.2.1. Materials and methods ..... 181*
*10.2.2. Results and discussion ..... 182*
*10.2.3. Conclusion ..... 187*
10.3. Thermogravimetric analysis of template removal ..... 188
*10.3.1. Material and methods ..... 188*
*10.3.2. Results and discussion ..... 189*
*10.3.3. Conclusion ..... 192*

**References ..... 193**

## List of Abbreviations

| | |
|---|---|
| **ACN** | Acetonitrile |
| **ANOVA** | Analysis of variance |
| **APTES** | (3-aminopropyl) triethoxysilane |
| **BET** | Brunauer-Emmet-Teller |
| **BJH** | Barrett-Joyner-Halenda method |
| **BPO** | Benzoyl peroxide |
| **c** | Molar concentration ($mol \cdot L^{-1}$ or $mmol \cdot L^{-1}$) |
| **$C_{18}$** | Functionalization with an octadecyl chain |
| **COVID-19** | Corona virus disease with detection in 2019 |
| **CP(s)** | Center point(s) |
| **CP/MAS** | Cross-polarized / magic angle spinning (NMR) |
| **$d_{90}/d_{10}$** | Measure for relative dispersity; |
| | $d_{90}$: ninth percentile, $d_{10}$: first percentile |
| **DBP** | Dibutyl phthalate |
| **df** | Degrees of freedom |
| **DoE** | Design of Experiments |
| **e.g.** | *exempli gratia* (for example) |
| **EDMA** | Ethylene glycol dimethacrylate |
| **Et al.** | *et alii/aliae* (and others) |
| **EtOH** | Ethanol |
| **FCD** | Face-centered central composite design |
| **FTIR** | Fourier transformation infrared spectroscopy |
| **GMA** | Glycidyl methacrylate |
| **HB(s)** | Hybrid bead(s) |
| **HCl** | Hydrochloric acid |
| **HPDEC** | High-power decoupled (NMR) |
| **HPLC** | High performance liquid chromatography |
| **i.e.** | *id est* (in other words) |

| | |
|---|---|
| **iSEC** | Inverse size exclusion chromatography |
| **IUPAC** | International Union of Pure and Applied Chemistry |
| $K_{SEC}$ | Distribution coefficient in size exclusion chromatography |
| **MeOH** | Methanol |
| **MPSM(s)** | Mesoporous silica microsphere(s) |
| **MVA** | Multivariate Data Analysis |
| $M_w$ | Molecular weight (Da or g·mol$^{-1}$) |
| **n** | Amount of substance (mol) |
| **$NH_3$** | Ammonia |
| **NMR** | Nuclear magnetic resonance |
| **ODTMS** | Trimethoxy (octadecyl) silane |
| **OFAT** | One-factor-at-at-time approach |
| **OPA** | *ortho*-phthalaldehyde |
| ***p*(GMA-*co*-EDMA)** | *Poly*(glycidyl methacrylate-*co*-ethylene glycol dimethacrylate) |
| **P@APTES** | APTES functionalized *p*(GMA-*co*-EDMA) particles |
| **P@TEPA** | TEPA functionalized *p*(GMA-*co*-EDMA) particles |
| **PD** | Pore diameter / Pore size (Å or nm) |
| **PLS-R** | Partial least square regression |
| **POL** | Project oriented learning |
| **PS** | Polystyrene |
| **p-value** | Probability value |
| **PVP** | Polyvinyl pyrrolidone |
| **$R^2$, $R^2_{adjusted}$, $R^2_{predicted}$** | Correlation coefficient, adjusted correlation coefficient under consideration of number of terms, correlation coefficient of prediction |
| **RP** | Reversed phase |
| **RSM** | Response Surface Methodology |
| **$R_{x\text{-}y}$** | Resolution in chromatography between two peaks (x and y) |
| **SARS-CoV-2** | Severe acute respiratory syndrome coronavirus type 2 |

| | |
|---|---|
| **SDS** | Sodium dodecyl sulfate |
| **SEM** | Scanning electron microscopy |
| **SNP(s)** | Silica nano particle(s) |
| **SNV** | Standard normal variate |
| **SSA** | Specific surface area ($m^2 \cdot g^{-1}$) |
| **Std** | Standard Order according to Yates |
| **TBOS** | Tetrabutyl orthosilicate |
| **TEOS** | Tetraethyl orthosilicate |
| **TEPA** | Tetraethylene pentaamine |
| **TFA** | Trifluoroacetic acid |
| **TGA** | Thermogravimetric analysis |
| **THF** | Tetrahydrofuran |
| **TMOS** | Tetramethyl orthosilicate |
| **TPOS** | Tetrapropyl orthosilicate |
| **v./v.** | volume-to-volume |
| $V_0$ | Elution volume of $t_0$ marker |
| $V_e$ | Elution volume |
| $V_i$ | Elution volume of totally permeating volume |
| $V_p$ | Pore Volume ($cm^3 \cdot g^{-1}$) |
| **wt%** | Weight percent |
| $\Phi_{50}$ | Median pore size (Å or nm) |

## Summary

The targeted design of monodisperse, mesoporous silica microspheres (MPSMs) as HPLC separation phases is still a challenge. The MPSMs can be generated via a multi-step template-assisted method. However, this method and the factors affecting the individual process steps and resulting material properties are scarcely understood, and specific control of the complex multi-step process has been hardly discussed.

In this work, the key synthesis steps were systematically investigated by means of statistical Design of Experiment (DoE). In particular, three steps were considered in detail: 1) the synthesis of porous *poly*(glycidyl methacrylate-*co*-ethylene glycol dimethacrylate) (*p*(GMA-*co*-EDMA)) particles, which as template particles, determine the structure for the final MPSMs. In this context, functional models were generated, which allow the control of the template properties pore volume, pore size and specific surface area. 2) In the presence of amino-functionalized template particles, the sol-gel process was carried out under Stöber process conditions. The water to tetraethyl orthosilicate (TEOS) ratio, as well as the concentration of ammonia as basic catalyst were varied according to a face-centered central composite design (FCD). The incorporation of silica nanoparticles (SNPs) into the pore network of the porous polymers was investigated by scanning electron microscopy (SEM), evaluation of the pore properties assessed by nitrogen sorption measurements and determination of the inorganic content by thermogravimetric analysis (TGA). Here, the material properties, such as the amount of attached silica, can be specifically controlled in the resulting organic/silica hybrid material (hybrid beads, HBs). Furthermore, depending on the sol-gel conditions three, potentially four, reaction regimes were identified, leading to different HBs. These range from porous polymer particles coated with a thin protective silica layer, to interpenetrating networks of polymer and silica, to potential particles consisting of a porous polymer core coated with a silica shell. Also, the effects of the use of different precursors and solvents on silica incorporation were investigated. 3) To obtain MPSMs from the HBs, the organic polymer template was removed by calcination. The effects of sol-gel process conditions on the resulting MPSMs were evaluated and relationships between process conditions and material properties were shown in predictive models. Fully porous, spherical, monodisperse silica particles with sizes ranging from 0.5 µm to 7.8 µm and pore sizes from 3.5 nm to 72.4 nm can be prepared specifically.
Subsequent to organo-functionalization, prepared MPSMs were applied as reversed-phase HPLC column materials. Here, the columns were successfully applied for the separation of proteins and amino acids. The separation performance of the materials depends largely on the property profile of the MPSMs, which is predetermined during the preparation of the HBs.

# Zusammenfassung

Das gezielte Design monodisperser, mesoporöser Silicapartikel im Mikrometermaßstab (mesoporous silica microspheres, MPSMs) als HPLC Trennphase stellt noch immer eine Herausforderung dar. MPSMs können über eine mehrschrittige templatgestützte Methode erzeugt werden. Diese Methode und die Einflussfaktoren auf die einzelnen Prozessschritte und daraus resultierende Materialeigenschaften sind jedoch wenig erforscht und eine gezielte Steuerung des komplexen mehrschrittigen Prozesses ist kaum diskutiert.

In dieser Arbeit wurden systematisch die Schlüsselsyntheseschritte mittels statistischer Versuchsplanung (Design of Experiment, DoE) untersucht. Im Speziellen wurden drei Schritte näher betrachtet: 1) die Synthese poröser *poly*(Glycidylmethacrylat-*co*-Ethylenglycoldimethacrylat) (*p*(GMA-*co*-EDMA)) Partikel, welche als Templatpartikel strukturgebend für das Endprodukt, die MPSMs, sind. Hierbei konnten funktionelle Modelle generiert werden, die die Steuerung der Templateigenschaften Porenvolumen, Porengröße und spezifische Oberfläche ermöglichen. 2) In Gegenwart aminofunktionalisierter Templatpartikel wurde der Sol-Gel Prozess unter Stöber Prozessbedingungen durchgeführt. Dabei wurden das Wasser zu Tetraethylorthosilicat (TEOS) Verhältnis, sowie die Konzentration von Ammoniak als basischer Katalysator entsprechend einem flächenzentrierten Versuchsplan (face-centered central composite design, FCD) variiert. Die Einlagerung von Silicananopartikeln (SNPs) in das Porennetzwerk der porösen Polymere wurde über die Analyse vom Rasterelektronenmikroskopie (scanning electron microscopy, SEM) Aufnahmen, Evaluierung der Poreneigenschaften mittels Stickstoffsorptionsmessungen und Bestimmung des anorganischen Anteils über thermogravimetrische Analyse (thermogravimetrical analysis, TGA) untersucht. Hierbei können die Materialeigenschaften, wie beispielsweise der Anteil an angelagertem Silica, im resultierenden organisch/anorganischen Hybridmaterial (hybrid beads, HBs) gezielt gesteuert werden. Darüber hinaus konnten in Abhängigkeit der Sol-Gel Bedingungen drei, potenziell vier, Reaktionsregime identifiziert werden, welche zu unterschiedlichen HBs führen. Die Spanne reicht von porösen Polymerpartikeln die mit einer dünnen schützenden Silica Schicht überzogen sind, über interpenetrierende Netzwerke aus Polymer und Silica bis hin zu potenziellen Partikeln aus einem porösen Polymerkern mit einer Silica Schicht umhüllt. Desweiteren wurden die Effekte des Einsatzes verschiedener Präkursoren und Lösemitteln auf die Silica Einlagerung untersucht. 3) Um MPSMs aus den HBs zu erhalten, wurde das organische Polymertemplat mittels Kalzinierung entfernt. Es wurden die Effekte der Sol-Gel Prozessbedingungen auf die resultierenden MPSMs evaluiert und Zusammenhänge zwischen Prozessbedingungen und Materialeigenschaften in Vorhersagemo-

dellen aufgezeigt. Vollständig poröse, kugelförmige, monodisperse Silicapartikel mit Größen von 0,5 µm bis 7,8 µm und Porengrößen von 3,5 nm bis 72,4 nm können gezielt hergestellt werden.
Nach Aufbringen einer Organofunktionalisierung wurden die hergestellten MPSMs als Umkehrphasen-HPLC Säulenmaterial angewandt. Hierbei wurden die Säulen erfolgreich für die Trennung von Proteinen sowie Aminosäuren angewandt. Die Trennleistung der Materialien hängt maßgeblich vom Eigenschaftsprofil der MPSMs ab, welche bereits bei der Präparation der HBs vorbestimmt wird.

## List of manuscripts included in this thesis

I. Steinbach, J.C.; Fait, F.; Wagner, S.; Wagner, A.; Brecht, M.; Mayer, H.A.; Kandelbauer, A. Rational Design of Pore Parameters in Monodisperse Porous Poly(glycidyl methacrylate-co-ethylene glycol dimethacrylate) Particles Based on Response Surface Methodology. *Polymers (Basel)* **2022**, *14*, 382, doi:10.3390/polym14030382.[1]

II. Fait, F.; Steinbach, J.C.; Kandelbauer, A.; Mayer, H.A. Impact of porosity and surface functionalization of hard templates on the preparation of mesoporous silica microspheres. *Microporous and Mesoporous Materials* **2023**, *351*, 112482, doi:10.1016/j.micromeso.2023.112482.[2]

III. Steinbach, J.C.; Fait, F.; Mayer, H.A.; Kandelbauer, A. Monodisperse Porous Silica/Polymer Nanocomposite Microspheres with Tunable Silica Loading, Morphology and Porosity. *International Journal of Molecular Sciences* **2022**, *23*, 14977, doi:10.3390/ijms232314977.[3]

IV. Steinbach, J.C.; Fait, F.; Mayer, H.A.; Kandelbauer, A. Sol-Gel-Controlled Size and Morphology of Mesoporous Silica Microspheres Using Hard Templates. *ACS Omega* **2023**, *8*, 30273–30284, doi:10.1021/acsomega.3c03098.[4]

V. Fait, F.; Steinbach, J.C.; Kandelbauer, A.; Mayer, H.A. Incorporation of silica nanoparticles into porous templates to fabricate mesoporous silica microspheres for high performance liquid chromatography applications. *Journal of Chromatography A* **2023**, *1705*, 464190, doi:10.1016/j.chroma.2023.464190.[5]

VI. Fait, F.; Wagner, S.; Steinbach, J.C.; Kandelbauer, A.; Mayer, H.A. Tailoring the Morphology of Monodisperse Mesoporous Silica Particles Using Different Alkoxysilanes as Silica Precursors. *International Journal of Molecular Sciences* **2023**, *24*, 11729, doi:10.3390/ijms241411729.[6]

## List of manuscripts not included in this thesis

1. Steinbach, J.; Goedicke-Fritz, S.; Tutdibi, E.; Stutz, R.; Kaiser, E.; Meyer, S.; Baumbach, J.I.; Zemlin, M. Bedside Measurement of Volatile Organic Compounds in the Atmosphere of Neonatal Incubators Using Ion Mobility Spectrometry. *Frontiers in Pediatrics* **2019**, *7*, 248, doi:10.3389/fped.2019.00248.[7]

2. Steinbach, J.C.; Schneider, M.; Hauler, O.; Lorenz, G.; Rebner, K.; Kandelbauer, A. A Process Analytical Concept for In-Line FTIR Monitoring of Polysiloxane Formation. *Polymers (Basel)* **2020**, *12*, 2473, doi:10.3390/polym12112473.[8]

3. Wagner, A.; Wagner, S.; Bredfeldt, J.-E.; Steinbach, J.C.; Mukherjee, A.; Kronenberger, S.; Braun, K.; Kandelbauer, A.; Mayer, H.A.; Brecht, M. Chemical Imaging of Single Anisotropic Polystyrene/Poly (Methacrylate) Microspheres with Complex Hierarchical Architecture. *Polymers (Basel)* **2021**, *13*, 1438, doi:10.3390/polym13091438.[9]

4. Wahrendorff, P.; Stefanakis, M.; Steinbach, J.C.; Allnoch, D.; Zuber, R.; Kapfhammer, R.; Brecht, M.; Kandelbauer, A.; Rebner, K. Simultaneous Determination of Droplet Size, pH Value and Concentration to Evaluate the Aging Behavior of Metalworking Fluids. *Sensors* **2021**, *21*, 8299, doi:10.3390/s21248299.[10]

5. Steinbach, J.C.; Golovko, D.S.; Kandelbauer, A.; Rebner, K. Real-Time Quantification of Meat Paste Constituents Displaying Nonlinear Blending Behavior Including Salt Using an In-Line NIR MEMS Sensor. *ACS Food Science and Technology* **2023**, *3*, 1288–1299, doi:10.1021/acsfoodscitech.3c00163.[11]

## Contributions to the manuscripts included in this thesis

I. Syntheses of these particles were split between Fabio Fait (six batches) and me (17 batches). All columns were packed by my colleague F. Fait. All inverse size exclusion chromatography (iSEC) measurements and infrared measurements were performed and analyzed by Fabio Fait and me. The processing of the scanning electron microscopy (SEM) images was performed by me. The conceptualization and evaluation of the response surface model, multivariate data analysis, visualization was done by myself. The manuscript writing was performed by F. Fait and myself.

II. F. Fait prepared all samples. Analyses by nitrogen adsorption and the protein separations and were done by F. Fait and me. The Fourier-transform infrared spectroscopy (FTIR) measurements were acquired and processed using multivariate data analysis of the FTIR data was performed by me. The manuscript was written by Fabio Fait and myself.

III. All syntheses and analyses described were planned and analyzed by myself. This includes design and evaluation of the response surface model. Nitrogen sorption measurements, thermogravimetric analysis (TGA) and the analysis of the SEM images was performed by F. Fait and me. The manuscript was written by me.

IV. All syntheses were planned and conducted by me. Fabio Fait performed the particle calcination and packing of the columns. Nitrogen sorption measurements, TGA and high performance liquid chromatography (HPLC) measurements were performed by F. Fait and me. I analyzed the measurements and SEM images and wrote the manuscript.

V. The syntheses were planned and prepared by F. Fait. The analysis of the particles by nitrogen sorption measurements, TGA and HPLC measurements were performed by Fabio Fait and me. The manuscript was written by F. Fait.

VI. The syntheses were planned and prepared by F. Fait and S. Wagner. The analysis of the particles by nitrogen sorption measurements, TGA and HPLC measurements were performed by Fabio Fait and me. The manuscript was written by F. Fait.

Fabio Fait prepared 41 syntheses included in chapter 10.1. Two POL projects (Project Oriented Learning) were conducted under the author's supervision[12,13]. The results of the POL projects are an are part of the present work.

The results of this PhD thesis have either already been published in peer-reviewed scientific journals, have been submitted for publication, or are prepared for submission. All results are be summarized and discussed in chapter 2. The manuscripts to which I contributed either as first or co-author are included in chapters 4.–9. The summary (chapter 2) will focus primarily on the manuscripts authored by me as first-author (chapters 4.–7.).

# 1. Introduction and objectives

## 1.1. Introduction

Porous silica particles are extensively studied due to their versatility in applications. They are used as drug carriers[14–16], in catalysis[17], in biosensors[18,19], and as column materials in purification and separation in chromatography[20–22].

High performance liquid chromatography is a key analytical method and is constantly improved further to keep up with increased application prerequisites[23,24]. Especially within medical research and pharmaceutics, HPLC is one of the most used methods for analysis and purification processes of biomolecules[25,26]. In this context, the demands on specificity and throughput are continuously increasing as many more applications and prerequisites are formed. In particular, the analysis and purification of amino acids[27], peptides and proteins[25,28] plays a key role in the development of new drugs and vaccines[24]. For example, in the context of the COVID-19 outbreak, the characterization of the SARS-CoV-2 spike protein[29], interaction studies[30], the screening of potential drugs[31,32], and the purification of the RNA vaccines[33,34] were empowered by liquid chromatography. To keep pace with the ongoing trend towards personalized medicine[35,36], the development of HPLC methods and column materials will continue to play a key role. Column properties are crucial for the separation performance[23], hence a tailored material for each application is desirable.

Most commercially available columns are based on silica packing materials because of their versatility in surface modification, high thermal and mechanical stability, and high resistance to common solvents[37,38]. To prepare separation phases with greater selectivity, the specific surface area can be enlarged by decreasing the particle size[39]. However, this increases the back pressure of the system and in turn raises equipment requirements. By introducing pores into the silica packing material, its surface area can be enlarged while maintaining the same particle size[40]. In addition, pores allow higher flow rates with a low back pressure, which is particularly important in the initial purification of peptides and proteins. In this context, the pore size plays a decisive role in which kind of proteins or peptides are separable. For proteins with high molecular weights, pore sizes of 30 nm to 200 nm are required while up to 2000 Daltons pores of approximately 10 nm are sufficient[41]. Likewise, the mass transfer resistance of wide pore materials is reduced, which has a positive effect on the separation efficiency[42]. Permeability of the packing can be improved by a narrow particle size distribution and a spherical shape of the particles[43]. Since the structural properties of the silica particles largely determine its column performance, control of the morphology and pore structure is of great importance[44].

Stöber's and Fink's method for the preparation of spherical silica particles with a narrow size distribution is a pioneer work in sol-gel chemistry. Alkoxysilanes undergo hydrolysis and condensation under basic conditions in alcoholic media and form uniform spherical silica particles in a range from 50 nm to 2000 nm[45]. Many modifications of this method have been studied since then. One of the most successful strategies to direct the properties of porous silica particles is to perform the synthesis using so-called templates, which already have desirable structural properties[46]. The synthesis route involves three steps: 1) the preparation of the template, 2) the subsequent synthesis of the silica structure, and 3) the removal of the structure-directing template[46–48]. The nature of the templates can be generally divided in "soft" and "hard" templates. Soft-templating methods use amphiphilic molecules with a hydrophilic and a hydrophobic domain. These are usually surfactants or amphiphilic block polymers[47,49–52]. In water or solvents, these assemble themselves hierarchically and thus control the deposition of the precursor, and consequently the properties of the resulting porous silica nanoparticles[53]. The pore sizes can be selectively controlled by varying synthesis parameters such as temperature, surfactant concentration, pH, and others using this method. However, a major drawback of soft templating is that the overall particles are often only a few hundreds of nanometers in size or irregular in shape[47,52,54]. Hard-templates are more rigid and thus are not prone to deformation, which allows a higher degree of uniformity. The scale of structural features that can be imprinted with hard template ranges from micrometer to nanometers[48]. Using this method, monodisperse, mesoporous silica microspheres (MPSMs) can be prepared[22,55]. Discrete porous *poly*(glycidyl methacrylate-*co*-ethylene glycol dimethacrylate) particles (*p*(GMA-*co*-EDMA)) have been used as hard templates as their structure and morphology can be modified while maintaining a monodisperse size distribution[1,56,57]. As the surface modification plays a critical role in the deposition of silica in or on the polymeric template[48], the easily modifiable epoxide function of *p*(GMA-*co*-EDMA)[58] is beneficial. After incorporation of silica in the porous polymer template by conduction of the sol-gel process under Stöber conditions, forming an intermediate organic/silica hybrid material, the organic template is removed by calcination, resulting in the MPSMs.

However, these synthesis strategies towards tailored materials are complex and underly multiple different influencing factors for each preparative step. Commonly, the effect of one factor is examined, while other factors are kept constant (one-factor-at-a-time approach, OFAT). The more factors are to be examined, the more elaborate the OFAT method becomes. However, by examining the factors in isolation, the OFAT method does not reveal system interactions between factors[59–61]. Therefore, a statistical approach with Design of Experiments (DoE) or Response Surface Methodology (RSM) is required, which provides an efficient experimental strategy by varying mul-

tiple variables simultaneously[59–61]. Compared to the OFAT, RSM allows the determination and quantification of both linear and non-linear factor effects, as well as their interactions with other studied factors, while minimizing the number of required experiments[62]. RSM establishes process models, which reflect the effects of various studied factors, making it an important tool for predicting the system behavior for each combination of factor settings within the design space and thus inferring causality in complex systems[61,63].

Due to the complex interplay and the large number of parameters in the synthesis of MPSMs via the hard-template route, the specific adjustment of pore properties for special application requirements represents a major challenge. Therefore, the aim of this work is to systematically characterize the respective steps of the multi-step synthesis and to reveal relationships between synthesis settings and material properties. This knowledge is crucial to enable a targeted preparation with a specific property profile.

## 1.2. Objectives

The main objective of this PhD thesis is to systematically characterize the template assisted multi-step process to enable the knowledge-based and targeted synthesis of MPSMs for the application as HPLC column material. The main goal can be divided into subobjectives, which are discussed in detail in manuscripts I–VI.

1. Selectively vary the pore properties of the *p*(GMA-*co*-EDMA) template while maintaining the monodisperse distribution and spherical appearance of the template particles.
2. Examine the effects of different template properties on the incorporation of silica and the resulting properties of the MPSMs.
3. Elucidate the effect of changes in the sol-gel process conditions on the properties of the organic/silica hybrid material and steering of the incorporation of silica nanoparticles into the porous polymer network.
4. Provide predictive models for the characteristics of MPSMs as a function of sol-gel process conditions and demonstrate the capability of the MPSMs as column material for the chromatographic separation of proteins and amino acids.

## 1.3. Mesoporous silica microspheres by a hard template assisted method – from monomers to packing materials

Porous materials can be categorized according to IUPAC based on their pore sizes[64]. Microporous materials have pores that are less than 2 nm in diameter, mesoporous materials have pores that are between 2 nm and 50 nm in diameter, while macroporous materials exhibit pore diameters exceeding 50 nm[65–67].

The method, which is examined in detail in this thesis for preparing mesoporous silica microspheres (MPSMs) with defined size and narrow size distribution is based on using a sacrificial polymeric hard template. The hard template in this work consists of a thermoset copolymer, which is formed by seeded swelling polymerization. The seed particles used in the swelling polymerization define the overall shape and dispersity and thus, are critical for the quality of the final end product –

the MPSMs. The general synthesis strategy is derived from the work of Xia et al.[56,57] and was refined by S. Wagner[68].

### 1.3.1. Reaction procedure for the preparation of MPSMs

In **Figure 1.1** the reaction scheme for the synthesis of MPSMs from initial reactants is given. The initial step is the preparation of the seed particles, which are monodisperse polystyrene (PS) particles. These are synthesized via dispersion polymerization in alcoholic media using benzoyl peroxide (BPO) as radical initiator (**Figure 1.1**a). The PS particles were activated using dibutyl phthalate (DBP), a small hydrophobic substance to enhance the diffusion of the organic phase. This ensures a uniform swelling for the subsequent seeded swelling polymerization to prepare porous thermoset spheres (**Figure 1.1**b). These porous polymer particles consisted of glycidyl methacrylate (GMA), and ethylene glycol dimethacrylate (EDMA), which acts as crosslinker (**Figure 1.1**b). The epoxide group allows the functionalization with tetraethylene pentamine (TEPA) via ring opening reaction (**Figure 1.1**c). This amino-functionalization increases the attractivity for silica nanoparticles in the subsequent sol-gel reaction under basic conditions. Using tetraethyl orthosilicate (TEOS) as precursor in a mixture of ethanol and water with ammonia as basic catalyst, the hydrolysis and condensation reaction takes place and the silica nanoparticles are incorporated into the network of the porous polymer template (**Figure 1.1**d). Subsequently, the sacrificial template is removed by calcination and the MPSMs remain (**Figure 1.1**e).

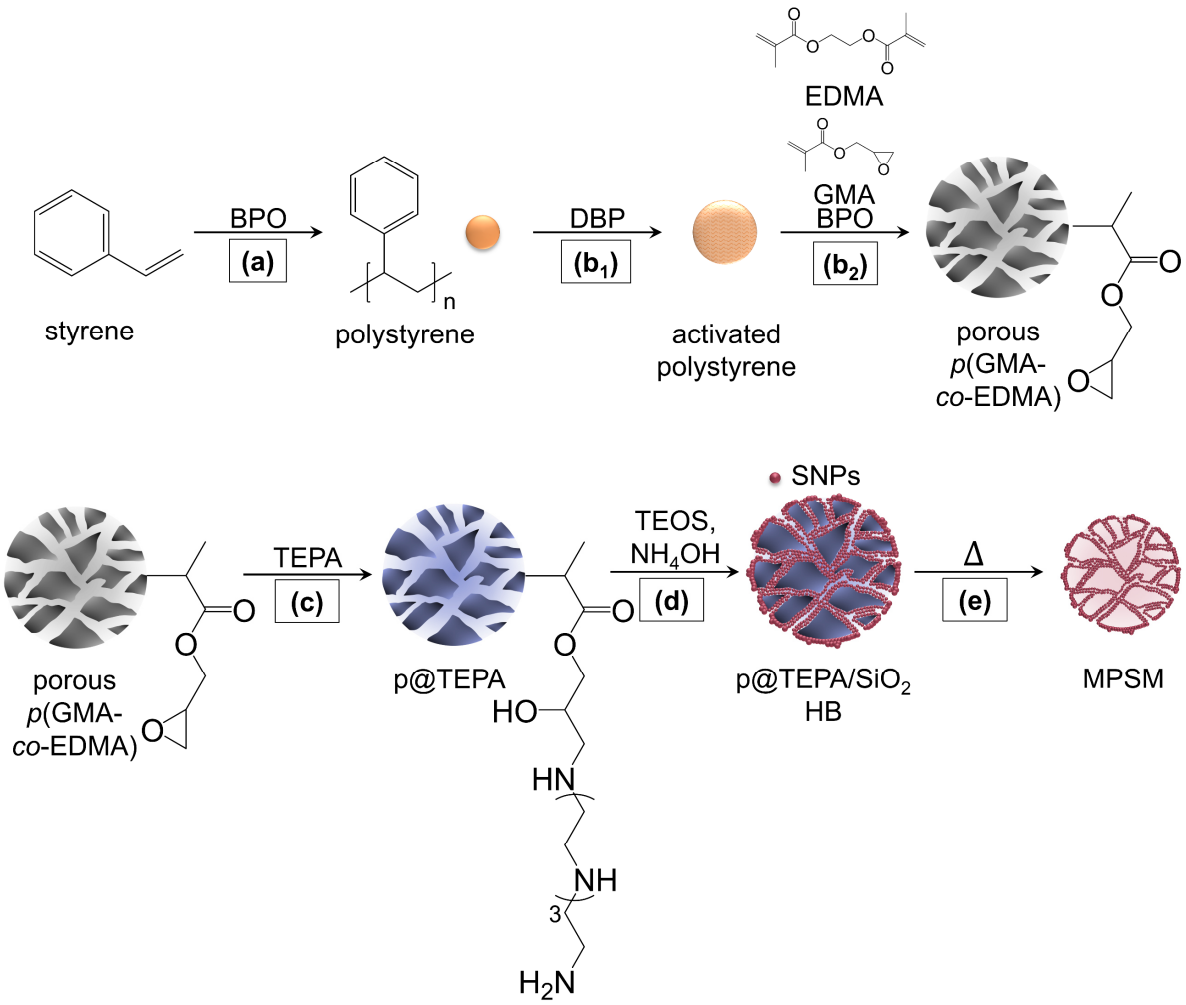


**Figure 1.1** Reaction procedure with reactants from seed particle via porous sacrificial hard template to mesoporous silica microsphere (MPSM). **a)** The polystyrene particles are prepared by dispersion polymerization and **b1)** are subsequently activated with dibutyl phthalate (DBP) and **b2)** used as seed particles during seed-swelling polymerization to prepare porous *p*(GMA-*co*-EDMA) particles. **c)** The *p*(GMA-*co*-EDMA) particles are then amino-functionalized to increase the attractiveness for silica incorporation. **d)** The silica is deposited into the porous network of the template by the sol-gel process. **e)** After calcination of the sacrificial template, the MPSMs remain as products[68].

### 1.3.2. Seed particle synthesis – Dispersion polymerization

The preparation of seed particles with a narrow size distribution is the initial step of the multi-step synthesis in achieving MPSMs. Since these seed particles are decisive for the size distribution, as well as the resulting particle shape of each successive step, their uniformity and shape are crucial.

Monodisperse and spherical polystyrene seeds can be prepared by dispersion polymerization. The attainable size varies between 0.1 µm up to 10 µm[69,70]. The monomer, initiator and stabilizer are soluble in the continuous alcoholic phase and form a homogeneous mixture at the onset of the reaction. After initiation of the polymerization, here by radical polymerization after thermal decomposition of BPO, oligomers start to form. The chain length increases until the solubility in the continuous phase is

exceeded and nuclei precipitate. The stabilizer adsorbs on the formed nuclei, prevents coagulation and influences the particle shape and stability. The PS particles grow by addition of monomers and oligomers from the continuous phase, resulting in their spherical shape[71–73]. The monomer, initiator and stabilizer type and concentration have an impact on the size and dispersity of the resulting PS particles. The effects of solvent type, monomer, initiator and stabilizer concentration, as well as the effect of added water to the continuous phase are investigated systematically and discussed in detail in chapter 10.1.

### 1.3.3. Porous polymeric template – Seed-swelling polymerization

Porous polymer particles can be prepared by suspension polymerization with the addition of inert solvents, so-called porogens, into the reaction mixture. However, particles prepared by suspension polymerization exhibit a broad particle size distribution which requires a subsequent classification[74–76]. This drawback of suspension polymerization can be overcome by using non-crosslinked polymer latexes, such as PS, as seed particles in the seed-swelling polymerization. This approach was implemented by Ugelstad et al.[77,78]. The general procedure of the seed-swelling polymerization as conducted in this thesis is shown in **Figure 1.2**.

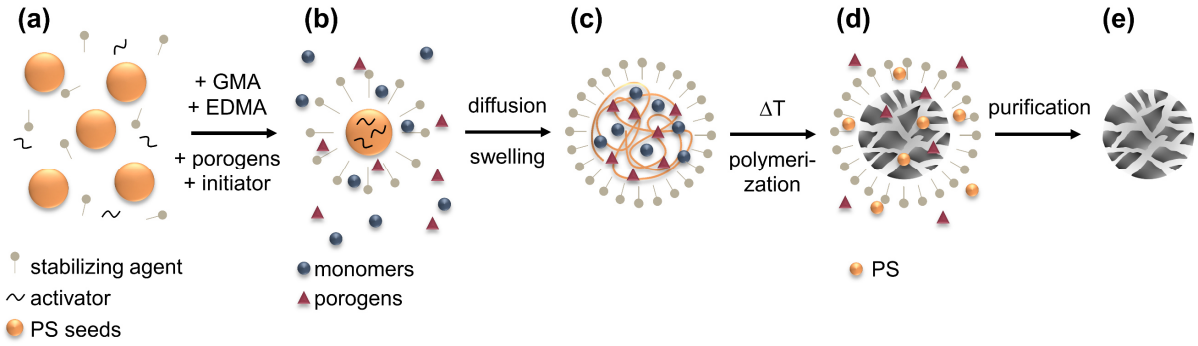


**Figure 1.2** Scheme of the seed-swelling polymerization procedure. **a)** PS seeds ● are dispersed in the continuous phase (water) in the presence of a stabilizing agent. The PS seeds are "activated" with a non-water-soluble low molecular weight substance ∼. **b)** An emulsion containing the monomers ●, the porogens ▲ and the initiator (not explicitly shown) is added to the activated seeds. **c)** The monomers and the porogens diffuse into the seeds and swelling occurs. The PS seeds are dissolved and its polymer chains become mobile. **d)** Thermal decomposition of the initiator starts the polymerization of the monomers. The shift of solubilities during the formation of the new polymer leads to the phase separation and the inert porogens form pores. **e)** During the washing process, residual PS, porogens and stabilizer are removed from the porous polymer particle[9].

Prior to swelling with monomers and porogens, an "activation" step is performed by adding a highly non-water-soluble compound with a low molecular weight, which is absorbed by the seeds (**Figure 1.2**a). This facilitates the subsequent seed swelling with monomers and porogens by diffusion into the seed particle[79,80] (**Figure 1.2**b), since the monomers in particular are often partially soluble in water. The size of the swollen

seeds increases uniformly while the shape and size distribution are maintained[78,79,81]. The degree of swelling depends on the amount of seeds and organic phase[82] (**Figure 1.2**c). The pore formation is based on solubilities of the monomers and porogens in the seed and the change in solubility during polymerization of the monomers (**Figure 1.2**.d). The progressing growth of the polymer network leads to phase separation as the polymer becomes insoluble in the seed and the porogens[70]. The solubility plays and important role in the formation of the pores. In the case when a good solvent for the resultant polymer is used as porogen, the phase separation occurs after the gel point of the network. Otherwise, the phase separation occurs prior to the gel point of the polymer network, if non-solvents or less suitable solvents are used that lead to only partial dissolution of the polymer. These phenomena are referred to as ν- and χ-induced syneresis, respectively[83]. A good solvent for the polymer results in a high specific surface area (SSA), smaller pores but a rather low pore volume while a less suitable solvent results in lower SSAs, larger pores and a higher pore volume[79].

The seed-swelling polymerization is a complex system, as the properties of the resulting porous polymer particles and their respective properties, such as pore size, SSA, and pore volume, depend on the type, the amount, and the relative composition of the reaction mixture. Additionally, the solubilities of all reactants and the resultant polymer within each other are also critical. The effects of the monomer to porogen ratio, the composition of the monomers with respect to the amount of cross-linker, and the composition of the porogen mixture on the properties of porous *p*(GMA-*co*-EMDA) particles were investigated to establish rational models to predict the particle properties[1] (see chapter 4. **Paper I**[1]).

### 1.3.4. Porous silica particles – Sol-gel process on hard templates

#### *1.3.4.1. Stöber process*

The Stöber method is a particular variant of the sol-gel process. It allows the controlled synthesis of spherical, nonporous silica particles with a narrow size distribution in a size range from 0.05 μm to 2.0 μm[45,84]. The hydrolysis and condensation reaction of alkoxysilanes is performed in alcoholic media and is catalyzed with ammonia. The gross reaction equation of the Stöber process for the hydrolysis and condensation reactions of tetra alkoxysilanes (R = alkyl group) to form three-dimensional $SiO_2$ networks[85] is given in equation (1.1).

$$n\ Si(OR)_4 + 2\ n\ H_2O \qquad n\ SiO_2 + 4n\ ROH \tag{1.1}$$

R = alkyl group

In a first step, the base-catalyzed hydrolysis, the alkoxysilanes undergo a nucleophilic substitution reaction ($S_N2$ mechanism[86]) with hydroxide ions to form silanols. The rate

of hydrolysis increases with higher degrees of hydrolysis as the steric hindrance from the alkoxy groups decreases and the electrophilicity of the silicon atom increases[85,87,88]. The subsequent condensation reaction starts as soon as first silanol species are formed[89]. The silanol group deprotonates under basic conditions and the formed silanolate ions attack another silicon atom to form siloxane bonds. Thereby, either two neighboring silanol groups can react, or condensation between a silanol and an alkoxy group occurs. These processes are called water and alcohol condensation, respectively[87].
Under basic conditions, the rate of hydrolysis is slower than the rate of condensation, as the silanol groups are deprotonated more easily than water. This favors the nucleophilic attack at the silicon atoms and results in preferred attachment to larger siloxane species rather than monomers or small oligomers[88,90].

The size of silica nanoparticles (SNPs) and the size distribution resulting from the Stöber method are dependent on the reaction conditions, as the rates of hydrolysis and condensation are affected by these. Reaction conditions affecting the silica formation include[45,85,91]:

- the chain length of the alkyl group of the precursor[45,68,85,89,91]
- the alkyl chain length of the solvent[68,85,91–94]
- the type and concentration of the catalyst[68,85,88,91–93,95–102]
- the water concentration[68,85,88,91,92,95–99,101–103]
- and the temperature[84,85,91,95,96,98,101].

### *1.3.4.2. Growth mechanisms of silica particles under Stöber process conditions*

For decades a tremendous effort has been dedicated to clarify the mechanism of particle growth. There are two predominant mechanisms: the monomer addition growth model (**Figure 1.3** and **Figure 1.4**a), and the aggregation model (**Figure 1.4**b)[88,104].

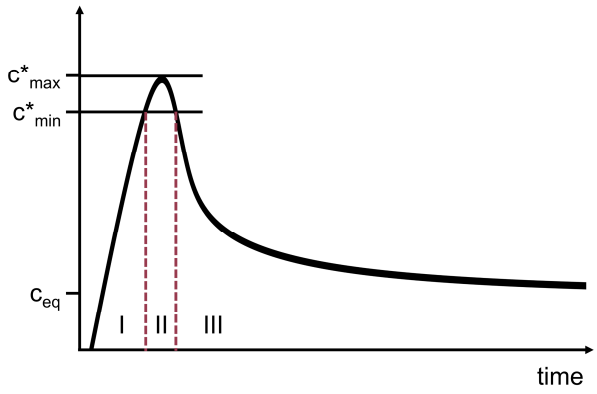


**Figure 1.3** Model of initial phase of particle formation by LaMer and Dinegar[105]. Phase I: Induction phase. Phase II: phase of rapid self-nucleation. Phase III: Growth by diffusion.

The initial stages until the formation of nuclei or primary particles is similar for both models. The alkoxy precursor is hydrolyzed and the hydrolyzed silanol species condense to form dimers, trimers and oligomers. This process continues until a critical supersaturation of hydrolyzed silanol species is reached (induction phase, **Figure 1.3**), the formed siloxane clusters become insoluble and collapse to nuclei/primary particles[84,105–108] (**Figure 1.3** phase II and **Figure 1.4** nucleation). The monomer addition growth model is based on the mechanism of sulfur hydrosols growth proposed by LaMer and Dinegar[105]. It was adapted to the silica formation and growth in Stöber process conditions by Matsoukas and Gulari[92,109,110]. After nucleation, the particles continue to grow by condensation of hydrolyzed monomers to the surface of preformed primary particles (**Figure 1.3** phase III).

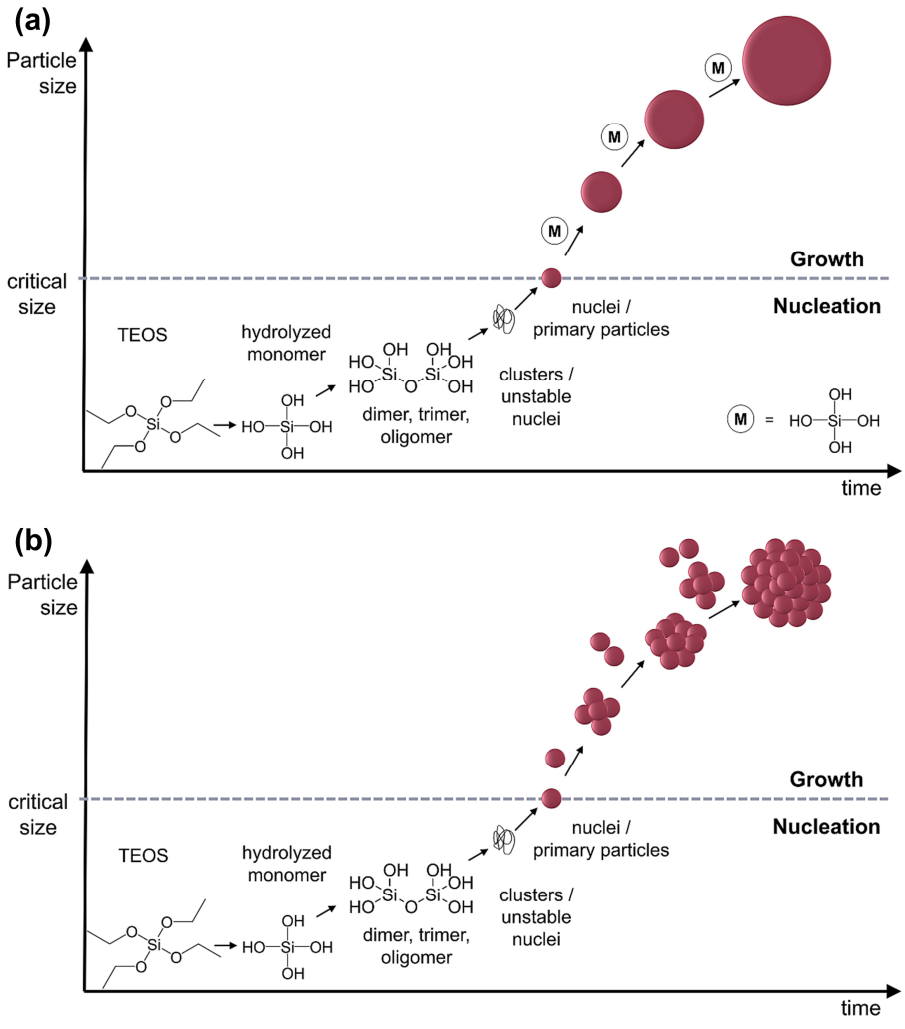


**Figure 1.4** Scheme of (silica) particle growth according to the two prevailing models starting from the monomer (here: tetraethyl orthosilicate (TEOS)): **a)** growth by monomer addition and **b)** by aggregation mechanisms[104,111].

The second model is the aggregation growth model by Bogush and Zukoski[95,112,113]. It proposes that the primary particles formed during the nucleation phase are unstable and thus aggregate to form larger particles (**Figure 1.4**b). However, the two models

cannot account for all variations in size and dispersity[88,104]. Later, mixed models were introduced, proposing a change of mechanism from aggregation of unstable primary particles in the initial stage, to monomer addition in the later stage[93,108,114]. Also, a dependency on the reaction conditions was proposed by Han et al.[88]. High or low ammonia ($c \geq 0.95$ mol·L$^{-1}$ or $c < 0.95$ mol·L$^{-1}$) concentrations led change the kinetic balance between hydrolysis and condensation, which leads to a change in mechanism. At higher ammonia concentrations, the hydrolysis is more effective and thus the induction phase and growth phase are clearly separated. For low concentrations, the hydrolysis is ineffective and the nucleation continues even after the start of the growth. Here, the secondary nucleation results in smaller particles with a broader size distribution[88].

#### *1.3.4.3. Sol-gel process in presence of polymeric hard templates*

To introduce pores into the silica particles, templating methods are required[48,53,115]. In contrast to soft templating, hard templates allow to generate MPSMs with particle sizes in the micrometer range, a spherical shape and a narrow size distribution[22,55,116].

Subsequent to the preparation of the template, the silica is incorporated into the pores under the formation of a composite and the final MPSMs are released after the template removal (**Figure 1.1**)[46–48,53,115]. If the pores of the templates are filled with the silica, this process is also known as "nanocasting", and if the template is coated and a hollow structure remains after calcination it is known as "nanocoating"[53,117]. However, this is a complex step as multiple requirements have to be met. The selected polymer template has to be stable during the templating process and be easily removable without destroying the newly formed structure[51,117]. The properties of the template, like pore size and volume, are not the only factors, which affect the resulting MPSMs. Moreover, the intermolecular interactions between template and precursor must be considered. This is necessary to ensure the incorporation of silica into the pores of the template and to prevent precipitation of silica in the continuous phase[48,53]. This can be accomplished through a surface modification, which introduces a favorable surface charge and creates an electrostatic attraction between template and the precursor/silica[48]. Effective surface modifications for the silica incorporation are hydroxy- or amino-functionalizations[48], whereas non-functionalized *p*(GMA-*co*-EDMA) are only coated with silica[68]. Other surface modifications also affect the morphology and properties of the resulting MPSMs. Grama et al. hydrolyzed the *p*(GMA-*co*-EDMA) to open the epoxy groups and to generate diol groups. However, the amount of incorporated silica into the template was limited (< 10 wt%)[118]. Xia et al. showed[56,57] that the incorporation of silica into the template was improved, when the *p*(GMA-*co*-EDMA) particles were functionalized with TEPA instead of ethylenediamine[55]. Chen et al. and Bai et al. used three different amino-functionalizations (3-aminopropyl) triethoxysilane

(APTES), trimethylamine hydrochloride (TMA) and TEPA, and attained MPSMs with different morphological properties and varying pore sizes[22,119]. Another way to steer the incorporation of silica into the template, besides the surface modification of the template, is the control of hydrolysis and condensation by adjusting the sol-gel process conditions using the process factors listed in chapter 1.3.4.1.

By incorporating the silica into the polymer template, an organic/silica hybrid material is obtained as an intermediate. To obtain the MPSM, the organic template is removed. The removal of the template, in case of *p*(GMA-*co*-EMDA) or other thermoset templates, is performed by means of calcination. The template is "sacrificed" to release the MPSM by thermal combustion of the polymer. Typical calcination temperature for the removal of a polymeric template lies at 500 – 600°C, depending on the material of the template[120]. Although, silica is generally thermally[38] stable it undergoes drying and shrinking[87,91]. Up to 190 °C the adsorbed water, including the monolayer, is removed from the surface *in vacuo*. However, the degree of hydroxylation of the dry silica is maximal with 4.6 OH-groups per $nm^2$[121]. At 400 °C vicinal OH-groups condense and the degree of hydroxylation is drastically reduced[120–122]. They undergo condensation and form Si-O-Si bonds, which results in shrinkage[85,121]. With further increasing temperatures, the siloxane network becomes denser and the loss of porosity occurs[68,121,123,124].

The above-mentioned process conditions and steps, result in a large number of possible control parameters that influence the final product, the MPSMs, listed below:

- the morphological properties of the template itself (chapter 4. **Paper I**[1] and chapter 5. **Paper II**[2]),
- the surface modification of the template[55,68,118,119],
- the process conditions of the sol-gel process (chapter 6. **Paper III**[3], chapter 7. **Paper IV**[4]**,** chapter 8. **Paper V**[5], and chapter 9. **Paper VI**[6]),
- and the template removal or calcination step (chapter 7. **Paper IV**[4] and chapter 10.3).

## 2. Summary of the main results

The preparation of mesoporous silica microspheres (MPSMs) with a narrow size distribution in the micrometer range is challenging. As mentioned above, MPSMs can be prepared in a template assisted multi-step synthesis approach. However, with each required step the number of influential factors that effectively impact the properties of the prepared MPSMs increases. Thus, a detailed insight into each individual synthesis step is essential. Within this thesis the reaction steps were investigated in detail, which is the main focus, as well as the effect across the preparation procedure (**Figure 2.1**).

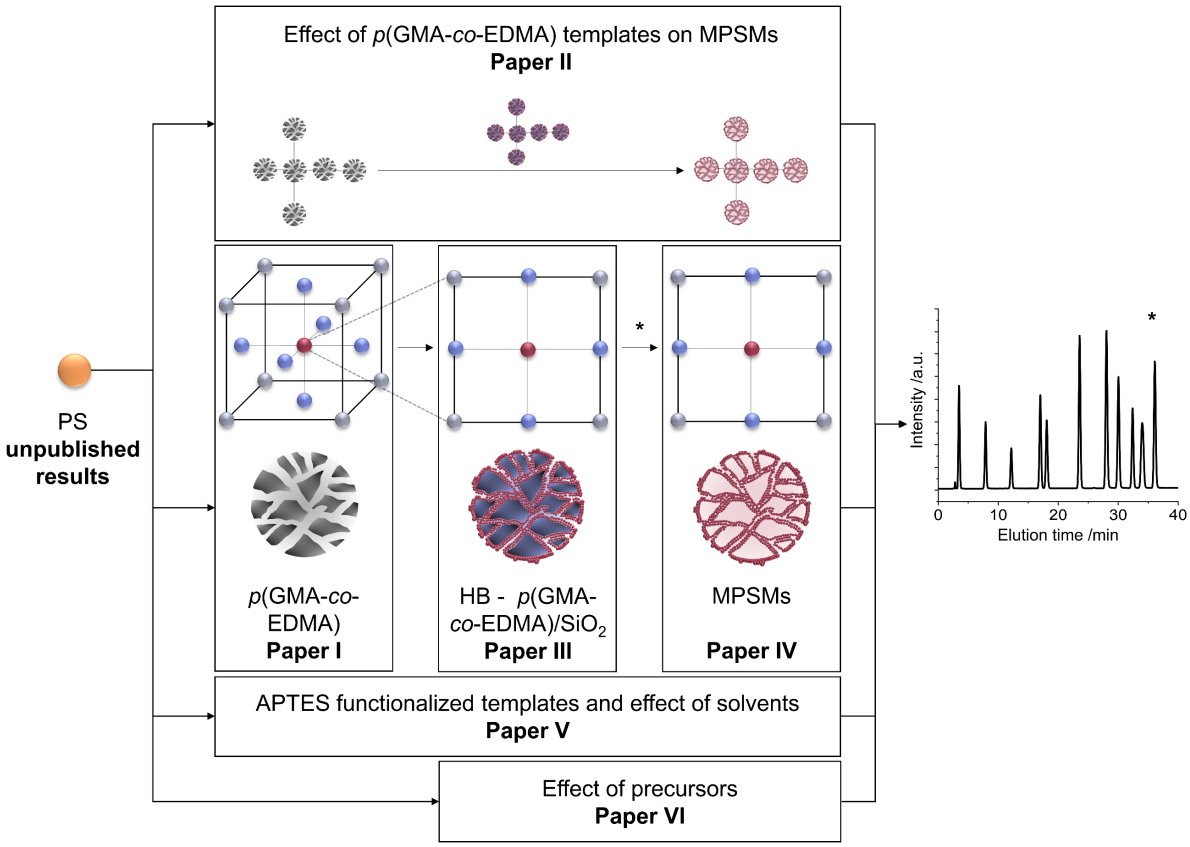


**Figure 2.1** Overview of the results included in this thesis. The synthesis of MPSMs was investigated both horizontally along subsequent reaction steps (**Paper II**[2], **Paper V**[5], and **Paper VI**[6]) and vertically within each reaction step (**Paper I**[1], **Paper III**[3], and **Paper IV**[4]). In **Paper I**, **Paper III**, and **Paper IV** the response surface methodology (RSM) design type is shown. Grey points mark the factorial points, red dots mark the center points, and blue points mark the axial points of the RSM. The main focus is on **Paper I** to **Paper IV**. The preparation of PS seed particles and studies to the process steps calcination and HPLC method optimization both indicated with an asterisk (*), are discussed in the chapter 10. unpublished results.

### 2.1. Preparation of monodisperse PS seeds

The preparation of monodisperse seed particles by dispersion polymerization of styrene is the initial step of the multi-step procedure. The size distribution obtained within this step is crucial, as it affects all following intermediates and the final MPSM.

In addition, the size of the PS seeds is also a contributing factor to the size of the subsequent porous *p*(GMA-*co*-EDMA) particles[82,125]. A comprehensive evaluation of the experimental design space was performed to determine the regions that yield monodisperse PS particles. Subsequently, the objective was to selectively vary the particle size by adjusting the process factor settings within these regions while maintaining a narrow size distribution (chapter 10.1). The effects of solvent type (ethanol or methanol), monomer wt%, stabilizer wt% initiator wt%, and ratio of solvent to water as continuous phase were investigated.

Changing the solvent from ethanol to methanol reduced the particle size. A similar trend was observed with the addition of water to the solvent. These observations results from diminished solubility of oligomer chains in the continuous phase as its polarity is increased, and consequently an earlier precipitation of PS occurs[126,127]. Although, smaller PS particles are favorable as seed particles for the subsequent seed-swelling procedure, the size distribution was broadened through the addition of water to the continuous phase up to the point, where bimodal distributions with size differences between the two dominant particle sizes of up to 150 times were observed. The size of the PS particles was also reduced by limiting the monomer and initiator concentrations. However, the yield was marginal and in some cases no precipitation occurred. Thus, the experimental range was focused on experiments with pure ethanol as solvent and higher concentrations of monomer and initiator, to ensure sufficient yield. With the restrained experimental design, models for the particle size, the dispersity and the yield were established with high predictive power ($R^2_{predicted} \geq 0.72$). Five of 16 factor level setting combinations lead to monodisperse PS particles, which varied in size between 0.54 µm and 2.60 µm.

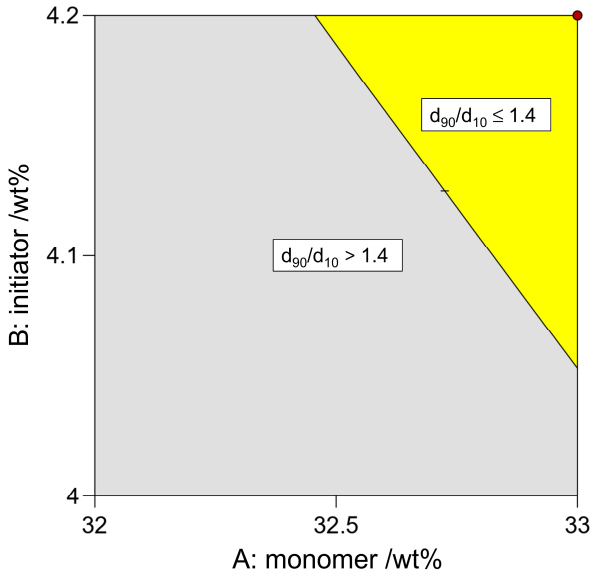


**Figure 2.2** Overlay contour plot depicting the process window in which monodisperse particles can be prepared with a yield ≥ 50 %. The yellow area indicates the region with $d_{90}/d_{10} \leq 1.4$.

Monodisperse particle distributions are attained by utilizing high monomer and high initiator concentrations or by utilizing low monomer concentrations in conjunction with low initiator concentrations. Within these regions, the stabilizer concentration allows to adjust the size without affecting the size distribution. However, a high yield (≥ 50 %) is only attainable in the higher range of the experimental space, as shown in **Figure 2.2**. Monodisperse PS particles in the range of 1.6 μm to 2.5 μm can be prepared by adjusting the required amount of stabilizer.

## 2.2. Designing the pore properties of *p*(GMA-*co*-EDMA) templates

Porous *p*(GMA-*co*-EDMA) prepared by seed-swelling polymerization exhibit desirable properties for use as hard templates in the template-assisted synthesis for MPSMs. Their narrow size distribution and the spherical shape are promoted by the seed particles. The pore properties of the *p*(GMA-*co*-EDMA) template particles can be varied by adjusting the reactant ratios. The formation of pores is largely dependent on the state of the reaction (prior to or after gel point), when the phase separation occurs, and on the solubility shifts in the system as polymerization progresses. In order to selectively adjust the material properties of SSA, pore size ($\Phi_{50}$) and pore volume ($V_p$), a statistical and systematic approach using RSM, was applied (chapter 4. **Paper I**[1]). This permits to establish a modeling of the effects of the process factors on the material properties in the investigated experimental space. For this purpose, three process factors of the seed-swelling polymerization were specifically and simultaneously varied according to the RSM: (A) the ratio between monomers and porogens, (B) the composition of the monomers, i.e. the ratio between cross-linker (EDMA) and monomer (GMA) bearing a functional group, and (C) the composition of the porogens consisting of two inert solvents (toluene and cyclohexanol). Nineteen particle batches were systematically prepared with varying factor level settings following a face-centered central composite design. The volume of the organic phase, the amount of seed particles and the initiator concentration were kept constant as criteria for comparability between syntheses. Four separate syntheses were conducted for the external validation of the established models with the use of another batch of PS seed particles, to test for the transferability of the models with seed batch variance.

Scanning electron microscopy images of the particles were obtained to characterize the morphology as well as to analyze the particle size. The prepared particles were packed into HPLC columns and characterized for their pore properties by inverse size exclusion chromatography. Additionally, all particles were analyzed using Fourier-transformed infrared spectroscopy in attenuated reflection mode (ATR-FTIR) to assess the relative ratio of epoxy groups in the final porous *p*(GMA-*co*-EDMA) particles. This is essential since the epoxy group offers versatility in functionalization through ring

opening reactions, making the *p*(GMA-*co*-EDMA) particles an adaptable platform polymer. Using multivariate data analysis, a partial least squares regression (PLS-R) was implemented. Frequencies, which contributed to the model were identified to correspond to the symmetric and asymmetric vibrations of the epoxy group[128] (845 $cm^{-1}$ and 910 $cm^{-1}$, respectively) and the C-O stretching vibration of the epoxy ring at 1270 $cm^{-1}$[128]. The model allows an accurate prediction of the relative GMA content in the reaction mixture ($R^2_{predicted}$ = 0.98). Thus, the epoxy groups remain functional during polymerization and are present for the subsequent functionalization in the same proportion as the previously used monomer. The dispersity of the *p*(GMA-*co*-EDMA) particles was not affected by changing process factor settings and the size distribution for all particles was narrow (**Figure 2.3**).

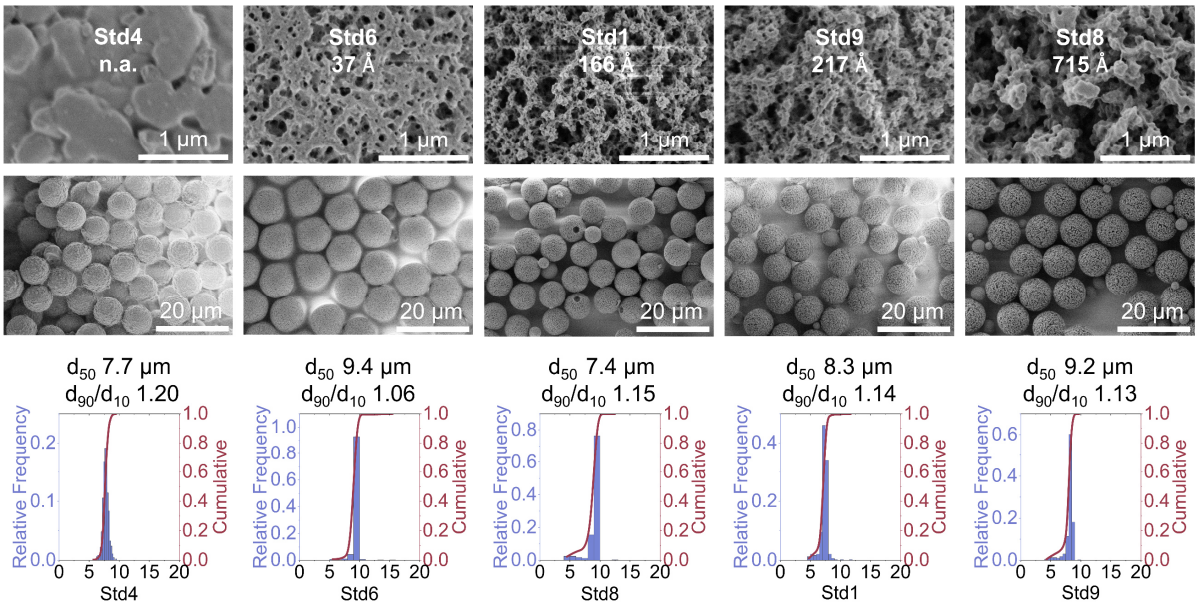


**Figure 2.3** Excerpt of *p*(GMA-*co*-EDMA) particles with different sizes and increasing pore sizes from left to right named by their standard order (Std) according to the applied RSM. Third row depicts the particle size distributions of the corresponding batch with the $d_{50}$ and the $d_{90}/d_{10}$ indicated. The process factors setting for A: monomer:porogen, B: GMA:EDMA, and C: toluene:cyclohexanol were set as follows: **Std4** (+|+|-), **Std6** (+|-|+), **Std1** (-|-|-), **Std9** (0|0|0) and **Std8** (+|+|+).

Regarding the effect of the process factor settings on the particle size, a significant effect of the porogen mixture composition (C) was observed. An increase in toluene ratio in the porogens resulted in a slight increase in particle size. However, this effect was rather small compared to the standard deviation of particles sizes within the design space (8.6±0.6 µm, mean ± standard deviation). **Figure 2.3** depicts five exemplary particles with scanning electron microscopy (SEM) images of the particles, their surface structure with the measured pore size and the particle size distributions. In the design space, particles with different morphologies were prepared – from outwardly dimpled structures (**Std4**) to particles with holes (**Std1**) or instable polymer shells (see chapter

4. **Paper I**[1]). Generally, the particle surface was smoother with higher EDMA and toluene ratio. Particles with a high monomer:porogen ratio exhibited less porous surfaces. The effect of increasing surface roughness with higher cyclohexanol content was further enhanced when more GMA was used in the monomer mixture. This interaction between GMA:EDMA and toluene:cyclohexanol was found to be statistically significantly affecting the pore volume and the pore size, supporting the observation of a rougher surface structure. A model for the dependence of the pore volume on the process factors was established. The pore volume decreased with increasing monomer:porogen ratio. The process factors GMA:EDMA and toluene:cyclohexanol are interdependent and synergistically influenced the pore volume. Thus, when the GMA:EDMA ratio is increased, the pore volume decreases when cyclohexanol is used as porogen but increases when toluene is used (**Figure 2.4**a). This behavior was due to a change in the time of occurrence of syneresis or phase separation before or after the gel point. The model for the pore volume has a high predictive capability with $R^2_{predicted}$ = 0.90.

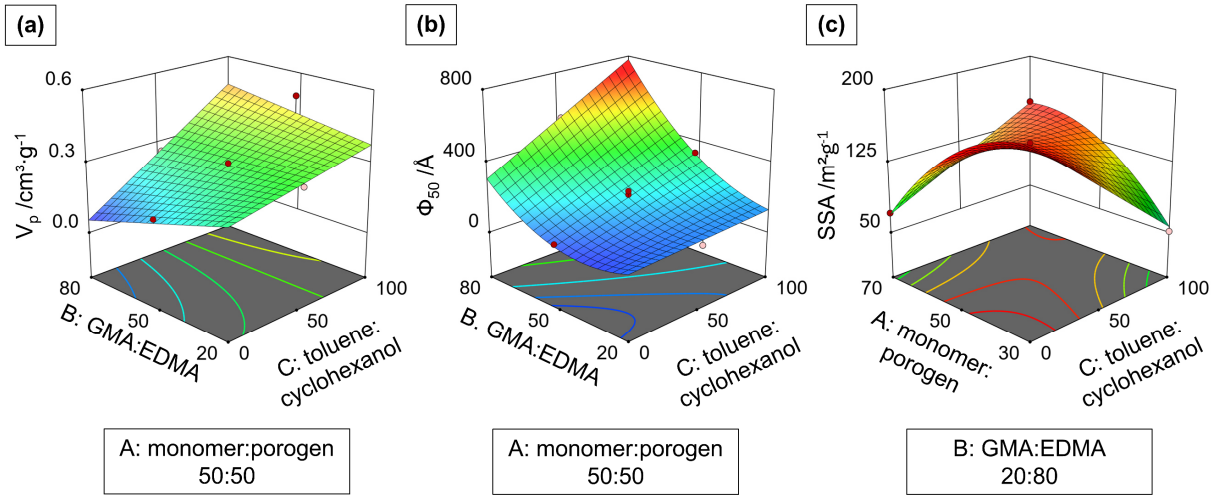


**Figure 2.4** Response surface plots of **a)** pore volume and **b)** pore size in dependence of GMA:EDMA ratio (B) and toluene:cyclohexanol ratio (C) at medium level of monomer:porogen ratio (A). **c)** Shows the response surface plot of the specific surface area in dependence on monomer:porogen and toluene:cyclohexanol ratio at with low GMA:EDMA ratio. Blue areas correspond to low response values, red areas correspond to high response values.

The pore size depends in a complex way on the process factors, which can be seen in the strong distortion of the response surface (**Figure 2.4**b). The pore size is subject to both linear and non-linear effects of the process factors and, like the pore volume, is affected by a twofold interaction of factors GMA:EDMA and toluene:cyclohexanol ratios. The pore size is reduced with increasing monomer:porogen ratio. However, this effect is attenuated at higher levels of monomer as the effect is non-linear. The effect of GMA:EDMA is also non-linear and involved in the twofold interaction. When the GMA:EDMA ratio is increased, the pore size increases. This increase is amplified as

more GMA is added. In addition, this effect can be further enhanced if, at the same time, the porogen mixture is increasingly composed of toluene. With $R^2_{predicted} = 0.95$, the predictive power of the model is high.
The specific surface area (SSA) is mathematically deducted from the pore size and pore volume according to Halász et al.[129]. Nevertheless, other effect terms are included in the modeling of the specific surface. Monomer:porogen ratio and GMA:EDMA ratio are both non-linear effects. More GMA leads to a decrease of the SSA. This is weakened with increasing GMA amount. The effect of increasing monomer quantity is subject to a twofold interaction with the composition of the porogen mixture. Thus, depending on the amount of monomer, a maximum of the SSA results, which shifts from low (30 %, with cyclohexanol) to high monomer:porogen ratio (70 %, with toluol) with increasing toluene content in the porogen mixture (**Figure 2.4**c). The model has a correlation coefficient of prediction of 0.87. These quantitative prediction models were validated by four external points. The measured pore properties and the pore properties predicted by the models agree well and show low residuals, which demonstrates the reliability and robustness of the models (**Table 4.7**, chapter 4. **Paper I**[1]).

The implementation of the quantitative prediction models thereby enables the targeted preparation of particles with desired property profiles (chapter 4. **Paper I**[1]). This selective controllability combined with the versatility of the epoxy group makes *p*(GMA-*co*-EDMA) particles a promising hard template for the preparation of MPSM.

## 2.3. Effect of the template pore properties on the MPSMs

After establishing predictive models to selectively adjust the template pore properties in the previous work, the effect of the template pores on the resulting MPSMs was examined (chapter 5. **Paper II**[2]). Therefore, six *p*(GMA-*co*-EDMA) templates were prepared. Four with increasing GMA:EDMA ratio from 20/80 v./v. to 80/20 v./v. at a monomer:porogen ratio of 50/50 v./v. (**P1–P4** respectively, see **Figure 2.5**a) and two additional points with 40/60 v./v. GMA:EDMA and varying monomer:porogen ratios (**P5**: 27/75 v./v. and **P6**: 75/25 v./v.). These *p*(GMA-*co*-EDMA) particles were aminated with TEPA. This increases the attractiveness of the template for SNPs to be incorporated into the template pores, during the subsequent Stöber process to form polymer/silica hybrid beads (HBs). To release the inorganic moieties, the HBs were calcinated to remove the organic template matter and to obtain the MPSMs (**Figure 2.5**b, see chapter 10.3).

The particles were analyzed using SEM to determine the particle size, dispersity and the morphology. A decrease in particle size of *p*(GMA-*co*-EDMA) particles with increasing GMA ratio was observed and attributed to different densities of GMA and

EDMA. An increase in particle size was also observed with increasing amount of monomers relative to the porogens. All particles exhibited a very narrow particle size distribution ($d_{90}/d_{10} \leq 1.2$). Regarding the morphology, a similar trend to the previous study (**Paper I**[1]) was observed. The surface becomes rougher with increasing GMA:EDMA ratio (**Figure 2.5**a) and increased amount of monomer.

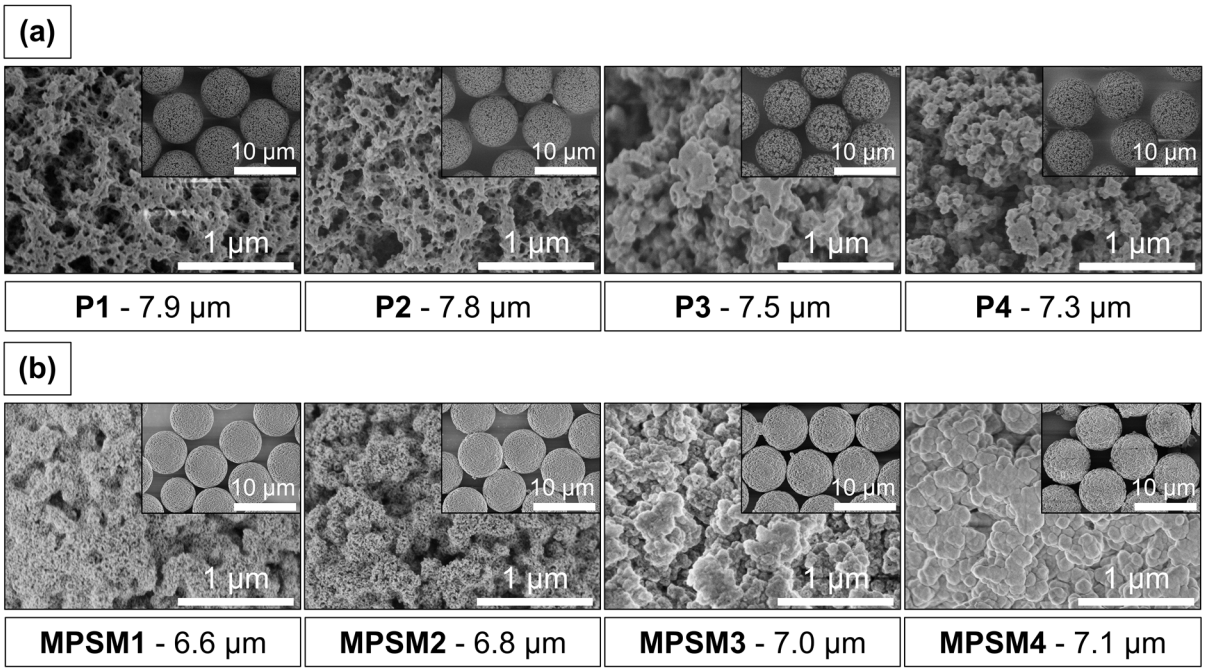


**Figure 2.5** SEM images of four out of six **a)** *p*(GMA-*co*-EDMA) particles with increasing GMA ratio (f.l.t.r.) and **b)** respective MPSMs in 50,000 × magnification and 5,000 × magnification (inset SEM images in respective corners).

Using nitrogen sorption analysis, the pore size, pore volume and SSA were determined for all particle types (see chapter 5 **Paper II**[2]: **Table 5.1**, **Table 5.3**, **Figure 5.3**, **Figure 5.7**). The *p*(GMA-*co*-EDMA) polymers exhibited a broad pore size between 10 nm and 100 nm, which lies in the range of meso- and macropores. The template particles with the lowest GMA ratio (**P1**) had the smallest pores with a mean pore size of 8 nm and were also the sole particles to possess microporosity. In general, the pore size increased with increasing GMA content (**P1** < **P2** < **P3** < **P4**) and decreased with increasing monomer content (**P6** < **P2** < **P5**). The SSA, showed a contrary trend with decreasing surface areas with higher amounts of GMA and monomer. In agreement with the previous study, this may be due to an occurrence of phase separation prior to the gel point during polymerization. An early onset of phase separation results in large pores and simultaneously reduced SSAs. In addition, higher amounts of EDMA, in its function as a crosslinker, generally lead to the formation of denser pore networks.

The amination of the *p*(GMA-*co*-EDMA) particles is crucial to exert an electrostatic attraction to negatively charged SNPs under Stöber conditions by providing a positively

charged template surface. This enables the incorporation of SNPs into the template. With different amounts of GMA and, thus epoxy groups in the template particles, the degree of amination and consequently the positive surface charge, varies with the GMA content. However, as only a functionalization of the surface can occur, the amination in comparison to the bulk material was rather small and fell below the detection limit of elemental analysis. To overcome this challenge, the polymer templates were spectrometrically characterized by ATR-FTIR prior to (**P1–P6**) and after amination with TEPA (**P1–P6@TEPA**) (**Figure 2.6**a). As in the previous work (**Paper I**[1]), a PLS-R model, based on these spectra, was used to predict the relative epoxy content of the particles. The PLS-R had a very small absolute residual mean square error of prediction of 0.6 % GMA and an $R^2_{precition} = 0.99$ (**Figure 2.6**b). Using this model, the remaining epoxy content after amination was determined. Since amination proceeds by a ring-opening reaction of the epoxy groups, the decrease in epoxy groups was used as an indirect measure of the degree of amination (**Figure 2.6**c). The amination and, thus the positive surface charge of the template, increased with increasing GMA ratio. When the monomer:porogen ratio was changed, the degree of amination remained relatively constant.

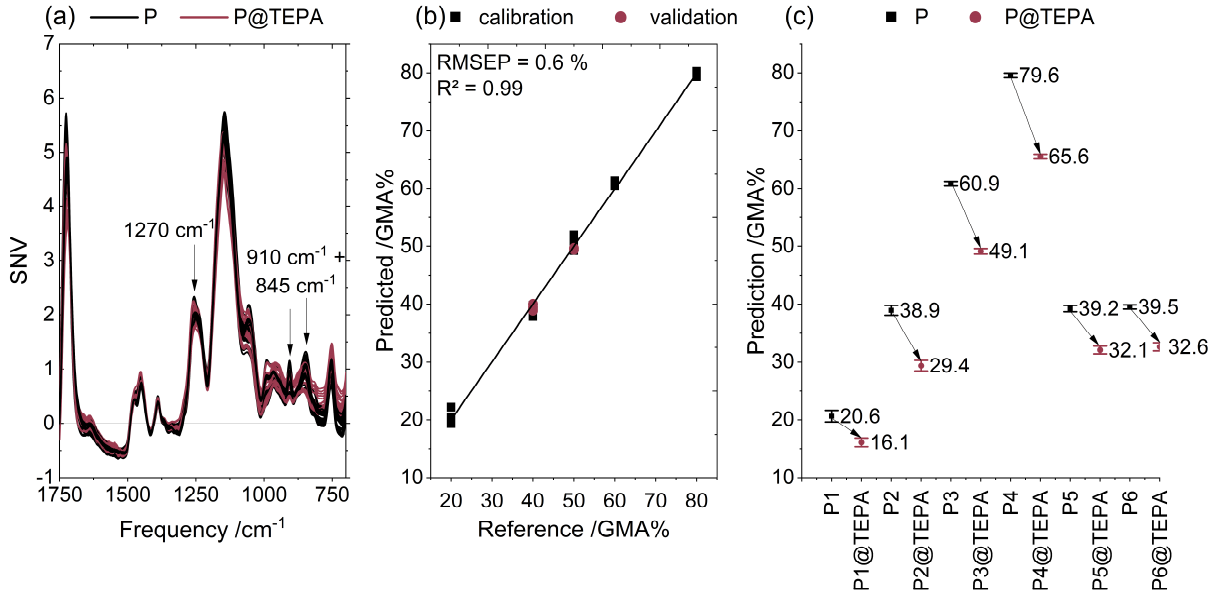


**Figure 2.6** PLS-R model for the prediction of relative GMA ratio. **a)** SNV corrected spectra of **P1–P6** (black) and **P1–P6@TEPA** (red) with important frequencies marked. **b)** Reference vs. predicted plot with the calibration and validation points indicated. **c)** Shows the predicted GMA% for **P1–P6** and for **P1–6@TEPA**. The predicted ratio, determined via the vibrations of the epoxy groups, indicate a decrease of epoxy groups after the amination (arrows).

All prepared MPSMs were monodisperse but their size varied in dependence on the degree of amination. Thus, the size increased in the following order **MPSM1** ~ **MPSM5** < **MPSM2** < **MPSM3** < **MPSM4** (**Figure 2.5**b). **MPSM6** exhibited a larger size than the

initial template **P6.** Here, a shell of nonporous SNPs formed around the template due to the small template pores and small pore volume. After calcination the hollow particles **MPSM6** remained. All MPSMs consist of interconnected SNPs. The change in the degree of amination, evidenced by PLS-R, affected the incorporation of SNPs into the polymeric pore network. These SNPs became larger the higher the GMA ratio (**Figure 2.5**b), hence the higher the degree of amination. The increase in SNP size also correlates with the increase in template pore size. The pores of the MPSMs were generally larger as the corresponding template pores but follow their trend of increased pore sizes with higher GMA ratio. Similarly, the SSA was reduced when the monomers contained more GMA.
Using thermogravimetrical analysis (TGA), the silica content of the HB materials was determined. All HBs had a constant silica content of ~ 30 wt%. Consequently, the size of SNPs depends on three main factors: 1) the kinetics of the sol-gel process (**Paper III**[3] to **Paper VI**[6]), 2.) the diffusion of SNPs into the template, controlled by the electrostatic attraction, and thus, the surface functionality of the template (**Paper II**[2] and **Paper III**[3]), and 3) the pore diameter of the template (**Paper II**[2]). SNPs formed in the solution diffuse into the template pores, where they aggregate into larger SNPs. As for increased template pore sizes, there is more room for aggregation, the SNP size increases with larger template pores. In the case of **MPSM6**, the template had a high positive surface charge and small pores. This led to the fact that larger SNPs were already formed in the continuous phase by slow diffusion and can therefore only attach to the template with the small pores as a shell.

To attain a reversed-phase HPLC column packing material, **MPSM1–4** were functionalized with trimethoxy (octadecyl) silane (chapter 5. **Paper II**[2],**Figure 5.8**). The $C_{18}$ functionalized materials (**MPSM1–4-C$_{18}$**) were packed into stainless steel columns and were applied for the separation of a protein mixture of ribonuclease A, cytochrome c, holo-transferrin and apomyoglobin. The prepared columns showed a high separation efficiency comparable to a commercially available column. For **MPSM1–3-C$_{18}$**, all peaks were baseline separated with a resolution $R > 2$. The column efficiency and peak symmetry improved from **MPSM1-C$_{18}$** to **MPSM3-C$_{18}$.** This correlates to the increase in pore size of the materials **MPSM1** < **MPSM2** < **MPSM3**. Although **MPSM4** exhibits even larger pores, the separation efficiency was decreased and peak broadening occurred. This phenomenon is due to the small SSA of 68 $m^2 \cdot g^{-1}$ and the large SNPs that close up the pores and limit their accessibility.

In this work (**Paper II**[2]), it was shown that the properties of MPSMs are directly affected by properties of the templates. Thereby, the size of the incorporated SNPs determines the pore size of the MPSMs. Small SNPs result in small pores, while larger

SNPs lead to the formation of larger pores of MPSMs. The size of SNPs themselves is a function of the template pore size and the degree of amination, which both depend on the GMA ratio chosen during the template preparation. Moreover, the successful application of $C_{18}$-functionalized MPSMs as reversed-phase packing materials for the separation of proteins was demonstrated. The pore properties are thereby an important parameter for the separation efficiency.

## 2.4. Effect of catalyst concentration and water-to-TEOS ratio on the incorporation of silica into the porous polymeric template

The organic/silica hybrid beads (HBs), are the intermediate step (**Figure 1.1**d and **Figure 2.1**) resulting from the incorporation of silica nanoparticles (SNPs) in the pore network of the template during the base-catalyzed sol-gel process. Here, the effects of altered sol-gel process factors and the silica incorporation can be directly assessed (**Paper III**[3]). The HBs consist of two interpenetrating networks: the porous network of the organic template and the silica network, which consists of interconnected SNPs. Thus, they fall in the category of nanocomposites, which are characterized by at least one component in the nanometer range[130], here the SNPs. HBs as nanocomposites represent an interesting material in their own respect, which can also be used in versatile applications[131–133]. The nanocomposite thereby exhibits different properties than the organic and the inorganic components themselves and thus offers interesting new material properties[134,135]. These properties are dependent on e.g. the ratio between organic and inorganic component and on the method of preparation[136]. Here, the HBs were prepared using the sol-gel process under Stöber conditions. The critical process factors water to precursor ratio ($n(H_2O)/n(TEOS)$) and the concentration of the basic catalyst, here ammonia ($c(NH_3)$), were systematically assessed. The lower setting of the water-to-TEOS ratio was set to be $n(H_2O)/n(TEOS) = 4$, as four water equivalents are needed for the complete hydrolysis of TEOS to silicic acid, as first step of the hydrolysis and condensation cascade[68,85,91,103]. 13 HBs were prepared with varying water-to-TEOS ratios and ammonia concentrations according to a face-centered central-composite design. To support the lower region of the design space, additional three HBs were prepared with a $n(H_2O)/n(TEOS) = 8$. All 16 HBs were obtained using the same template, which was prepared with the same settings as the center point of **Paper I**[1] (**Figure 2.1**). The template was subsequently amino-functionalized using TEPA, to increase the template attractivity for SNPs.

The HB particle properties particle size, dispersity, morphology, pore size, pore volume, specific surface area and the $SiO_2$ content were characterized using SEM, nitrogen sorption analysis and TGA. A possible mechanism for the incorporation of SNPs in the template in dependence of the reaction conditions was proposed (**Paper III**[3]).

The size of the obtained HBs varied between 8.3 µm and 8.6 µm and had very narrow size distributions of $d_{90}/d_{10} \leq 1.15$. Although the effect of n($H_2O$)/n(TEOS) on the HB sizes was statistically significant, the effect was very small across the investigated design space. The obtained HB sizes were very similar to those of the template (8.3 µm, $d_{90}/d_{10} = 1.05$), concluding that the template predominantly affects the HB sizes and dispersity. This was further strengthened by the fact that the HBs consisted of considerably different mass fractions of silica, which was determined by TGA. The $SiO_2$ contents varied from 0.1 wt% to 31.2 wt%. A highly statistically significant and predictive model ($R^2_{prediction} = 0.95$) was established for the dependence of $SiO_2$ content of the HBs on the water-to-TEOS ratio and the ammonia concentration. An increase in n($H_2O$)/n(TEOS) ratio resulted in increased incorporation of silica. However, this behavior was non-linear and the increase in silica content leveled off at a ratio of water-to-TEOS of ~60:1 and a maximum of incorporated silica was reached (~ 30 wt%) (**Figure 2.7**a).

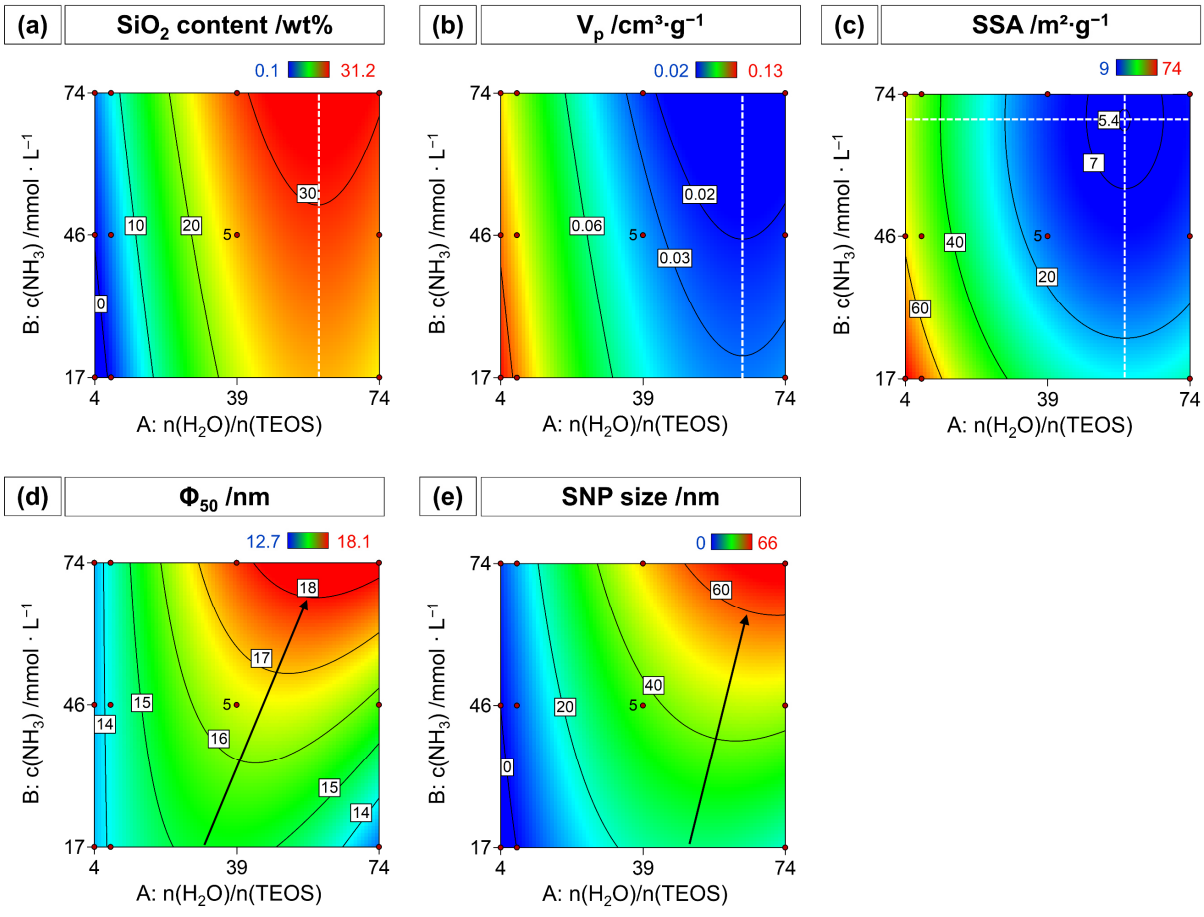


**Figure 2.7** Contour plots of the material properties in dependence on n($H_2O$)/n(TEOS) and c($NH_3$). **a)** $SiO_2$ content and **b)** pore volume of the HBs. The dashed line marks the maximum of $SiO_2$ and minimum of $V_P$ at A ≈ 60. **c)** SSA of the HBs with the dashed lines marking the process factor settings of a global minimum (A ≈ 58, B ≈ 68 mmol·$L^{-1}$). **d)** Median pore size and **e)** SNP size of the HBs. Black arrows indicate the shift in maximum across the design space. Blue areas mark low response values and red areas mark high response values.

In turn, the effect of the ammonia concentration was linear, and higher ammonia concentrations resulted in greater silica incorporation. Interestingly, the model to describe the pore volume in dependence on the process factors ($R^2_{prediction} = 0.96$) was affected by the same effects but with opposing direction (**Figure 2.7**b). An increase in silica incorporation led to a decline in pore volume. The non-linear effect of the water-to-TEOS ratio was observed as well.

The specific surface area was determined via nitrogen sorption measurements and showed a non-linear dependence on both, water-to-TEOS ratio and ammonia concentration ($R^2_{predicted} = 0.95$) (**Figure 2.7**c). The surface area decreased with increasing water content. This decrease was attenuated at elevated levels of $n(H_2O)/n(TEOS)$. A similar attenuating behavior was observed for increasing ammonia concentrations. From the two non-linear effects, a global minimum surface area was obtained at a water-to-TEOS ratio of 58:1 and an ammonia concentration of 68 $mmol \cdot L^{-1}$ (**Figure 2.7**c).

Similar to the size of the HB particles, the pore size distribution was significantly affected by the existing pore size distribution of the initial template. Thus, the pore size distributions of the HBs had broad distributions in a range between 5 nm and 100 nm exhibiting mesopores and macropores. When silica is incorporated into the pores, the median of the pore size distribution shifts towards higher values, since small pores are filled more rapidly. The model for the pore size was statistically highly significant and had an acceptable correlation coefficient of prediction with $R^2_{prediction} = 0.55$. The pore size is subject to a statistically significant synergistic interaction between the water-to-TEOS ratio and the ammonia concentration (**Figure 2.7**d). Thus, the effect strength of one process factor depends on the setting of the other process factor. While at a low water-to-TEOS ratio there is hardly any increase in pore size with increasing ammonia concentration, at high water-to-TEOS ratios the increase in pore size with increasing ammonia content is very pronounced. The complexity of the model is even increased by a non-linearity in the effect of $n(H_2O)/n(TEOS)$ resulting in a maximum in pore size, which shifts with to higher $n(H_2O)/n(TEOS)$ levels when the ammonia concentration is increased (**Figure 2.7**d). The combination of $A^2$ and AB results in highly twisted response surface, which is sensitive to small changes, especially in the region of the center point. This thus explains the limited predictive power of the model compared to the $R^2_{adjusted} = 0.76$.

The morphology of the HBs was shaped by the pore structure of the templates. However, at a certain threshold of settings, particulate SNPs were observed on the surface of the HBs. These increased in size with increasing process factor settings (**Figure 2.7**e) and thus, higher hydrolysis and condensation rates. For the two HBs prepared with the highest water-to-TEOS ratio and medium or high ammonia concentration, a turbid filtrate was observed. SEM measurement of the filtrate confirmed the formation of

non-porous secondary particles (200 – 300 nm, **Figure A. 6.3 Paper III**).
The sizes of the SNPs at the surface of the HBs were affected by n($H_2O$)/n(TEOS) and c($NH_3$) in a similar manner as the pore sizes (**Figure 2.7**e). Here, also a highly statistically significant synergistic interaction and a non-linear effect of the water-to-TEOS ratio were observed ($R^2_{predicted}$ = 0.98). The increase in size of the SNPs is more pronounced for the increase in ammonia concentration, when the water-to-TEOS ratio is increased concurrently. The non-linearity of the water-to-TEOS ratio is shown in a maximum in SNP size, which shifts as a function of the ammonia concentration in the design space (**Figure 2.7**e). Although correlations between the response variables were observed, their dependence on the process factors n($H_2O$)/n(TEOS) and c($NH_3$) differed for each material property. This clearly demonstrates the complexity of the sol-gel process for the incorporation of silica into a hard template.

To obtain an insight into mechanism of the incorporation of SNPs into the template pores as a function of the sol-gel process factors, it was considered which pores of the template were primarily closed. For this purpose, the relative change in pore volume as a function of pore sizes prior and after silica incorporation were analyzed (**Paper III**[3], **Figure 6.6**). With low silica incorporation, i.e. low ratio of water-to-TEOS and thus an inefficient hydrolysis and condensation reaction, pores < 10 nm were partly closed, while larger pores remained almost unchanged. At intermediate and high water-to-TEOS ratios, and thus more efficient hydrolysis condensations, pores < 10 nm were almost completely filled by silica (pore volume reduction of 60 to 100 %), while the reduction of pore volume was smaller for larger pores. However, the relative reduction of the pore volume of pores > 10 nm decreased linearly the larger the pores were considered. The steepness of the decrease was similar for all HBs prepared with medium or high n($H_2O$)/n(TEOS). This was accounted for by the formation of uniformly thick layers of agglomerated SNPs, which adhere to the pore walls of the template. In conjunction with the observation of the increase of the SNP size at the HBs surface and the formation of secondary particles at high n($H_2O$)/n(TEOS) and medium to high ammonia concentrations, a mechanism for the incorporation of silica into the amino-functionalized template was proposed and divided into three reaction regimes (**Figure 2.8**).

In the continuous phase, TEOS undergoes hydrolysis and condensation. Hydrolyzed silanol species accumulate in the continuous phase until the supercritical saturation concentration is exceeded. Rapid condensation and formation of small SNPs in the range of a few nanometers occurs[93]. Following the monomer addition theory[92,105], without the presence of the template, SNPs would continue to grow by monomer addition (**Figure 1.3**). However, the amino-functionalized template acts as a filter due to

its electrostatic attraction to negatively charged SNPs. The formed SNPs rapidly diffuse into the template, where they attach to the pore walls. There, in absence of hydrolyzed silanol species, they agglomerate and form uniformly thick layers of silica. Zhao et al. reported that if the rate of consumption of monomer was lower than the hydrolysis, the critical supersaturation was exceeded repeatedly, releasing a new burst of SNPs[137]. As in presence of the template, the SNPs are removed from the continuous phase permanently by diffusion into the template pores (**Figure 2.8**a), further growth of SNPs, and thus monomer consumption in the continuous phase is suppressed.

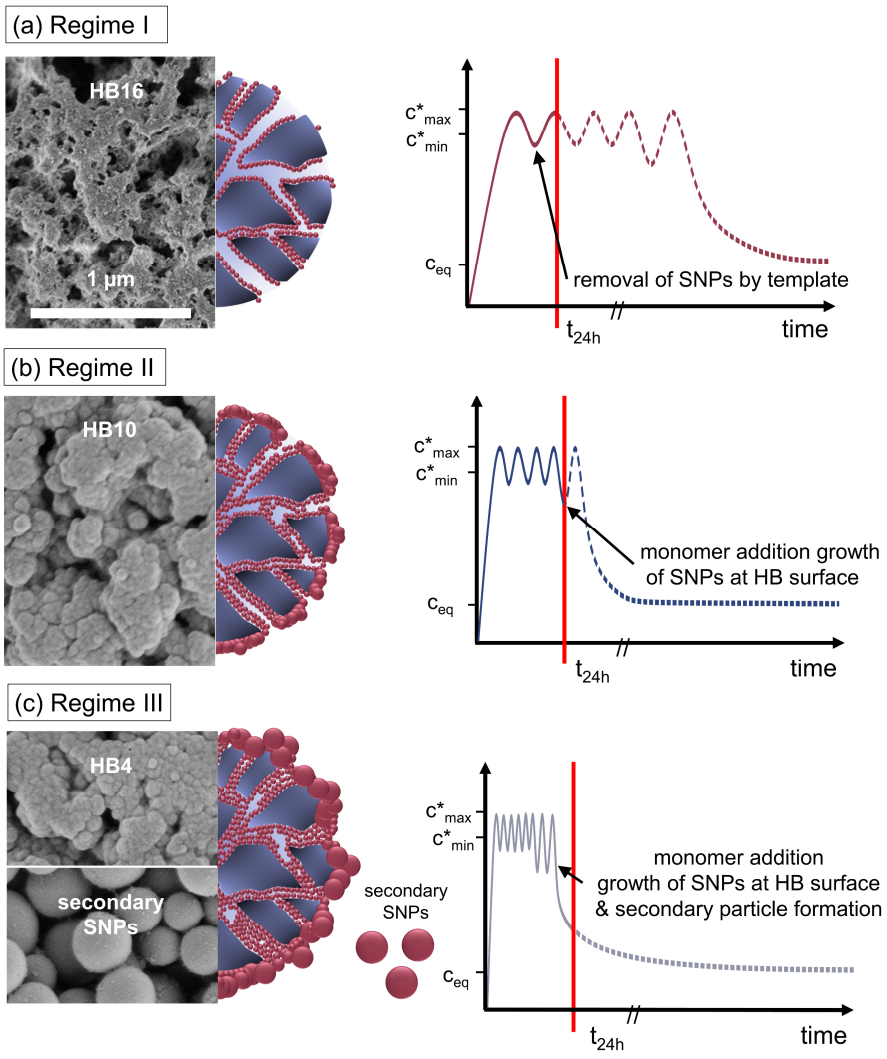


**Figure 2.8** from left to right: SEM images of exemplary particle, schematic representation of HB and reaction schema deducted from the LaMer theory[105] (**Figure 1.3**) in presence of an amino-functionalized template for each reaction regime. $t_{24h}$ indicates the time when the reaction was terminated in the present study. **a) Regime I:** Hydrolysis and condensation rates are low. Only a few SNPs are formed and attached at the template walls, where they aggregate and form a thin silica layer. **b) Regime II:** By increasing the relative rates of hydrolysis and condensation, the frequency of the cycles for SNP formation increases. SNPs fill the pores and attach to the HBs outer surface. There, the SNPs grow by monomer addition as they are in contact with the continuous phase. **c) Regime III:** Hydrolysis and condensation rates are increased to a point, where they exceed the diffusion rate of SNPs into the template after pore filling. The SNPs form non-porous secondary particles by aggregation and monomer addition growth within the continuous phase.

Hydrolyzed species reaccumulate and new SNPs are formed to relieve the supersaturation. Different starting conditions of the sol-gel process affect the relative rates of hydrolysis and condensation. Thus, the frequency of the self-nucleation cycles and the incorporation of SNPs into the porous template are controlled by the n($H_2O$)/n(TEOS) ratios and ammonia concentration (**Figure 2.8**). By the systematic variation of the critical process factors within our experimental design space, HBs with different morphological characteristics were prepared, the formation of which can be assigned to three reaction regimes depending on the sol-gel starting conditions (**Figure 2.8**). At low water-to-TEOS ratios, and thus low hydrolysis and condensation rates, only few SNPs are formed and attached to the template pore walls (**Figure 2.8**a, Regime I). Increasing the n($H_2O$)/n(TEOS) ratio results in higher hydrolysis and condensation rates[92]. More SNPs are formed and incorporated into the template, as more nucleation cycles occur. As the template pores are subsequently filled, SNPs also attach at the HB surface. There they are in contact with the continuous phase and can undergo growth by monomer addition (**Figure 2.8**b, Regime II), which lowers the concentration of hydrolyzed silanol species. If the rates of hydrolysis and condensation are even more elevated, they exceed the rate of diffusion and incorporation of SNPs into the template. Thus, the SNPs grow within the continuous phase and become too large to be incorporates into the template pores. They form non-porous secondary particles (**Figure 2.8**c, Regime III).

In this work (chapter 6. **Paper III**[3]) the complex interactions between the sol-gel process factors n($H_2O$)/n(TEOS) and c($NH_3$) were demonstrated, emphasizing the importance of simultaneous consideration of synthesis parameters. The complex effects of the sol-gel process factors on the material characteristics of the prepared HBs were depicted in quantitative predictive models. This allows the tailoring of the material property profiles. Depending on the synthesis settings and the respective relative rates of hydrolysis and condensation, different types of nanocomposite materials can be prepared: polymer particles coated with a thin, protective layer of silica and materials whose pores are filled with silica. If relative hydrolysis and condensation rates are further increased, the growth rate massively exceeds the incorporation rate of SNPs into the template and the SNPs become too large to be deposited within the template pores. They attach at the outer surface of the template and form particles with a porous polymeric core covered by a silica shell. This represents a conceivable fourth reaction regime.

## 2.5. Effect of sol-gel process factor settings on MPSMs

The properties of MPSMs depend on the reaction steps and intermediates prepared prior to calcination. Calcination itself also affects the resulting MPSMs. Insufficient calcination leads to contamination with residual carbon[68,120], whereas too high temperatures or extensive calcination duration lead to closure of the pores and shrinkage of the particles[68,120,138,139]. While **Paper II**[2] focused on the effect of template properties, **Paper III**[3] investigated the effect of sol-gel synthesis conditions on the hybrid materials. Now, to examine the effect of sol-gel process conditions on the MPSMs, the HBs prepared in **Paper III**[3] were calcined in a standardized manner at 600 °C for 10 h (chapter 10.3). The MPSMs were characterized using SEM imaging for the determination of the size and dispersity, as well as to assess the morphology of the MPSMs, while pore volume, pore size and specific surface were determined by nitrogen sorption measurements. A wide range of MPSM materials was achieved.
While the size of the preceding HBs changed only slightly as a function of the sol-gel process factors n($H_2O$)/n(TEOS) and c($NH_3$) (**Paper III**[3]), the size of the MPSMs varied tremendously after the removal of the template (**Paper IV**[4]). The MPSMs sizes ranged from 0.5 µm to 7.8 µm, while their spherical shape and narrow size distribution with $d_{90}/d_{10}$ of < 1.4 was maintained (**Figure 2.9**).

The effect of n($H_2O$)/n(TEOS) was non-linear (**Figure 2.9**a) and approximately twice as strong as the linear factor effect of c($NH_3$) (**Figure 2.9**b). When the stoichiometric ratio of water-to-TEOS and/or the ammonia concentration are increased, the rate of hydrolysis increases[91,92]. Since the hydrolysis rate is the rate-limiting step in basic sol-gel conditions, the overall reaction rate increases. Thus, SNP formation is more effective and more SNPs can be incorporated into the template pores. In addition, at high water-to-precursor ratios, the nucleation rate is also higher[106]. The non-linear behavior of n($H_2O$)/n(TEOS) results from the shift of the ratio of the diffusion rate of SNPs into the template and that of the hydrolysis and condensation rate. If the incorporation of SNPs is slower than the hydrolysis and condensation, the SNPs continue to grow in the continuous phase. This can be assigned to regime III from our previous work (**Paper III**[3]). If this behavior occurs, no more SNPs are incorporated into the template, resulting in a generally lower silica incorporation in the hybrid material. As a result, the growth of the MPSM levels off (**Figure 2.9**a). Similarly, the hydrolysis and condensation rates are accelerated with increased levels of ammonia as basic catalyst, which improves the template filling (**Figure 2.9**b). If the template pores are filled adequately, the amount of shrinkage is reduced during template removal via calcination. Thus, at higher settings of n($H_2O$)/n(TEOS) and c($NH_3$), either (high|medium), (medium|high), or (high|high), the MPSM shrink only < 20 % in diameter compared to the preceding HB.

The model for the prediction of MPSM sizes in dependence on the water-to-TEOS ratio and the ammonia concentration is very robust and has a high predictive power with $R^2_{predicted} = 0.95$.

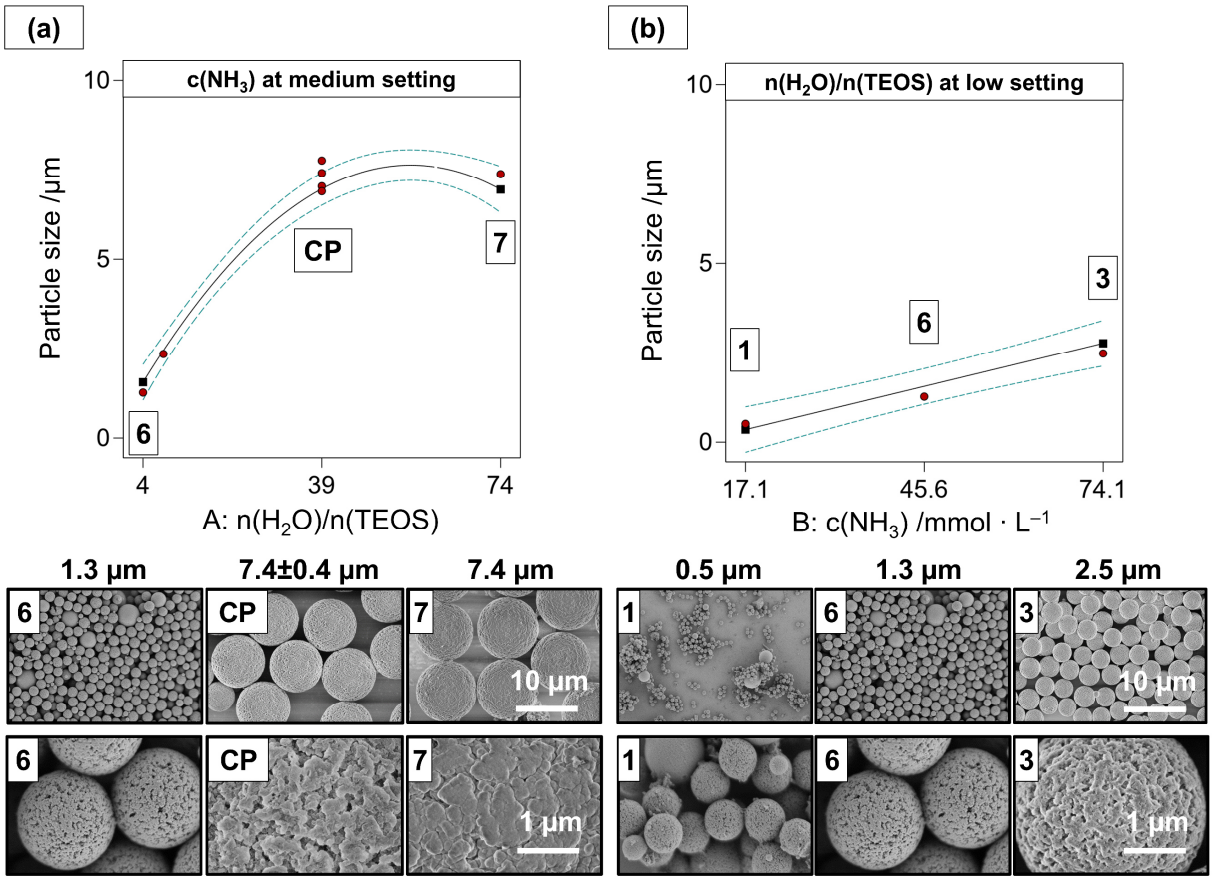


**Figure 2.9** One-factor plots and corresponding SEM images (upper row 5,000 × magnification, lower row 50,000 × magnification) for the MPSM size in **a)** dependence on n($H_2O$)/n(TEOS) at medium factor level setting level of c($NH_3$) and **b)** dependence on c($NH_3$) at low factor level setting of n($H_2O$)/n(TEOS). Numbers indicate the corresponding sample number. Red points mark the factorial points, the black solid line marks the model fit and dashed blue lines indicate the 95 % confidence intervals. The SEM images are shown in a larger scale in chapter 7 **Figure 7.3**.

Regarding the morphology of the MPSMs from **Paper IV**[4] (**Figure 2.9**), all MPSMs are clearly porous, even the smallest MPSMs with a size of 0.5 µm. The MPSMs are formed from interconnected SNPs, which underwent grain growth[140]. The effect of grain growth was more prominent in the lower region of the design space, where less silica and smaller SNPs were incorporated in the template pores (**Paper III**[3]). According to the scaling law, smaller SNPs reach a higher degree of sintering under the same calcination conditions as larger SNPs[140,141]. Thus, for MPSMs consisting of smaller SNPs, the interconnection is pronounced and the surface appears smoother (**Figure 2.9**b), while at sol-gel setting, which result in the incorporation of larger SNPs, a more particular surface structure is visible (**Figure 2.9**a – **CP** or **Figure 7.3**b – **MPSM4, MPSM9** in **Paper IV**[4]).

The dependence of MPSM size, on the hydrolysis and condensation rates was also observed in **Paper VI**[6]. Here, the effect of changing alkoxysilane chain length of the precursor was investigated. With increasing alkyl chain length from tetramethyl orthosilicate to tetrabutyl orthosilicate, the hydrolysis rates decrease[45,68,89]. This results in smaller SNPs incorporated into the template pores and thus, a smaller MPSM size according to the precursor's alkyl chain length. Thus, a decrease in hydrolysis rate either through changes in precursor, ammonia concentration or ratio of water-to-precursor results in smaller SNPs incorporated and higher degree of shrinkage during template removal.

The pore sizes of the MPSMs were mostly characterized by broad size distributions. The pore size mean values varied between 3.2 nm and 14.8 nm. However, MPSMs which underwent a higher degree of shrinkage and were smaller in MPSM size (< 6 μm), exhibited narrower pore size distributions and generally smaller pores. For shrinkages > 30 % in diameter compared to the preceding HB, also micropores with sizes below 2 nm were observed. It should be noted that three MPSMs could not be analyzed by nitrogen sorption measurements, as their yield after calcination was below 10 mg and thus not sufficient for analysis. However, as they correspond to the smallest MPSMs (including **MPSM1** in **Paper IV**[4]), it is expected that they also exhibit small pores down to micropores, similar to **MPSM3** (in **Paper IV**) with a mean pore size of 3.5 nm (**Figure 2.9**b). The predicted pore size for **MPSM1** (in **Paper IV**[4]) with the lowest setting for water-to-TEOS ratio and ammonia concentration was ~ 2 nm. This represents a realistic prediction, as the presence of pores is still clearly visible in the SEM image for **MPSM1** (**Figure 2.8** and **Figure 7.3** in **Paper IV**[4]). The model for mean pore size ($R^2_{adjusted}$ = 0.90) was highly complex and includes the synergistic interaction between the non-linear effect of water-to-TEOS ratio with the linear effect of the ammonia concentration (**Figure 2.10**a). Increasing the ammonia concentration generally results in larger pores, but the steepness of the increase depends on the n($H_2O$)/n(TEOS) level. At low c($NH_3$), the effect of the water-to-ammonia concentration is linear and the mean pore size increases with higher amounts of water (**Figure 2.10**a). If simultaneously the ammonia concentration is increased, the effect of n($H_2O$)/n(TEOS) changes to a non-linear behavior and the steepness of the pore size increase levels off with higher water amounts (**Figure 2.10**a). This results from the change in mechanism from reaction regime II to regime III and the formation of non-porous secondary particles (**Paper III**[3]), due to increased hydrolysis and condensation rates. This behavior is similar to the effect of the sol-gel process factors on the SNP size in the HBs and a clear correlation between the SNP size and the pore size of the MPSMs was observed (**Figure S. 7.5**). A similar correlation between SNP size in HBs and pore

size in subsequent MPSMs was also found in **Paper II**[2]. Larger SNPs thereby result in larger pores of the MPSMs.

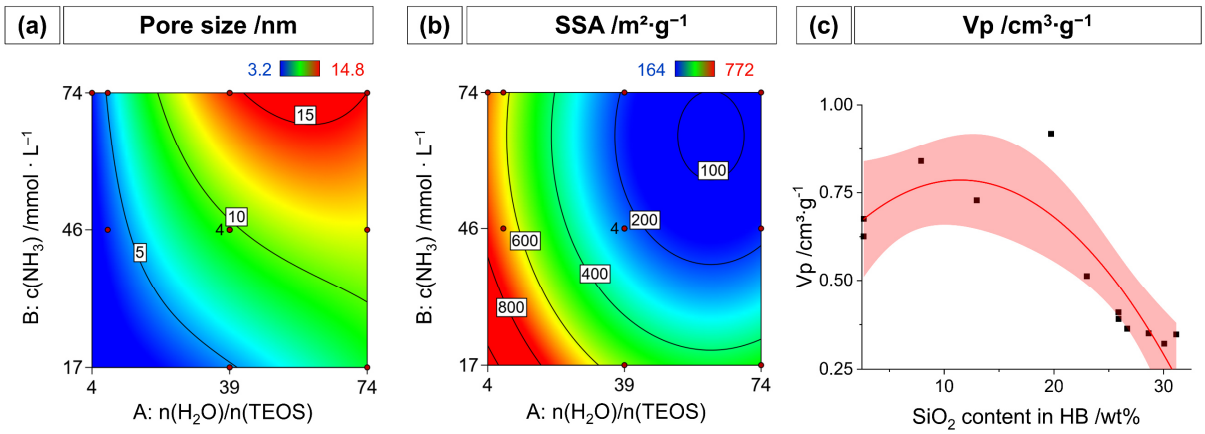


**Figure 2.10** Contour plots of the MPSM properties in dependence on n($H_2O$)/n(TEOS) and c($NH_3$). **a)** Pore size **b)** SSA of the MPSMs. Blue areas mark low response values and red areas mark high response values. **c)** Depicts the non-linear model of the correlation between silica content of the preceding HBs and the pore volume of the MPSMs resulting after calcination ($R^2_{adjusted}$ = 0.73). Shaded area indicates the 95 % confidence interval.

In **Paper V**[5], the effect of different alcoholic solvents on the MPSM formation was investigated. Here, a clear increase in SNP size and amount of incorporated silica was observed, when the alkyl chain length of the co-solvent increased, and vice versa the solvent polarity decreased. As a result of the incorporation of large SNP, as was observed for alkyl chain length increase, also larger pores and smaller SSAs of the corresponding MPSMs occur. This repeated behavior emphasizes the importance of the size of incorporated SNPs for the pore size in the MPSMs and the dependence on the kinetics of the sol-gel process.

The specific surface areas of the MPSMs from **Paper IV**[4] ranged from 164 $m^2 \cdot g^{-1}$ to 772 $m^2 \cdot g^{-1}$. Both, n($H_2O$)/n(TEOS) and c($NH_3$) exhibited non-linear effects and an increase of either of the factors resulted in a decreased SSA, with the effect attenuating at higher factor level setting ($R^2_{predicted}$ = 0.90) (**Figure 2.10**b).

Although the model for the prediction of the MPSM pore volume on the process factors was highly significant, the predictive power was lacking. However, a clear non-linear correlation (second order polynomial) between the amount of silica incorporated in the preceding HBs and the pore volume of the MPSMs after calcination was observed (**Figure 2.10**c, $R^2_{adjusted}$ = 0.73). As a function of the amount of silica, the pore volume increased the lower the silica incorporation, up to around 12 wt%. Below this threshold, the pore volume of the MPSMs receded. This behavior was explained by changing mechanisms during calcination. For samples where the template pores were filled completely, new pores were formed from the removal of the template walls (negative imprint) (**Figure 7.6**a). If the template pores were only covered with a layer of

silica, the former template pores were not filled completely and led to additional pore volume on top of the MPSM pores formed by template wall removal (**Figure 7.6**b). If little silica was incorporated into the templates (< 12 wt%), the shrinkage was very prominent and reduced the MPSM pore volume again (**Figure 7.6**c).

To examine the effect of different MPSM properties onto the separation efficiency of reversed-phase separations of proteins (**Figure 2.11**a and c) and amino acids (**Figure 2.11**b and d), two scaled up MPSM batches were prepared and $C_{18}$-functionalized. As the template pores for the scaled-up batches exhibited larger pores and a higher pore-volume, more SNPs were incorporated and aggregated to larger SNPs. As the SNP size is critical for the pore properties of the resulting MPSM, the MPSMs also differed compared to the MPSMs prepared in the response surface design with the same sol-gel process factor settings. This phenomenon was observed in **Paper II** (and chapter 2.3). Both packed columns were capable of separating four proteins (ribonuclease A, cytochrome c, holo-transferrin and apomyoglobin) as well as eleven amino acids. Column **MPSM-$C_{18}$-1** (**Figure 2.11**a and b) had smaller pores but a larger surface area (16.6 nm and 246 $m^2 \cdot g^{-1}$) compared to **MPSM-$C_{18}$-2** (20.8 nm and 186 $m^2 \cdot g^{-1}$). While the elution time of the protein separation was increased for **MPSM-$C_{18}$-2** (**Figure 2.11**c), the elution time of the amino acids was lower when **MPSM-$C_{18}$-2** (**Figure 2.11**d) was used.

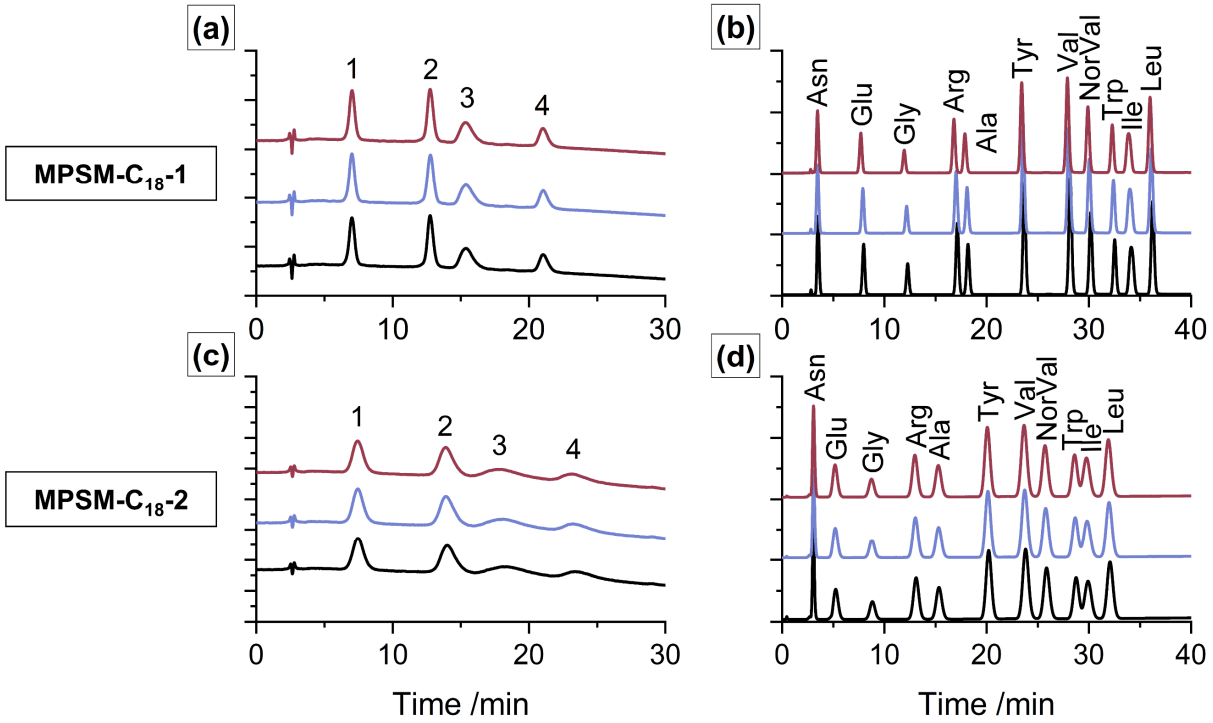


**Figure 2.11** Stacked chromatograms of the separations of proteins (**a,c**) and amino acids (**b,d**) for columns **MPSM-$C_{18}$-1** (**a,b**) and **MPSM-$C_{18}$-2** (**c,d**)

As the separation mechanism of the proteins is dominated by size exclusion, the larger pores of **MPSM-$C_{18}$-2** increase the diffusion length for the proteins resulting in broader

peaks and longer retention. For the amino acids, the interaction with the $C_{18}$-functionalized surface is more relevant. Thus, the retention for amino acids was decreased for **MPSM-$C_{18}$-2**, as its SSA is smaller than that of **MPSM-$C_{18}$-1**. Generally, **MPSM-$C_{18}$-1** had higher peak resolutions and narrower peaks than **MPSM-$C_{18}$-2**. With **MPSM-$C_{18}$-1**, baseline separation of all four proteins and all eleven amino acids was possible, indicating the suitability of MPSMs prepared via the hard template assisted method for the separation of biomolecules. The separation performance also depends on the material properties, which can be influenced by the individual synthesis steps.

Here, it has been shown that tailoring of the sol-gel process conditions and consequent control of the hydrolysis and condensation kinetics facilitates the preparation of manifold MPSMs, while maintaining the spherical shape and narrow size distribution, even when using the same hard template. This data space can be arbitrarily expanded by changing the properties of the template, which adds a new dimension to the data space. Thus, materials can be prepared for a variety of applications if this data space is navigated appropriately using the models established in this work.

## 3. Conclusion

The preparation of mesoporous silica microspheres (MPSMs) using a hard template-assisted method is highly complex, due to the large number of reaction steps and corresponding process factors required, which affect the MPSM properties.
Here, by systematic and statistical analysis using the approach of Response Surface Methodology (RSM), quantitative models elucidating the effects of synthesis conditions on material properties were established for the three main steps of the template-based method: 1) controlling the properties of the hard template 2) incorporation of the silica into the template and 3) effects on the MPSMs after template removal by calcination. These models allow the targeted navigation of the n-dimensional design space of possible process factors, as a better understanding of the complex systems along the synthesis pathway was obtained.

The pore properties of the hard-template *p*(GMA-*co*-EDMA) can be tailored using the process factors monomer:porogen, GMA:EDMA, and toluene:cyclohexanol ratios. The incorporation of silica into the template pores occurs by adsorption of *in situ* formed silica nano particles (SNPs). The properties of the template, in terms of pore size, pore volume and surface functionality, affect the properties of subsequent MPSMs. Templates with larger pores allow *in situ* formed SNPs to agglomerate to larger SNPs within the template pores. After template removal the MPSMs exhibit larger pores if larger SNPs were incorporated into the template (**Figure 3.1**b). The SNP size also affects the MPSM size (**Figure 3.1**a) and specific surface area (**Figure 3.1**c).

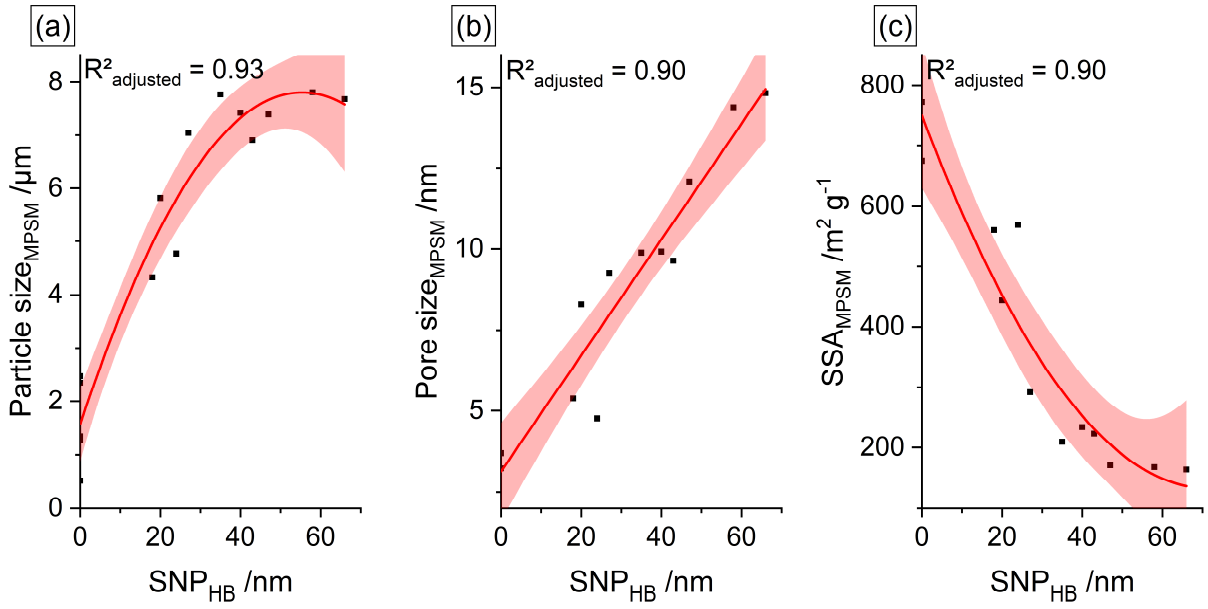


**Figure 3.1** Effect of the size of the SNPs incorporated into the polymer templates during sol-gel processing on the **a)** particle size, **b)** pore size and **c)** specific surface area of the resulting MPSMs.

The incorporation depends on the sol-gel process conditions and can be divided into three reaction regimes: (I) for low hydrolysis and condensation rates, and thus ineffective SNP formation, only thin layers of silica adsorb to the pore walls. MPSMs formed upon removal of the template undergo substantial shrinkage and may exhibit micropores in addition to mesopores. (II) If a good ratio between sol-gel kinetics, respective SNP formation, and diffusion of SNPs into the template pores is achieved, the template pores are filled with silica. After calcination, the MPSM gives a negative imprint of the template and exhibit a broad pores size distribution form mesopores to macropores. (III) If the rate of hydrolysis and condensation exceeds the rate of SNP incorporation, non-porous secondary particles are formed during the sol-gel process and no further size increase in MPSMs is observed. At sol-gel rates >> SNP incorporation by diffusion and adsorption, a fourth regime (IV) with formation of hybrid beads with a porous polymer core and a silica shell or, after calcination, hollow silica microspheres are considerable.

The sol-gel kinetics can be significantly influenced by catalyst concentration, water-to-precursor, solvent or precursor type. Thereby, fundamental, reproducibly recurring trends and correlations were discussed, and robust quantitative models were developed for individual reaction steps. The control of sol-gel parameters in the hard template-assisted preparation of MPSMs allows the preparation of a wide range of material properties, while maintaining spherical appearance and a narrow size distribution. Changing the properties of the template extends this space arbitrarily. The application of the materials as reversed-phase HPLC columns for biomolecules, such as proteins and amino acids, was successfully demonstrated.

Further optimization of HPLC separations is possible by matching and optimizing the column material and separation method. As shown here, this can be done effectively, and in a resource-efficient manner, by the approach of RSM. This enables the development of HPLC column materials to keep pace with the requirements of specialized applications, as those of relevance in personalized medicine, and also allows to design materials for other applications in a targeted manner.

# 4. Paper I

## Rational Design of Pore Parameters in Monodisperse Porous Poly(glycidyl methacrylate-co-ethylene glycol dimethacrylate) Particles Based on Response Surface Methodology

*Julia C. Steinbach [1,2,†], Fabio Fait [1,2,†], Stefanie Wagner [2], Alexandra Wagner [1,3], Marc Brecht [1,3], Hermann A. Mayer [2] and Andreas Kandelbauer [1,4,*]*

[1] Process Analysis & Technology, Reutlingen Research Institute, Reutlingen University, Alteburgstraße 150, 72762 Reutlingen, Germany; andreas.kandelbauer@boku.ac.at (A.K.); Julia.Steinbach@Reutlingen-University.de (J.C.S.); Fabio.Fait@Reutlingen-University.de (F.F.); Alexandra.Wagner@Reutlingen-University.de (A.W.); Marc.Brecht@Reutlingen-University.de (M.B.); Andreas.Kandelbauer@Reutlingen-University.de (A.K.)

[2] Institute of Inorganic Chemistry, University of Tübingen, Auf der Morgenstelle 18, 72076 Tübingen, Germany; stefaniewagnersb@googlemail.com (S.W.); hermann.mayer@uni-tuebingen.de (H.A.M.)

[3] Institute of Physical and Theoretical Chemistry, University of Tübingen, Auf der Morgenstelle 18, 72076 Tübingen, Germany

[4] Department of Material Sciences and Process Engineering (MAP), Institute of Wood Technology and Renewable Materials, University of Natural Resources and Life Sciences, Gregor-Mendel-Straße 33, 1180 Vienna, Austria

[*] Correspondence: andreas.kandelbauer@reutlingen-university.de; Tel.: +49-(0)7-12-1271-2009

[†] These authors contributed equally to this work.



Steinbach, J.C.; Fait, F.; Wagner, S.; Wagner, A.; Brecht, M.; Mayer, H.A.; Kandelbauer, A. Rational Design of Pore Parameters in Monodisperse Porous Poly(glycidyl methacrylate-co-ethylene glycol dimethacrylate) Particles Based on Response Surface Methodology. *Polymers (Basel)* **2022**, *14*, 382, doi:10.3390/polym14030382.[1]

## Abstract

Monodisperse porous *poly*(glycidyl methacrylate-*co*-ethylene glycol dimethacrylate) particles are widely applied in different fields, as their pore properties can be influenced and functionalization of the epoxy group is versatile. However, the adjustment of parameters which control morphology and pore properties such as pore volume, pore size and specific surface area is scarcely available. In this work, the effects of the process factors monomer:porogen ratio, GMA:EDMA ratio and composition of the porogen mixture on the response variables pore volume, pore size and specific surface area are investigated using a face-centered central composite design. Non-linear effects of the process factors and second order interaction effects between them were identified. Despite the complex interplay of the process factors, targeted control of the pore properties was possible. For each response a response surface model was derived with high predictive power (all $R^2_{predicted} > 0.85$). All models were tested by four external validation experiments and their validity and predictive power was demonstrated.



## Keywords

porous microspheres; design of experiment; seed swelling polymerization; *p*(GMA-*co*-EDMA); particles; monodisperse; pores; morphology; process optimization


## 4.1. Introduction

Porous polymer particles have attracted considerable interest in various applications ranging from clinical diagnostics[142], immobilization support for biocatalysts[143], separation processes like chromatography[79,125,144,145], ion exchange phases[146] to applications as adsorption materials[147,148] or as hard-templates[46,55,56] for inorganic materials with defined structures. In particular, porous poly(glycidyl methacrylate-*co*-ethylene glycol dimethacrylate) (*p*(GMA-*co*-EDMA)) has been widely used, as the epoxy ring of GMA can be derivatized in various ways by ring opening reactions[143,149–151]. This allows application-specific functionalization and makes the *p*(GMA-*co*-EDMA) a versatile platform polymer. *p*(GMA-*co*-EDMA) particles have been used as chromatographic column material[79,152], as carriers for biocatalysts[153], for solid phase extraction[147] or as hard template for porous silica particles with defined pore structure[56].

For many applications involving particles, a small size distribution is advantageous. Monodispersity in these porous microspheres can be achieved through seeded swelling polymerization[75,154]. This approach allows not only to influence dispersity and size of microspheres, but also to tailor surface properties[155]. Thereby the increase in size is mainly dependent of the ratio of the organic phase to the amount of seed particles[82,156]. It has been reported that the specific surface area, porosity and pore volume depend

on the composition of the organic phase of seeded swelling polymerization[156–162]. The organic phase usually consists of the monomers, here EDMA as crosslinker and GMA as monomer with a functional epoxide ring, and the porogen mixture, which are inert solvents, here cyclohexanol and toluene.

However, due to the high complexity of the system and the dependency on the different solubilities of the components, previous studies have been rather confined to semi quantitative statements from considerations of isolated process factors ("one-factor-at-a-time", OFAT), which do not allow a specific control of the synthesis and the pore and surface properties. In contrast to the common OFAT approach, in response surface methodology (RSM) multiple process factors are simultaneously and systematically varied and their effects are analyzed using a statistical approach. RSM provides not only insight in the effect strengths of single process factors but also allows to detect the presence of non-linear behavior and synergistic interactions between multiple process factors. This provides a detailed causal model of the studied process[59–61]. Currently, to the best of our knowledge, there is no predictive causal model available that is actually based on the numerical effects of the process factors on the morphological properties of porous *p*(GMA-*co*-EDMA) particles and thus allow for demand-driven control of particle properties.

The present study aims at demonstrating a valid and robust model allowing for tailored modification of pore parameters in porous *p*(GMA-*co*-EDMA) particles using RSM. For this purpose, the statistical significance and effect strengths of the process factors involved in the synthesis a) monomer:porogen ratio, b) GMA:EDMA ratio and c) composition of the porogen mixture (toluene:cyclohexanol) were determined with respect to the responses pore volume, pore size and specific surface area using a face-centered central composite experimental design. The pore properties were analyzed using inverse size exclusion chromatography (iSEC). To enable further application-specific functionalization, the conversion of the epoxide groups in the particles was studied by FTIR in combination with multivariate calibration by partial least squares regression (PLS-R). Additional particles were prepared using four sets of factor level combinations as external validation experiments and characterized to verify the robustness and validity of the response surface models (RSM) established. The RSM approach has offered a better understanding of the seeded swelling polymerization for porous *p*(GMA-*co*-EDMA) and has provided valid, predictive models for the pore volume, pore size and specific surface area, which allow targeted adjustment of these quantities.

## 4.2. Materials and methods

### 4.2.1. Chemicals

Styrene (99 %), and ethylene glycole dimethacrylate (EDMA, 98 %) were purchased from Fisher Scientific GmbH (Schwerte, Germany). Polyvinylpyrrolidone K30 (PVP), benzoyl peroxide (BPO, 75 %), dibutyl phthalate (DBP, 99 %) and glycidyl methacrylate (GMA, ≥97 %) were purchased from Sigma-Aldrich Chemie GmbH (Taufkirchen, Germany). Polyvinyl alcohol (PVA, hydrolyzed 86–89 %) was purchased from abcr GmbH (Karlsruhe, Germany). Sodium dodecyl sulfate (SDS, ≥99 %) was purchased from Carl Roth GmbH + Co. KG (Karlsruhe, Germany). Ethanol 96 % was purchased from VWR Chemicals (Darmstadt, Germany). All chemicals were used as delivered.

For the iSEC analysis tetrahydrofuran 99.9 % was purchased from Carl Roth GmbH + Co. KG (Karlsruhe, Germany) and the polystyrene (PS) standards were purchased from PSS Polymer Standards Service GmbH (Mainz, Germany).

### 4.2.2. Instrumentation

An Ultra-Turrax T50 (IKA®-Werke GmbH & CO. KG, Staufen, Germany) was used for homogenization of the prepared emulsions.

iSEC measurements were carried out using an Agilent 1100 series system (Agilent Technologies, Waldbronn, Germany) equipped with a quaternary pump with degasser, an auto sampling system, 6-port valve for column selection and a DAD detector (254 nm). Instrument control, data acquisition and automated data analysis was performed by the Chem-Station software (B.04.03, Agilent Technologies, Waldbronn, Germany).

Spectral characterization was performed using a Frontier 2 FTIR (PerkinElmer LAS GmbH, Rodgau, Germany) with an attenuated total reflection accessory. The resolution was 2 $cm^{-1}$ with 4 scans. For data processing the spectral region was reduced to the region from 1750 to 700 $cm^{-1}$ which carried the highest amount of relevant information. The spectra were smoothed using a Savitzky-Golay filter and were treated with standard normal variate transformation, to remove multiplicative scattering interferences[63,163].

A partial least square regression model (PLS-R, kernel algorithm) was applied for multivariate calibration of the relative GMA ratio. A total of 155 spectra from particles **Std1–19** were used for modelling. From the 24 spectra of particles **Val1–4** the predictive power of the model was verified. The processing software Unscrambler-X (CAMO Software AS, version 10.5.1, Oslo, Norway) was employed for spectral preprocessing, spectral analysis and multivariate data analysis.

### 4.2.3. Seeded suspension polymerization of porous *p*(GMA-*co*-EDMA) particles

The porous *p*(GMA-*co*-EDMA) particles were synthesized by seeded suspension polymerization using toluene and cyclohexanol as porogens. The polystyrene (PS) seeds were prepared according to the procedure provided in the Appendix 4.5.1. 0.3 g PS seeds and 5 mL of a 2.0 $g \cdot L^{-1}$ SDS solution were sonicated for 10 min. An emulsion containing 2.0 mL of the activator DBP and 150 mL of SDS (2.53 $g \cdot L^{-1}$) were homogenized for 10 min at 5000 rpm and added to the seed particle suspension. The mixture was stirred for 24 h at 200 rpm at room temperature. Thereafter an emulsion (10 min, 5000 rpm) containing 150 mL of SDS (3.33 $g \cdot L^{-1}$), initiator BPO (0.4 g), porogens and acrylate monomers was added. The relative amount of added monomers (GMA:EMDA) and porogens (toluene:cyclohexanol) was systematically varied according to the experimental design (**Table 4.1**). The absolute volume of added monomers and porogens was 30 mL for each synthesis.

**Table 4.1** Range of process factors level setting as used in the face-centered central composite experimental design (FCD).

| Factor | Name | Low Setting (-) | Center Point (0) | High Setting (+) |
|---|---|---|---|---|
| **A** | Monomer /vol% | 30 | 50 | 70 |
| **B** | GMA /vol% | 20 | 50 | 80 |
| **C** | Toluene /vol% | 0 | 50 | 100 |

To allow for complete swelling, the system was stirred at 200 rpm for another 24 h. 150 mL of a 23.3 $g \cdot L^{-1}$ PVA solution was added to the mixture as stabilizer. The reaction mixture was heated to 70 °C and stirred at 200 rpm for 24 h for polymerization. After polymerization the porous particles were filtered off and washed three times with ethanol and three times with water. The porous copolymer particles were then dried prior to analysis.

### 4.2.4. Experimental design

A face-centered central composite experimental design (FCD) was set up, allowing the mathematical description of non-linear terms[164,165]. A total of 19 particle batches were synthesized with five center point (CP) replications to determine reproducibility and system variance.

The effects of three factors were investigated by systematic variation according to an FCD response surface design, with the low, intermediate and high factor level settings given in **Table 4.1**. As factors the ratio of monomer (methacrylates) to porogens (A: monomer:porogen vol%), the ratio of monomer with the functional group (GMA) to the crosslinker (EDMA) (B: GMA:EDMA vol%) and the ratio of the porogens toluene to cyclohexanol (C: toluene:cyclohexanol vol%) were varied.

The effects were analyzed using analysis of variance (ANOVA). The significance level

was $\alpha = 0.05$, meaning that a model or model term was considered statistically significant if its $p$-value was $p \leq 0.05$.

For model validation four additional syntheses within the design space were conducted. The validation experiments **Val1–Val4** were selected as a series with increasing GMA content moving through the experimental space along one factor axis, see **Table 4.2**. This would correspond to a one-factor-at-a-time experiment. The run order is the randomized order in which the experiments were actually performed to compensate for systematic errors.

**Table 4.2** Factor level settings and the corresponding particle properties specific pore volume, pore size, specific surface area (SSA), particle size and dispersity $d_{90}/d_{10}$ listed according to Yates standard order (Std).

| | | Factor Level Settings | | | Response Values | | | | |
|---|---|---|---|---|---|---|---|---|---|
| | | **A** | **B** | **C** | | | | | |
| **Std** | **Run** | **Monomer: Porogen ratio** | **GMA: EDMA ratio** | **Toluene: Cyclohexanol ratio** | **Pore Volume $V_P$** | **Pore Size $\Phi_{50}$** | **Specific Surface Area SSA** | **Particle Size** | **$d_{90}/d_{10}$** |
| | | /vol% | /vol% | /vol% | /mL·g$^{-1}$ | /Å | /m$^2$·g$^{-1}$ | /µm | - |
| ***1** | **2** | 30 | 20 | 0 | 0.52 | 166 | 126 | 7.41 | 1.15 |
| **2** | **5** | 70 | 20 | 0 | 0.06 | 37 | 71 | 8.15 | 1.11 |
| ***3** | **3** | 30 | 80 | 0 | 0.44 | 631 | 28 | 7.42 | 1.08 |
| **4** | **7** | 70 | 80 | 0 | n.a. | n.a. | n.a. | 7.74 | 1.20 |
| **5** | **4** | 30 | 20 | 100 | 0.55 | 426 | 51 | 8.82 | 1.16 |
| **6** | **8** | 70 | 20 | 100 | 0.18 | 49 | 148 | 9.41 | 1.06 |
| **7** | **10** | 30 | 80 | 100 | n.a. | n.a. | n.a. | n.a. | n.a. |
| **8** | **9** | 70 | 80 | 100 | 0.25 | 715 | 14 | 9.22 | 1.13 |
| **9** | **1** | 50 | 50 | 50 | 0.30 | 217 | 56 | 8.31 | 1.14 |
| **10** | **6** | 50 | 50 | 50 | 0.30 | 237 | 50 | 8.09 | 1.11 |
| **11** | **11** | 50 | 50 | 50 | 0.26 | 197 | 53 | 8.83 | 1.11 |
| **12** | **13** | 30 | 50 | 50 | 0.49 | 438 | 45 | 8.56 | 1.05 |
| **13** | **19** | 70 | 50 | 50 | 0.09 | 126 | 28 | 9.10 | 1.06 |
| **14** | **18** | 50 | 20 | 50 | 0.30 | **83** | 146 | 9.07 | 1.04 |
| **15** | **14** | 50 | 80 | 50 | 0.26 | 538 | 20 | 8.81 | 1.07 |
| **16** | **15** | 50 | 50 | 0 | 0.17 | 88 | 77 | 8.39 | 1.06 |
| **17** | **17** | 50 | 50 | 100 | 0.50 | 332 | 60 | 9.38 | 1.04 |
| **18** | **16** | 50 | 50 | 50 | 0.29 | 177 | 66 | 8.92 | 1.05 |
| **19** | **12** | 50 | 50 | 50 | 0.28 | 193 | 58 | 8.37 | 1.07 |
| **Val1** | **20** | 50 | 20 | 73 | 0.41 | 124 | 132 | 8.41 | 1.09 |
| **Val2** | **21** | 50 | 40 | 73 | 0.56 | 141 | 159 | 7.81 | 1.15 |
| **Val3** | **22** | 50 | 60 | 73 | 0.37 | 370 | 40 | 7.87 | 1.15 |
| **Val4** | **23** | 50 | 80 | 73 | 0.36 | 744 | 20 | 7.19 | 1.19 |

* marks model outliers.

### 4.2.5. Pore characterization using inverse size exclusion chromatography (iSEC)

The particles were packed into stainless steel columns (4.6 x 250 mm) using the slurry method with ethanol/water (50:50 vol%:vol%). For characterization of the pore properties the columns were analyzed by iSEC. A set of 19 polystyrene (PS) standards from $M_w$ = 162 Da–2.5 mDa with a molar-mass dispersity of < 1.1 were applied. 10 µL of each 2.5 g·L$^{-1}$ PS in THF were separately injected (10 µL) three times. The lowest molecular weight standard was used as a $t_0$ marker. All standards were measured with THF as eluent and a flow rate of 0.25 mL·min$^{-1}$.

The pore parameters were analyzed in accordance to the method of Halász et al. (1978)[129]. The pore volume $V_P$ is calculated using Equation (4.1):

$$V_p = V_0 - V_i \tag{4.1}$$

as the difference between the dead volume $V_0$ (= elution volume of $t_0$ marker) and $V_i$ the interstitial volume (= elution volume of totally permeating volume).

The distribution coefficient $K_{SEC}$ is dependent on the pore size of the particles. It can be derived from the experimentally determined elution volume $V_e$, the interstitial volume $V_i$ and the elution volume of the totally permeating solute $V_p$, see Equations (4.2) and (4.3):

$$V_e = V_i + V_p \times K_{SEC} \tag{4.2}$$

$$K_{SEC} = \frac{V_e - V_i}{V_p} \tag{4.3}$$

According to Halász et al. the exclusion values (pore size) $\Phi$ in Å of linear PS in a good solvent can be calculated based on the molecular weights $M_w$ (Da) of the PS standards as follows:

$$\Phi \cong 0.62\ {M_w}^{0.59} \tag{4.4}$$

The mean pore size $\Phi_{50}$ is determined from the lognormal distribution plot of $K_{SEC}$ as function of log($\Phi$) the at $K_{SEC}$ = 50 %.

From the pore volume $V_p$ (mL) and the mean pore size $\Phi_{50}$ (Å) the specific surface area $S$ can be derived according to Equation (4.5):

$$\mathrm{S} = \frac{4000 \times V_p}{\Phi_{50}} \tag{4.5}$$

### 4.2.6. Scanning electron microscopy images (SEM)

For the evaluation of morphology, particle size and dispersity SEM images were acquired using a Hitachi SU8030 (Hitachi High-Tech Europe GmbH, Krefeld, Germany).

The size and dispersity were assessed semi-automatically from the SEM images using a self-written MATLAB script. 400–500 particles were measured (min. 374), except for **Std7** were no sufficient number of intact particles could be evaluated. The median particle diameter is given as particle size in μm. The dispersity is given by the $d_{90}/d_{10}$ value which indicates the width of the particle size distribution. Here $d_{90}$ is the value below which 90 % of the distribution lies, with $d_{10}$ corresponding to 10 % of the distribution. A $d_{90}/d_{10}$ value smaller than 1.4 is considered as a monodisperse distribution.

## 4.3. Results and discussion

For systematic evaluation of the synthesis factors which influence the particle size, pore volume, pore size, specific surface area and morphology of the porous particles, approach of RSM was applied. Compared to single-factor variation-based experiments, RSM not only offers a more time- and resource-efficient approach, but also allows the determination of non-linear effects and interactions of the parameters[62].

Factor level settings of the process factors A: monomer:porogen ratio, B: GMA:EDMA ratio and the porogen composition C: toluene:cyclohexanol were systematically varied according to the FCD design given in **Table 4.2**. All *p*(GMA-*co*-EDMA) particles **Std1–19** (**Table 4.2**) were synthesized using a seeded swelling polymerization process. The employed seed PS particles were 1.95 μm in size and had a narrow size distribution of $d_{90}/d_{10}$ = 1.09 (span: 0.09). They were all from the same batch. **Std1** and **Std3** were defined as outliers due to their untypically large residuals and increased lack of fit. These two experiments were excluded from further analysis.

### 4.3.1. Particle size and dispersity

The *p*(GMA-*co*-EDMA) particle sizes varied between 7.41–9.38 μm and particles of all batches showed a monodisperse distribution with a $d_{90}/d_{10}$ range between 1.04 and 1.20 (CV% max. 15.8 %), see **Figure 4.1**. No statistically significant effects of the factors on the dispersity were found. The median $d_{90}/d_{10}$ is 1.08. This is in accordance to the finding that the dispersity of the seed particle is crucial for the dispersity of the product[166].

For the final particle size, a statistically significant effect (p = 0.0004) of the porogen composition is found. The model equation in terms of coded factors of the effect onto the particle size is given in Equation (4.6):

$$\text{Particle size } /\mu\text{m} = 8.69 + 0.5521\ C \tag{4.6}$$

The higher the ratio of toluene:cyclohexanol /vol% larger particles are obtained (p = 0.0004). The model quality parameters are $R^2 = 0.6070$ and $R^2_{predicted} = 0.4942$.

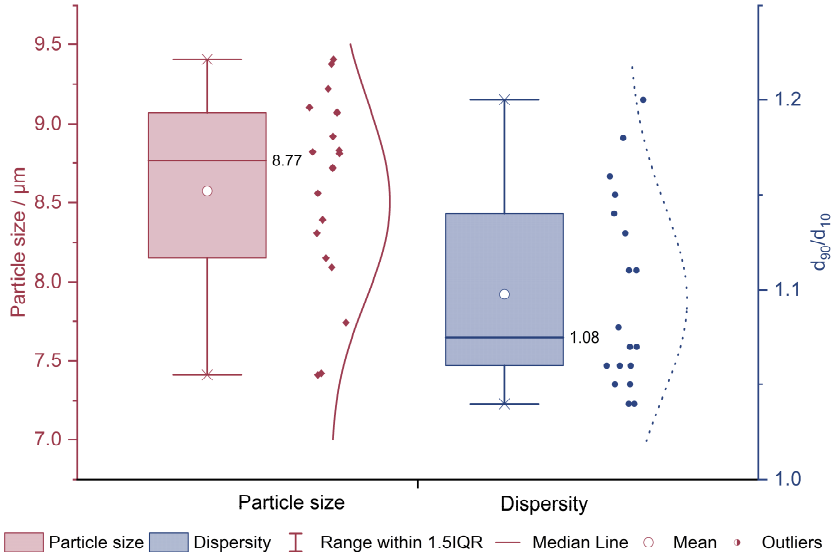


**Figure 4.1** Box-Whisker-Plot with lognormal distribution curve of single values for particle sizes (left hand, red) and $d_{90}/d_{10}$ (right hand, blue) of standard order 1–19. Box displays 1. and 3. quartile, whiskers display 1. and 3. quantile + 1.5 · interquartile range. x= minimum and maximum values.

### 4.3.2. Morphology

A clear change in morphological characteristics is observed with the systematic variation factor level settings, (**Figure 4.2**). Increasing the monomer ratio of the organic phase, generates less porous particles. This effect is especially pronounced at high levels of GMA content of the monomers. The toluene:cyclohexanol ratio strongly affects the surface roughness. While a high content of toluene generates a smooth particle surface, high cyclohexanol content leads to a rough dimpled appearance. The roughness and surface irregularities are intensified with increasing GMA ratio in the monomer composition. Interestingly, **Std1** and **Std3** show a hole at one side of the particle, which is approximately 2 µm in diameter. Both batches were synthesized with a high content of cyclohexanol as the porogen (70 vol% of organic phase). Similar behavior was found earlier when high amounts of cyclohexanol were used[75,167]. This finding can be related to the solubility of the seed particle PS in the overall composition of the organic phase. The suitability of solvents can be approximated using the relative energy difference (RED), which is the ratio of the distance in Hansen space $R_a$ to the radius of the interaction sphere in the Hansen space $R_0$ (here for PS). Good solvents show RED values below 1, solvents around 1 are found to only partly dissolve the solute (or swell it), while RED values higher are non-solvents[168]. Cyclohexanol is the least suitable solvent for PS used in the experiments and shows a RED of 0.96 (GMA 0.82, toluene 0.65, DBP 0.59). While the seed particle is soluble in the organic phase still containing the monomers, with progressing polymerization the solubility decreases until the solubility limit is exceeded and the seed particle is reformed. Therefore, no polymeri-

zation of methacrylate takes place in this area, leaving a hole after the PS is detached during purification. In contrast to the syntheses shown here, the seed swelling polymerization of *p*(GMA-*co*-EDMA) using 1-hexanol as porogen results in polystyrene caps persisting on the particle surface instead of holes[9]. A dependence on the solubilities is assumed. This could also be the reason for the higher studentized residuals, for the analysis see **Table 4.2**.

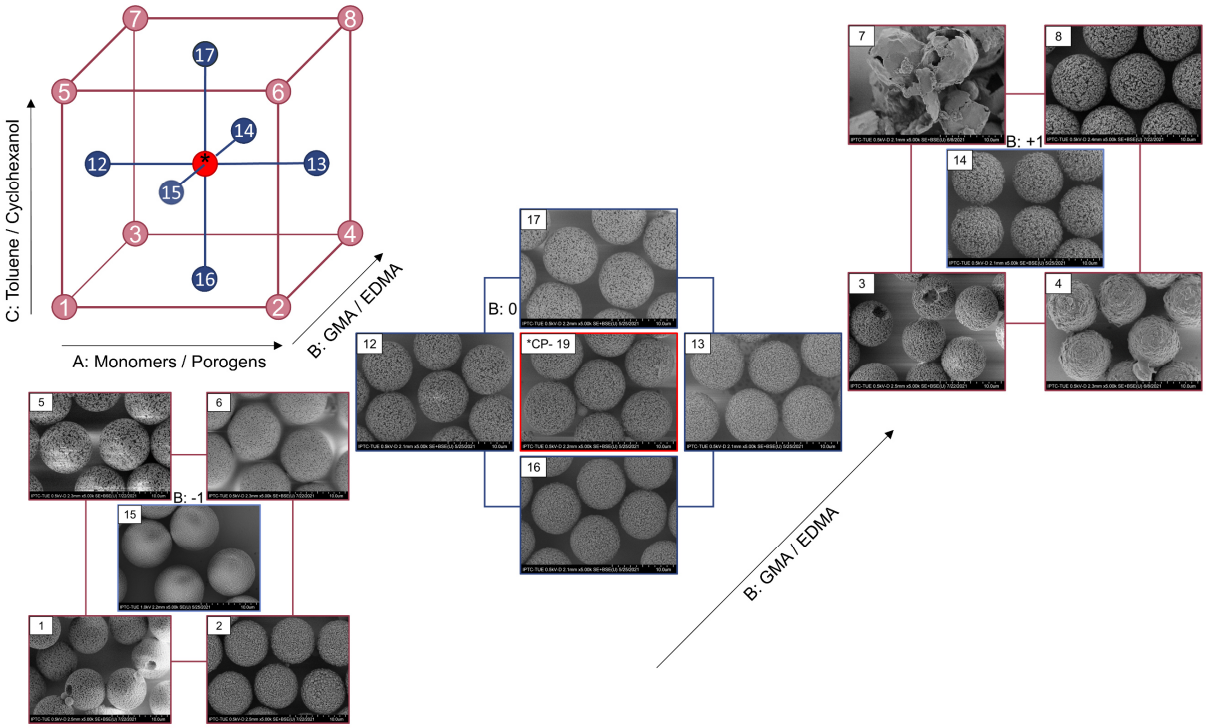


**Figure 4.2** SEM images with 10,000 × magnification of each particle batch numbered by standard order. The design cube is divided according to the level of factor B: GMA:EDMA ratio. Factorial points are numbered according to the standard order given in **Table 4.2** and are displayed burgundy, central point is displayed red and axial points are displayed blue.

With the reaction conditions **Std7** with a high porogen content consisting of 100 vol% toluene and a high GMA ratio of monomers, no stable particles were obtained. From SEM pictures the particles look like empty shells or skins with a smooth outer layer (**Figure 4.2**). This phenomenon could result from low solubility of toluene in water, leading to a displacement of monomers at the interface with the continuous aqueous phase to minimize surface tension. Thus, a polymeric skin is formed during polymerization around the toluene which is present in and accumulated on the inside of the particle[70,155].

Particles obtained with factor settings according to **Std4** exhibited no visible porosity, but rather outwardly curved dimple structures (**Figure 4.2**). This effect results from high monomer content with small ratio of GMA and the usage of pure cyclohexanol as porogen. Due to the lack in porosity no iSEC analysis could be performed with these particles.

### 4.3.3. Multivariate calibration model for epoxy functionalization

With the epoxy group as functional group the *p*(GMA-*co*-EDMA) particles can easily be converted to a desired functionalization. For multivariate calibration a PLS-R model based on nine factors was calculated from the spectra of **Std1–19** (**Figure 4.3**). To test the predictive power of the model, the GMA content of validation experiments **Val1–4** was predicted (**Table 4.3**), based on the corresponding SNV pre-treated spectra (**Figure 4.3**c). The explained variance plot is given in **Figure A. 4.1**.

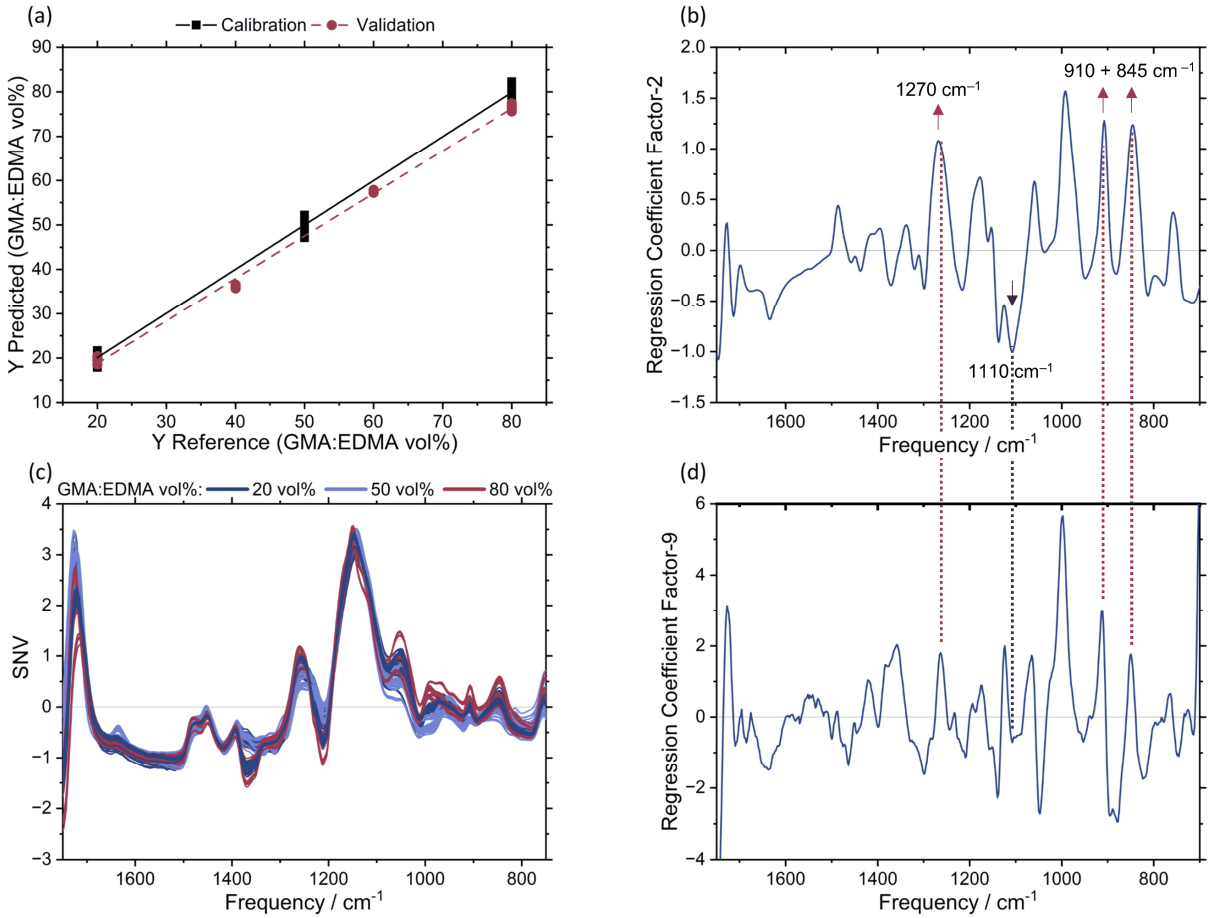


**Figure 4.3** PLS-R with nine factors for GMA:EDMA ratio based on FTIR spectra**. a)** shows the predicted vs. reference of GMA:EDMA ratio for calibration (■) and validation (●). The SNV pre-treated spectra of GMA:EDMA ratio of 20 vol% (dark blue), 50 vol% (light blue) and 80 vol% (red) are displayed in **c). b)** and **d**) show the regression coefficients for factor two (highest explained variance) and factor nine (model regression coefficient) and influential frequencies are highlighted.

With an $R^2_{calibration} = 0.99$ and $R^2_{predicted} = 0.98$ the model quality is very good (**Figure 4.3**a). The root-mean-square-error of calibration is 1.2 vol%, and that of prediction is 2.9 vol% GMA. The model allows an accurate determination of the GMA:EDMA monomer ratio (relative deviation predicted/actual < 5 %) used in the synthesis (**Table 4.3**). The highest explained variances lie on factors 1 and 2 (88 %, **Figure 4.3**b). However, due to the complex interplay between the process factors used in the system[63], nine regression coefficients are required to build a robust model with high predictive power. From the

regression coefficients, the relevant absorbance signals carrying the distinguishing information can be identified. The most important frequencies are indicated in **Figure 4.3**b.

**Table 4.3** Actual versus Prediction values of GMA:EDMA ratio / vol% and deviation

| Std | Actual GMA /vol% (GMA:EDMA) | Predicted GMA /vol% (GMA:EDMA) | Δ /vol% |
|---|---|---|---|
| **Val1** | 20 | 19.8 | −0.2 |
| **Val2** | 40 | 57.4 | −2.6 |
| **Val3** | 60 | 76.6 | −3.4 |
| **Val4** | 80 | 36.3 | −3.7 |

For increasing EDMA ratio (and vice versa decreasing GMA content) the symmetric C-O-C stretching vibration at 1110 $cm^{-1}$[128] is increasing (**Figure 4.3**). The characteristic frequencies increasing with GMA ratio are mainly related to vibrations of the epoxide group, with the symmetric and asymmetric ring vibration of the epoxide ring at 845 $cm^{-1}$[128] and 910 $cm^{-1}$[128], respectively. The C-O stretching vibration of the epoxide ring at 1270 $cm^{-1}$[128] also responds to changes in GMA ratio. This shows that the monomers are converted proportional to the mixture components and epoxide groups are present in the respective amounts in the final product. Hence, the degree of functionalization can be controlled.

### 4.3.4. Pore volume

The effects of the process factors on the pore volume were analyzed by ANOVA are given in **Table 4.4**.

**Table 4.4** Analysis of variance (ANOVA) for the analysis of FCD design of pore volume.

| Source | Sum of Squares | df | Mean Square | F-value | p-value | |
|---|---|---|---|---|---|---|
| **Model** | 0.2660 | 4 | 0.0665 | 77.64 | < 0.0001 | significant |
| **A**-Monomer | 0.1741 | 1 | 0.1741 | 203.24 | < 0.0001 | |
| **B**-GMA | 0.0026 | 1 | 0.0026 | 3.04 | 0.1118 | |
| **C**-Toluene | 0.0785 | 1 | 0.0785 | 91.59 | < 0.0001 | |
| **BC** | 0.0110 | 1 | 0.0110 | 12.88 | 0.0049 | |
| | | | | | | |
| **Residual** | 0.0086 | 10 | 0.0009 | | | |
| Lack of Fit | 0.0074 | 6 | 0.0012 | 4.43 | 0.0856 | not significant |
| Pure Error | 0.0011 | 4 | 0.0003 | | | |
| **Cor Total** | 0.2746 | 14 | | | | |

A statistically significant model ($p < 0.0001$) describing the pore volume in dependence of four effects was obtained. The effect of factors monomer:porogen ratio ($p < 0.0001$), toluene:cyclohexanol ratio ($p < 0.0001$) and the interaction effect between GMA:EDMA

ratio and toluene:cyclohexanol ratio (p = 0.0049) are statistically significant. The linear term B (GMA:EDMA ratio) is only added to comply with model hierarchy[10]; since B is involved in an interaction effect it must be included in the model although by itself B was no statistically significant effect term. The lack of fit is non-significant with p > 0.05. The strengths of the effects are given as coded equation in Equation (4.7):

$$V_p/mL \cdot g^{-1} = 0.2903 - 0.1984\ A - 0.0249\ B + 0.1366\ C + 0.0749\ BC \quad (4.7)$$

Equation (4.7) shows a linear negative effect of A: monomer:porogen ratio on the pore volume and is also the strongest effect. As the amount of monomer increases or the amount of porogen on the organic phase decreases during swelling, the polymer network becomes denser, less space is occupied by inert porogen, and thus the pore volume is reduced[167,169].

However, **Figure 4.3** and Equation (4.7) show that not only the monomer:porogen ratio influences the pore volume, but also the composition of the porogen mixture and its synergistic interaction with the GMA:EDMA ratio. The porogen composition was examined in a range of 0/100 v/v ratio of toluene:cyclohexanol to a ratio of 100/0 v/v of toluene:cyclohexanol.

Depending on the suitability of the solvent for the polymer either χ-induced or ν-induced syneresis takes place, corresponding to a phase separation before or after the gel point, respectively[70]. Good solvents lead to smaller pores, smaller pore volumes and larger surface areas through ν-induces syneresis[70]. Nonsolvent or even linear polymeric porogens, like the PS from the seed particle, lead to larger pores with higher pore volume but reduced specific surface area through χ-induced syneresis[79]. According to the Hildebrandt solubilities of the *p*(GMA-*co*-EDMA) polymer with 24.0 $Mpa^{1/2}$[170], toluene with 18.2 $MPa^{1/2}$[168] and cyclohexanol with 22.4 $MPa^{1/2}$[168], cyclohexanol is a better suited solvent for the polymer and should therefore result in smaller pores and smaller pore volumes. Since the amount of PS seed is constant, its influence as linear polymeric porogen is assumed to be constant for all conducted syntheses. The factor C: toluene vol% shows a generally positive effect on the pore volume. With increasing amount of toluene in the porogen composition, the pore volume increases as well. This is supported by the Hildebrand solubilities.

However, **Figure 4.4**a shows that this relationship is not linear, since the interaction term BC between GMA:EDMA ratio and porogen composition has a high significant (p = 0.0066). While particles which have a low GMA content, show similar pore volumes for high and low toluene ratio in the porogen mixture, a difference for particles with high GMA content is visible. With increasing GMA content lower pore volumes are obtained with low toluene ratio whereas high pore volumes are accessible with a

high toluene ratio (**Figure 4.4**b). The interaction BC could therefore be caused by changing solubilities depending on the porogen and monomer mixture, indicating a better solubility of GMA in cyclohexanol. The relationships of the factors on the pore volume are very complex, due to the influence of the solubilities. Nevertheless, the model shows a very good correlation with $R^2 = 0.9688$ and $R^2_{predicted} = 0.9012$.

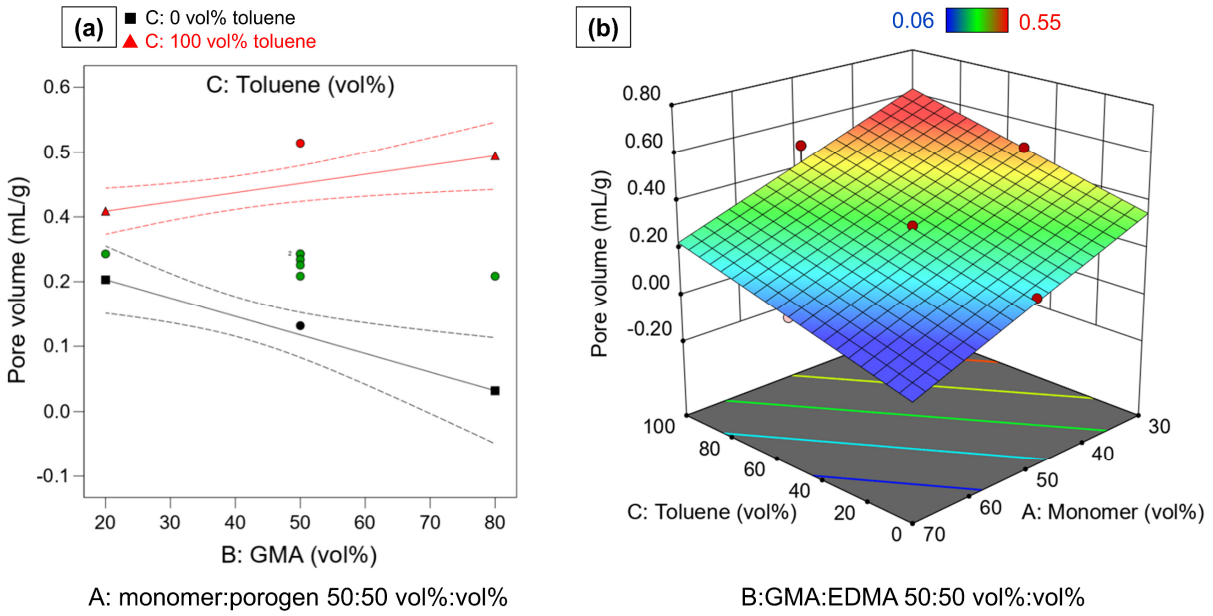


**Figure 4.4 a)** Interaction plot of BC GMA:EDMA*toluene:cyclohexanol at medium level of factor A. Red triangles indicate measured pore volume at high toluene content. Black squares indicate measure particle volume at 0 vol% toluene (100 vol% cyclohexanol). Green circles indicate measured pore volume at medium toluene level. Dashed lines indicate 95 % confidential intervals. **b)** Shows response surface of pore volume in dependence of factors A and C. Blue areas correspond to low pore volumes, red areas correspond to high pore volume.

### 4.3.5. Pore size

The effects of the variations in process factor levels on pore size were also found to be highly statistically significant ($p < 0.0001$). The pore size is dependent on factor A: monomer:porogen ratio, factor B: GMA:EDMA ratio, and factor C: toluene:cyclohexanol ratio. However, the interrelationships between the factors are more complex, as can be seen from the fact that not only the non-linear effects terms $A^2$ and $B^2$ are required to describe the influences on the response, but there is also a synergistic interaction (second order interaction term, 2FIA) between the factors BC, the ratio of the monomers and the composition of the porogen mixture. This means the effect of neither the monomer nor the porogen composition can be adequately discussed without considering the other factor. The statistical parameters for the single model terms and the overall model are collected in **Table 4.5**.

**Table 4.5** Analysis of variance (ANOVA) for the analysis of FCD design of pore size.

| Source | Sum of Squares | df | Mean Square | F-value | p-value | |
|---|---|---|---|---|---|---|
| **Model** | $5.341\times10^5$ | 6 | 89009.19 | 132.49 | < 0.0001 | significant |
| **A**-Monomer | $1.171\times10^5$ | 1 | $1.171\times10^5$ | 174.28 | < 0.0001 | |
| **B**-GMA | $1.563\times10^5$ | 1 | $1.563\times10^5$ | 232.68 | < 0.0001 | |
| **C**-Toluene | 54489.80 | 1 | 54489.80 | 81.11 | < 0.0001 | |
| **BC** | 21969.58 | 1 | 21969.58 | 32.70 | 0.0004 | |
| **$A^2$** | 24163.44 | 1 | 24163.44 | 35.97 | 0.0003 | |
| **$B^2$** | 40191.80 | 1 | 40191.80 | 59.82 | < 0.0001 | |
| **Residual** | 5374.59 | 8 | 671.82 | | | |
| Lack of Fit | 3217.79 | 4 | 804.45 | 1.49 | 0.3539 | not significant |
| Pure Error | 2156.80 | 4 | 539.20 | | | |
| **Cor Total** | $5.394\times10^5$ | 14 | | | | |

The model shown provides a very good indication of the complex effects of the process factors on the response pore size. It allows a very good correlation with the data $R^2$ = 0.9900. Furthermore, a prediction of the pore size with an $R^2_{predicted}$ = 0.9452 is possible.

The effect of the synthesis parameters in coded form is given in Equation (4.8):

$$\Phi_{50}\,/\text{Å} = 200.92 - 167.93\,A + 215.35\,B + 127.15\,C + 109.11\,BC + 98.38\,A^2 + 126.88\,B^2 \quad (4.8)$$

The factor effect term B (GMA:EDMA) strongly influences the pore size of the particles, as both the linear and non-linear term show high positive values of factor effect coefficients. With an increase of GMA ratio the pore size increases, whereby the positive non-linear $B^2$ term indicates the even stronger influence the higher the GMA ratio is. As far as the chemical composition is concerned this finding can be explained through decreasing cross-linking degree in the polymer structure, since the EDMA cross-linker content diminishes. However, due to the pronounced 2FIA of GMA:EDMA and toluene:cyclohexanol ratio, the effect of the GMA content cannot be understood without at the same time considering the composition of the porogen mixture. Yet, the synergistic effect is less pronounced and the second smallest with a coefficient of +109.11.

**Figure 4.5**a shows the interaction plot for the 2IA BC at a 50:50 vol% ratio for monomer:porogen. It can be seen that the higher the proportion of toluene in the porogen mixtures, the greater is the increase in pore size with increasing GMA content. This effect can be explained by the fact that with increasing GMA content toluene becomes less suitable as a solvent. As a result, phase separation starts earlier and earlier in relation to the gel point, which in turn leads to larger pores. A similar effect has already been shown for the pore volume.

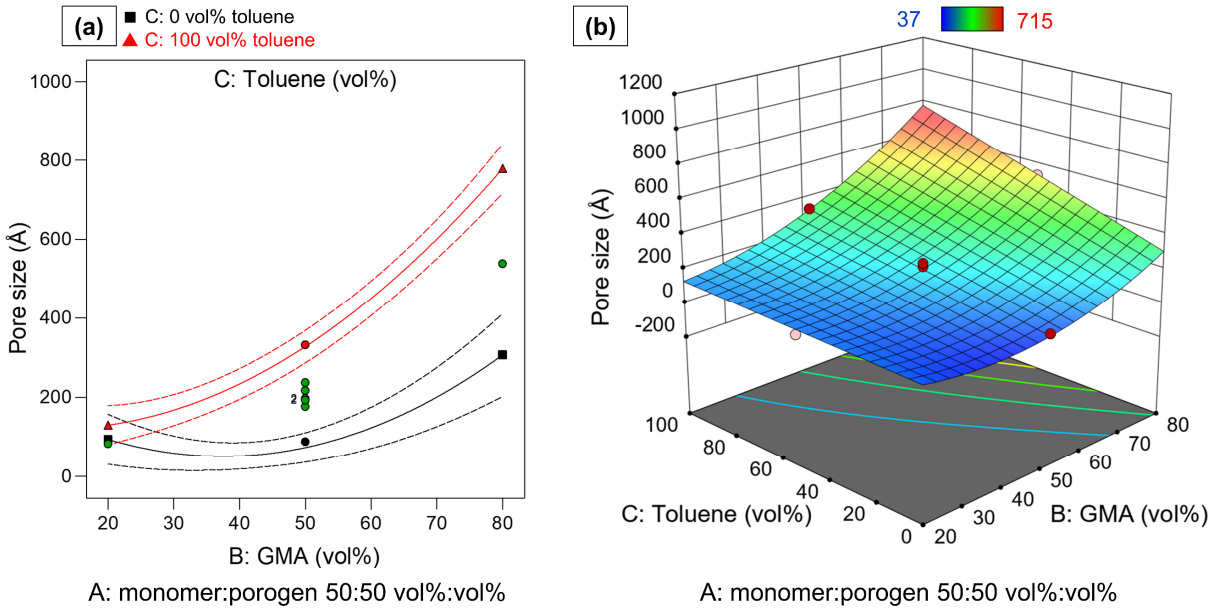


**Figure 4.5 a)** Interaction plot of the synergistic interaction between GMA:EDMA*toluene:cyclohexanol at medium level of factor monomer:porogen ratio. Red triangles indicate measured pore size at high toluene content. Black squares indicate measure pore size at 0 vol% toluene (100 vol% cyclohexanol). Green circles indicate measured pore size at medium toluene level. Dashed lines indicate 95% confidential intervals. **b)** Shows response surface of pore size in dependence of factors B and C at high level of A. Blue areas correspond to low pore sizes, red areas correspond to high pore sizes.

The only factor with a negative effect on the pore size is "A": an increasing ratio of monomer:porogen ratio results in smaller pore sizes. The positive effect of the non-linear term $A^2$ shows a diminishing effect strength for higher monomer ratios, i.e. at higher monomer ratios the depleting effect on "shrinking" pore sizes is less pronounced. Therefore, according to the model, the highest pore sizes should be achieved with a low monomer:porogen ratio, a high amount of GMA or a low amount of EDMA crosslinker, and a high toluene ratio in the porogen mixture (see **Figure 4.5**b). However, it should be noted that this very extreme setting (-/+/+) also corresponds to the synthesis und reaction conditions **Std7** which did not lead to any stable particles (compare **Figure 4.2**). This area of the experimental space represents a critical combination of process factor levels.

The largest pore size with stable particles was achieved in the experiment with reaction conditions **Std8** (+/+/+) at a high monomer content. Even higher pore sizes for stable particles are expected up to a range of about 40–70 vol% monomer at high toluene levels. If lower amounts of toluene are used in the porogen mixture, even lower monomer ratios can lead to stable particles (**Std1** (-/+/-) 631 Å).

### 4.3.6. Specific surface area

The specific surface area is an important characteristic for many applications that depend on surface interactions. Therefore, the specific surface area was determined as the third response value and calculated according to Equation (4.4). The specific surface area is a function of the two previously discussed properties pore volume and pore size. Data analysis was again performed via an ANOVA which is given in **Table 4.6**. Of the linear terms, only B, the GMA:EDMA ratio is statistically significant by itself. The other linear terms are A: monomer:porogen and C: toluene:cyclohexanol were added to preserve model hierarchy, since they are involved in the significant interaction term AC.

**Table 4.6** Analysis of variance (ANOVA) for the analysis of FCD design of specific surface area.

| Source | Sum of Squares | df | Mean Square | F-value | p-value | |
|---|---|---|---|---|---|---|
| **Model** | 20322.72 | 6 | 3387.12 | 51.49 | < 0.0001 | significant |
| **A**-Monomer | 164.25 | 1 | 164.25 | 2.50 | 0.1527 | |
| **B**-GMA | 17190.05 | 1 | 17190.05 | 261.34 | < 0.0001 | |
| **C**-Toluene | 627.78 | 1 | 627.78 | 9.54 | 0.0149 | |
| **AC** | 5132.17 | 1 | 5132.17 | 78.02 | < 0.0001 | |
| **$A^2$** | 1980.56 | 1 | 1980.56 | 30.11 | 0.0006 | |
| **$B^2$** | 839.34 | 1 | 839.34 | 12.76 | 0.0073 | |
| **Residual** | 526.22 | 8 | 65.78 | | | |
| Lack of Fit | 379.02 | 4 | 94.75 | 2.57 | 0.1910 | not significant |
| Pure Error | 147.20 | 4 | 36.80 | | | |
| **Cor Total** | 20848.93 | 14 | | | | |

However, the non-linear effects $A^2$ and $B^2$ are highly statistically significant. Although the specific surface area is deducted from the pore volume and the respective pore size, a different combination of factor effects is statistically significant and required for model building. While the linear terms A and C were highly statistically significant for the other two parameters, these are only hierarchical in the model for the specific surface area. The interaction AC, on the other hand, was not relevant for any of the other responses. This shows that the relationship of the specific surface area and the process factors is highly complex and not predictable in a simple way. The relative impact of each process factor on the specific surface area can be seen in Equation (4.9) in terms of coded factors:

$$SSA\ /m^2 \cdot g^{-1} = 61.04 - 6.98\ A - 64.34\ B - 13.65\ C + 52.74\ AC - 28.16\ A^2 + 18.34\ B^2 \quad (4.9)$$

The strongest effect on the specific surface area results from the negative coefficient for the B: GMA:EDMA ratio. With increasing amount of GMA, the specific surface area

is reduced. This general trend has been reported in literature[156,157,169]. However, through application of RSM the non-linearity of this effect ($B^2$) was shown. The strength of the effect is leveled off with increasing GMA ratio as indicated by non-linear effect of $B^2$. The terms A, C, $A^2$ and $C^2$ are strongly interrelated through the 2FIA term AC, which is the second largest effect, i.e., the system is strongly dominated by the synergistic behavior of two non-linear effects.

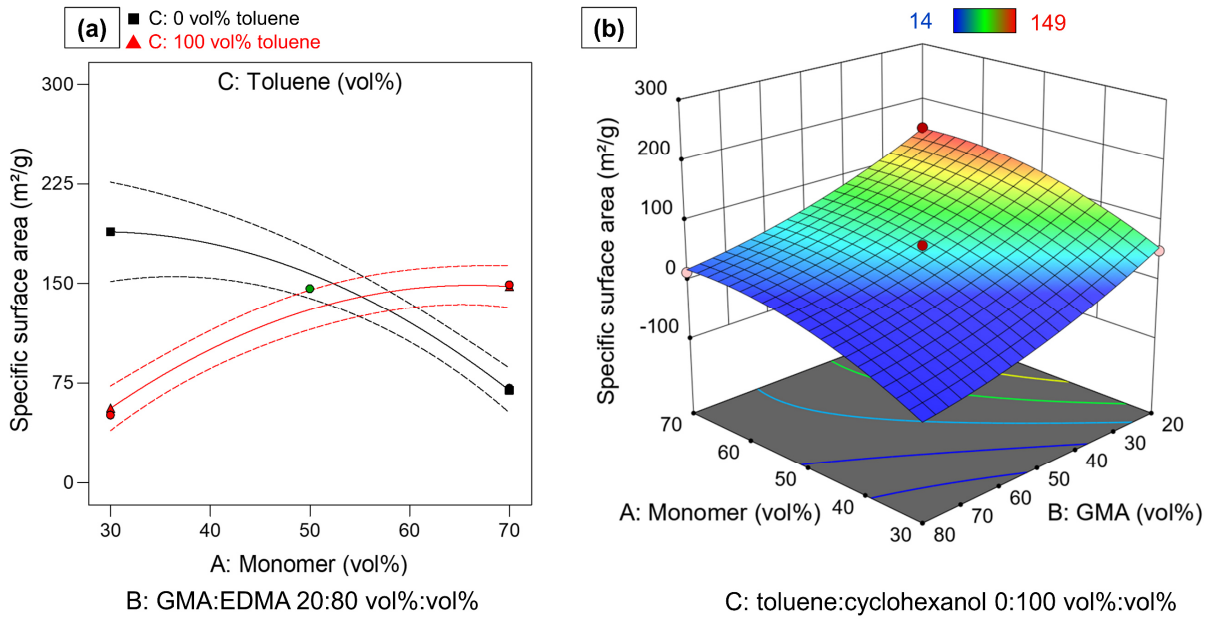


**Figure 4.6 a)** Interaction plot of AC monomer:porogen×toluene:cyclohexanol at medium level of factor B for specific surface area. Red triangles indicate determined specific surface area at high toluene content. Black squares indicate determined specific surface area at 0 vol% toluene (100 vol% cyclohexanol). Green circles indicate determined specific surface area at medium toluene level. Dashed lines indicate 95 % confidential intervals. **b)** Shows response surface of specific surface area in dependence of factors A and B at low level of c. Blue areas correspond to low specific surface areas, red areas correspond to high specific surface areas.

The non-linear $A^2$ term shows a maximum for the specific surface area, but since the factor A: monomer:porogen ratio is involved in an 2FIA with factor C (toluene:cyclohexanol ratio of the porogen mixture), it cannot be discussed individually. This interaction results in a shift in maximum for the specific surface area, the maximum being strongly dependent on the level of A and C. This behavior is clearly visible in the interaction plot given in **Figure 4.6**a. For low toluene content a maximum specific surface area can be seen at a monomer content of approximately 35 vol%. With further increase in monomer ratio, the specific surface decreases. For high toluene content the opposite effect is visible. With increasing monomer ratio, the specific surface area increases until a maximum at around 60 vol% is obtained and then decreases again slightly. This effect is not influenced by the GMA:EDMA ratio of the monomers (**Figure 4.6**b). Again, this behavior can be explained by the different solubilities of monomers, PS seed and polymer particle in the porogens. These opposing effects could lead to the shift of max-

imal specific surface as a function of process factors levels. This rather complex behavior can also be described by the model equation in terms of coded factor effect terms (Equation (4.9)). The model describes the data very well with $R^2 = 0.9748$. It also shows a high predictive power with $R^2_{predicted} = 0.8678$.

### 4.3.7. Model validation

For validating the models for pore volume, pore size and specific surface area, four validation experiments were performed and particles were synthesized under reaction conditions, that were not used to build the model. The corresponding factor level settings for the experiments are given **Table 4.2**. **Table 4.7** lists the values for the response values that were predicted by the model and the actual values, as well as the residuals (the deviations from the model) for all validation points regarding pore volume, pore size and specific surface area. It can be seen from **Table 4.7**, that all values predicted by the models are in good agreement with the experiments, except for the value for pore size of validation experiment **Val4**. This combination of process factor level settings is in an extreme area of the design space where small changes in process factors cause large changes in the response (high model sensitivity). All values for all of the three pore parameters pore volume, pore size and specific surface area were correctly predicted within the 95 % predictive interval (PI) and show only small deviations (residuals) from the predicted values. Therefore, the models were confirmed to be correct and show a high predictive power. It should be particularly noted that the validation points were synthesized using a PS from a different batch to test the transferability of the models to other seed batches. As a result, the findings are also transferable to the other seed particle batch, which shows high model robustness.

**Table 4.7** Actual vs. predicted values (with low and high 95 % prediction interval PI with alpha = 0.05) and corresponding residuals for the validation points **Val1–4**. Values exceeding the 95 % PI range are written bold.

| Std | Predicted / Actual / Residual | Pore Volume | Pore size | Specific surface area |
|---|---|---|---|---|
| | | /mL·g$^{-1}$ | /Å | /m²·g$^{-1}$ |
| **Val1** | Predicted Value | 0.34 | 121 | 137 |
| | (±95 %PI) | (0.27–0.42) | (48–194) | (115–160) |
| | Actual Value | 0.41 | 124 | 132 |
| | Residual | 0.06 | 3 | -5 |
| **Val2** | Predicted Value | 0.35 | 185 | 78 |
| | (±95 %PI) | (0.28–0.42) | (119–251) | (58–99) |
| | Actual Value | 0.37 | 233 | 63 |
| | Residual | 0.02 | 48 | -15 |
| **Val3** | Predicted Value | 0.36 | 362 | 35 |
| | (±95 %PI) | (0.29–0.43) | (297–427) | (15–56) |
| | Actual Value | 0.37 | 370 | 40 |
| | Residual | 0.01 | 8 | 5 |
| **Val4** | Predicted Value | 0.36 | 652 | 9 |
| | (±95 %PI) | (0.29–0.44) | (576–728) | (0–33) |
| | Actual Value | 0.36 | **744** | 20 |
| | Residual | 0.00 | 92 | 11 |

## 4.4. Conclusions

In this work, the effects of the synthesis parameters (factors) monomer:porogen, the ratios of functional and crosslinking monomer GMA:EDMA and the composition of the porogen mixture of toluene:cyclohexanol on the particle properties pore volume, pore size and specific surface area of monodisperse porous poly-(glycidyl methacrylate-*co*-ethyleneglycole dimethacrylate) particles were systematically studied by applying response surface methodology or Design of Experiment.

The multivariate regression analysis ($R^2_{predicted}$ = 0.98) based on FTIR data of the porous particles showed that the proportion of functional epoxy groups in the porous *p*(GMA-*co*-EDMA) particles depends directly on the proportion of the functional monomer. This allows the targeted adjustment of the degree of functional groups contained in the platform particles, which is required for application-specific re-functionalization.

The effects of the synthesis factors on the pore volume, pore size and specific surface area parameters could all be described by robust and predictive models ($R^2_{predicted}$ 0.9012, 0.9452 and 0.8678, respectively). Non-linear effects of factors and synergistic interaction effects among factors were identified and quantified and were found to

affect all response variables. This highlights the underlying complexity of seed swelling polymerization for the generation of porous monodisperse polymer particles.

The complexity of the interrelationships in this system could only be demonstrated by simultaneously considering numerous factors simultaneously by the RSM approach. The method of isolated consideration of individual synthesis parameters (one-factor-at-a-time approach), which has prevailed in the literature up to now, has not provided any information about interactions so far and cannot be expected to do.

Despite this complexity of the system, it was successfully achieved to obtain validated, robust models that allow prediction and tuning of particle properties such as pore volume, pore size, specific surface area with a certain amount of epoxy groups.

It can be assumed that other systems based on seed swelling polymerization, e.g., other monomers or porogen mixtures, exhibit similarly complicated behavior and are also subject to complex solubility phenomena. The approach described in this work was demonstrated to be suitable for evaluating such a system quickly and to deliver reliable and comprehensive information for enabling tailored adjustment of pore characteristics. Thus, RSM is a powerful tool for enabling the rational design of porous polymer particles.

## 4.5. Appendix

### 4.5.1. Synthesis of polystyrene (PS) seed particles

PS seed particles were synthesized using dispersion polymerization in alcoholic media. 20 mL styrene (99 %) and 80 mL ethanol (96 %) were added in a three-necked round-bottom flask (250 mL). After the addition of 1.0 g PVP k30 as stabilizer and 0.5 g BPO as initiator the suspension was sonicated for 10 min. The suspension was stirred with 120 rpm with a magnetic stirrer at room temperature for 30 min while purging with Argon. Thereafter the temperature was elevated to 70 °C for 24 h under reflux. The PS seed particles were centrifugated for 2 min at 7500 rpm and were washed three times with ethanol and three times with deionized water to remove the reaction solution. The particles were freeze-dried under vacuum for 72 h.

### 4.5.2. Explained variance of multivariate calibration model for epoxy functionalization

**Figure A. 4.1** shows the explained variance plot for the PLS-R model building for epoxy functionalization and the validation, and explained variance with > 90 % is obtained using nine PLS-R factors.

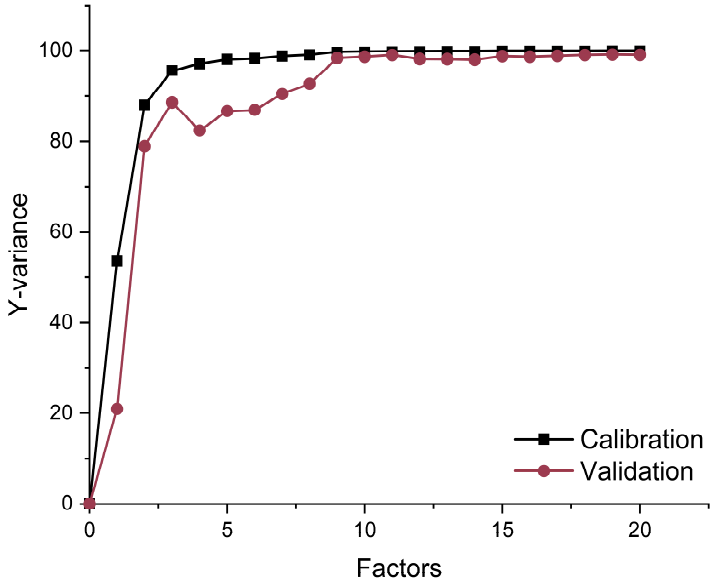


**Figure A. 4.1** Plot of explained variance for the PLS-R depending on the factors used to predict epoxy functionalization for calibration (■) and validation (●).

**Author Contributions:** Conceptualization, J.C.S., F.F., S.W., H.A.M. and A.K.; methodology, J.C.S. and A.K.; software, J.C.S.; validation, J.C.S. and F.F.; formal analysis, J.C.S.; investigation, J.C.S. and F.F.; resources, H.A.M. and A.K.; data curation, J.C.S., writing—original draft preparation, J.C.S.; writing—review and editing, F.F., A.W., M.B., H.A.M. and A.K.; visualization, J.C.S.; supervision, H.A.M. and A.K.; project administration, M.B., H.A.M. and A.K.; funding acquisition, H.A.M. and A.K. All authors have read and agreed to the published version of the manuscript.

**Funding:** This research was funded by Bundesministerium für Bildung und Forschung (BMBF), grant number 13FH647IX6. The article processing charge was funded by the "Ministerium für Wissenschaft, Forschung und Kunst Baden-Württemberg". The funders had no role in study design, data collection and analysis, decision to publish, or preparation of the manuscript.

**Data Availability Statement:** Data are available upon request from the authors.

**Acknowledgments:** The authors thank Natalia Behring, Katrin Markus, Patrick Wahrendorff and Mark Wolf for experimental support during particle synthesis. Furthermore, we would like to thank our co-operation partner Dr. Maisch GmbH for their support in preparing the iSEC columns. We thank Elke Nadler for contributing the SEM measurements.

**Conflicts of Interest:** The authors declare no conflict of interest.

# 5. Paper II

## Impact of Porosity and Surface Functionalization of Hard Templates on the Preparation of Mesoporous Silica Microspheres

*Fabio Fait[a,b,1], Julia C. Steinbach[a,b,1], Andreas Kandelbauer[b,c] and Hermann A. Mayer[a,*]*

[a] Institute of Inorganic Chemistry, University of Tübingen, Auf der Morgenstelle 18, 72076 Tübingen, Germany

[b] Process Analysis and Technology (PA&T), Reutlingen Research Institute, Reutlingen University, Alteburgstrasse 150, 72762 Reutlingen, Germany

[c] Institute of Wood Technology and Renewable Materials, Department of Material Sciences and Process Engineering (MAP), University of Natural Resources and Life Sciences, Gregor-Mendel-Straße 33, 1180 Vienna, Austria

* Correspondence: hermann.mayer@uni-tuebingen.de

[1] Fabio Fait and Julia C. Steinbach equally contributed to this work.

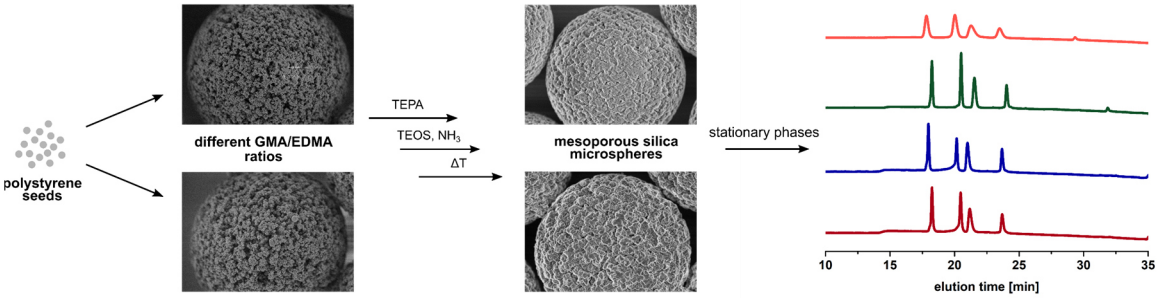




Fait, F.; Steinbach, J.C.; Kandelbauer, A.; Mayer, H.A. Impact of porosity and surface functionalization of hard templates on the preparation of mesoporous silica microspheres. *Microporous and Mesoporous Materials* **2023**, *351*, 112482, doi:10.1016/j.micromeso.2023.112482.[2]

## Abstract

Mesoporous silica microspheres (MPSMs) find broad application as separation materials in high liquid chromatography (HPLC). A promising preparation strategy uses *p*(GMA-*co*-EDMA) as hard templates to control the pore properties and a narrow size distribution of the MPSMs. Here six hard templates were prepared which differ in their porosity and surface functionalization. This was achieved by altering the ratio of GMA to EDMA and by adjusting the proportion of monomer and porogen in the polymerization process. The various amounts of GMA incorporated into the polymer network of **P1–6** lead to different numbers of tetraethylene pentamine in the *p*(GMA-*co*-EDMA) template. This was established by a partial least squares regression (PLS-R) model, based on FTIR spectra of the templates. Deposition of silica nanoparticles (SNP) into the template under Stöber conditions and subsequent removal of the polymer by calcination result in **MPSM1–6**. The size of the SNPs and their incorporation depends on the pore parameters of the template and degree of TEPA functionalization. Moreover, the incorporated SNPs construct the silica network and control the pore parameters of the **MPSMs**. Functionalization of the MPSMs with trimethoxy (octadecyl) silane allows their use as a stationary phase for the separation of biomolecules. The pore characteristics and the functionalization of the template determine the pore structure the silica particles and, consequently, their separation properties.



## Keywords

glycidylmethacrylate (GMA), ethylenglycol dimethacrylate (EDMA), mesoporous silica microspheres (MPSM), hard template method, high performance liquid chromatography (HPLC)


## 5.1. Introduction

Silica based materials serve as platforms in a wide range of applications e.g. in coatings, as filler materials, in catalysis, in chemical sensors and in separation methods or medical diagnostics[171–176]. Furthermore, porous silica microspheres are widely used due to their high specific surface area, chemical stability and the possibility to vary their properties by surface functionalization[17,177,178]. Especially in high performance liquid chromatography (HPLC), porous silica microspheres are employed in column materials as stationary phases. With the continuous progress of HPLC and the ever-increasing demands on separation methods, further improvement of column materials is essential.

A high surface area is beneficial for separation efficiency in HPLC applications. As the relative surface area increases with decreasing particle diameter, this can be achieved

by reducing the sizes of the particles. Unfortunately, this increases the backpressure which demands special and costly requirements for the HPLC equipment[23,37]. This challenge can be overcome by introducing mesopores and/or macropores into micron sized silica particles, which allow for good effective interaction of the liquid phase with the surface of the stationary phase in diffusion-controlled processes such as HPLC[179].

Currently, micron sized mesoporous silica particles are produced in industrial scale by emulsion process or spray drying[180–182]. These methods generate high yields but result in a broad particle size distribution. Processing and separation techniques such as sieving, sedimentation or air classification are necessary to obtain monodisperse particle distributions. These are costly and time-consuming.

The method presented by Stöber et al. for the preparation of monodisperse silica particles posed a fundamental development in sol-gel chemistry. Under basic conditions the hydrolysis and condensation of alkoxysilane precursors in alcoholic media form spherical silica species. However, their size is limited to a range of 50 to 800 nm[45,84]. Although special techniques allow to expand the particle size into the micrometer range, they remain nonporous[183–185].

The preparation of porous silica materials with discrete sizes can be achieved by different template methods[53,123,186]. A hard template method has been demonstrated to be suitable for the targeted synthesis of mesoporous silica microspheres (**MPSMs**) with a narrow size distribution[22,57,119]. Thus amino-functionalized porous organic co-polymers based on glycidyl methacrylate and ethylene glycol dimethacrylate (*p*(GMA-*co*-EDMA)) thermosets were successfully applied as hard templates in the preparation of **MPSMs**[75,157,187]. In the presence of these polymer templates, the hydrolysis and condensation of alkoxysilanes under Stöber conditions generate silica nanoparticles (SNP), which accumulate in the pores of the polymer network. The SNPs aggregate in the pores and build a new silica network, which is interpenetrating the organic template. The organic polymer can be removed via calcination, leaving **MPSMs** (**Scheme 5.1**). Their morphology and pore properties are selectively controlled while maintaining a spherical shape with a narrow size distribution[22,55,57,119].

We reported earlier the systematic evaluation of process parameters in seeded suspension polymerization of GMA and EDMA[1]. The particle and pore properties of the polymer were controlled in targeted manner by variation of the GMA to EDMA ratio, the monomer to porogen ratio and the composition of the porogens. For *p*(GMA-*co*-EDMA) templates, higher proportions of GMA resulted in larger pores and smaller surface areas[1].

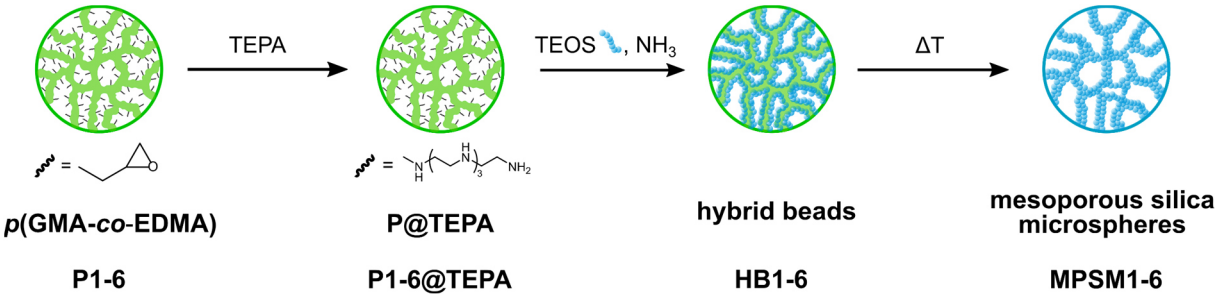


**Scheme 5.1** Synthesis of mesoporous silica microspheres with different *p*(GMA-*co*-EDMA) polymer templates.

Here we demonstrate that the pore structures of the hard polymer template affect the size and pore properties of the mesoporous silica microspheres, which have implications on their performance in HPLC.

## 5.2. Materials and methods

### 5.2.1. Chemicals

Polyvinyl alcohol (PVA, 87–89 % hydrolyzed, mean average 88,000 – 97,000 g $mol^{-1}$), tetraethyl orthosilicate (TEOS) and trimethoxy (octadecyl) silane (ODTMS) were acquired from abcr GmbH. Ethyleneglycol dimethacrylate (EDMA) was bought from Acros Organics and ammonia (28–30 % aqueous solution) was obtained from Alfa Aesar. Cyclohexanol and sodium dodecyl sulfate (SDS) were purchased from Carl Roth. Dibenzoyl peroxide (BPO), dibutyl phthalate (DBP), ethanol (EtOH), glycidyl methacrylate (GMA), hydrochloric acid, methanol (MeOH), 2-propanol, triethylamine, trifluoroacetic acid (TFA) and the protein test mixture H2899 (ribonuclease A, cytochrome c, holo-transferrin and apomyoglobin) were obtained from Sigma-Aldrich. Acetonitrile (ACN, HPLC grade), tetraethylenepentamine (TEPA), and water (HPLC grade) were bought from fisher scientific. Toluene and deionized water were cleaned through a solvent purification system (SPS-800, MBraun).

### 5.2.2. Characterizations

Scanning electron microscopy (SEM) images were taken with a Hitachi SU8030 instrument and used to determine the size, dispersity, and morphology of the particles. The size and dispersity of the particles were assessed by evaluating at least 400 particles per batch. Thermogravimetric studies of the hybrid beads were performed on a Mettler Toledo TGA/DSC I. For this purpose, the samples were calcinated in an alumina crucible with a heating rate of 5 K $min^{-1}$ under synthetic air (50 mL $min^{-1}$). The remaining mass corresponds to the amount of silica.

Infrared (IR) spectra were acquired using a Frontier 2 FTIR (Perkin Elmer) with an attenuated total reflection accessory. Each sample was measured five times in a spec-

tral range from 4000 $cm^{-1}$ to 500 $cm^{-1}$ with a spectral resolution of 2 $cm^{-1}$ and four scans. A partial least squares regression model (PLS-R) was built similar to previous work[1] To increase model quality, another two *p*(GMA-*co*-EDMA) templates with 50:50 GMA:EDMA from previous work (central points, CPs) were added for model building. The spectra were preprocessed by smoothing with a Savitzky-Golay filter (polynomial order: 2., over eleven points) and a subsequent removal of multiplicative scattering effects using a standard normal variate transformation. The analyzed spectral range was 1750–700 $cm^{-1}$. The spectra of the *p*(GMA-*co*-EDMA) templates (five spectra of **P1–4**, two spectra from **P5** and **P6** and seven spectra from the CPs) were used as test set and were validated externally (three spectra of **P5** and **P6**, as well as three spectra of the central points from our previous work). For spectral preprocessing and the multivariate data analysis, the software Unscrambler-X (CAMO Software AS) was used. The PLS-R model was applied for the prediction of GMA content for all particles **P1–6** and **P1–6@TEPA**, to assess the change in epoxy groups after amination as indicative measure for the degree of amination.

To determine the pore size, volume, and specific surface area of the particles, $N_2$ adsorption-desorption measurements were performed on a BELSORP MiniX from Microtrac Retsch GmbH. The samples were preheated with a BELSORP VACII to remove possible physisorbed substances and to establish a reproducible equilibrium state. At a final vacuum of $2 \cdot 10^{-2}$ mbar, polymer samples were evacuated at 30 °C for 24 h, and silica samples were pretreated at 300 °C for 3 h, respectively. Nitrogen adsorption measurements were performed at 77 K. BELMaster 7 software was used to evaluate the isotherms. The specific surface area of the particles was determined according to the method of Brunauer, Emmet, and Teller (BET). The pore size distributions were obtained by applying the Barrett-Joyner-Halenda (BJH) method to the desorption and adsorption isotherms for the polymer templates and desorption isotherms for the silica particles. This was done taking into account that the peaks around 4 nm (**Figure S. 5.3**, S.I.) are the result of the tensile strength effect rather than a bimodal pore size distribution[188]. The median of the pore sizes differs hardly between adsorption and desorption isotherms (**Table 5.1**). This is the reason why the pore size distributions of the adsorption isotherms are shown in **Figure 5.3** for the polymer templates. The pore volume was estimated from a single point adsorption at $p/p_0$ of 0.95.

Analytical high performance liquid chromatography was performed on an Agilent 1100 series system (Agilent Technologies, Waldbronn, Germany) equipped with a quaternary pump with degasser, an auto sampling system, column oven and a diode array detector. Instrument control, data acquisition and automated data analysis was performed by the Chem-Station software (B.04.03, Agilent Technologies, Waldbronn, Ger-

many). A gradient elution was performed using water with 0.1 % TFA (eluent A) and acetonitrile with 0.08 % TFA (eluent B) with a gradient starting at 20 % B to 85 % B within 25 minutes. 5 µL of the protein mixture H2899 (1 mg $mL^{-1}$ each protein in 90/10 A/B) were injected and detected at a wavelength of 215 nm. A commercially available column (ProSphere C18, 300 Å, 10 µm, 250 x 4.6 mm) was used as reference column. The prepared particles were packed into stainless-steel columns (250 x 4.6 mm).

### 5.2.3. Synthesis

#### *5.2.3.1. Preparation of porous p(GMA-co-EDMA) particles* ***P1–6***

Monodisperse polystyrene (PS) microspheres with diameters of 1.9 ± 0.1 µm were prepared as reported earlier (**Figure S. 5.1**, S.I.)[57].

0.3 g of polystyrene particles and 5 mL of an aqueous SDS solution (0.25 wt%) were dispersed in a 250 mL flask. 2 mL of DBP were emulsified in 150 mL of an aqueous SDS solution (0.25 wt%) with a homogenizer at 4500 rpm for 15 min and then added to the polystyrene suspension. The mixture was stirred for 24 h at 200 rpm. Depending on the experiment the volume ratios of GMA and EDMA and the monomer to porogen ratios were varied according to **Table 5.1**. As porogen a mixture of toluene and cyclohexanol (73/27 v./v.) was applied.

**Table 5.1** Particle properties of *p*(GMA-*co*-EDMA) microspheres **P1–6** prepared with varying GMA/EDMA and monomer/porogen ratios.

| | **GMA/ EDMA** | **monomer/ porogen** | **particle size** | **dispersity** | **median pore size** | | **pore volume** | **specific surface area** |
|---|---|---|---|---|---|---|---|---|
| | v./v. | v./v. | /µm | $d_{90}/d_{10}$ | /nm[a] | /nm[b] | /$cm^3\ g^{-1}$ | /$m^2\ g^{-1}$ |
| **P1** | 20/80 | 50/50 | 7.9 | 1.1 | 6.1 | 8.0 | 0.29 | 270 |
| **P2** | 40/60 | 50/50 | 7.8 | 1.2 | 12.2 | 12.6 | 0.19 | 123 |
| **P3** | 60/40 | 50/50 | 7.5 | 1.1 | 20.6 | 21.1 | 0.09 | 43 |
| **P4** | 80/20 | 50/50 | 7.3 | 1.2 | 35.5 | 35.4 | 0.03 | 15 |
| **P5** | 40/60 | 25/75 | 7.6 | 1.2 | 26.7 | 27.9 | 0.25 | 132 |
| **P6** | 40/60 | 75/25 | 7.9 | 1.2 | 15.1 | 8.5 | 0.06 | 31 |

[a]From adsorption isotherm, [b]From desorption isotherm

In all experiments a total volume of 30 mL of the organic phase was maintained. The monomer and porogen mixture, 0.4 g of BPO and 150 mL of an aqueous SDS solution (0.25 wt%) were emulsified with a homogenizer at 4500 rpm for 15 min. This emulsion and the activated polystyrene particles were transferred to a 500 mL three-necked flask and stirred for 24 h at 200 rpm. 150 mL of an aqueous PVA solution (2.3 wt%) was added to the reaction and Argon was passed into the reaction mixture for 30 minutes

and then heated to 70 °C for 24 hours. The particles were separated from the solution, washed three times with EtOH and three times with $H_2O$ and dried at 65 °C for 16 h.

*5.2.3.2. Preparation of mesoporous silica microspheres* ***MPSM1–6***

5 g of particles **P1–6** were dispersed in 200 mL of $H_2O$, 7.5 mL of tetraethylen pentamine were added and the solution was stirred for 24 h at 80 °C (200 rpm). The **P1–6@TEPA** particles were washed three times with $H_2O$ and EtOH, each and dried at 65 °C for 16 h.

5 g of **P1–6@TEPA** particles were dispersed in 270 mL of 2-propanol and 30 mL of $H_2O$. Then 12.5 mL of TEOS and 1.25 mL of an ammonia solution were added and stirred at room temperature (130 rpm) for 24 h. The particles were separated from the solution, washed three times with $H_2O$ and EtOH, each and dried at 65 °C for 16 h. After calcination at 600 °C for 10 h mesoporous silica microspheres **MPSM1–6** remained.

*5.2.3.3. Octadecyl functionalization of* ***MPSM1–4*** *for chromatographic measurements*

5 g of **MPSM1–4** were dispersed in 600 mL of hydrochloric acid (3.7 %) and stirred for 3 h at 100 °C (130 rpm). The particles were separated from the solution, washed with EtOH and $H_2O$ until neutral and dried at 65 °C for 16 h. The particles were then dispersed in 75 mL of toluene, 25 mL of trimethoxy (octadecyl) silane (ODTMS) and 0.5 mL of triethylamine were added, and the mixture was stirred at 100 °C (130 rpm) for 6 h. The particles were separated from the solution, washed three times with toluene, three times with EtOH and twice with MeOH and dried at 65 °C for 16 h.

The functionalized particles were packed in a slurry with acetone and MeOH / $H_2O$ (85/15 v./v.) as pressure medium.

## 5.3. Results and discussion

### 5.3.1. Modification of *p*(GMA-*co*-EDMA) microspheres with different GMA and EDMA ratios

The spherical porous *p*(GMA-*co*-EDMA) polymer particles **P1–6** were prepared by a seeded swelling suspension polymerization of monodisperse polystyrene (PS) microspheres[57]. PS with a diameter of 1.9 ± 0.1 µm (**Figure S. 5.1**, S.I.) were applied as seeds in the polymerization of glycidyl methacrylate and ethylene glycol dimethacrylate as crosslinker as well as toluene and cyclohexanol as porogens. The amount of GMA and EDMA (v./v.) and the ratio of monomers to porogens (v./v.) were varied according to **Table 5.1**.

The size and morphology of the *p*(GMA-*co*-EDMA) templates were characterized with scanning electron microscopy (SEM) (**Figure 5.1** and **Figure 5.2**). The particle sizes of **P1–4** slightly decrease from 7.9 to 7.3 µm which correlates with the increasing amount

of GMA (**Table 5.1**). As the density of GMA is lower than that of EDMA the swelling factor is reduced when the amount of GMA is increased at the expense of EDMA[82].

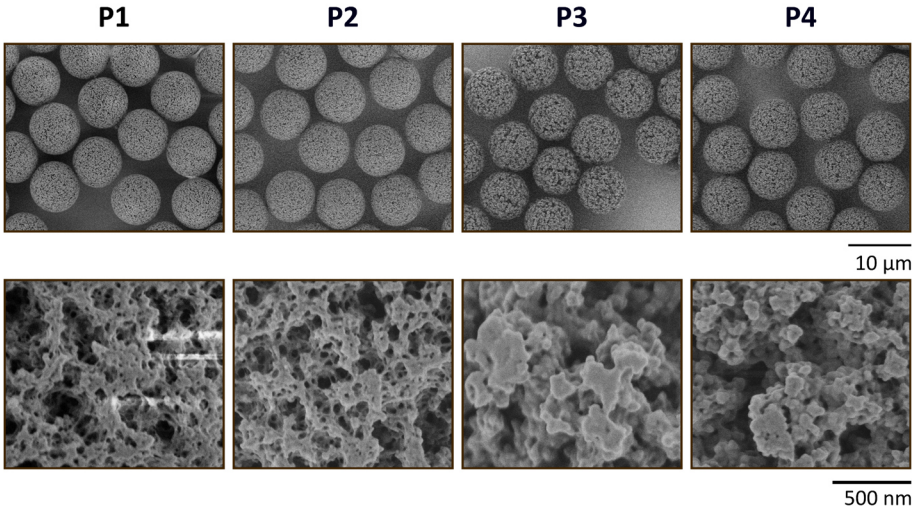


**Figure 5.1** SEM images of *p*(GMA-*co*-EDMA) templates **P1–4** with increasing GMA to EDMA ratio (from left to right). 2,000 (top row) and 50,000 (bottom row) magnification.

Changing the proportion of monomers to porogens at a constant GMA/EDMA ratio, increases the particle size of the template with increasing monomer content (**P5** < **P2** < **P6**, **Table 5.1**). This is attributed to the increased number of swelling monomers. All templates show a smooth morphology with different porous networks. Independent of the ratio of GMA to EDMA and the ratio of monomer to porogen uniform porous polymer templates with a narrow size distribution are obtained (**Table 5.1**, **Figure 5.1**and **Figure 5.2**).

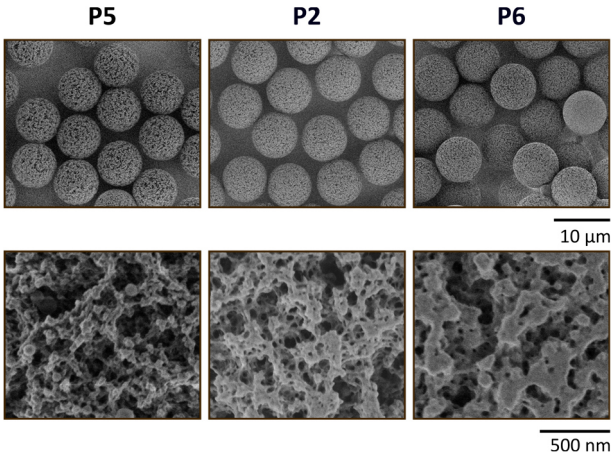


**Figure 5.2** SEM-images of *p*(GMA-*co*-EDMA) templates **P5**, **P2** and **P6** with increasing monomer to porogen ratio (from left to right). 2,000 (top row) and 50,000 (bottom row) magnification.

Specific surface areas, pore sizes and pore volumes of **P1–6** were determined from nitrogen adsorption-desorption isotherms (**Figure 5.3** and **Figure S. 5.2**, S.I.) All *p*(GMA-*co*-EDMA) templates (**P1–6**) display a broad pore size distribution between 5 and 100 nm (**Figure 5.3**). In addition, contrary to the rest of the templates, P1 shows a propor-

tion of small pores (2 nm). With increasing amounts of monomer GMA the median pore size increases from 6 to 35 nm. Consequently, the surface areas of the particles decrease from 270 $m^2 g^{-1}$ to 15 $m^2 g^{-1}$ in the same order (**P1** > **P2** > **P3** > **P4**, **Table 4.1**).

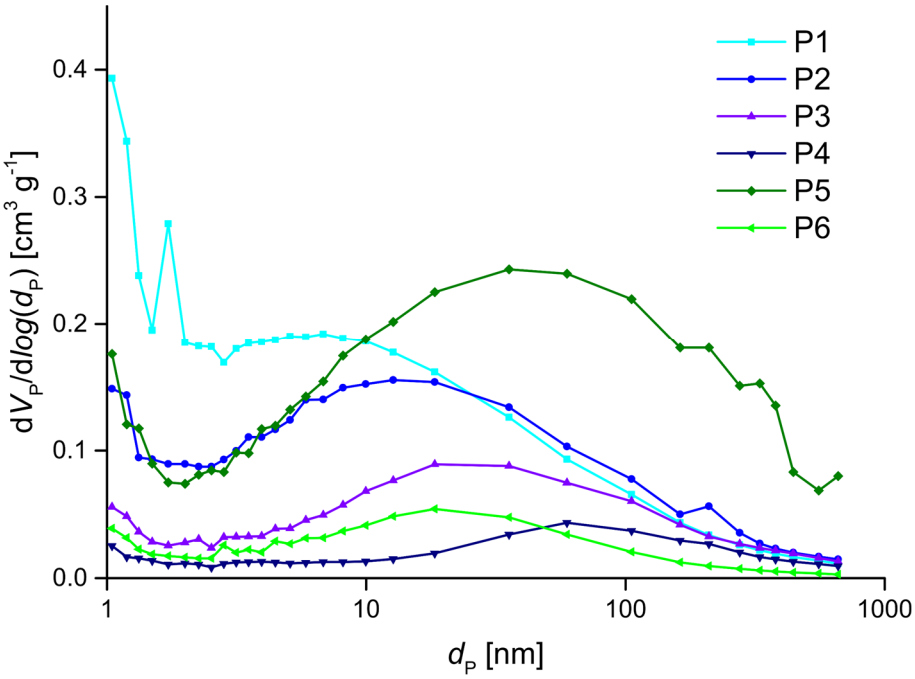


**Figure 5.3** Pore size distributions from the adsorption isotherms of the *p*(GMA-*co*-EDMA) templates **P1–6.**

The more GMA is applied the less EDMA is present, which leads to fewer branches and thus a lower degree of cross-linkage. As a result, the pores become larger. On the other hand, a higher amount of GMA leads to earlier phase separation, which also results in larger pores[1]. The finer network structure, resulting from a higher cross-linking degree with higher EDMA ratios is also visible in the morphology of the polymer particles (**Figure 5.1**). With increasing GMA content from **P1** to **P4**, the surface texture becomes rougher. The pore volume of the particles decreases with higher amount of GMA. Comparing the templates **P5**, **P2** and **P6** the pore parameters decrease with higher amount of monomer and consequently lesser amount of porogen. Since during the polymerization a lower proportion of porogens is present, this results in smaller pores and a smaller pore volume.

### 5.3.2. Spectral analysis of *p*(GMA-*co*-EDMA) and **P@TEPA** microspheres

The functionalization of the *p*(GMA-*co*-EDMA) polymer particles with amino groups provides a positive surface charge which supports the deposition of negatively charged silica species into the polymer network under sol-gel conditions[3,22]. To introduce amino functions, the porous templates **P1–6** were treated with tetraethylen pentamine to generate **P1–6@TEPA** particles via ring opening reactions of the epoxy groups (**Scheme 5.1**). As the degree of amination at the polymer surface depends on

the amount of GMA incorporated into the template the number of TEPA groups and, thus, the positive charges differ in the **P1–6@TEPA** particles. Unfortunately, the amount of TEPA in the **P1–6@TEPA** particles is rather small compared to their bulk compositions, so that any changes of nitrogen content falls below the limit of detection via elemental analyses (**Table S. 5.1**, S.I.).

Thus, a partial least squares regression (PLS-R) model, based on FTIR spectra of the particles, which predicts the decrease in the GMA ratio through amination of polymers **P1–6** was applied as indirect and indicative measure. The aim is to assess differences in degrees of amination for the **P1–6@TEPA** particles in dependence of the initial relative GMA content. The intensities of characteristic IR frequencies which vary with the amount of GMA are those of the symmetric and asymmetric ring vibration of the epoxide at 845 and 910 $cm^{-1}$, respectively[128]. The C-O stretching vibration of the epoxide ring at 1270 $m^{-1}$ also responds to changes in GMA ratio (**Figure S. 5.4**d, S.I.). The established PLS-R model, based on four regression coefficients, has a high predictive power with an $R^2_{predicted}$ = 0.9922 and a low error with RMSEP = 0.6 % and can hence be used to effectively determine the relative ratio of GMA in **P1–6@TEPA** (**Figure S. 5.4**a-c, S.I.).

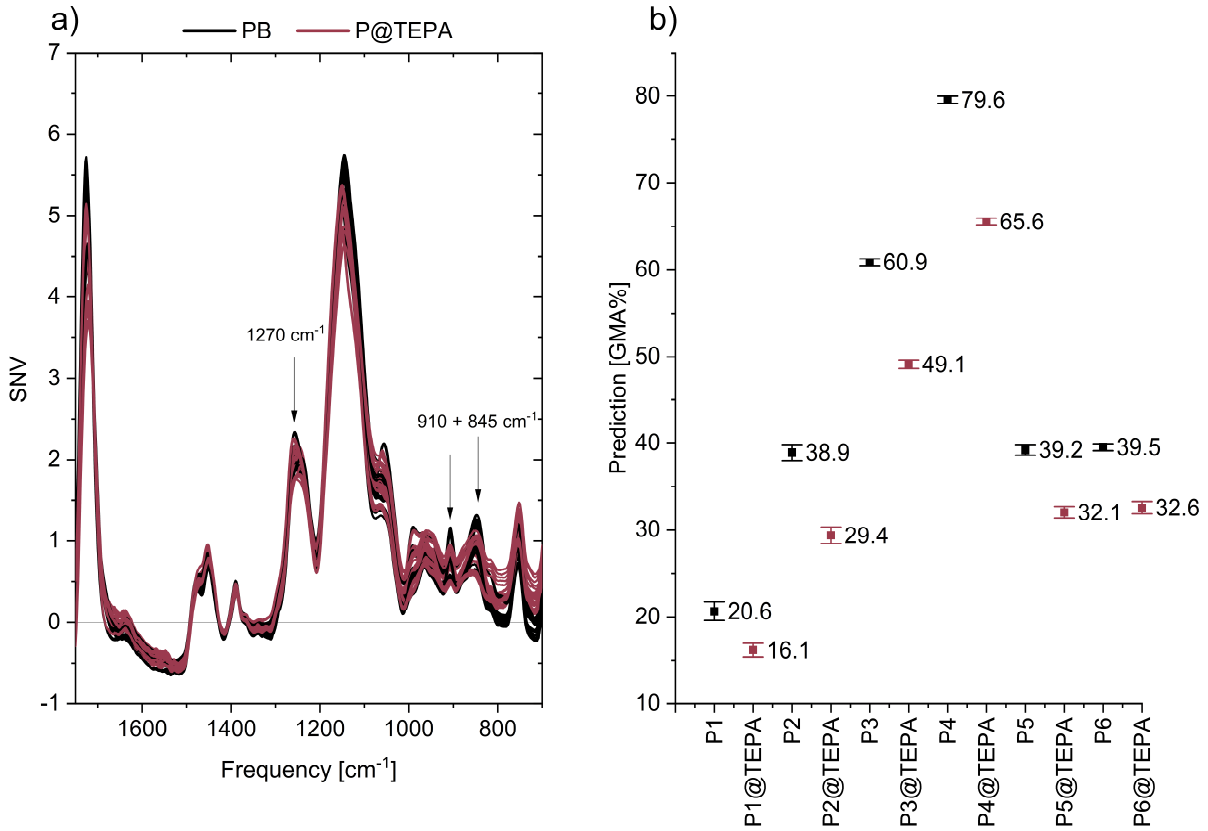


**Figure 5.4 a)** Spectra of **P1–6** and **P1–6@TEPA** templates after spectral preprocessing with standard normal variate transformation and **b)** predicted values of mean epoxy content with standard deviation across all spectra used for prediction. **P1–6** are depicted in black and **P1–6@TEPA** templates in red.

After the functionalization with TEPA, the vibrations corresponding to the epoxide groups decrease in absorbance. Consequently, the intensities of the vibrations from the epoxy groups decrease within increasing functionalization of the particles (**Figure 5.4**). The established PLS-R was used for the prediction of the GMA content of **P1–6** and **P1–6@TEPA** particles. The predicted values are given in **Figure 5.4**b. The low deviations of predicted values from the actual values of the polymers and the small standard deviation for each prediction indicate a high model accuracy (**Table 5.2**, **Figure 5.4**b).

**Table 5.2** Actual and predicted GMA ratios of **P1–6** and **P1–6@TEPA**.

| | actual GMA ratio of ***p*(GMA-*co*-EDMA)** | predicted GMA ratio | | predicted GMA ratio of **P@TEPA** | **Δ *p*(GMA-*co*-EDMA) – P@TEPA** |
|---|---|---|---|---|---|
| **P1** | 20 | 20.6 | **P1@TEPA** | 16.1 | 4.5 |
| **P2** | 40 | 38.9 | **P2@TEPA** | 29.4 | 9.5 |
| **P3** | 60 | 60.9 | **P3@TEPA** | 49.1 | 11.8 |
| **P4** | 80 | 79.6 | **P4@TEPA** | 65.6 | 14.1 |
| **P5** | 40 | 39.2 | **P5@TEPA** | 32.1 | 7.1 |
| **P6** | 40 | 39.5 | **P6@TEPA** | 32.6 | 6.9 |

The predicted residual GMA ratios for the amino functionalized particles **P1@TEPA** to **P6@TEPA**, respectively, correspond to a decrease in epoxy ratio during amination respectively (**Table 5.2**). The degree of TEPA functionalization follows the order **P1** < **P5** ~ **P6** < **P2** < **P3** < **P4**.

### 5.3.3. Preparation of mesoporous silica microspheres (**MPSM1–6**)

The **P1–6@TEPA** particles were applied as hard templates in a base catalyzed sol-gel process. In the presence of 2-propanol and $H_2O$, the corresponding amino functionalized polymer templates, and tetraethyl orthosilicate (TEOS) formed polymer/silica hybrid beads (**HB1–6, Scheme 5.1**, and **Figure S. 5.5** and **Figure S. 5.6** and **Table S. 5.2**, S.I). Calcination of the **HB1–6** at 600 °C for 10 h removed the organic polymer which leaves the mesoporous silica particles **MPSM1–6** (**Scheme 5.1** and **Figure 5.5** and **Figure 5.6**).

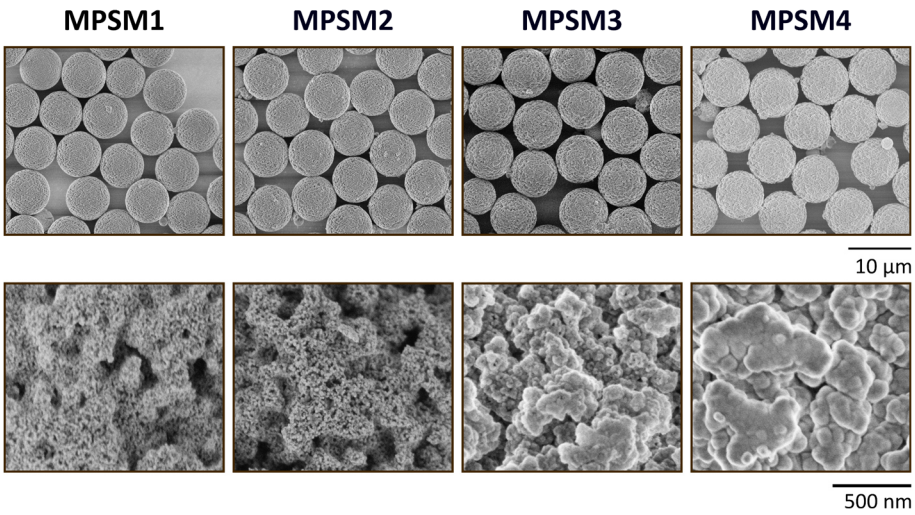


**Figure 5.5** SEM images of mesoporous silica microspheres **MPSM1–4** using polymer templates with different amount of GMA. 2,000 (top row) and 50,000 (bottom row) magnification.

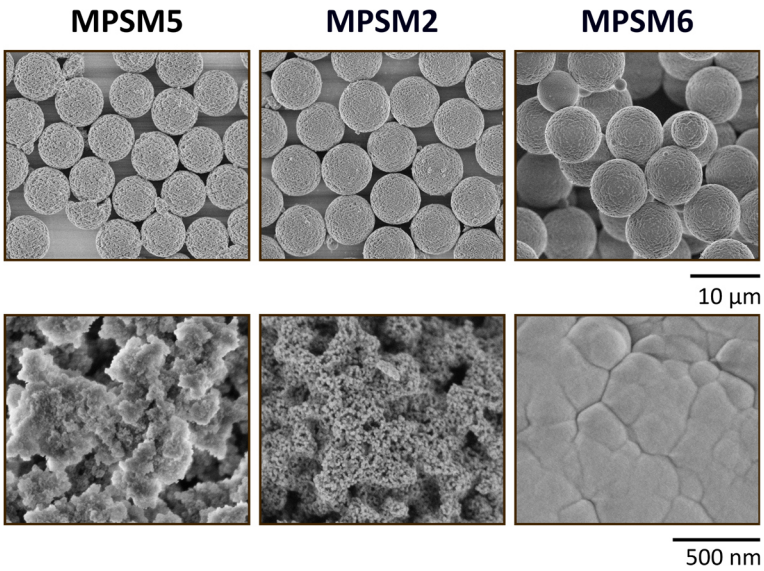


**Figure 5.6** SEM images of mesoporous silica microspheres **MPSM2, 5, 6** using polymer templates with different monomer to porogen ratio. 2,000 (top row) and 50,000 (bottom row) magnification.

An evaluation of the SEM images of **MPSM1–6 Figure 5.6** shows that the high monodispersity as specified by the template particles is maintained (**Figure 5.5** and **Figure 5.6**, **Table 5.1** and **Table 5.3**). Although the diameters of the templates **P1–6@TEPA** differ by only 0.6 µm (**Table 5.1**), the range of silica particle size is extended to 1.6 µm (**Table 5.3**). The smallest silica particles **MPSM1** and **MPSM5** with a particle size of 6.3 and 6.6 µm, respectively, result from those templates which contain the smallest amount of TEPA (**P1@TEPA** and **P5@TEPA**). With increasing amount of TEPA in the templates (**Table 5.2**) the silica materials become larger (**MPSM2**, **MPSM3** and **MPSM4**). Interestingly, **MPSM6** with a particle size of 8.2 µm is larger than the corresponding **P6@TEPA** template (**Table 5.1** and **Table 5.3**). In this case also nonporous

secondary nanoparticles with a size of 230 nm were found in the filtrate of the washing procedure (**Figure S. 5.7**, S.I.). The morphology of **HB6** and **MPSM6** (**Figure S. 5.5** and **Figure 5.6**) indicate that the pores of the template are closed, and large silica nanoparticles aggregate to a shell around the template. SEM images of purposely destroyed **MPSM6** show that the particles are hollow and a shell of silica remains after calcination (**Figure S. 5.8**, S.I.) The silica network of **MPSM1** and **MPSM2** is made up of small nanometer-sized silica particles which create many small pores and a rough surface (**Figure 5.5**). With increasing amount of TEPA the SNPs become larger (**MSMP3** and **MSMP4**), the number of small particles is declining and the surface becomes smoother (**Figure 5.5**).

**Table 5.3** Properties of mesoporous silica microspheres **MPSM1–6**.

| | **particle size** | **dispersity** | **median pore size** | **pore volume** | **specific surface area** |
|---|---|---|---|---|---|
| | /μm | $d_{90}/d_{10}$ | /nm[a] | /$cm^3\ g^{-1}$ | /$m^2\ g^{-1}$ |
| **MPSM1** | 6.6 | 1.2 | 15.4 | 0.71 | 342 |
| **MPSM2** | 6.8 | 1.2 | 19.2 | 0.56 | 252 |
| **MPSM3** | 7.0 | 1.2 | 23.0 | 0.22 | 139 |
| **MPSM4** | 7.1 | 1.2 | 72.4 | 0.12 | 68 |
| **MPSM5** | 6.3 | 1.1 | 12.1 | 0.88 | 382 |
| **MPSM6** | 8.2 | 1.1 | - | - | - |

[a]From desorption isotherms

Removing the organic template leaves more space behind so that the median pore sizes, pore volumes and specific surface areas of **MPSM1–5** increase compared to those of the corresponding polymer particles **P1–5** (**Table 5.2**). Moreover, the pore parameters of **MPSMs** follow the same course as those of the polymer particles. Based on the t-plots of the adsorption isotherms, the MPSMs do not exhibit microporosity and possess pre-dominantly mesopores.

The mesoporous silica microspheres **MPSM1–6** are composed of nonporous silica nanoparticles (SNPs) of different size and shape. The size of the SNPs and their deposition into the template depends on three factors: (i) the rate of the growth of the SNPs in the continuous phase which is based on the sol-gel parameters, (ii) the diffusion rate of the SNPs into the template which is controlled by the ability of the template to attract negatively charged SNPs from the solution and (iii) the pore parameters of the template. For all experiments the sol-gel process parameters are the same and thus the rates of the SNP growth are comparable. This agrees with the overall amount of deposited silica (30 wt%) into the porous polymer network independent of the polymer composition (**Figure S. 5.9**, S.I.).

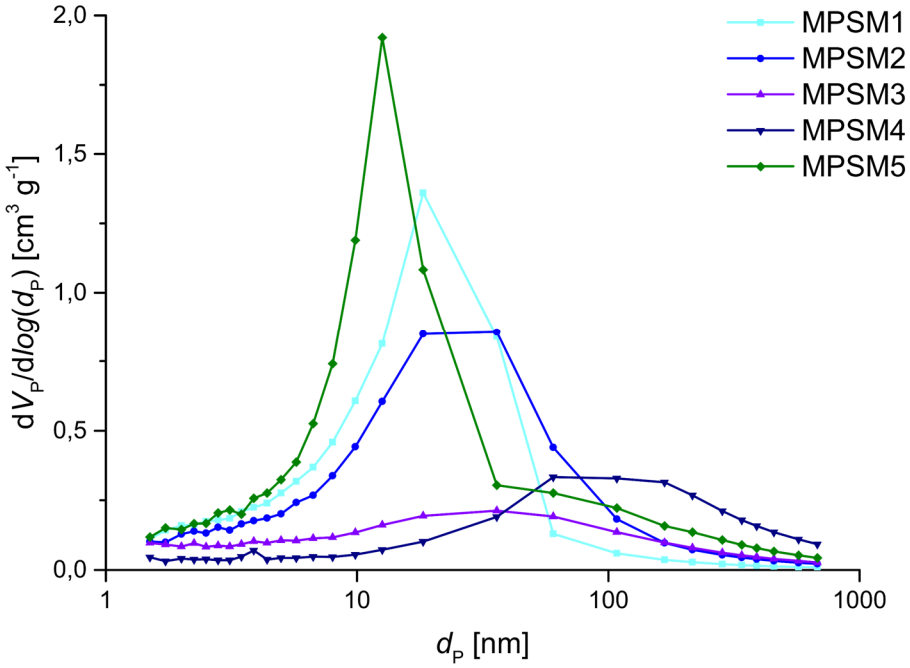


**Figure 5.7** Pore size distributions from the desorption isotherms of the mesoporous silica microspheres **MPSM1–5**.

Under the present reaction conditions the amino groups of the attached TEPA functions are still partly protonated which provides the template surface with a positive charge. A higher amount of TEPA generates a higher positive charge. Templates with higher TEPA content extract negatively charged silica species from the reaction mixture at an early state of the SNP growth. Small silica particles are deposited in the pores of the template where they aggregate and form larger SNPs. This is the case for **MPSM4** and **6**. Furthermore, the larger pore structure of the **P4@TEPA** template provides more space for agglomeration resulting in larger SNPs. In case of **P6@TEPA** the combination of small pores and large SNPs closed the pores at the surface of the template. A silica shell around the polymer is observed. At a lower TEPA content, the attraction of SNPs is weaker, so that they diffuse into the template at a later state of the growth process. Consequently, the SNPs are larger when they are incorporated into the silica network and maintain their size as they are more stable than the smaller SNPs. In the case of **MPSM1**, a particle size of the SNPs of about 15 nm is observed.

### 5.3.4. Protein separation using $C_{18}$-functionalized **MPSM1–4** as stationary phases

Functionalization of silica materials to generate reversed stationary phases with trimethoxy (octadecyl) silane is an established method that is widely used[189]. Thus, the **MPSM1–4** with different pore parameters were functionalized with trimethoxy (octadecyl) silane ($C_{18}$) and packed into 250 x 4.6 mm stainless steel columns using the slurry method. **MPSM5** and **MPSM6** were too fragile and broke during the packing process. The resulting reversed phase columns **MPSM1-$C_{18}$**-**MPSM4-$C_{18}$**, and the commercially

available column ProSphere C18, (300 Å, 10 µm, 250 x 4.6 mm) as reference, were applied for the separation of a protein mixture consisting of ribonuclease A, cytochrome c, holo-transferrin and apomyoglobin. The chromatograms in **Figure 5.8** show a baseline separation of the proteins with all prepared $C_{18}$ columns.

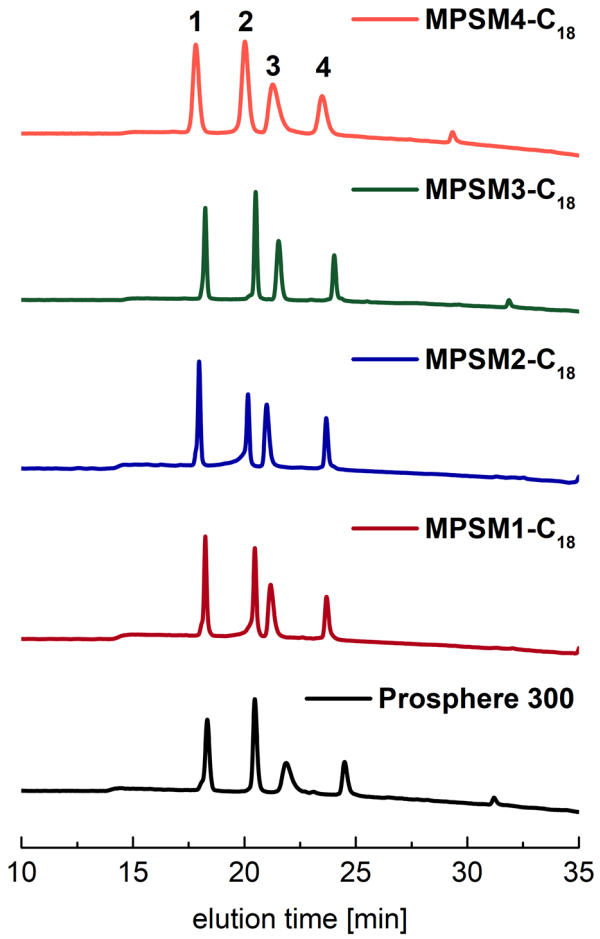


**Figure 5.8** Chromatograms of protein mixture H2899 separation with the prepared C18 functionalized stationary phases and a commercially available ProSphere 300. Chromatographic settings: column dimension: 250 x 4.6 mm; mobile phase A: $H_2O$ with 0.1 % TFA, mobile phase B: ACN with 0.08 % TFA; gradient from 20 % B to 85 % B within 25 minutes; test mixture: 4 mg $mL^{-1}$ (each 1 mg $mL^{-1}$) with 5 µL injection volume, 1 – ribonuclease A, 2 – cytochrome c, 3 – holo-transferrin, 4 – apomyoglobin; column temperature: 30 °C; detection wavelength: 215 nm.

Thus, the prepared packing materials show a separation efficiency comparable to those of the commercial column. Also, the resolutions (**Table 5.4**) between the protein peaks are comparable or even better than that of the commercially available column. Overall, the separation efficiency increases from **MPSM1-C$_{18}$** to **MPSM3-C$_{18}$**. This correlates well with the increase in median pore size of the **MPSM** packing material, as the accessibility for bigger proteins is facilitated. Especially the resolution between cytochrome c and holo-transferrin ($R_{2\text{-}3}$, **Table 5.4**) increase with increasing GMA ratio in

the polymeric template which corresponds well to the increased pore sizes of **MPSM3**. Also, the overall peak symmetry is improved. For **MPSM4** the larger SNPs at the surface and the nearly closed morphology restrict the diffusion into the pores, resulting in broader peaks and decreasing column performance.

**Table 5.4** Column performance for separation of protein mixture H2899 of the **MPSM-C$_{18}$** columns and a commercially available column.

| | **Resolution $R_{1-2}$** | **Resolution $R_{2-3}$** | **Resolution $R_{3-4}$** |
|---|---|---|---|
| **MPSM1-C$_{18}$** | 9.39 | 1.97 | 6.56 |
| **MPSM2-C$_{18}$** | 9.39 | 2.67 | 8.20 |
| **MPSM3-C$_{18}$** | 9.74 | 3.37 | 7.63 |
| **MPSM4-C$_{18}$** | 4.10 | 1.74 | 2.88 |
| **ProSphere 300** | 6.24 | 2.49 | 4.36 |

## 5.4. Conclusion

Nonporous SNPs are the building blocks of the mesoporous silica microspheres (**MPSM1–6**) prepared by the hard template assisted approach. Both pore properties and degree of amino-functionalization of the templates have a strong impact on the size of the deposited SNPs. A low proportion of GMA with small pores (**P1**) and large pores (**P5**) leads to small inserted SNPs. A high proportion of GMA with small pores (**P6**) results in the formation of a hollow silica shell. If the pores are large enough as in **P4** large SNPs can be incorporated. Thus, the particle and pore properties of the **MPSM1–6** are controlled by the size of the SNPs. Small nanoparticles generate small pore sizes and high specific surface areas, while larger nanoparticles lead to larger pores and lower surface areas of **MPSM**s. Interestingly, the GMA to EDMA ratio and the monomer to porogen ratio in the preparation of the template control the pore parameters of the final **MPSMs**. This allows access to stationary phases for specific separation problems in HPLC.

## 5.5. Supplementary Information

### 5.5.1. Chemicals

Polyvinylpyrrolidone $K_{30}$ (PVP, mean average 40000 g $mol^{-1}$) was purchased from abcr GmbH. Styrene was obtained by Fisher Chemicals. Dibenzoyl peroxide (BPO) was bought from Sigma-Aldrich.

### 5.5.2. Synthesis of polystyrene

Monodisperse polystyrene particles with diameters of 1.9 ± 0.1 µm were prepared as reported earlier[57] (**Figure S. 5.1**).

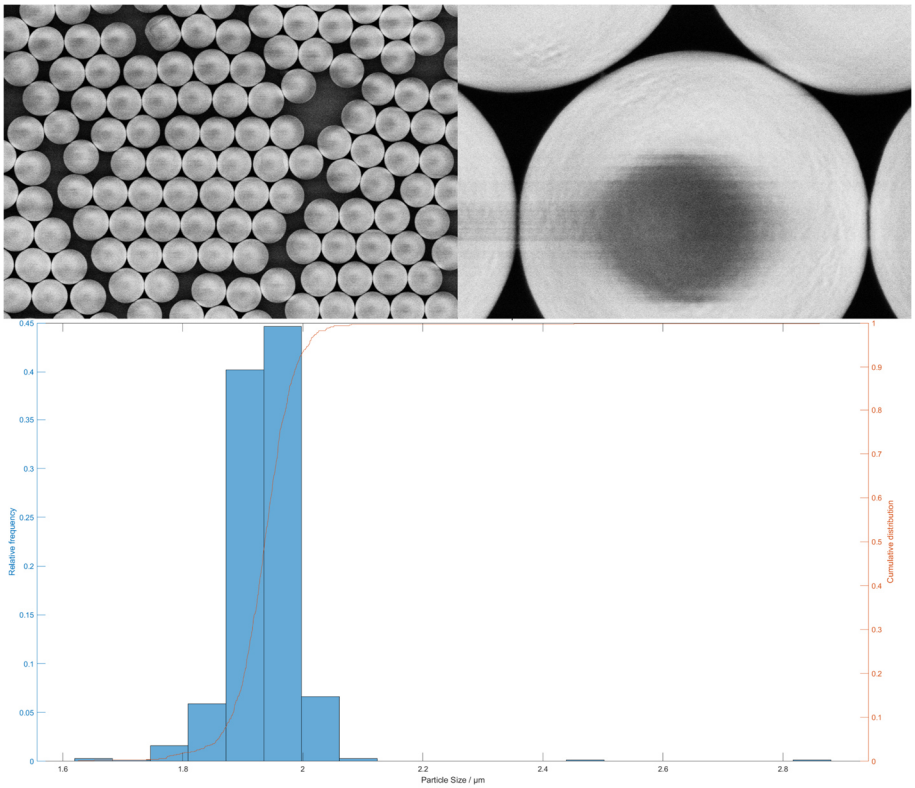


**Figure S. 5.1** SEM images of applied polystyrene particles (top) and their particle size distribution (bottom).

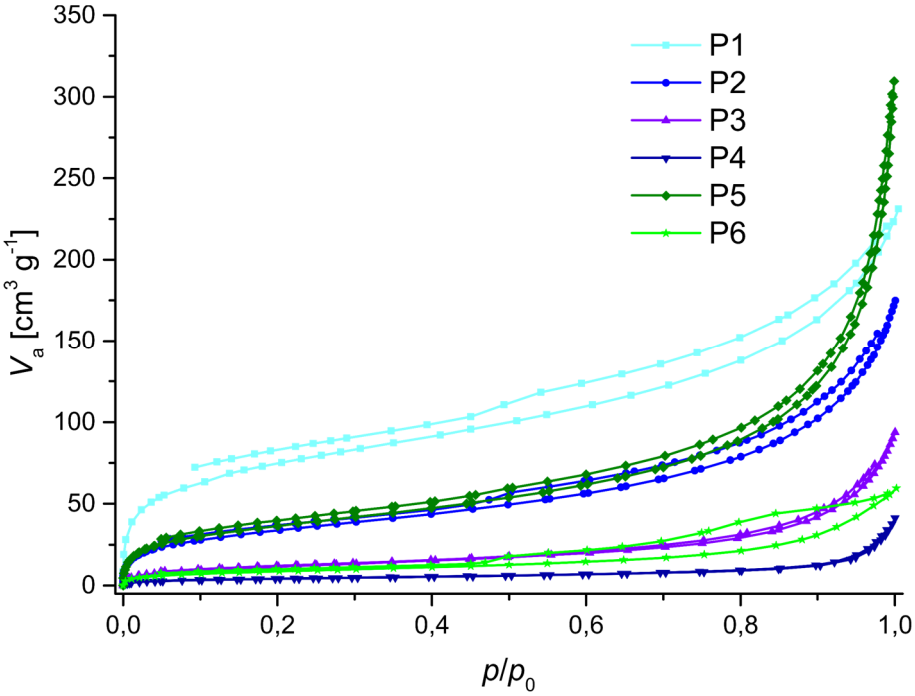


**Figure S. 5.2** Isotherms of the *p*(GMA-*co*-EDMA) templates.

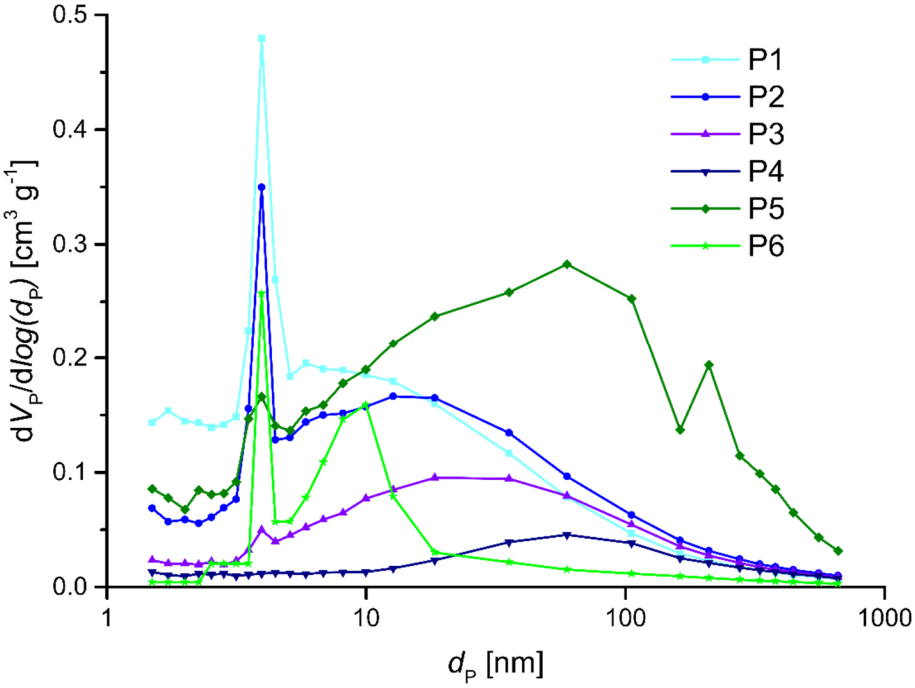


**Figure S. 5.3** Pore size distributions from the desorption isotherms of the *p*(GMA-*co*-EDMA) templates **P1–6**.

**Table S. 5.1** Elementary analysis of **P1–6@TEPA**

| | H | C | N |
|---|---|---|---|
| | /% | /% | /% |
| **P1@TEPA** | 7.63 | 57.14 | 2.06 |
| **P2@TEPA** | 7.70 | 56.74 | 2.43 |
| **P3@TEPA** | 7.59 | 56.70 | 2.12 |
| **P4@TEPA** | 7.72 | 55.42 | 2.14 |
| **P5@TEPA** | 7.79 | 56.99 | 2.50 |
| **P6@TEPA** | 7.65 | 57.24 | 2.24 |

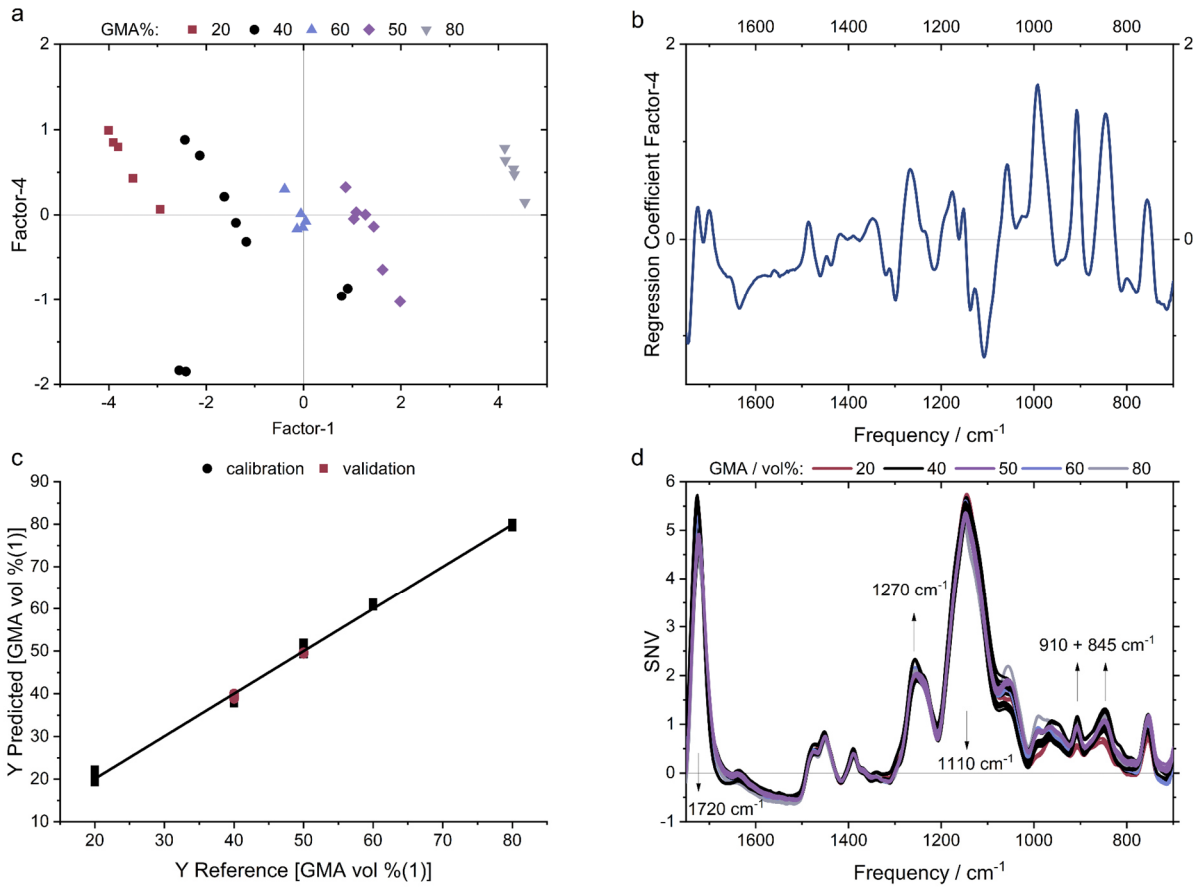


**Figure S. 5.4** PLS-R model for the determination of GMA% from IR spectra. **a)** Scores plot of Factor-1 and Factor-4 with groups colored according to the GMA% used in preparation of the PBs. **b)** Regression coefficient of Factor-4 giving the importance of each frequency for the model. **c)** Predicted versus reference plot for the GMA% and **d)** shows the SNV pretreated spectra used for model building with important frequencies highlighted

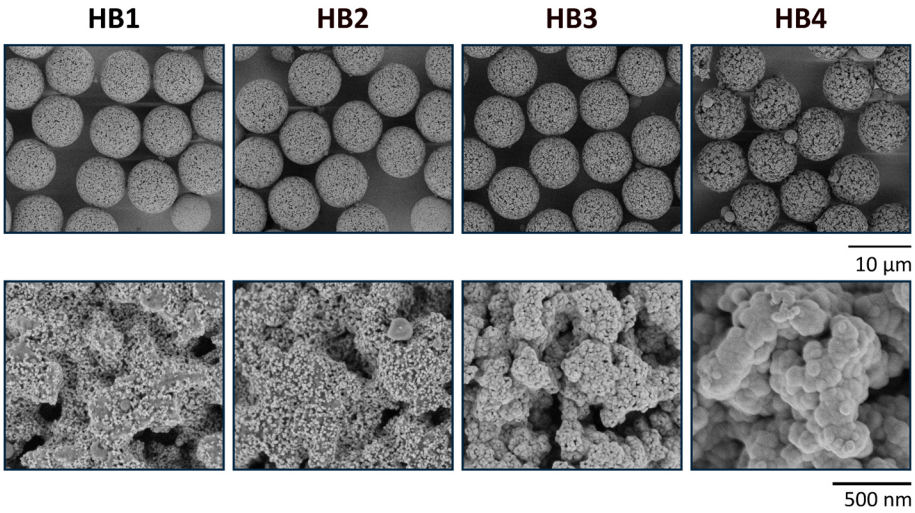


**Figure S. 5.5** SEM images of polymer/$SiO_2$ hybrid beads with varying GMA to EDMA ratio. 2,000 (top row) and 50,000 (bottom row) magnification.

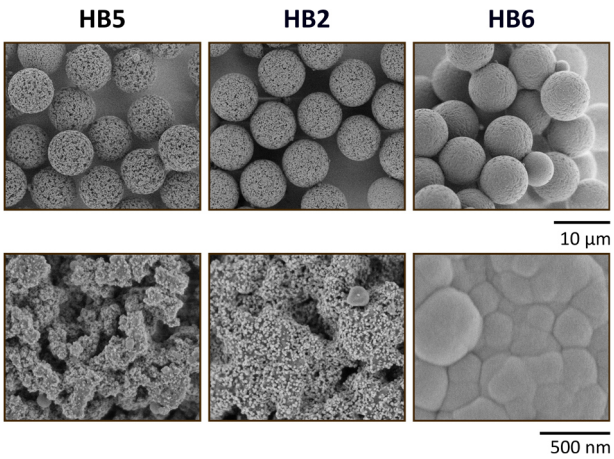


**Figure S. 5.6** SEM images of polymer/$SiO_2$ hybrid beads with varying monomer to porogen ratio. 2,000 (top row) and 50,000 (bottom row) magnification.

**Table S. 5.2** Properties of hybrid beads **HB1–6** using different polymer templates with different amount of GMA.

| | **P** | | **HB** | | **MPSM** | |
|---|---|---|---|---|---|---|
| | **particle size** | **change** | **particle size** | **change** | **particle size** | **shrinkage** |
| | /µm | /µm | /µm | /µm | /µm | /% µm³ |
| **HB1** | 7.9 | + 0.3 | 8.2 | - 1.6 | 6.6 | 47.9 |
| **HB2** | 7.8 | + 0.5 | 8.3 | - 1.5 | 6.8 | 45.0 |
| **HB3** | 7.5 | + 0.6 | 8.1 | - 1.1 | 7.0 | 35.5 |
| **HB4** | 7.3 | + 0.9 | 8.2 | - 1.1 | 7.1 | 35.1 |
| **HB5** | 7.6 | + 0.6 | 8.2 | - 1.9 | 6.3 | 54.6 |
| **HB6** | 7.9 | + 0.9 | 8.8 | - 0.6 | 8.2 | 19.1 |

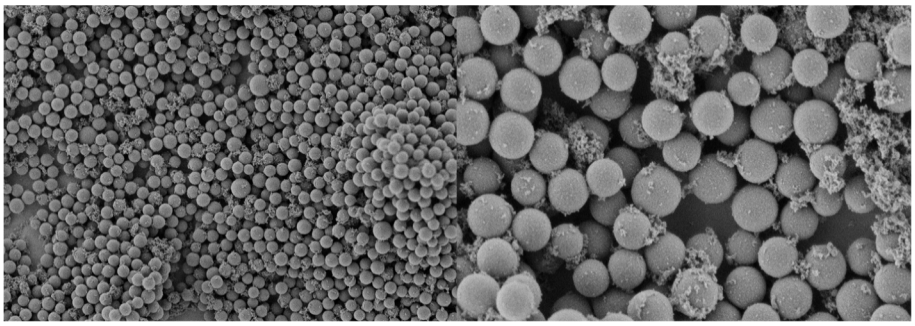

**Figure S. 5.7** SEM images of filtrate of polymer/$SiO_2$ hybrid bead **HB6** after washing process.

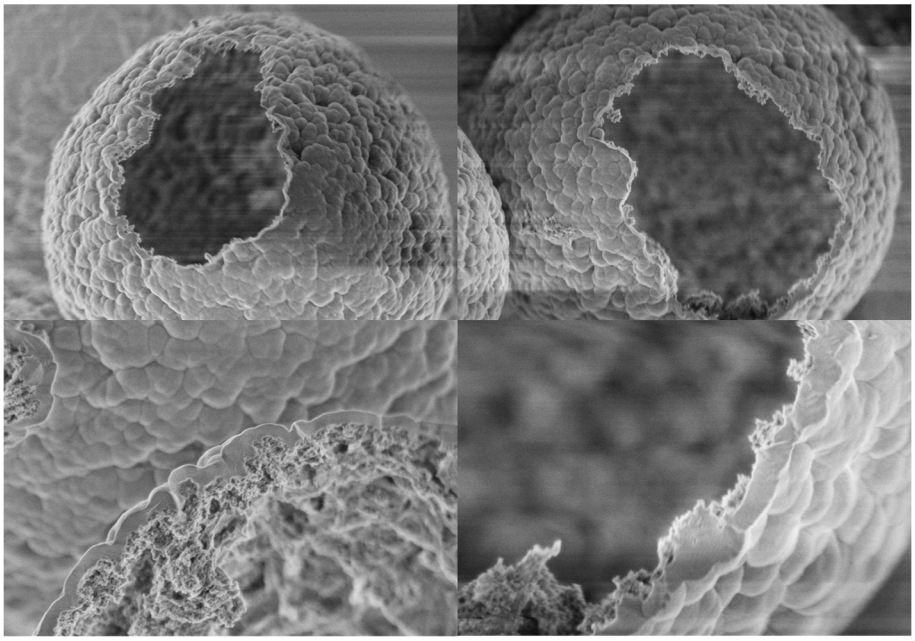

**Figure S. 5.8** SEM images of broken silica microspheres of **MPSM6**.

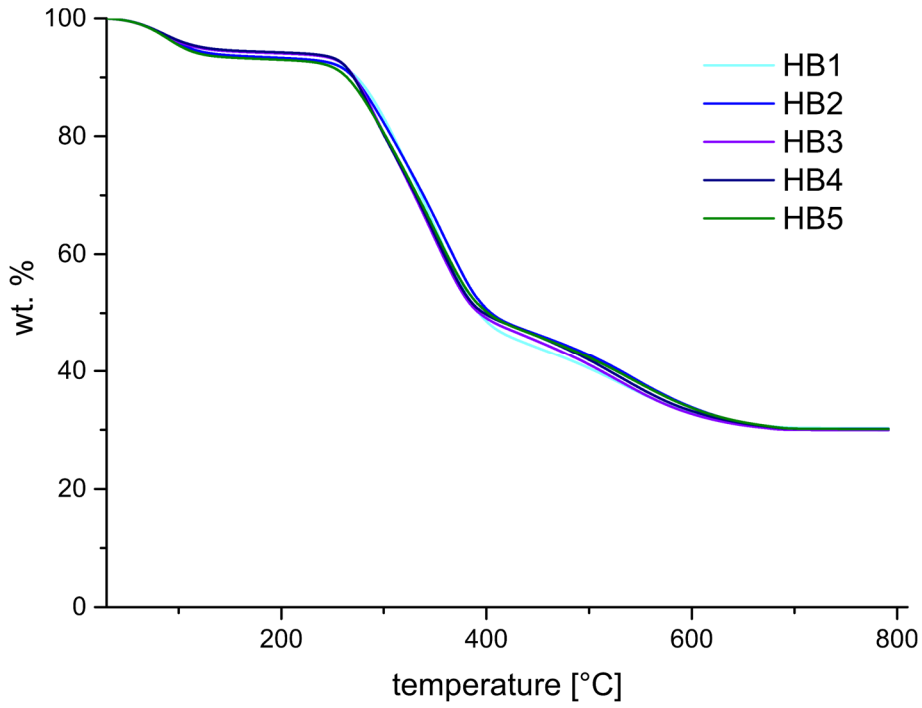


**Figure S. 5.9** TGA measurements of hybrid beads **HB1–5**.

**CRediT authorship contribution statement: Fabio Fait:** Writing – original draft, Visualization, Methodology, Investigation, Data curation. **Julia C. Steinbach:** Writing – original draft, Visualization, Methodology, Investigation, Formal analysis, Data curation. **Andreas Kandelbauer:** Writing – review & editing, Supervision, Project administration, Funding acquisition, Conceptualization. **Hermann A. Mayer:** Writing – review & editing, Supervision, Resources, Project administration, Funding acquisition, Data curation, Conceptualization. **Fabio Fait** and **Julia C. Steinbach** equally contributed to this work.

**Declaration of competing interest:** The authors declare that they have no known competing financial interests or personal relationships that could have appeared to influence the work reported in this paper.

**Acknowledgments:** This research was funded the by Bundesministerium für Bildung und Forschung (BMBF, grant number 13FH647IX6) and the Bundesministerium für Wirtschaft und Energie (AiF/ZIM, grant number ZF4019203SL8). Furthermore, we would like to thank our cooperation partner Dr. Maisch GmbH for their support in preparing the columns. We thank Elke Nadler for contributing the SEM measurements.

# 6. Paper III

## Monodisperse Porous Silica/Polymer Nanocomposite Microspheres with Tunable Silica Loading, Morphology and Porosity

*Julia C. Steinbach [1,2], Fabio Fait [1,2], Hermann A. Mayer [2] and Andreas Kandelbauer [1,3,*]*

[1] Process Analysis & Technology, Reutlingen Research Institute, Reutlingen University, Alteburgstraße 150, 72762 Reutlingen, Germany; Julia.Steinbach@Reutlingen-University.de (J.C.S.); Fabio.Fait@Reutlingen-University.de (F.F.); Andreas.Kandelbauer@Reutlingen-University.de (A.K.)

[2] Institute of Inorganic Chemistry, University of Tübingen, Auf der Morgenstelle 18, 72076 Tübingen, Germany; hermann.mayer@uni-tuebingen.de (H.A.M.)

[3] Department of Material Sciences and Process Engineering (MAP), Institute of Wood Technology and Renewable Materials, University of Natural Resources and Life Sciences, Gregor-Mendel-Straße 33, 1180 Vienna, Austria

[*] Correspondence: andreas.kandelbauer@reutlingen-university.de; Tel.: +49-(0)7-12-1271-2009

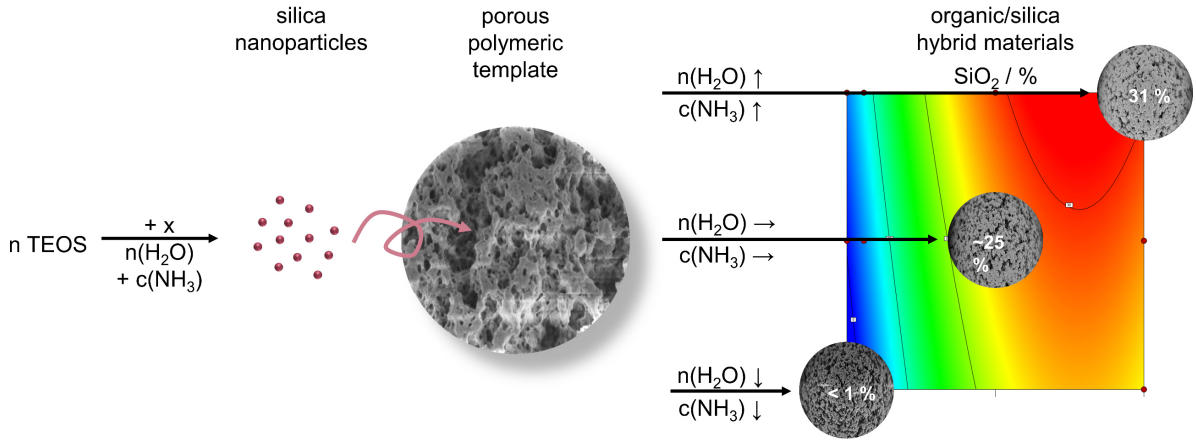




Steinbach, J.C.; Fait, F.; Mayer, H.A.; Kandelbauer, A. Monodisperse Porous Silica/Polymer Nanocomposite Microspheres with Tunable Silica Loading, Morphology and Porosity. *International Journal of Molecular Sciences* **2022**, *23*, 14977, doi:10.3390/ijms232314977.[3]

## Abstract

Hybrid organic/inorganic nanocomposites combine the distinct properties of the organic polymer and the inorganic filler resulting in overall improved system properties. Monodisperse porous hybrid beads consisting of tetraethylene pentamine functionalized *poly*(glycidyl methacrylate-*co*-ethylene glycol dimethacrylate) particles and silica nanoparticles (SNPs) were synthesized under Stöber sol-gel process conditions. A wide range of hybrid organic/silica nanocomposite materials with different material properties was generated. The effects of n($H_2O$)/n(TEOS) and c($NH_3$) on the hybrid bead properties particle size, $SiO_2$ content, median pore size, specific surface area, pore volume and size of the SNPs were studied. Quantitative models with high robustness and predictive power were established using a statistical and systematic approach based on response surface methodology. It was shown that the material properties depend in a complex way on the process factor settings and exhibit non-linear behaviors as well as partly synergistic interactions between the process factors. Thus, silica content, median pore size, specific surface area, pore volume and size of the SNPs are non-linearly dependent on water to precursor ratio. This is attributed to the effect of the water to precursor ratio on the hydrolysis and condensation rates of TEOS. A possible mechanism of SNP incorporation into the porous polymer network is discussed.



## Keywords

nanocomposites; porous microspheres; design of experiment; response surface methodology; rational design; sol-gel processing


## 6.1. Introduction

The combination of organic and inorganic materials provides composites exhibiting different properties than the inorganic and organic components alone and is, therefore, of great interest in material sciences[134,135,190,191]. The incorporation of inorganic components, such as silica nanoparticles (SNPs) into organic networks, allows the design of material properties which affect their thermal and/or mechanical stability[192,193], electronic behavior[194] and enhance biocompatibility[195]. Thus, hybrid materials are applied in catalysis[131], separation technologies[132] and as drug delivery systems[133,195]. Moreover the organic component can function as a sacrificial template to generate defined porous inorganic structures[22,55,56,187].

For many applications, defined specific surface areas are favorable, which are achieved by introducing porous networks into the material. Good effective accessibility of the porous material for diffusion controlled processes, such as separation processes or catalysis, is achieved by mesopores and/or macropores[49]. The properties of porous

*poly*(glycidyl methacrylate-*co*-ethylene glycol dimethacrylate) (*p*(GMA-*co*-EDMA)) particles in the micron scale are adjustable specifically[1,70,155,157], which makes them an adaptable polymer matrix with a broad pore size distribution.

Nanocomposites are multiphase materials with at least one component in the nanometer range[130]. The preparation of hybrid organic/silica nanocomposites can be achieved by (1) blending of dispersed polymer and silica nanoparticles, (2) in situ polymerization of monomers in presence of silica and (3) performing the sol-gel process from precursors in the presence of a polymer matrix[136]. The sol-gel process allows the preparation of tailored silica materials with e.g. defined nanoparticle sizes and dispersion under mild process conditions and is, therefore, particularly suitable to prepare tailored organic/silica composites[196].

Discrete SNPs with narrow size distributions are readily synthesized under basic reaction conditions by the Stöber method. The sizes of silica nanoparticles obtained with this method vary between 0.05 µm and 2.0 µm[45]. The Stöber method exploits the basic hydrolysis and condensation reactions of alkoxysilanes in alcoholic media[45]. The hydrolysis of the precursor (Equation (6.1)), e.g. tetraethyl orthosilicate (TEOS), proceeds under formation of silanol groups (n = 1–4). The condensation with formation of siloxane bonds and entire silica networks occurs either between silanol groups as water condensation (Equation (6.2)) or between silanol and ethoxy groups as alcohol condensation (Equation (6.3)).

Hydrolysis: $$Si(OC_2H_5)_4 + n\ H_2O \rightleftharpoons Si(OC_2H_5)_{4-n}(OH)_n + n\ C_2H_5OH \quad (6.1)$$

Water condensation: $$\equiv Si(OH) + (HO)Si\equiv \rightleftharpoons \equiv Si{-}O{-}Si\equiv + H_2O \quad (6.2)$$

Alcohol condensation: $$\equiv Si(OC_2H_5) + (HO)Si\equiv \rightleftharpoons \equiv Si{-}O{-}Si\equiv + C_2H_5OH \quad (6.3)$$

Immediately after the addition of TEOS to an ammonia solution, progressing hydrolysis and condensation of the precursor starts. After reaching a critical supersaturation concentration, neighboring silanol monomers condense under formation of clusters, which collapse to form primary particles[84,105,106]. There are two prevailing models to describe the further growth mechanism of silica particles. The monomer addition model[92], which depicts the growth as addition of monomer to already formed primary particles and the aggregation only model[113], which explains particle growth through aggregation of primary particles and subsequent addition of oligomers. Small silica particles are not stable and aggregate, while stable large silica particles grow by the addition of monomers[88]. The size of the resulting SNPs depends on the relative rates of the hydrolysis and condensation reactions of the precursor. These are controlled by the relative concentrations of ammonia, TEOS and water as well as the reaction temperature, and the alcohol chosen as the solvent[94].

As the sol-gel process is very susceptible to changes in the process conditions, a univariate study focusing on the effects of single factors only, cannot depict the system complexity. The one-factor-at-a-time approach does not allow to cover a multidimensional experimental space and therefore to identify synergistic interplay between two factors. The observation of the influence of single factor variations cannot straightforwardly be transferred to other systems settings, since even small changes have a strong impact on the results. This is reflected by the sometimes even contradicting conclusions when the experimental findings of different studies are compared with one another, although by themselves they are self-consistent. Especially for the sol-gel process, where the relative rates of hydrolysis and condensation are affected by many parameters[84,88,106], a study where at least two process factors are simultaneously varied is required to understand the impacts and possible interaction effects between experimental variables. Response surface methodology (RSM) provides a statistical and systematic approach for the observation and quantification of not only linear but also nonlinear behavior. Moreover, possible synergistic interactions between process factors are identified and provide detailed causal models for multiple process factors[1,59–61]. This approach has been used to study a wide range of chemical processes[10,62,164,197] and has also been successfully applied for the preparation of SNPs[96,97,100,198,199].

In this study, micron sized monodisperse porous hybrid organic/silica hybrid beads (HBs) are generated performing a sol-gel process under Stöber reaction conditions in the presence of porous amino-functionalized *p*(GMA-*co*-EDMA) particles (p@TEPA) as hard templates. The hybrid beads consist of two interpenetrating networks. The organic network of the template, which remains unchanged due to the mild reaction conditions, and the new silica network, which is composed of aggregated silica nanoparticles of different sizes[55,56]. The aim is to achieve a range of such hybrid materials with different and defined properties like $SiO_2$ content, median pore size, specific surface area, and pore volume. Thus, the two critical process factors for the sol-gel process, water to precursor ratio ($n(H_2O)/n(TEOS)$) and the ammonia concentration ($c(NH_3)$) were investigated in presence of a porous polymeric template. These were systematically changed according to a face-centered-central composite design (FCD) to establish response surface models describing the process factor effects on the morphological characteristics. Moreover, a possible mechanism of silica nanoparticle incorporation into the porous polymer matrix is proposed and discussed.

## 6.2. Results

The preparation of micron sized porous hybrid beads (HBs) with tunable ratio of organic components to silica and morphological properties was systematically investigated using response surface methodology (RSM) (**Figure 6.1**).

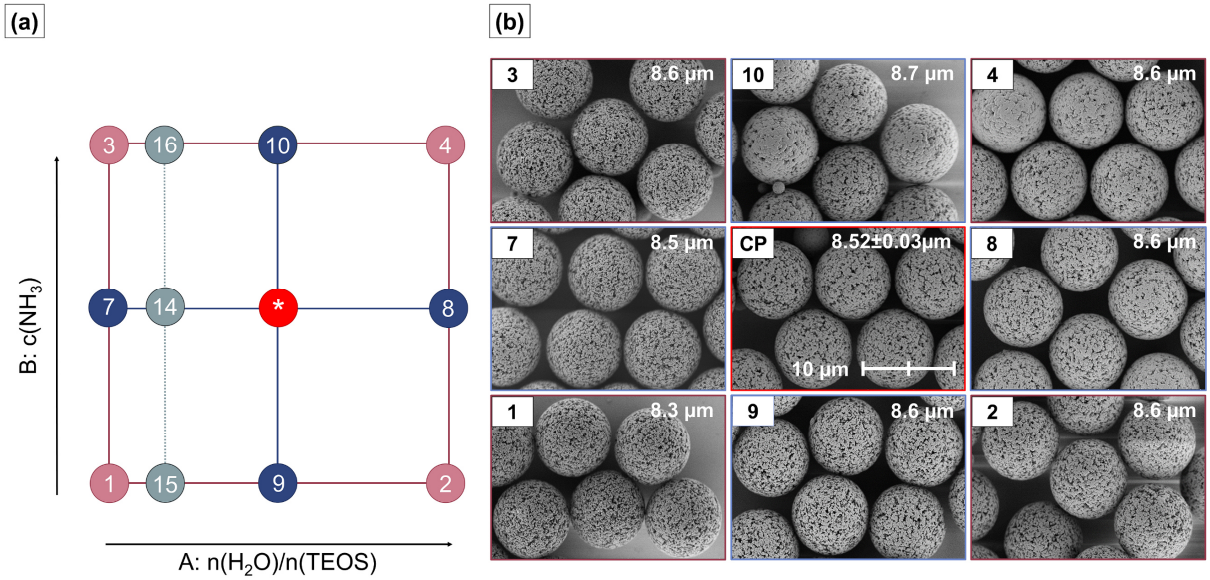


**Figure 6.1 a)** Illustration of the face-centered central composite design including additional points **HB14–16 b)** Systematic overview over SEM images at 5,000× magnification of HBs. The median size of each sample is indicated in the respective image corner. For the CPs, the average particle size and its standard deviation over all five samples is given. SEM image of **HB13** is shown as a representative example for the CPs. Factorial design points **(HB1–4**) are displayed in dark red, center points (CPs) are displayed in red (**HB5–6**, **HB11–13**) and axial design points (**HB7–10**) are displayed in blue, additional design points are shown in grey (**HB14–16**). SEM images of additional design points **HB14–16** are shown separately in **Figure A. 6.1**. * indicates the center point experiments at intermediate factor level settings.

The organic porous *p*(GMA-*co*-EDMA) template was prepared by seeded swelling polymerization (see Appendix 6.6.1)[1]. Tetra ethylene pentamine (TEPA) was covalently bound to the porous polymer surface via ring opening reactions of the prevalent epoxy groups[58,118]. The TEPA functionalization of polymer particles (p@TEPA) has been shown to provide a well-suited surface modification for depositing silica into the polymer network[56,119]. The prepared **p@TEPA** template had a median particle size of 8.3 µm and was highly monodisperse with a $d_{90}/d_{10}$ value of 1.04. The median pore diameter ($\Phi_{50}$) of the **p@TEPA** was 13.0 nm in combination with a specific surface area (SSA) of 63.79 $m^2 \cdot g^{-1}$ and a pore volume ($V_p$) of 0.12 $cm^3 \cdot g^{-1}$.

The hybrid beads **HB1–HB16** consisting of p@TEPA/$SiO_2$ were prepared by varying the sol-gel process conditions according to **Table 6.1** in the presence of the **p@TEPA** template. With RSM, linear and non-linear effects of the process factors $n(H_2O)/n(TEOS)$ and $c(NH_3)$, as well as their possible synergistic interactions, on the material properties $SiO_2$ content, $\Phi_{50}$, $V_p$, SSA and size of the SNPs were analyzed using

a face-centered central composite design (FCD). **Figure 6.1**a shows schematically the experimental space covered by the FCD. Selected HBs which result from different process factor settings according to the RSM are shown in **Figure 6.1**.

**Table 6.1** summarizes the factor level settings of n($H_2O$)/n(TEOS) and c($NH_3$) and the resulting values of the measured response properties. The samples are listed in the Yates standard order. In addition to the HB samples, the material properties of the template (**p@TEPA**) are given for comparison. One of the axial design points, **HB9**, was identified as an outlier based on the extremely high values of its residuals for the pore volume and silica content. Thus, it was not used for model building. Model quality likewise improved for the models of all other targeted responses as well upon omission of **HB9**.

**Table 6.1** Factor level settings and their corresponding particle properties particle size, dispersity, specific surface area, pore diameter, pore volume *(at $p/p_0 = 0.95$)*, $SiO_2$ content, and size of the SNPs. The experiments are listed according to Yates standard order (Std). *Outlier - HB9 is marked italic and was not included in model building. †No SNPs visible or not measurable (below image resolution of SEM).

| | **Factor level settings** | | **Response values** | | | | | | |
|---|---|---|---|---|---|---|---|---|---|
| **Std** | **A n($H_2O$)/ n(TEOS)** | **B n($NH_3$)** | **Particle size** | **$d_{90}/d_{10}$** | **SSA** | **Pore diameter $\Phi_{50}$** | **Pore volume $V_p$** | **$SiO_2$ content** | **SNP size** |
| | | /mmol·$L^{-1}$ | /μm | | /$m^2 \cdot g^{-1}$ | /nm | /$cm^3 \cdot g^{-1}$ | /wt% | /nm |
| **p@TEPA** | - | - | 8.3 | 1.04 | 63.79 | 13.0 | 0.12 | 0 | - |
| **HB1** | 4 | 17.1 | 8.3 | 1.11 | 73.87 | 12.9 | 0.13 | 0.1 | 0† |
| **HB2** | 74 | 17.1 | 8.6 | 1.14 | 35.11 | 12.6 | 0.03 | 19.7 | 20 |
| **HB3** | 4 | 74.1 | 8.6 | 1.06 | 55.86 | 12.7 | 0.10 | 2.7 | 0† |
| **HB4** | 74 | 74.1 | 8.6 | 1.07 | 8.75 | 18.1 | 0.02 | 31.2 | 66 |
| **HB5** | 39 | 45.6 | 8.5 | 1.09 | 20.87 | 16.1 | 0.04 | 22.6 | 27 |
| **HB6** | 39 | 45.6 | 8.5 | 1.08 | 12.92 | 17.8 | 0.03 | 26.9 | 35 |
| **HB7** | 4 | 45.6 | 8.5 | 1.06 | 62.72 | 13.8 | 0.12 | 0.4 | 0† |
| **HB8** | 74 | 45.6 | 8.6 | 1.06 | 9.63 | 16.5 | 0.02 | 30.1 | 47 |
| ***HB9**** | *39* | *17.1* | *8.6* | *1.05* | *47.38* | *17.5* | **0.09* | **13.0* | *24* |
| **HB10** | 39 | 74.1 | 8.7 | 1.07 | 12.02 | 17.1 | 0.03 | 28.6 | 58 |
| **HB11** | 39 | 45.6 | 8.6 | 1.06 | 13.51 | 16.3 | 0.03 | 26.7 | 35 |
| **HB12** | 39 | 45.6 | 8.5 | 1.07 | 17.10 | 15.5 | 0.05 | 25.9 | 43 |
| **HB13** | 39 | 45.6 | 8.5 | 1.08 | 14.32 | 17.0 | 0.03 | 25.9 | 40 |
| **HB14** | 8 | 45.6 | 8.5 | 1.07 | 50.76 | 15.5 | 0.10 | 2.7 | 0† |
| **HB15** | 8 | 17.1 | 8.5 | 1.06 | 64.03 | 14.2 | 0.12 | 0.2 | 0† |
| **HB16** | 8 | 74.1 | 8.3 | 1.15 | 47.03 | 14.9 | 0.09 | 7.9 | 18 |

### 6.2.1. Size and dispersity

The particle sizes of the produced **HB1–HB16** vary in a narrow range from 8.3 to 8.6 μm (8.5±0.1 μm) and are monodisperse with a particle size distribution with $d_{90}/d_{10}$ values between 1.05–1.15 (1.08±0.08). SEM images of the particles obtained at each design point are given in **Figure 6.1**b. Thus, the polymeric hard template is mainly determining the size of the HBs within the examined design space and the narrow dispersity of the template particles is very well reproduced by the HBs. However, a small positive effect of the ratio $n(H_2O)/n(TEOS)$ on the particle size was found to be statistically significant (see **Table 6.2**). This indicates that an increase in $n(H_2O)/n(TEOS)$ leads to a minor increase in HB particle size. The rather poor values for the model quality parameters $R^2 = 0.3642$ and $R^2_{predicted} = 0.1684$ indicate that an effect can be detected, but, however, is too weak to be quantitatively modeled sufficiently well within the range of the examined design space.

**Table 6.2** Excerpt from the analysis of variance (ANOVA) tables with p-values for the response surface models of the target response variables particle size, $SiO_2$ content, median pore diameter ($\Phi_{50}$), specific surface area (SSA), pore volume ($V_P$) and size of the SNPs, as well as their fit statistics. Complete ANOVA tables for each model are given in **Table S. 6.1–6**

| | p-values | | | | | |
|---|---|---|---|---|---|---|
| **Response** | **Particle size** | **$SiO_2$** | **$\Phi_{50}$** | **SSA** | **$V_P$ *($p/p_0 = 0.95$)*** | **SNP size** |
| | /μm | /wt% | /nm | /$m^2 \cdot g^{-1}$ | /$cm^3 \cdot g^{-1}$ | /nm |
| **Model** | 0.0172 | < 0.0001 | 0.0007 | < 0.0001 | < 0.0001 | < 0.0001 |
| **A** – $n(H_2O)/n(TEOS)$ | 0.0172 | < 0.0001 | 0.0099 | < 0.0001 | 0.0007 | < 0.0001 |
| **B** – $c(NH_3)$ | n.s. | 0.0011 | 0.0051 | < 0.0001 | < 0.0001 | < 0.0001 |
| **AB** | n.s. | n.s. | 0.0074 | n.s. | n.s. | 0.0026 |
| **$A^2$** | n.s. | < 0.0001 | 0.0050 | < 0.0001 | < 0.0001 | 0.0009 |
| **$B^2$** | n.s. | n.s. | n.s. | 0.0146 | n.s. | n.s. |
| **Lack of fit** | 0.0163 | 0.2204 (n.s.) | 0.4990 (n.s.) | 0.4397 (n.s.) | 0.9670 (n.s.) | 0.6132 (n.s.) |
| **$R^2$** | 0.3624 | 0.9780 | 0.8299 | 0.9840 | 0.9800 | 0.9545 |
| **$R^2_{adjusted}$** | 0.3152 | 0.9720 | 0.7618 | 0.9776 | 0.9745 | 0.9364 |
| **$R^2_{predicted}$** | 0.1684 | 0.9459 | 0.5529 | 0.9535 | 0.9635 | 0.8874 |

n.s. = not statistically significant

### 6.2.2. $SiO_2$ content

The amount of silica, which is deposited in the pores of the template, was determined thermogravimetrically (see section 1016.4.5). The $SiO_2$ content in the hybrid materials is described by a statistically highly significant model ($p < 0.0001$) with high robustness $R^2_{predicted} = 0.9459$, and, hence, good predictive power (**Table 6.2**).

The model effect terms A – n($H_2O$)/n(TEOS) and $A^2$, as well as B – c($NH_3$) are statistically highly significant at an $\alpha$-value of 0.05. The effect strengths in terms of coded factors are given in Equation (6.4):

$$SiO_2 = 25.49 + 13.34\ A + 3.55\ B - 11.80\ A^2 \quad (6.4)$$

The stoichiometric ratio of water to precursor shows by far the strongest effect and a non-linear behavior. The positive effect leads to an increase in the amount of deposited silica in the polymer with increasing molar ratio. The negative $A^2$ effect term describes the non-linear behavior of the increase in silica deposition with increasing n($H_2O$)/n(TEOS) ratio. At a stoichiometric ratio of water to precursor of ~60:1 the silica deposition reaches a maximum (**Figure 6.2**a – c).

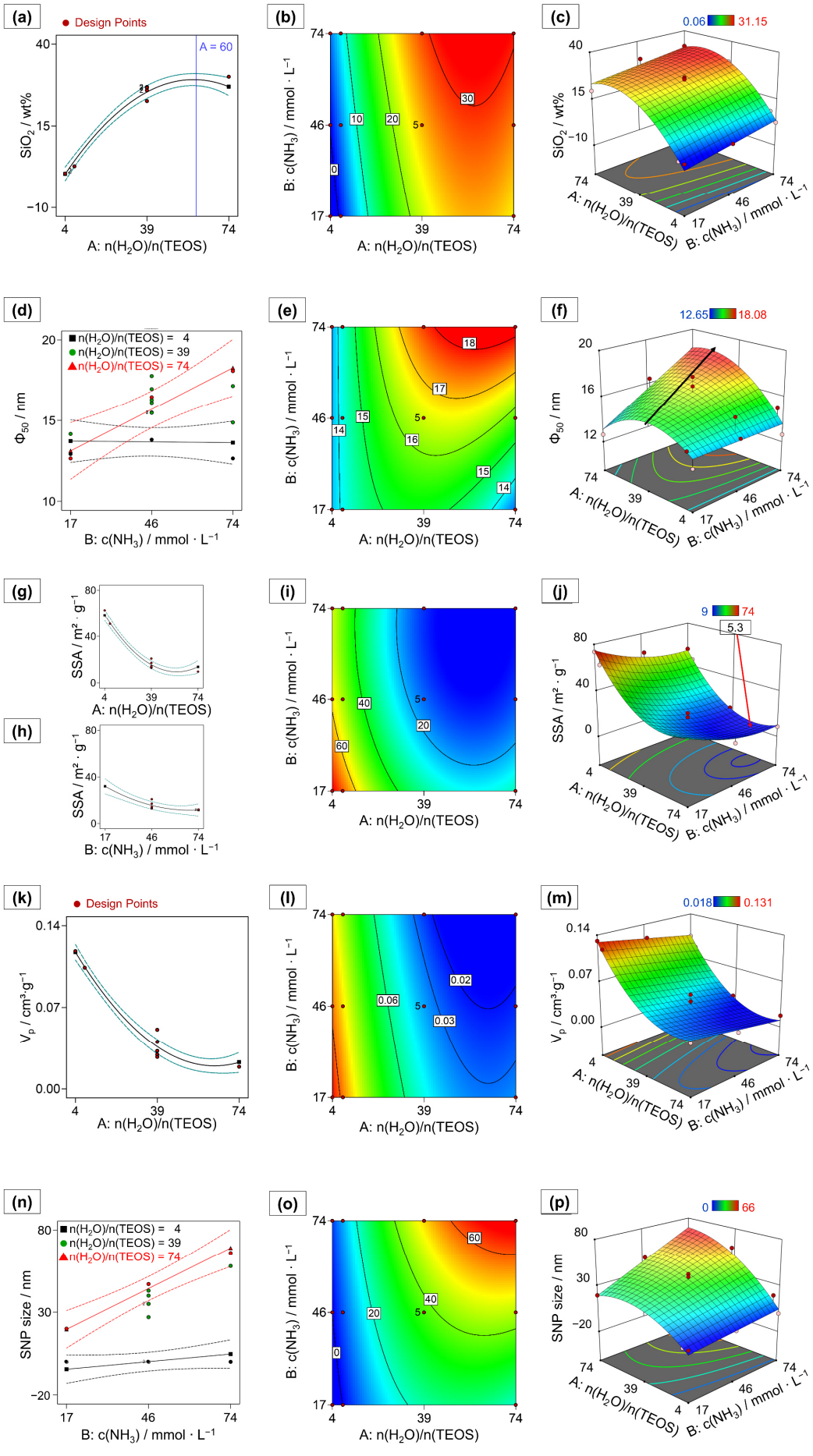
(a)
Design Points
A = 60
SiO2 / wt%
A: n(H2O)/n(TEOS)
(b)
B: c(NH3) / mmol · L−1
A: n(H2O)/n(TEOS)
(c)
0.06
31.15
SiO2 / wt%
A: n(H2O)/n(TEOS)
B: c(NH3) / mmol · L−1
(d)
n(H2O)/n(TEOS) = 4
n(H2O)/n(TEOS) = 39
n(H2O)/n(TEOS) = 74
Φ50 / nm
B: c(NH3) / mmol · L−1
(e)
B: c(NH3) / mmol · L−1
A: n(H2O)/n(TEOS)
(f)
12.65
18.08
Φ50 / nm
A: n(H2O)/n(TEOS)
B: c(NH3) / mmol · L−1
(g)
SSA / m² · g−1
A: n(H2O)/n(TEOS)
(h)
SSA / m² · g−1
B: c(NH3) / mmol · L−1
(i)
B: c(NH3) / mmol · L−1
A: n(H2O)/n(TEOS)
(j)
9
74
5.3
SSA / m² · g−1
A: n(H2O)/n(TEOS)
B: c(NH3) / mmol · L−1
(k)
Design Points
Vp / cm³ g−1
A: n(H2O)/n(TEOS)
(l)
B: c(NH3) / mmol · L−1
A: n(H2O)/n(TEOS)
(m)
0.018
0.131
Vp / cm³ g−1
A: n(H2O)/n(TEOS)
B: c(NH3) / mmol · L−1
(n)
n(H2O)/n(TEOS) = 4
n(H2O)/n(TEOS) = 39
n(H2O)/n(TEOS) = 74
SNP size / nm
B: c(NH3) / mmol · L−1
(o)
B: c(NH3) / mmol · L−1
A: n(H2O)/n(TEOS)
(p)
0
66
SNP size / nm
A: n(H2O)/n(TEOS)
B: c(NH3) / mmol · L−1

**Figure 6.2** Overview over all relevant model graphs – one factor effect plots, depicting the effect of a single factor on the response at a medium level of the other studied process factor **(a, g, h, k)**; interaction plots showing the dependence of the response on the settings of the two synergistically interacting factors (■=low setting, ●=medium setting, ▲=high setting) and visualizing the strengths of the synergistic interactions **(d, n)**, contour plots, displaying a heatmap for each response variable dependent on both process factors **(b, e, i, l, o)**; and response surface plots, showing the values for the responses predicted by the response surface model across the design space for each combination of process factor settings **(c, f , j, m, p)**. Note, that in the 3D-plots **j** and **m** the axes of n($H_2O$)/n(TEOS) are given in opposite direction to **c, f, p** for better visibility. Dashed lines indicate 95 % confidence intervals for one factor and interaction plots. Red areas correspond to high, blue areas correspond to low response values in the response surface models. The responses are as follows: **(a-c)** $SiO_2$ content, blue line indicates maximum $SiO_2$ deposition, **(d-f)** median pore size ($\phi_{50}$), the black arrow indicates a shift of maximal $\phi_{50}$ across the design space, **(g-j)** specific surface area (SSA) with the minimal SSA within the experimental space indicated by a flag, **(k-m)** pore volume ($V_p$) and **(n-p)** SNP size.

### 6.2.3. Pore size

Pore characteristics were determined by nitrogen adsorption measurements at 77 K. The pore size was calculated according to the Barrett-Joyner-Halenda (BJH) method from the desorption curve. For response surface modeling, the median of the pore size was used. The pore size distributions of all HBs, after incorporation of in-situ prepared SNPs into the porous template network, and the template are shown in **Figure 6.3**and the median pore size values are listed in **Table 6.1**.

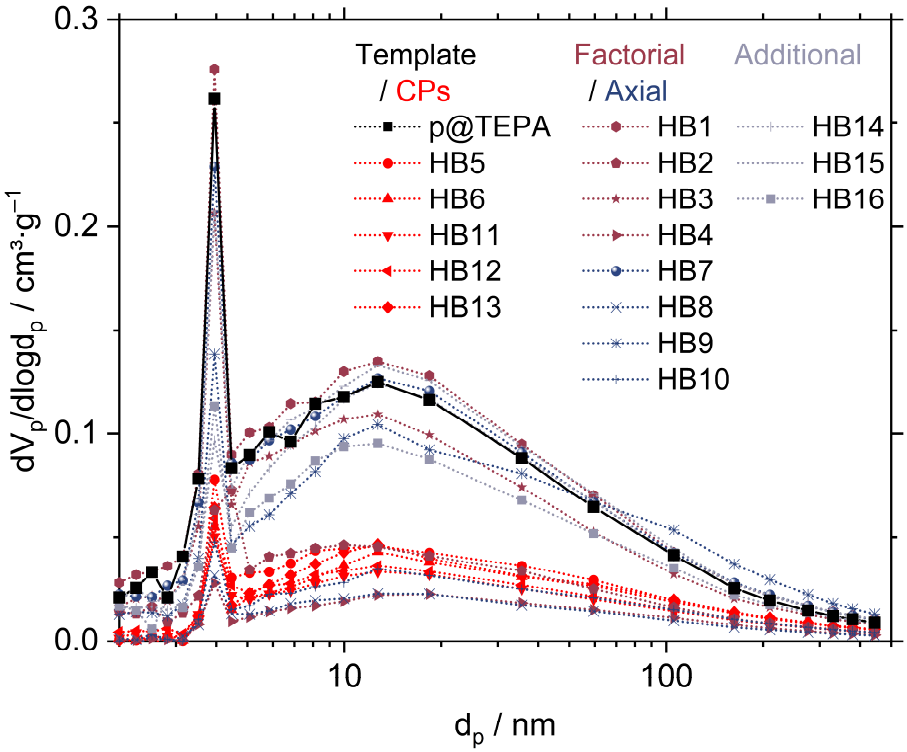


**Figure 6.3** Pore size distribution of the porous **p@TEPA** template (solid line) and porous HBs (dotted lines). The template is shown in black, factorial design points in dark red, center points (CPs) in red, axial design points in blue, and additional design points in grey.

The pore size distribution of the HBs is mainly determined by the pore size distribution already present in the **p@TEPA** template. It displays a very wide distribution from meso- to macroporous range. Compared to the template, the median of the pore sizes is shifted to larger pores in the hybrid materials, see **Table 6.1**.

With a correlation coefficient of $R^2 = 0.8299$ and a regression coefficient of prediction of $R^2_{predicted} = 0.5529$ the model ($p < 0.001$) can well describe the pore size median. The median of the pore sizes is statistically significantly affected by the effect terms A – $n(H_2O)/n(TEOS)$, B – $c(NH_3)$, the synergistic interaction effect term AB between water to precursor ratio and ammonia concentration and the non-linear effect term $A^2$. The relative importance of the factors is evident from Equation (6.5), the model equation in terms of coded factors:

$$\Phi_{50} = 16.49 + 1.01\ A + 1.26\ B + 1.31\ AB - 1.80\ A^2 \quad (6.5)$$

The synergistic interaction effect term AB quantifies the interdependence between the two factors. Consequently, restricting the discussion to only one of the factors is not meaningful, since the behavior of one factor depends on the factor level setting of the other and changes in dependence of the second factor involved in the interaction. **Figure 6.2**d shows the two-factor interaction (2FIA) plot for the median pore size with the ammonia concentration depicted on the abscissa. For small ratios A – $n(H_2O)/n(TEOS)$, the ammonia concentration has very little to no effect on the median pore size, while for large $n(H_2O)/n(TEOS)$ ratios the median pores size distinctly increases with increasing B – $c(NH_3)$. Increasing the ratio $n(H_2O)/n(TEOS)$ amplifies the effect of the $NH_3$ concentration. Comparing **HB1** (-/-) and **HB3** (-/+), the median pore size is almost constant (12.9 nm and 12.6 nm, respectively), while for high water to precursor the median pore size increases strongly from **HB2** (+/-) at 12.7 nm to **HB4** (+/+) at 18.1 nm with increasing ammonia concentration.

The non-linear $A^2$ term shows that the increase of the median pore size towards higher values with increasing $n(H_2O)/n(TEOS)$ becomes less pronounced at higher levels of $n(H_2O)/n(TEOS)$. It also indicates that there is a maximum mean pore size, the location of which depends on the corresponding level of ammonia concentration used. This is especially visible in the trajectory of the contour plot, **Figure 6.2**e, and in the curvature of the response surface (**Figure 6.2**f), at high ammonia concentrations. The shift of the maximum pore size median is indicated by an arrow.

The combination of the non-linear $A^2$ term with the synergistic interaction term AB, results in a twisted response surface with a steep ascent and a shifting maximum which shows a high sensitivity towards small changes in the factor level settings of both the $n(H_2O)/n(TEOS)$ ratio and the ammonia concentration. This sensitivity is also

reflected by the relatively large statistical variance of the pore sizes observed within the replicated CP experiments.

### 6.2.4. Specific surface area

For many applications, the specific surface area (SSA) is of great importance, since it is crucial for the surface available for e.g. the amount of functionalization or adsorption. The SSA was determined by nitrogen adsorption measurements under application of the Brunauer-Emmet-Teller (BET) theory[65]. All samples showed values for the C parameter from the BET equation, referring to the surface interaction energy, between 48.7 (**HB3**) and 133.7 (**HB2**). This indicates a sufficiently well discriminated knee in the adsorption isotherm to determine the theoretical formation of the molecular monolayer[65]. The SSAs of the prepared HBs are modeled with high predictive power and robustness ($R^2 = 0.9840$ and $R^2_{predicted} = 0.9535$, respectively). The model is highly statistically significant ($p < 0.0001$) and includes the statistically significant factor effect terms A – $n(H_2O)/n(TEOS)$ and B – $c(NH_3)$, as well as both non-linear factor effect terms $A^2$ and $B^2$ (**Table 6.2**). No synergistic interactions between the two factors were found. The coded equation describing the relative effect strengths is given in Equation (6.6):

$$SSA = 15.59 - 22.38\ A - 10.17\ B + 20.57\ A^2 + 6.22\ B^2 \quad (6.6)$$

The SSAs of the HBs are mainly determined by the ratio $n(H_2O)/n(TEOS)$, which has a strong negative effect. The SSAs decrease with increasing water ratio. This effect is attenuated by the positive $A^2$ effect term accounting for the minimum which is observed at high $n(H_2O)/n(TEOS)$ ratios (**Figure 6.2**g).

A similar behavior is seen for increasing ammonia concentrations. The negative linear effect term B combined with the positive non-linear effect term $B^2$ indicate a decrease of the SSAs with increasing ammonia concentrations, which again levels off at higher concentrations (**Figure 6.2**h – i). A minimum in SSA of approximately 5.3 $m^2 \cdot g^{-1}$ is found in the experimental space at A = 58 and B = 68 $mmol \cdot L^{-1}$ which is highlighted in the response surface plot of **Figure 6.2**j.

### 6.2.5. Pore volume

The pore volumes $V_P$ of the HB samples which were determined at $p/p_0 = 0.95$ are expressed by a highly statistically significant RSM ($p < 0.0001$) as a function of the process factor effect terms A – $n(H_2O)/n(TEOS)$ and B – $c(NH)_3$ and the non-linear factor effect term $A^2$. The dependence of $V_P$ on the process factors is given in terms of coded factor effect terms in Equation (6.7):

$$V_P = 0.0362 - 0.0473\ A - 0.0122\ B + 0.0388\ A^2 \quad (6.7)$$

The factor effect term A has the strongest influence determining the pore volume. The pore volume of the HBs decreases with increasing water to precursor ratio. However, this decrease is attenuated at higher ratios by the positive nonlinear $A^2$ term, see **Figure 6.2**k.

In addition, increasing ammonia concentrations also lead to a decrease in pore volume, but this effect is much less pronounced and is only about one fourth of the magnitude of the effect of factor A. This results in the highest pore volumes found at low factor level settings for both factors A and B (**Figure 6.2**l and m). The model quality parameters $R^2 = 0.9800$ and $R^2_{predicted} = 0.9635$ indicate an excellent predictive power and model robustness.

### 6.2.6. Morphology and silica nanoparticle size

The morphology of the HBs is structured by the morphological properties of the template (**Figure 6.4** and **Figure A. 6.1**). Textural changes result from the sol-gel process to varying degrees in dependence on the factor level combinations. They are especially pronounced at high factor level settings and are not visible below a certain threshold.

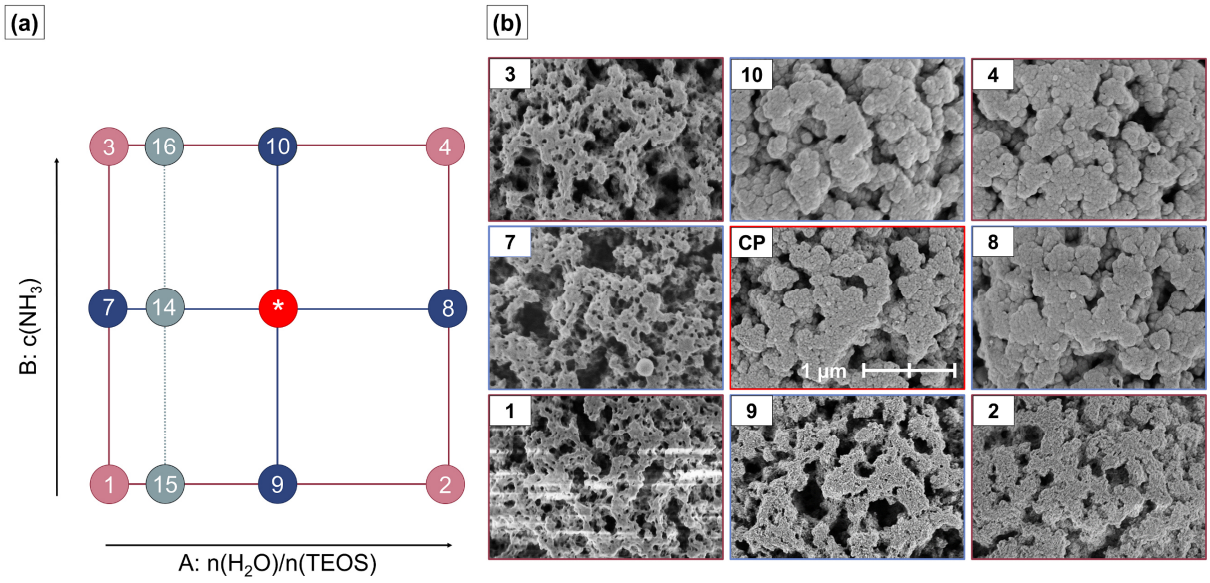


**Figure 6.4 a)** Schematic representation of the design space covered by the factor level combinations used in the face-centered central composite design including additional design points **HB14–16 b)** Systematic overview over SEM images at 50,000× magnification of each sample obtained at the various factor level combinations. As representative example for the center point (CP) combinations, **HB13** is shown. Factorial design points (**HB1–4**) are displayed in dark red, center points are displayed red (**HB5–6**, **HB11–13**) and axial design points (**HB7–10**) are displayed blue, additional design points are shown in grey (**HB14–16**). Numbers reflect the Yates standard order. SEM images of additional design points **HB14–16** are shown separately in **Figure A. 6.2**. * indicates the center point experiments at intermediate factor level settings.

Distinct differences in surface appearance are observed for the first time for the factor level combinations of particle **HB16** ($n(H_2O)/n(TEOS) = 8$, $c(NH_3) = 74.1$ mmol) (**Figure**

**A. 6.2**b). Instead of the smooth surfaces between the pore structures, small SNPs deposited in and onto the **p@TEPA** lead to an apparently rough surface texture. At medium and higher levels of n($H_2O$)/n(TEOS) ratio, all produced HB particles exhibit a nanoparticulate surface texture (**Figure 6.4**). However, with higher ammonia concentrations, the discrimination between the SNPs from each other becomes less distinct. For **HB4** and **HB8**, nonporous secondary particles were observed in the filtrate (**Figure A. 6.3**). For **HB4**, these secondary particles were stable enough to be isolated. They showed a median size of ~300 nm and a $d_{90}/d_{10}$ value of 1.88. For **HB8**, agglomeration occurred during the evaporation of the solvent. Secondary particles were obtained with a median size of ~240 nm and a $d_{90/d10}$ value of 2.05. However, since agglomeration occurred this indicates that at least a portion of the secondary particles' original size was below 50 nm[84].

The sizes of the SNPs are statistically significantly affected by the process factor A – n($H_2O$)/n(TEOS) in combination with the non-linear factor effect $A^2$, the linear effect B – c($NH_3$) and the synergistic interaction AB. The statistically significant model ($p < 0.0001$) shows a good data fit ($R^2 = 0.9545$) and allows to predict new observations well ($R^2_{predicted} = 0.8874$). The relative importance of the factor effects is again evident from the coefficients in Equation (6.8) in coded terms:

$$\text{SNP size} = 37.24 + 22.11\ A + 14.65\ B + 10.06\ AB - 15.02\ A^2 \quad (6.8)$$

The positive direction of the synergistic interaction AB (**Figure 6.2**n) results in a pronounced increase in SNP size in dependence of increasing ammonia concentrations at the higher levels of n($H_2O$)/n(TEOS) ratios. The non-linear $A^2$ term is negative and reduces the increase of the size of the SNPs for higher n($H_2O$)/n(TEOS) levels and the SNP size approaches a limiting value (at a factor level setting of $A \approx 60$).

## 6.3. Discussion

The response surfaces of the five response variables $SiO_2$ content, $\phi_{50}$, SSA, $V_P$ and the sizes of the SNPs show similarities with respect to the factor effect directions and indicate similar interdependencies (**Figure 6.2**). To illustrate how the various target responses depend on each other, all variables were plotted in pairs against each other in scatterplots. **Figure 6.5** summarizes the resulting correlation matrix for each combination of response variables with Pearson r and $R^2_{adjusted}$ correlation coefficients. Pearson r is a measure of linear correlation with an indication of direct or indirect proportionality and $R^2_{adjusted}$ is a measure for correlation adjusted by the number of model terms relative to the number of experiments to avoid overfitting.

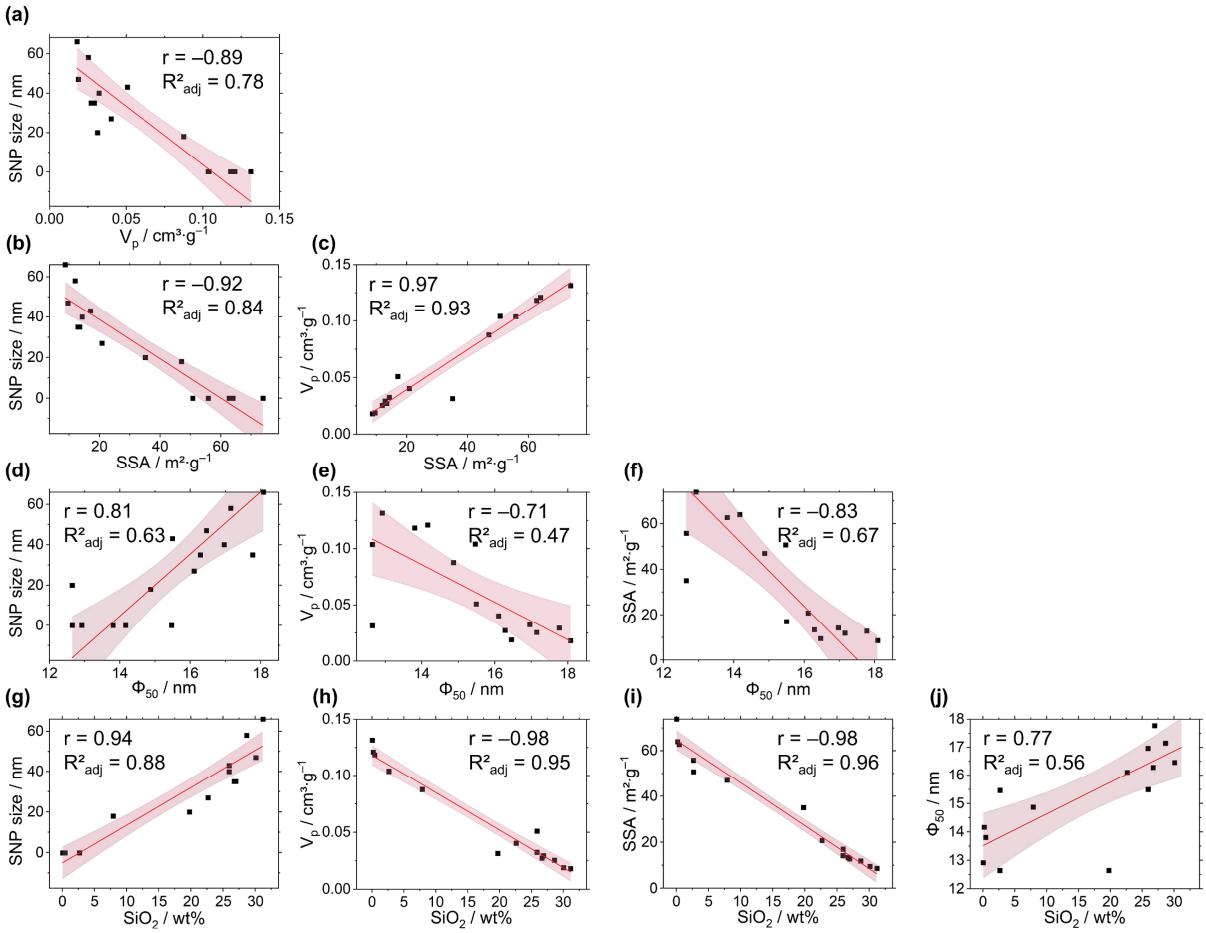


**Figure 6.5 a– j)** Multiple scatterplot illustrating the correlations between response variables with Pearson correlation coefficients r and $R^2_{adjusted}$ fit parameters. Red lines indicate linear fits. 95 % confidence intervals are given by shaded areas.

All linear correlations are statistically significant at an $\alpha$-level of 0.05. Here, the correlations with $SiO_2$ content are generally the best (**Figure 6.5**g – j), while the median pore size shows a rather poor but still statistically significant correlation (**Figure 6.5**d – f). With an increase in $SiO_2$ deposition the $V_p$ and SSA decrease, while the size of the SNPs at the HB surfaces increases (**Figure 6.5**h, i, g). Furthermore, the median of the pore size increases as well, which results from a decrease of the number of smaller pores. The positive correlation between median pore size and SNP size shows, that the median pore sizes of the HBs increase with increasing size of SNPs (**Figure 6.5**d).

**Figure 6.6** compares the relative changes in pore volume as a function of pore diameter of the HBs and the template. From this data it is deduced how the process factor settings influence the deposition of silica as a function of the pore size.

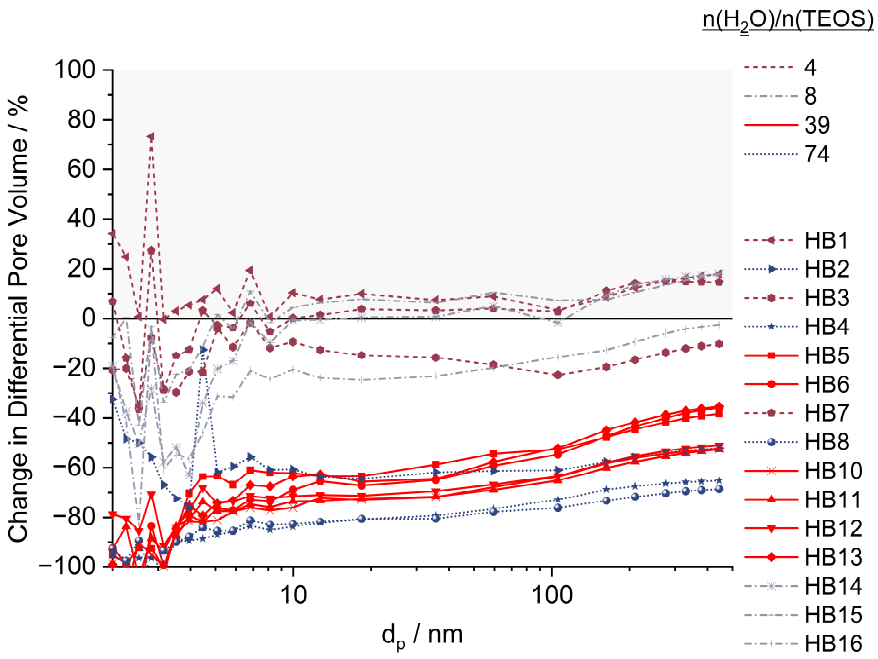


**Figure 6.6** Relative change in pore volume distribution in dependence of the pore size compared to the template particle. Line colors and types are grouped according to n(H2O)/n(TEOS) level setting - n(H2O)/n(TEOS) = 4 as burgundy dashed line, n/n = 8, as grey dashed-dotted line, n/n = 39 as solid red line and n/n = 74 as dotted blue line.

The most prominent difference in relative $V_P$ change compared to the porous template **p@TEPA** occurs at pore sizes < 5 nm. Samples which exhibit an increase in $V_P$ are **HB1** (-/-), **HB7** (-/0) and to some extent **HB14** (8/0), as well as **HB15** (8/-). Apart from HB1, which shows an increase in the pore volume across the entire pore size range, the relative pore volume for pore sizes < 10 nm decreases for **HB7**, **HB14** and **HB15**, as a result of silica deposition in small pores. Starting from pore sizes > 10 nm, the relative pore volume also increases compared to the template. These samples were prepared with low water to TEOS ratios and low ammonia concentrations. This group of particles is found in the lower left corner of the experimental design space (**Figure 6.4**a). Here, very small mass depositions of $SiO_2$ were observed with values of < 1 wt% (except for **HB14** 2.67 wt%). In this region of the experimental design space, deposition of silica is almost negligible. In contrast, the pores of these HB particles are observed to be enlarged. Lacking protective silica deposits on the pore walls, in these HBs the pores are still accessible to the solvent. This can lead to mechanical washing out effects and dissolution of non-crosslinked small polymer residues into the continuous phase of the sol-gel process which consists of isopropyl alcohol. This external influence superimposes the effects of the controlled process factor variations. For all other samples, where the silica deposition prevents solubility and mechanical washing out effects, this external influence on the relative pore volume changes does not play a role. Here,

the change in pore volume can be fully explained by the following controlled process factors: water-to-precursor ratio and ammonia concentration.

The decrease in pore volume is most pronounced for small pores, which are simply closed by silica deposition. Syntheses, which were carried out at low ratios of $n(H_2O)/n(TEOS)$ display the lowest silica deposition and the smallest loss of pore volume at pore diameters of < 10 nm. Syntheses with medium (CPs, in red) or high water/precursor ratios lead to an almost total closure of small pores < 5 nm (–80 to –100 %). Above around 5 nm, the decrease is then very uniform, with a slight increase in preserved pore volume for larger pores. This indicates the formation of a uniformly thick silica layer on the pore walls. These findings suggest an adsorptive deposition of silica onto the **p@TEPA** pore walls.

Although the response variables correlate well with each other linearly (**Figure 6.5**), they are each affected by the varied process factors in different ways and strengths. **Table 6.3** shows the relative factor effect strengths, with the factors normalized to factor A – $n(H_2O)/n(TEOS)$. This allows to compare the relative strengths of the effects for the factor B – $c(NH_3)$, the synergistic interaction effect AB and the nonlinear effect terms $A^2$ and $B^2$ between the models for the respective response variable.

**Table 6.3** Relative effect strength normalized to A = ±1.00 in terms of coded factors for particle size, $SiO_2$ content, median pore diameter, specific surface area, pore volume and SNP size.

| | $SiO_2$ | $\Phi_{50}$ | SSA | $V_P$ | SNP size |
|---|---|---|---|---|---|
| | /wt% | /nm | /$m^2 \cdot g^{-1}$ | /$cm^3 \cdot g^{-1}$ | /nm |
| **A** – $n(H_2O)/n(TEOS)$ | +1.00 | +1.00 | -1.00 | -1.00 | +1.00 |
| **B** – $c(NH_3)$, | +0.27 | +1.25 | -0.45 | -0.26 | +0.66 |
| **AB** | | +1.30 | | | +0.45 |
| $\mathbf{A^2}$ | -0.88 | -1.78 | +0.92 | +0.71 | -0.68 |
| $\mathbf{B^2}$ | | | +0.28 | | |

The effect of $c(NH_3)$ always has the same algebraic sign as the effect term of factor A in all models and therefore always acts in the same direction as the ratio $n(H_2O)/n(TEOS)$. However, effect of the ammonia concentration is always smaller than the effect of the stoichiometric ratio of water to TEOS, except for the model of the median pore size. The $SiO_2$ content and $V_P$ not only show a strong negative correlation (**Figure 6.2**b and l), but are also very similar in relative effect strengths but with opposing effect directions. With normalized factor strengths for the ammonia concentration of B = + 0.27 and B = – 0.26 and an $A^2$ = – 0.88 and $A^2$ = + 0.71 for $SiO_2$ content and $V_P$, respectively, the $V_P$ declines gradually with SNP deposition inside the porous template. The deposition of SNPs thus takes place inside the porous network of the template within the observed experimental space, except for **HB4** and **HB8**, where non-

porous secondary particles were formed. Here, a critical factor level combination of A = 60 and B = 45.6 mmol·L$^{-1}$ was exceeded.

In contrast to the $V_P$, the SSA shows a non-linear dependence on the ammonia concentration. The effect strength of ammonia is nearly twice as strong, but the decline in SSA with increasing ammonia concentration levels off. This results from the deposition of SNPs at the outer surface of the template, which leads to a rougher surface texture of the HBs and an increase in the available particle surface (**Figure 6.3**g and **Figure 6.4**b). This counterbalances the steep decline in SSA due to the closure of pores which prevents the accessibility of the inner pore walls even for small molecules like nitrogen.

For all models the linear A term is coupled to a non-linear $A^2$ in opposing effect direction. This means that the ratio of n($H_2O$)/n(TEOS) always has a non-linear component which leads to the diminishing of the overall influence with increasing ratios of water to precursor n($H_2O$)/n(TEOS). Non-linear behavior of the water to TEOS ratio has already been discussed regarding the size of the SNPs by other groups and was summarized by Bourebab et al.[103], who report a maximum size of the SNPs occurring between 10–35 wt% water. In the present study, the maximum size of the SNP was at an approximate water content of 20 wt%, which corresponds to a n($H_2O$)/n(TEOS) ratio of 60. When this critical level was exceeded, a comparatively smaller increase in SNP size with increasing water content was found, which is reflected by the statistically significant $A^2$ term. Here, with the factor level combination used as the starting conditions in the synthesis of **HB4** and **HB8** (**Figure 6.4**b and **Figure A. 6.3**) the formation of secondary particles in the continuous phase was observed. As the hydrolysis and condensation rate increases with the increase of n($H_2O$)/n(TEOS), and simultaneously elevated levels of ammonia, the fast-growing SNPs become too large to penetrate into the pores of the template.

Since all HB particles which result from the combinations of factor level settings according to the FCD were prepared at a pH between 10.5 and 11.0, the amino groups of the TEPA functionalization are still partly protonated and thus the template carries a positive surface charge[119]. At the same time, the surface near silanol groups of the SNPs, which are produced in the continuous phase, are deprotonated and form negatively charged –Si-O$^-$ functions. Small SNPs have a higher surface-to-volume ratio than larger ones and, thus a higher silanol concentration[134]. This results in a high negative charge-to-volume ratio coupled to increased mobility for small SNPs[200]. As a consequence of the strong electrostatic attraction of the negatively charged SNPs with the positively charged amino-functionalized polymer surface, SNPs are readily incorporated into the porous network of the **p@TEPA** template. The **p@TEPA** template acts like a filter which removes small SNPs permanently from the reaction medium and

withdraws them from reaction equilibria and thus prevents further growth. Therefore, as long as the rate of diffusion of SNPs into the porous template exceeds the rate of particle growth they cannot grow beyond a certain size on the outside, despite sufficient monomer being available. This is the case at low n($H_2O$)/n(TEOS) ratios. On the other hand, monomer and other hydrolyzed silanol species do not diffuse into the template as they rapidly undergo hydrolysis and condensation reactions in the continuous phase. Inside the porous network of the template, the small silica particles adsorb onto the positively charged pore walls, agglomerate and form uniform layers on the pore walls.

By the systematic variation of the critical process factors within our experimental design space, HBs with different morphological characteristics were produced, the formation of which can be assigned to three reaction regimes depending on the sol-gel starting conditions (**Figure 6.7**). At low water to TEOS ratios, hydrolysis is slow. Small SNPs formed are readily attracted by the template and completely deposited inside the pores of **p@TEPA**. Thus, few silica particles are formed which attach to the pore walls on the inside of the template (**HB1, 3, 7, 14–16**) (Regime I, **Figure 6.7**a). If the water ratio is increased (**HBs 2, 9, 10** and **CPs**) and the rate of hydrolysis is accelerated[92], the amount of silica deposition is increased. Those particles which are deposited on the outer surface of the template are still in contact with the reaction medium and continue to grow by monomer addition (Region II, **Figure 6.7**b).

The particle growth is further promoted by increasing the ammonia concentration[88]. This behavior affects the size of SNP on the outer surface of the HBs and the HB pore size median (**Figure 6.2**n – p and d – f). Furthermore, more SNPs are deposited in the pores on the inside of the HBs resulting in thicker silica layers covering the pore walls.

If hydrolysis and condensation rates are increased to an extent at which they exceed the diffusion of the SNPs into the **p@TEPA** pores, SNPs remain in the reaction medium. There they undergo further growth and form nonporous secondary particles (Region III **Figure 6.7**c). This is the case for n($H_2O$)/n(TEOS) ≥ 60 combined with a c($NH_3$) of 45.6 mmol·$L^{-1}$ or higher (**HB4** and **8**, see **Figure A. 6.3**).

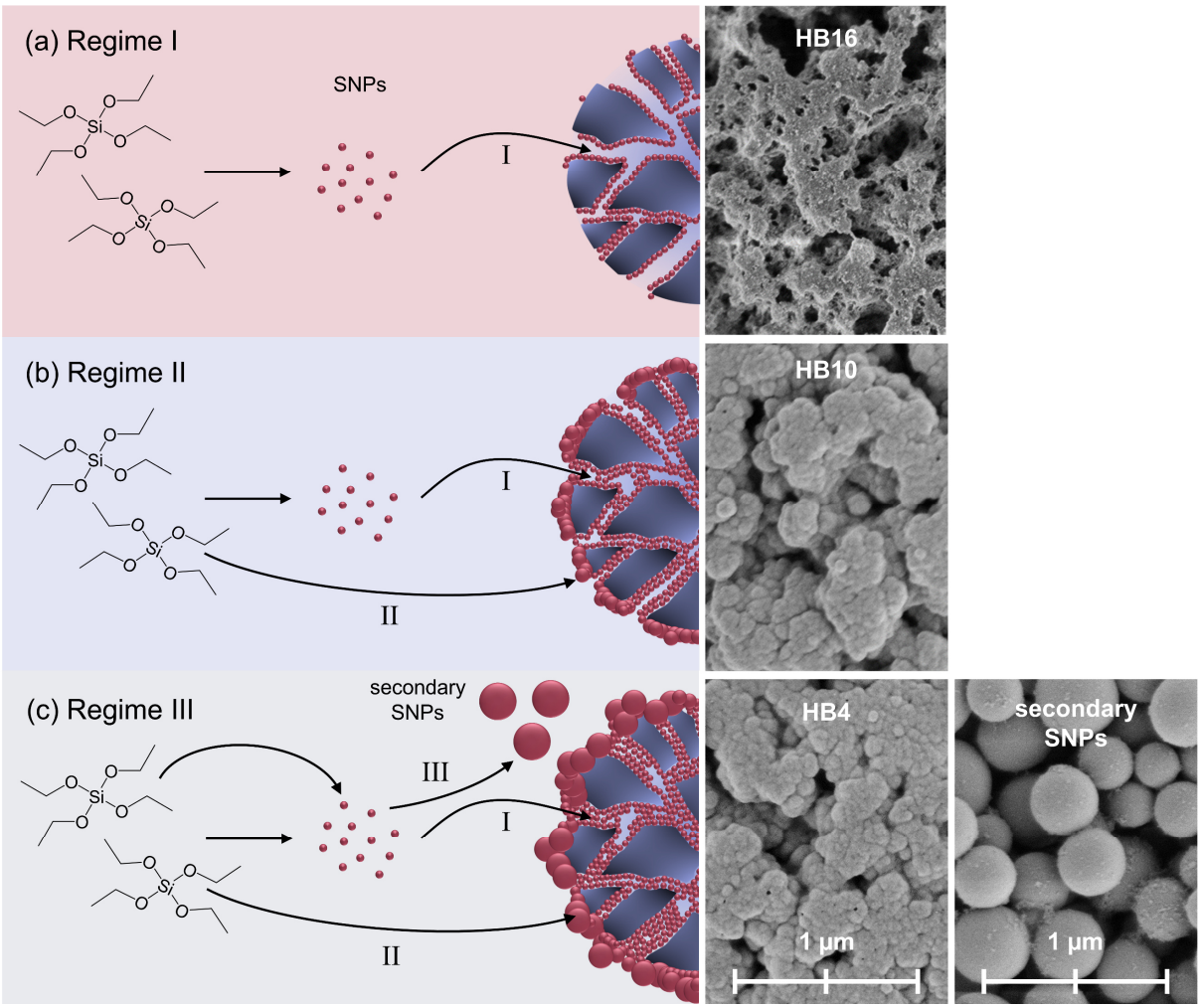


**Figure 6.7 a)** Regime I correspond to relatively low water values, **b)** Regime II to medium and **c)** Regime III to high water to precursor ratios. Exemplarily, the regions are derived from the particles **HB16**, **HB10** and **HB4**, respectively. It shows the diffusion of SNPs, after exceeding supersaturation concentration, into the template. There they aggregate in absence of monomer (I). As the hydrolysis is accelerated (Regime II) which deposit in the pores (I) and on the HB surface, where they undergo both, aggregation of SNPs and monomer addition as they are in contact with the reaction medium (II). In Regime III, with highest hydrolysis/condensation rate, SNPs additionally undergo monomer addition (III) in the continuous phase forming secondary particles, which are not attached to the HB.

## 6.4. Materials and methods

### 6.4.1. Chemicals

Ammonia solution (28–30 %), benzoyl peroxide (BPO, 75 %), dibutyl phthalate (DBP, 99%), glycidyl methacrylate (GMA, ≥ 97 %), tetraethyl orthosilicate (TEOS) and toluene (anhydrous 99.8 %) were purchased from Sigma-Aldrich Chemie GmbH (Traufkirchen Germany). Polyvinyl alcohol (PVA, hydrolyzed 86–89 %) was supplied from abcr GmbH (Karlsruhe, Germany). Cyclohexanol (99 %), ethylene glycole dimethacrylate (EDMA, 98%), HPLC grade water and tetraethylene pentamine (TEPA) were purchased from Fisher Scientific GmbH (Schwerte, Germany). Sodium dodecyl sulfate

(SDS, ≥ 99 %) and 2-propanol (HPLC grade > 99.8 %) were purchased from Carl Roth GmbH + Co. KG (Karlsruhe, Germany). All chemicals were used as received.

### 6.4.2. Preparation of HBs

The hybrid microspheres were synthesized using a polymeric hard template. The porous *p*(GMA-*co*-EDMA) particles were synthesized according to the procedure described previously[1] with scale up. Further information is given in the Appendix 6.6.1. The HBs were synthesized under basic hydrolysis-condensation conditions. The ammonia concentration and the molar ratio of n($H_2O$)/n(TEOS) was systematically changed according to a face-centered central composite design (FCD) to assess the synthesis parameter effects on HB particle morphology, surface and pore characteristics, as well as silica deposition behavior. The range of process factor levels is given in **Table 6.4**.

**Table 6.4** Range of process factor level settings as used in the face-centered central composite experimental design (FCD).

| Factor | Name | Low setting (-) | Center Point (0) | High setting (+) |
|---|---|---|---|---|
| **A** | n($H_2O$)/n(TEOS) | 4 | 39 | 74 |
| **B** | c($NH_3$) /mmol·$L^{-1}$ | 2.39 | 6.38 | 10.37 |

The absolute amount of TEOS was the same for all particle syntheses. Depending on the molar ratio of n($H_2O$)/n(TEOS), the amount of additional water was calculated and varied accordingly. The water content of the $NH_4OH$ solution was included in these calculations. A total volume of 140 mL was used and the volume of the reaction mixtures was adjusted using 2-propanol. The changes in 2-propanol volume were < 8 %. Generally, 2 g of the p@TEPA particles were dispersed in a 2-propanol/$H_2O$ mixture and sonicated for 5 minutes. Then the $NH_4OH$ solution was added as the basic catalyst under stirring, followed by the addition of 21.5 mmol TEOS. The mixture was stirred with 550 rpm for 24 h at room temperature. The HBs were filtered off and washed three times with ethanol and water. The particles were then dried at room temperature prior to analysis.

### 6.4.3. Nitrogen adsorption measurements

For the determination of specific surface area, pore size and pore volume the BELSORP MiniX (Microtrac Retsch GmbH, Haan, Germany) was used for nitrogen adsorption measurements. The sample mass was ~ 150 mg (145±14 mg) except for samples with very small surface area which were measured with an increased sample amount of ~ 300 mg (**HB4** with 291 mg and **HB8** with 290 mg). All samples were degassed at 30 °C

for 24 h up to a final vacuum of about $2 \cdot 10^{-2}$ mbar, to eliminate possible physisorbed substances and to achieve a reproducible intermediate state[67]. The samples were evacuated using the BELSORP VACII (Microtrac Retsch GmbH, Haan, Germany). The $N_2$-adsorption and desorption measurements were performed at 77 K. The analysis of adsorption and desorption isotherms was performed using the BELMaster 7 software (7.3.2.0, Microtrac Retsch GmbH, Haan, Germany). Specific surface area was analyzed according to the Brunauer-Emmet-Teller method (BET)[66,201]. For this, the relative pressure range of $p/p_0$ 0.05–0.3 was used[65]. The pore size distribution was determined using Barrett-Joyner-Halenda (BJH) method from the desorption branch using the Harkins-Jura standard isotherm. The pore size diameters were analyzed in the range from 2 to 500 nm. The pore volume was determined from a single adsorption point at $p/p_0$ of 0.95.

### 6.4.4. Scanning electron microscopy images (SEM)

SEM images were acquired using a Hitachi SU8030 (Hitachi High-Tech Europe GmbH, Germany) to assess surface morphology, particle size and dispersity. A self-written MATLAB script was used to semi-automatically measure the size and dispersity from the SEM images. At least 120 particles were measured. The dispersity is given by the $d_{90}/d_{10}$ value which indicates the width of the particle size distribution. Here, $d_{90}$ is the value below which 90 % of the measured values of the particle sizes lie. $d_{10}$ is the value below which 10 % of the measured particle sizes lie. A $d_{90}/d_{10}$ value smaller than 1.4 was considered as a monodisperse distribution.

### 6.4.5. Thermogravimetric (TGA) determination of $SiO_2$ content

The amount of deposited $SiO_2$ content was determined using thermogravimetric analysis (TGA) using the TGA/DSC I from Mettler Toledo. Portions of 119.9–121.4 mg (125.8±3.1mg) sample were weighed into a 900 µL alumina crucible and thermal analysis was performed under synthetic air (50 $mL \cdot min^{-1}$). A heating rate of 5 $K \cdot min^{-1}$ in a temperature range from 30 to 800 °C was performed. The relative mass of the remaining residue is the proportion of $SiO_2$ to the mass of the hybrid material.

### 6.4.6. Experimental design

The mathematical description of linear, non-linear and interaction effect terms[164,165] was done by systematic analysis based on a FCD. 16 HB particle batches were synthesized with five center point (CP) replications to determine reproducibility and system variance. Three additional syntheses were conducted with $n(H_2O)/n(TEOS) = 8$ to support model stability in the critical model region with low molar ratios. The effects of two factors and their possible synergistic interactions, $c(NH_3)$ and $n(H_2O)/n(TEOS)$,

were investigated by systematic variations of the factor level settings according to the FCD response surface design. The factor levels for low, intermediate and high settings are given in **Table 6.4**. The model effect terms were analyzed using analysis of variance (ANOVA). A model or model term was considered statistically significant when its p-value was $p \leq 0.05$. For model conceptualization and analysis, the Design Expert DX12 (Version 12.0.12.0, Stat-Ease Inc., Minneapolis, USA) software package was used.

## 6.5. Conclusion

The process factors $n(H_2O)/n(TEOS)$ and $c(NH_3)$ specifically control the silica deposition on the inside and the outside of the **p@TEPA** template. Three discrete process regimes were identified. At low water conditions, only pores < 5 nm are filled with deposited silica to some extent. At medium to high water to precursor ratios, pores < 5 nm are almost completely filled with silica and the pore volume of pores > 5 nm decreases uniformly. This suggests the formation of a uniform silica layer inside the porous template network through primary particle adsorption at the pore walls and aggregation within the porous network of the template. The present work demonstrates under which conditions the pores are closed in which way and presents a mechanistic proposal for the construction for a silica network in a porous organic template. This allows access to new tailor-made hybrid materials with different properties. Specific hybrid materials can be created in which the organic template is coated with a thin silica layer, e.g. to protect the organic matter. These silica layers covering the pore walls can be further build up until the pores are filled with silica.

Furthermore, extending the presented experimental space towards even higher ammonia and water concentrations and thus higher rate of hydrolysis and condensation, the formation of large SNPs exceeds the rate of diffusion which hinders the incorporation of SNPs into the porous network of the template. This leads to the formation of particles with a porous organic core protected by a silica shell.

## 6.6. Appendix

### 6.6.1. Preparation of amino-functionalized porous polymer template

0.9 g monodisperse polystyrene seeds (1.95 µm, of $d_{90}/d_{10}$ = 1.09) were sonicated for 10 minutes in 15 mL of a 2.0 $g \cdot L^{-1}$ SDS solution. An emulsion of 6.0 mL DBP and 450 mL of a 2.53 $g \cdot L^{-1}$ SDS solution (10 minutes at 5000 rpm) was added to the seed particle suspension. The suspension was stirred for 24 h at 200 rpm at room temperature.

450 mL of SDS (3.33 $g \cdot L^{-1}$), the initiator BPO (1.2 g), 22.5 mL of each cyclohexanol, EDMA, GMA and toluene were homogenized for 10 minutes at 5000 rpm. The emulsion was added and the system stirred at 200 rpm for another 24 h. 450 mL of a PVA solution (23.3 $g \cdot L^{-1}$) was added to the mixture as stabilizer. The reaction mixture was stirred at 200 rpm for 24 h at 70 °C for polymerization. Thereafter the porous *p*(GMA-*co*-EDMA) particles were washed three times with ethanol and three times with water.

For amino functionalization 35 g of dried *p*(GMA-*co*-EDMA) particles were suspended in 1400 mL deionized water and sonicated for 15 min. Then 0.256 mol of TEPA were added dropwise under stirring (200 rpm). After addition the mixture was heated to 80 °C for 24 h. The functionalized particles were filtered off and washed three times with ethanol and water. The particles will be further referred to as **p@TEPA**.

### 6.6.2. Supplementary SEM images

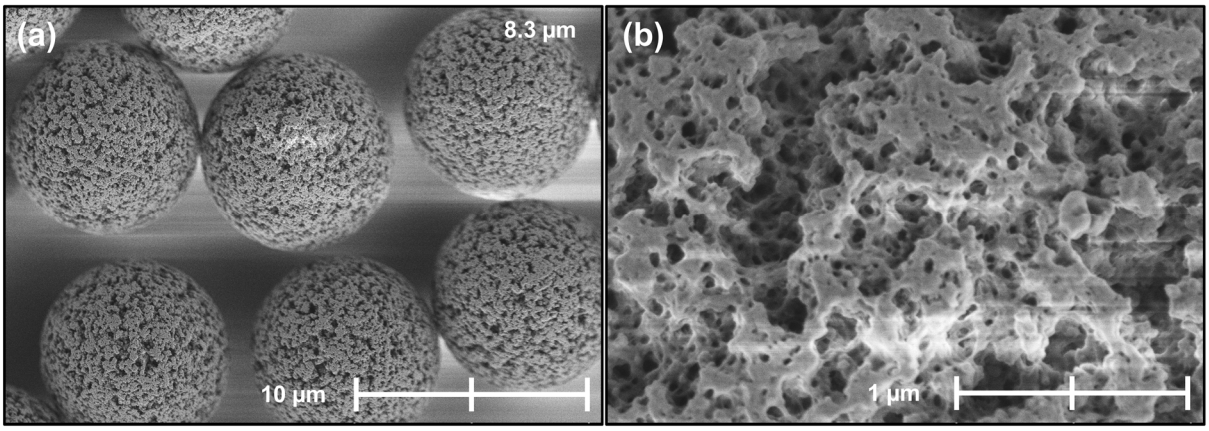


**Figure A. 6.1** SEM image of *p*(GMA-*co*-EDMA) template batch at **a)** 5,000× and **b)** 50,000× magnification. Particle size: 8.3 µm, $d_{90}/d_{10}$: 1.04, SSA: 63.79 $m^2 \cdot g^{-1}$, $V_P$: 0.12 $cm^3 \cdot g^{-1}$, $\phi_{50}$: 14.47 nm.

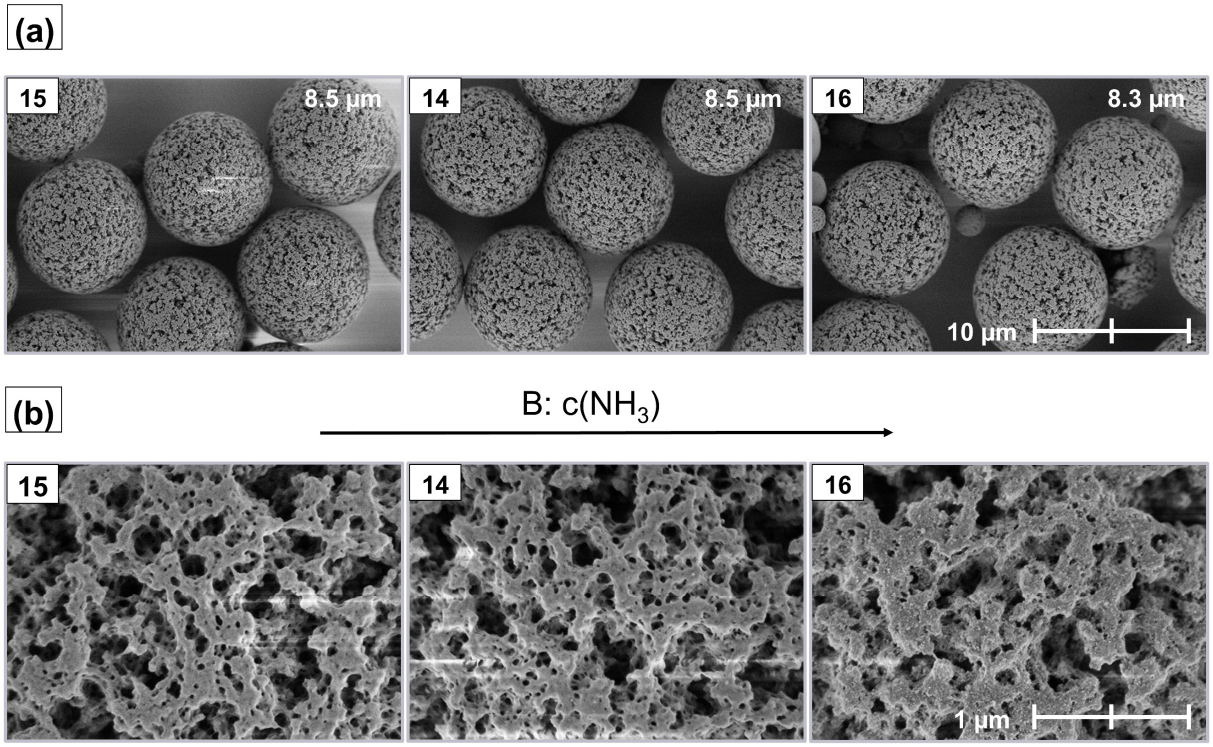


**Figure A. 6.2** SEM image of additional samples **HB14–16** with n($H_2O$)/n(TEOS) = 8 sorted by increasing c($NH_3$) (l.t.r.) at **a)** 5,000× and **b)** 50,000× magnification.

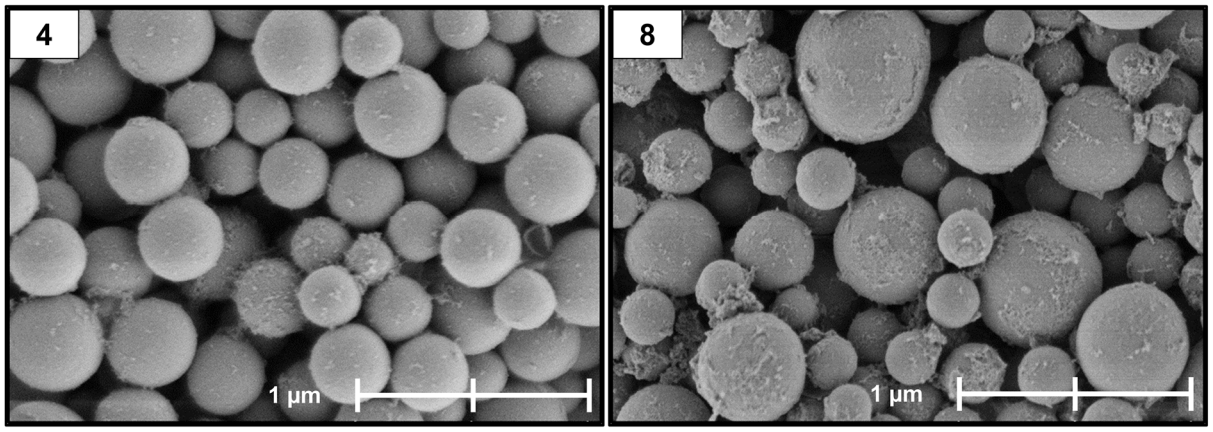


**Figure A. 6.3** SEM image of filtrates with secondary particles of **HB4** and **HB8** at 50,000× magnification.

### 6.6.3. ANOVA Tables for the RSMs

**Table S. 6.1** Analysis of variance (ANOVA) for the analysis of FCD design of the median particle size.

| Source | Sum of Squares | df | Mean Square | F-value | p-value | |
|---|---|---|---|---|---|---|
| Model | 0.0561 | 1 | 0.0561 | 7.45 | 0.0172 | significant |
| A – n($H_2O$)/n(TEOS) | 0.0561 | 1 | 0.0561 | 7.45 | 0.0172 | |
| Residual | 0.0980 | 13 | 0.0075 | | | |
| Lack of Fit | 0.0943 | 9 | 0.0105 | 11.26 | 0.0163 | significant |
| Pure Error | 0.0037 | 4 | 0.0009 | | | |
| Cor Total | 0.1541 | 14 | | | | |

**Table S. 6.2** Analysis of variance (ANOVA) for the analysis of FCD design of $SiO_2$ content.

| Source | Sum of Squares | df | Mean Square | F-value | p-value | |
|---|---|---|---|---|---|---|
| Model | 2187.31 | 3 | 729.10 | 162.91 | < 0.0001 | significant |
| A – n($H_2O$)/n(TEOS) | 1381.35 | 1 | 1381.35 | 308.65 | < 0.0001 | |
| B – c($NH_3$) | 86.00 | 1 | 86.00 | 19.21 | 0.0011 | |
| $A^2$ | 432.20 | 1 | 432.20 | 96.57 | < 0.0001 | |
| Residual | 49.23 | 11 | 4.48 | | | |
| Lack of Fit | 39.41 | 7 | 5.63 | 2.29 | 0.2204 | not significant |
| Pure Error | 9.82 | 4 | 2.45 | | | |
| Cor Total | 2236.54 | 14 | | | | |

**Table S. 6.3** Analysis of variance (ANOVA) for the analysis of FCD design of the median pore size $\phi_{50}$.

| Source | Sum of Squares | df | Mean Square | F-value | p-value | |
|---|---|---|---|---|---|---|
| Model | 38.43 | 4 | 9.61 | 12.20 | 0.0007 | significant |
| A – n($H_2O$)/n(TEOS) | 7.93 | 1 | 7.93 | 10.07 | 0.0099 | |
| B – c($NH_3$) | 10.03 | 1 | 10.03 | 12.74 | 0.0051 | |
| AB | 8.81 | 1 | 8.81 | 11.19 | 0.0074 | |
| $A^2$ | 10.08 | 1 | 10.08 | 12.79 | 0.0050 | |
| Residual | 7.88 | 10 | 0.7879 | | | |
| Lack of Fit | 4.84 | 6 | 0.8074 | 1.06 | 0.4990 | not significant |
| Pure Error | 3.03 | 4 | 0.7586 | | | |
| Cor Total | 46.31 | 14 | | | | |

**Table S. 6.4** Analysis of variance (ANOVA) for the analysis of FCD design of the SSA.

| Source | Sum of Squares | df | Mean Square | F-value | p-value | |
|---|---|---|---|---|---|---|
| Model | 7539.12 | 4 | 1884.78 | 153.80 | < 0.0001 | significant |
| A – n($H_2O$)/n(TEOS) | 3882.36 | 1 | 3882.36 | 316.80 | < 0.0001 | |
| B – c($NH_3$) | 681.83 | 1 | 681.83 | 55.64 | < 0.0001 | |
| $A^2$ | 989.61 | 1 | 989.61 | 80.75 | < 0.0001 | |
| $B^2$ | 106.41 | 1 | 106.41 | 8.68 | 0.0146 | |
| Residual | 122.55 | 10 | 12.25 | | | |
| Lack of Fit | 79.47 | 6 | 13.25 | 1.23 | 0.4397 | not significant |
| Pure Error | 43.08 | 4 | 10.77 | | | |
| Cor Total | 7661.67 | 14 | | | | |

**Table S. 6.5** Analysis of variance (ANOVA) for the analysis of FCD design of the $V_p$.

| Source | Sum of Squares | df | Mean Square | F-value | p-value | |
|---|---|---|---|---|---|---|
| Model | 0.0249 | 3 | 0.0083 | 179.66 | < 0.0001 | significant |
| A – n($H_2O$)/n(TEOS) | 0.0174 | 1 | 0.0174 | 375.80 | < 0.0001 | |
| B – c($NH_3$) | 0.0010 | 1 | 0.0010 | 21.98 | 0.0007 | |
| $A^2$ | 0.0036 | 1 | 0.0036 | 76.88 | < 0.0001 | |
| Residual | 0.0005 | 11 | 0.0000 | | | |
| Lack of Fit | 0.0001 | 7 | 0.0000 | 0.2028 | 0.9670 | not significant |
| Pure Error | 0.0004 | 4 | 0.0001 | | | |
| Cor Total | 0.0254 | 14 | | | | |

**Table S. 6.6** Analysis of variance (ANOVA) for the analysis of FCD design of the SNP size.

| Source | Sum of Squares | df | Mean Square | F-value | p-value | |
|---|---|---|---|---|---|---|
| Model | 6865.92 | 4 | 1716.48 | 52.49 | < 0.0001 | significant |
| A – n($H_2O$)/n(TEOS) | 3797.04 | 1 | 3797.04 | 116.11 | < 0.0001 | |
| B – c($NH_3$) | 1346.92 | 1 | 1346.92 | 41.19 | < 0.0001 | |
| AB | 517.00 | 1 | 517.00 | 15.81 | 0.0026 | |
| $A^2$ | 699.79 | 1 | 699.79 | 21.40 | 0.0009 | |
| Residual | 327.01 | 10 | 32.70 | | | |
| Lack of Fit | 179.01 | 6 | 29.84 | 0.8064 | 0.6132 | not significant |
| Pure Error | 148.00 | 4 | 37.00 | | | |
| Cor Total | 7192.93 | 14 | | | | |

**Author Contributions:** Conceptualization, A.K. and H.A.M.; methodology, J.C.S., F.F., H.A.M. and A.K.; validation, J.C.S. and F.F.; formal analysis, J.C.S.; investigation, J.C.S. and F.F.; resources, H.A.M. and A.K.; data curation, J.C.S.; writing—original draft preparation, J.C.S.; writing—review and editing, F.F., H.A.M. and A.K.; visualization, J.C.S.; supervision, H.A.M. and A.K.; project administration, H.A.M. and A.K.; funding acquisition, A.K. All authors have read and agreed to the published version of the manuscript.

**Funding:** This research was funded by Bundesministerium für Bildung und Forschung (BMBF), grant number 13FH647IX6. The article processing charge was funded by the Baden-Württemberg Ministry of Science, Research and Arts and by Reutlingen University in the funding program Open Access Publishing.

**Supplementary Materials:** Not applicable.
**Institutional Review Board Statement:** Not applicable.
**Informed Consent Statement:** Not applicable.

**Data Availability Statement:** The data presented in this study are available within this article or are available from the authors upon request.

**Acknowledgments:** We thank Elke Nadler for contributing the SEM measurements. We also thank Leon Rösch for the experimental support.

**Conflicts of Interest:** The authors declare no conflict of interest. The funders had no role in the design of the study; in the collection, analyses or interpretation of the data; in the writing of the manuscript; or in the decision to publish the results.

# 7. Paper IV

## Sol-Gel-Controlled Size and Morphology of Mesoporous Silica Microspheres Using Hard Templates

Julia C. Steinbach [1,2], Fabio Fait [1,2], Hermann A. Mayer[2] and Andreas Kandelbauer [1,3,*]

[1] Process Analysis & Technology, Reutlingen Research Institute, Reutlingen University, Alteburgstraße 150, 72762 Reutlingen, Germany; julia.steinbach@reutlingen-university.de (J.C.S.); fabio.fait@reutlingen-university.de (F.F.)

[2] Institute of Inorganic Chemistry, University of Tübingen, Auf der Morgenstelle 18, 72076 Tübingen, Germany; hermann.mayer@uni-tuebingen.de (H.A.M.)

[3] Institute of Wood Technology and Renewable Materials, Department of Material Sciences and Process Engineering (MAP), University of Natural Resources and Life Sciences, Gregor-Mendel-Straße 33, 1180 Vienna, Austria

* Correspondence: andreas.kandelbauer@reutlingen-university.de; Tel.: +49-(0)7121-271-2009

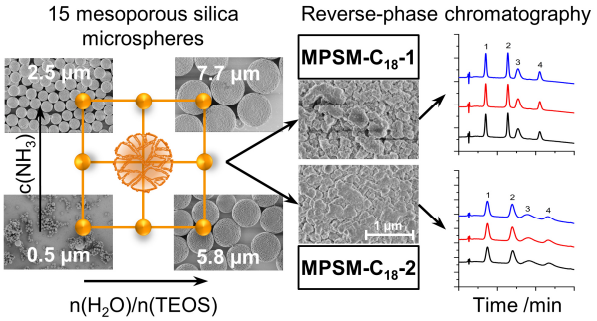




Steinbach, J.C.; Fait, F.; Mayer, H.A.; Kandelbauer, A. Sol-Gel-Controlled Size and Morphology of Mesoporous Silica Microspheres Using Hard Templates. *ACS Omega* **2023**, *8*, 30273–30284, doi:10.1021/acsomega.3c03098.[4]

**Abstract**

Mesoporous silica microspheres (MPSMs) represent a promising material as a stationary phase for HPLC separations. The use of hard templates provides a preparation strategy for producing such monodisperse silica microspheres. Here, 15 MPSMs were systematically synthesized by varying the sol-gel reaction parameters of water-to-precursor ratio and ammonia concentration in presence of a porous *p*(GMA-*co*-EDMA) polymeric hard template. Changing the sol-gel process factors resulted in a wide range of MPSMs with varying particle sizes from smaller than one to several micrometers. The application of response surface methodology allowed to derive quantitative predictive models based on the process factor effects on particle size, pore size, pore volume, and specific surface area of the MPSMs. A narrow size distribution of the silica particles was maintained over the entire experimental space. Two larger-scale batches of MPSMs were prepared and the particles were functionalized with trimethoxy (octadecyl) silane for the application as stationary phase in reversed-phases liquid chromatography. The separation of proteins and amino acids was successfully accomplished, and the effect of the pore properties of the silica particles on separation was demonstrated.

**Keywords**

mesoporous silica microspheres (MPSM), sol-gel, hard template, High performance liquid chromatography (HPLC), response surface methodology (RSM)

## 7.1. Introduction

Porous silica particles are relevant in catalysis[17], in biosensors[18,19], as drug carriers[14–16], and as column material in purification and separation via chromatography[20–22]. To fit the requirements of a particular application, the control of particle size, size distribution, morphology, specific surface area and pore parameters of these silica particles is of great importance. For instance, in drug delivery, silica particles as drug carriers require a size of < 5 μm to be able to penetrate through the skin and release the drug in the tissue. Larger particles remain on the surface of the skin, where they may form a protective layer, as known from e.g. sunscreen[202]. For high performance liquid chromatography (HPLC) applications, silica-based packing materials are very common. The properties of the stationary phase dictate to a large extent the separation efficiency for various separation operations. The specific surface area is important for the column performance in many separation processes and chromatographic applications, as it affects the number of contact events available for interaction between analyte and stationary phase and, thus, retention time. As smaller particles have a higher surface to volume ratio, particles with small average diameters are preferably used as column

packing materials to increase the available interaction surface[37]. However, smaller particles also result in higher backpressures within the system and thus higher requirements are imposed on the equipment in terms of pressure resistance and some analytes, cannot be measured non-destructively under such conditions[23,37,203]. One way to increase the surface area without decreasing the particle size is the incorporation of pores into the particles. The introduction of meso-/macropores allows a good effective accessibility of the porous material for diffusion controlled processes[49]. Templating methods have been widely applied to prepare porous silica materials with tunable size and pore characteristics[47,50,52,204]. While soft templates are successfully used to prepare nanometer sized silica particles[47,52,54], hard templates are the choice to synthesize micron sized mesoporous silica spheres (MPSMs)[22,55]. This is because hard templates such as *poly*(glycidyl methacrylate-*co*-ethylene glycol dimethacrylate) particles (*p*(GMA-*co*-EDMA))[1,2,22,55,56,119] are usually formative, i.e. determining the three-dimensional morphology[47,51,52]. Template-assisted methods for the preparation of MPSMs consist usually of three sequential steps[46,48,117]: a) synthesis of the formative template[1,2] b) synthesis and/or incorporation of silica into the template[2,3] c) subsequent removal of the template[120,205] (**Figure 7.1**).

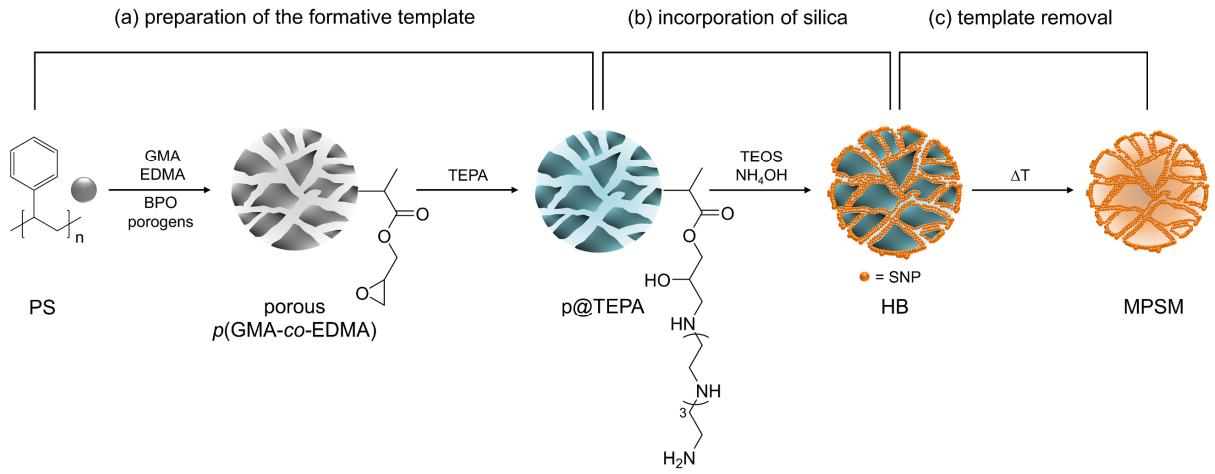


**Figure 7.1** Reaction scheme for the preparation of MPSMs by a hard-template method used in this study.

The sol-gel process is particularly suitable because of its mild reaction conditions. Here in the presence of the template *in situ* generated silica nanoparticles (SNPs) diffuse into the pores of the template and build up the silica network. Thus, tailored MPSMs with narrow size distributions and defined particle sizes are formed after removal of the sacrificial porous polymer template by calcination[45,196]. The main advantage of this approach is that the template determines the shape of the resulting MPSM, which allows the generation of spherical particles with narrow size distribution. Earlier work suggests[22,47,55,57] that the way silica is deposited in the pores of the template has a large impact on the characteristics of the final MPSMs.

Our previous study[3] determined how the sol-gel process factors water-to-precursor ratio (here: tetraethyl ortho silicate, TEOS) and the ammonia concentration affects the silica deposition within the porous network of polymeric hard-templates[1]. By systematically varying the sol-gel process conditions according to response surface methodology, three reaction regimes were identified[3]. These regimes result from changes in the relative reaction rates of hydrolysis and condensation depending on the sol-gel process factors, as well as the diffusion rate of *in situ* generated SNPs into the polymer pore network. The polymer templates are either just coated with a thin silica layer (regime I), the pores of the polymer template are almost completely filled with silica (regime II) or the formation of silica nanoparticles exceeds the diffusion rate of SNPs into the polymer pores and thus results in the additional formation of secondary nonporous SNPs in the continuous phase outside of the template[3]. The prepared hybrid materials are the intermediate step of the preparation of porous silica particles before template removal (**Figure 7.1**b).

The present study focuses on the removal of the sacrificial organic polymer template via calcination, which is the third step of the template-assisted approach (**Figure 7.1**c). The effects of the sol-gel process factors n($H_2O$)/n(TEOS) and c($NH_3$) and their potential synergistic interaction effects on particle size, size distribution, morphology and porosity were systematically examined using the approach of response surface methodology[59–62]. By this, quantitative models are established that allow the correlation and prediction of the effects of the sol-gel process factors on the material properties of MPSMs prepared using the hard-template assisted preparation method. Furthermore, two larger-scale batches of MPSMs were prepared, functionalized with trimethoxy (octadecyl) silane and were used as reversed-phased column packing material for the separation of proteins and amino acids.

## 7.2. Materials and methods

### 7.2.1. Chemicals

Polyvinyl alcohol (PVA, hydrolyzed 86–89 %) and trimethoxy (octadecyl) silane were purchased from abcr GmbH (Karlsruhe, Germany). Sodium dodecyl sulfate (SDS ≥ 99 %) and 2-propanol (HPLC grade > 99.8 %) were obtained from Carl Roth GmbH + Co. KG (Karlsruhe, Germany). Ammonia solution (28–30 %), benzoyl peroxide (BPO, 75 %), dibutyl phthalate (DBP, 99 %), ethanol, glycidyl methacrylate (GMA ≥ 97 %), hydrochloric acid (37 %), methanol, tetraethyl orthosilicate (TEOS), toluene (anhydrous 99.8 %), triethylamine (pure) and the protein test mixture H2899 were bought from Sigma-Aldrich Chemie GmbH (Traufkirchen Germany). Acetonitrile (ACN, HPLC grade), cyclohexanol (99 %), ethylene glycole dimethacrylate (EDMA, 98 %),

HPLC grade water and tetraethylene pentamine (TEPA) were purchased from Fisher Scientific GmbH (Schwerte, Germany). All chemicals were used as received. Ortho-phthalaldehyde (OPA) reagent for pre-column derivatization of the amino acids was provided by Dr. Maisch HPLC, Germany.

### 7.2.2. Preparation of MPSMs

The MPSMs were prepared using a hard-templating method with a multi-step synthesis sequence schematically shown in **Figure 7.1**. A porous *p*(GMA-*co*-EDMA) template was prepared by a seed swelling-polymerization with polystyrene particles as seeds[1] and subsequently amino-functionalized with TEPA (see supplementary information S. I.).

The method for preparation of organic/silica hybrid beads (HBs) **HB1–15** has been extensively reported on earlier[3] and is therefore only briefly summarized here. The sol-gel process was conducted under basic conditions with varying water to precursor ratios ($n(H_2O)/n(TEOS)$) and ammonia concentrations ($c(NH_3)$) in presence of the p@TEPA particles as template to generate the hybrid beads **HB1–15**.

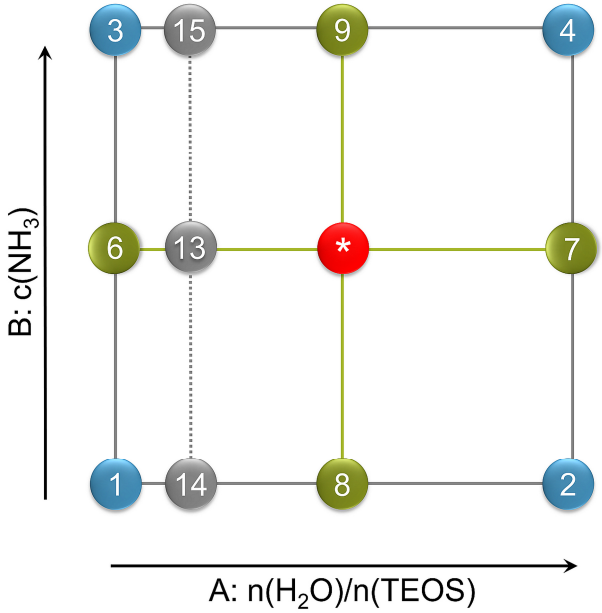


**Figure 7.2** Illustration of the face centered central composite design. The numbers correspond to the sample numbers given in Table 2. Factorial points are displayed in blue, axial in points green, additional points in grey and the CPs in red.

The ammonia concentration and the molar ratio of $n(H_2O)/n(TEOS)$ were systematically changed according to a face-centered central composite design (FCD) (**Figure 7.2**). The range within which the of process factor levels are varied is given in **Table 7.1**. All experiments were performed in random order. The pH values were determined after 24 h of stirring for each synthesis (**Table S. 7.1**, S.I.)

**Table 7.1** Range of process factors level setting as used in the face-centered central composite experimental design (FCD)

| Factor | Name | Low setting (-) | Center Point (0) | High setting (+) |
|---|---|---|---|---|
| **A** | $n(H_2O)/n(TEOS)$ | 4 | 39 | 74 |
| **B** | $c(NH_3)$ /mmol·L$^{-1}$ | 2.39 | 6.38 | 10.37 |

The sacrificial polymer templates of the HBs were removed by calcination under synthetic air flow (50 mL·min$^{-1}$) at 600 °C for 10 h (heating rate 200 K·h$^{-1}$) to give the **MPSM1–15** (**Table 7.2**).

### 7.2.3. Preparation of reversed-phase HPLC column materials

For the preparation of trimethoxy (octadecyl) silane ($C_{18}$) functionalized MPSMs as HPLC column packing material, an additional batch of porous polymer template was prepared and TEPA functionalized. Two different sol-gel process factor level combinations within the FCD design space were used to generate two types of HB particles with significantly different pore parameters. The synthesis was scaled up by a factor of 3.75. The prepared HB materials were calcinated at 600 °C for 10 h under synthetic air flow to yield the MPSMs (heating rate of 200 K·h$^{-1}$).

3 g of MPSM were rehydroxylated with 360 mL 3.7 % HCl at 100 °C for 3 h under continuous stirring (mechanic stirrer, 300 rpm). After cooling to room temperature, the rehydroxylated MPSM were thoroughly washed three times with water and three times with ethanol. After drying the rehydroxylated MPSMs at 70 °C over night, they were $C_{18}$ functionalized with trimethoxy (octadecyl) silane.

3 g of rehydroxylated MPSM were dispersed in 45 mL toluene and 15 mL of trimethoxy (octadecyl) silane. As catalyst, 0.3 mL of triethylamine were added. The mixture was stirred at 100 °C for 6 h (300 rpm, magnetic stirrer) and washed three times with toluene, ethanol and methanol after cooling to room temperature. The MPSM-$C_{18}$ were then dried at 70 °C over night.

To test the MPSM-$C_{18}$ for their applicability as reversed HPLC phase, the particles were packed with acetone as slurry and MeOH / $H_2O$ (85 / 15 vol% / vol%) as a pressure medium into 4.0 x 250 mm stainless steel columns.

### 7.2.4. Nitrogen sorption measurements

BELSORP MiniX (Microtrac Retsch GmbH, Haan, Germany) for nitrogen sorption measurements was used for the determination of specific surface area, pore size and pore volume. The sample mass was 50 mg of the MPSMs. To eliminate possible physisorbed substances and to achieve a reproducible intermediate state all particles were vacuum degassed at 300 °C for 3 h under a final vacuum of about $2 \cdot 10^{-2}$ mbar[67] (p 96). The samples were pretreated using the BELSOPR VACII (Microtrac Retsch GmbH, Haan, Germany). The $N_2$ adsorption and desorption measurements were performed at 77 K. The BELMaster 7 software (7.3.2.0, Microtrac Retsch GmbH, Haan, Germany) was applied to perform the analysis of adsorption and desorption isotherms. Specific surface area was analyzed according to the Brunauer-Emmet-Teller method (BET)[66,201] in a relative pressure range of $p/p_0$ 0.05–0.30[65]. Using the Barret-Joyner-Helenda method (BJH) the pore size distribution was determined from the desorption branch using the Silica-BEL standard isotherm. The pore volume was determined from a single point adsorption at $p/p_0$ of 0.95.

### 7.2.5. Scanning electron microscopy images (SEM)

To assess surface morphology, particle size and dispersity SEM images were acquired using a Hitachi SU8030 (Hitachi High-Tech Europe GmbH, Germany). The size and dispersity from the SEM images were analyzed using a self-written MATLAB script. A minimum of 248 particles were measured. The $d_{90}/d_{10}$ value indicates the width of the particle size distribution. A monodisperse distribution is reflected by a $d_{90}/d_{10}$ value $\leq 1.4$[206].

### 7.2.6. Experimental design

The mathematical description of linear, non-linear and interaction effect terms[164,165] was enabled through systematic analysis using a face-centered central composite experimental design (FCD). A total of 15 MPSMs were synthesized. The center point (CP) experiment was replicated four times to determine reproducibility and system variance. To support model stability in the critical region of low molar ratios, three of the syntheses were conducted with $n(H_2O)/n(TEOS) = 8$. The systematic variation of the factor level setting allows the investigation of the effects of two factors and their possible synergistic interactions, $c(NH_3)$ and $n(H_2O)/n(TEOS)$. The factor levels for the low, intermediate and high settings are given in **Table 7.1**. The model effect terms were analyzed using analysis of variance (ANOVA). A model or model term was considered statistically significant if its p-value was $p \leq 0.05$.

### 7.2.7. HPLC analyses

The high performance liquid chromatography (HPLC) was performed on an Agilent 1100 series system (Agilent Technologies, Waldbronn, Germany). The setup included a degasser, quaternary pump, autosampler, column oven, diode array detector and a fluorescence detector. The detector was chosen according to the separation application. The OpenLAB CDS (Rev. C.01.07 SR3, Agilent Technologies, Waldbronn, Germany) was used for instrument control, data acquisition and automated data analysis.

For the protein separation, the protein mixture H2899 (ribonuclease A, cytochrome c, holo-transferrin and apomyoglobin) was dissolved in 90:10 eluent A ($H_2O$, 0.1 % TFA) and eluent B (acetonitrile, 0.08 % TFA). 5 µL of the sample (1 $mg \cdot L^{-1}$ of each protein) was injected and measured at 30 °C. A gradient elution was performed with 25 % B to 70 % B within 40 minutes with a flow of 1.0 $mL \cdot min^{-1}$. The detection wavelength was 215 nm.

The separation of eleven D/L-amino acids (asparagine, glutamic acid, glycine, arginine, alanine, tyrosine, valine, norvaline, tryptophan, iso-leucine and leucine) was performed by a linear gradient elution of phosphate buffer (25 mM, pH 7.2) with 0.75 vol% THF as eluent A and a mixture of methanol:acetonitrile:phosphate buffer (35/15/50 vol%) as eluent B. The gradient was 0 % B to 100 % B in 50 minutes with a flow of 1.0 $mL \cdot min^{-1}$. 20 µL sample (2.1 $\mu mol \cdot \mu L^{-1}$ of each amino acid) were injected and measured at 30 °C. Detection of the amino acids was performed through pre-column derivatization (90 s performed with the injector program) with OPA reagent with $\lambda_{excitation}$ = 330 nm and $\lambda_{emission}$ = 450 nm.

## 7.3. Results and discussion

The set of **HB1–15** particles which was prepared by variation of the sol-gel process conditions according to a statistical experimental design (Design of Experiment) in presence of a p@TEPA template forms the basis for the investigations discussed here (**Table 7.2**, **Figure 7.1**)[1]. The sacrificial template was removed by calcination and the final **MPSM1–15** were characterized by SEM and nitrogen adsorption measurements to determine their particle size, dispersity, specific surface area, pore diameter, and pore volume (**Table 7.2**).

**Table 7.2** Factor level settings and their corresponding particle properties particle size, dispersity ($d_{90}/d_{10}$), specific surface area (SSA), pore diameter (PD) and pore volume ($V_P$) (at $p/p_0 = 0.95$), as well as the silica content in the HBs.

| | Factor level settings | | Response variables | | | | | Material property |
|---|---|---|---|---|---|---|---|---|
| | **A** $n(H_2O)/n(TEOS)$ | **B** $n(NH_3)$ | **Particle size** | $\frac{d_{90}}{d_{10}}$ | **SSA** | **PD** | $V_P$ | $SiO_2$ **in HB** |
| | | /mmol·L$^{-1}$ | /µm | | /m$^2$·g$^{-1}$ | /nm | /cm$^3$·g$^{-1}$ | /wt% |
| **p@TEPA** | - | - | 8.3 | 1.04 | 63.8 | 8.6 | 0.12 | - |
| **MPSM1** | 4 | 17.1 | 0.5 | 1.31 | a) | a) | a) | 0.1 |
| **MPSM2** | 74 | 17.1 | 5.8 | 1.18 | 443.7 | 8.3 | 0.92 | 19.7 |
| **MPSM3** | 4 | 74.1 | 2.5 | 1.32 | 771.6 | 3.2 | 0.63 | 2.7 |
| **MPSM4** | 74 | 74.1 | 7.7 | 1.14 | 163.8 | 14.8 | 0.35 | 31.2 |
| **MPSM5** | 39 | 45.6 | 7.0 | 1.09 | 291.6 | 9.3 | 0.51 | 23.0 |
| **MPSM6** | 4 | 45.6 | 1.3 | 1.32 | a) | a) | a) | 0.4 |
| **MPSM7** | 74 | 45.6 | 7.4 | 1.13 | 170.9 | 12.1 | 0.32 | 30.1 |
| **MPSM8** | 39 | 17.1 | 4.8 | 1.18 | 568.6 | 4.8 | 0.73 | 13.0 |
| **MPSM9** | 39 | 74.1 | 7.8 | 1.14 | 167.8 | 14.4 | 0.35 | 28.6 |
| **MPSM10** | 39 | 45.6 | 7.8 | 1.13 | 209.3 | 9.9 | 0.36 | 26.7 |
| **MPSM11** | 39 | 45.6 | 6.9 | 1.25 | 222.9 | 9.6 | 0.39 | 25.9 |
| **MPSM12** | 39 | 45.6 | 7.4 | 1.15 | 233.8 | 9.9 | 0.41 | 25.9 |
| **MPSM13** | 8 | 45.6 | 2.4 | 1.37 | 674.7 | 3.7 | 0.68 | 2.7 |
| **MPSM14** | 8 | 17.1 | 1.3 | 1.22 | a) | a) | a) | 0.2 |
| **MPSM15** | 8 | 74.1 | 4.2 | 1.19 | 559.8 | 5.4 | 0.84 | 7.9 |
| **p@TEPA-2** | - | - | 8.9 | 1.06 | 75.7 | 13.6 | 0.16 | - |
| **MPSM-$C_{18}$-1** | 74 | 17.1 | 7.5 | 1.11 | 246.3 | 16.6 | 0.57 | 26.5 |
| **MPSM-$C_{18}$-2** | 39 | 45.6 | 7.9 | 1.10 | 186.4 | 20.8 | 0.44 | 28.2 |

a) For the particles **MPSM1**, **MPSM6** and **MPSM14** no nitrogen adsorption analysis could be performed as the obtained amounts of MPSMs (< 10 mg) were too poor. These samples were therefore only included in the model for particle size.

### 7.3.1. Particle size and morphology

After calcination the particle diameters of **MPSM1–15** varied widely within the range from 0.5 µm to 7.8 µm (**Figure S. 7.1**, S. I.). This is in contrast to the HBs, from which the MPSMs were derived. The size of the HBs remained constant when the sol-gel conditions were varied[3]. Interestingly, for each factor level setting a narrow size distribution with $d_{90}/d_{10}$ values below 1.4 is observed (**Figure 7.3**, **Table 7.2** and **Figure S. 7.1**, S. I.).).

The effect of the two process factors on the size distribution of the **MPSM1–15** can be accurately described by a statistically highly significant model ($p < 0.0001$) (**Table 7.3**).

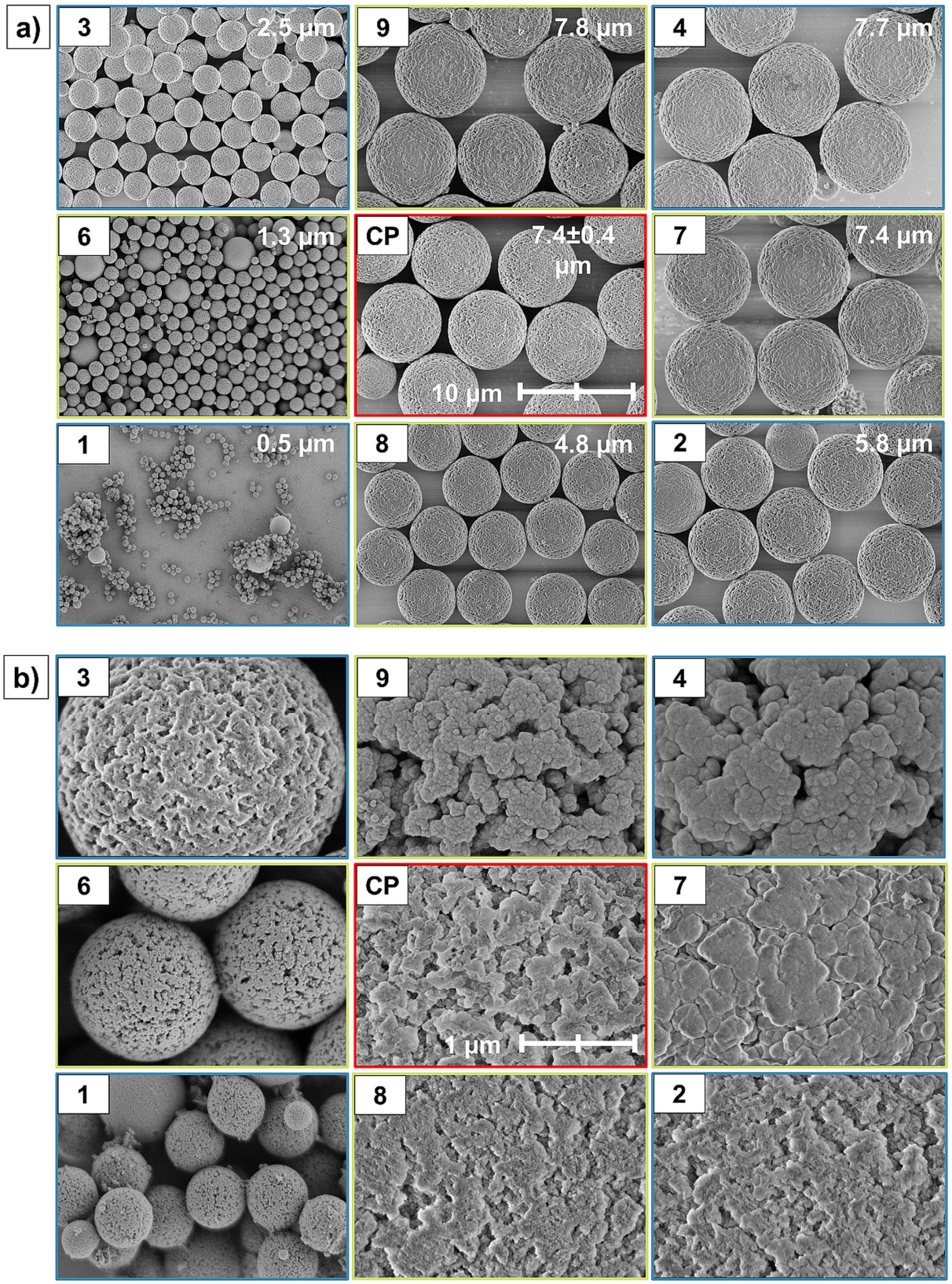


**Figure 7.3** SEM images of the MPSMs according to the face-centered central-composite design. **a)** MPSMs in 5,000x magnification with the particle size median given. For the center points the size ± standard deviation is indicated. **b)** MPSMs in 50,000x magnification. For CPs **MPSM5** is shown. Factorial points are highlighted in blue, axial points in green and CPs in red.

**Table 7.3** Excerpt from the analysis of variance (ANOVA) tables with p-values for the response surface models of the target responses particle size, pore diameter (PD), specific surface area (SSA) and pore volume ($V_p$) and shrinkage compared to the HB, as well as their fit statistics. Complete ANOVA tables for each model are given in **Table S. 7.2** to **Table S. 7.5** S. I

| Response | Particle size | PD | SSA | $V_p$ |
|---|---|---|---|---|
| | /µm | /nm | /$m^2 \cdot g^{-1}$ | /$cm^3 \cdot g^{-1}$ |
| **Model** | < 0.0001 | < 0.0001 | < 0.0001 | 0.0068 |
| **A** – n($H_2O$)/n(TEOS) | < 0.0001 | < 0.0001 | < 0.0001 | 0.0072 |
| **B** – c($NH_3$) | < 0.0001 | < 0.0001 | 0.0001 | 0.0029 |
| **AB** | n.s. | 0.0018 | n.s. | n.s. |
| **$A^2$** | < 0.0001 | < 0.0001 | 0.0002 | 0.0420 |
| **$B^2$** | n.s. | n.s. | 0.0041 | 0.0181 |
| **$A^2B$** | - | 0.0001 | - | - |
| **Lack of fit** | 0.3067 (n.s.) | 0.5145 (n.s.) | 0.2588 (n.s.) | 0.1459 (n.s.) |
| | | | | |
| **$R^2$** | 0.9727 | 0.9968 | 0.9697 | 0.8373 |
| **$R^2_{adjusted}$** | 0.9652 | 0.9941 | 0.9523 | 0.7443 |
| **$R^2_{predicted}$** | 0.9470 | n.a. | 0.8991 | 0.3806 |

The high predictive power ($R^2_{predicted}$ = 0.9470) of the model allows prediction of the expected particle size as a function of the statistically significant factor effects of n($H_2O$)/n(TEOS) ratio, its non-linear effect term and the comparatively lower effect of c($NH_3$) (**Figure 7.4**). Model equation (7.1) gives the relation between the statistically significant effect and interaction effect terms on the particle size in terms of the coded equation:

$$\text{Particle size } /\mu m = 6.96 + 2.69A + 1.21B - 2.71\ A^2 \quad (7.1)$$

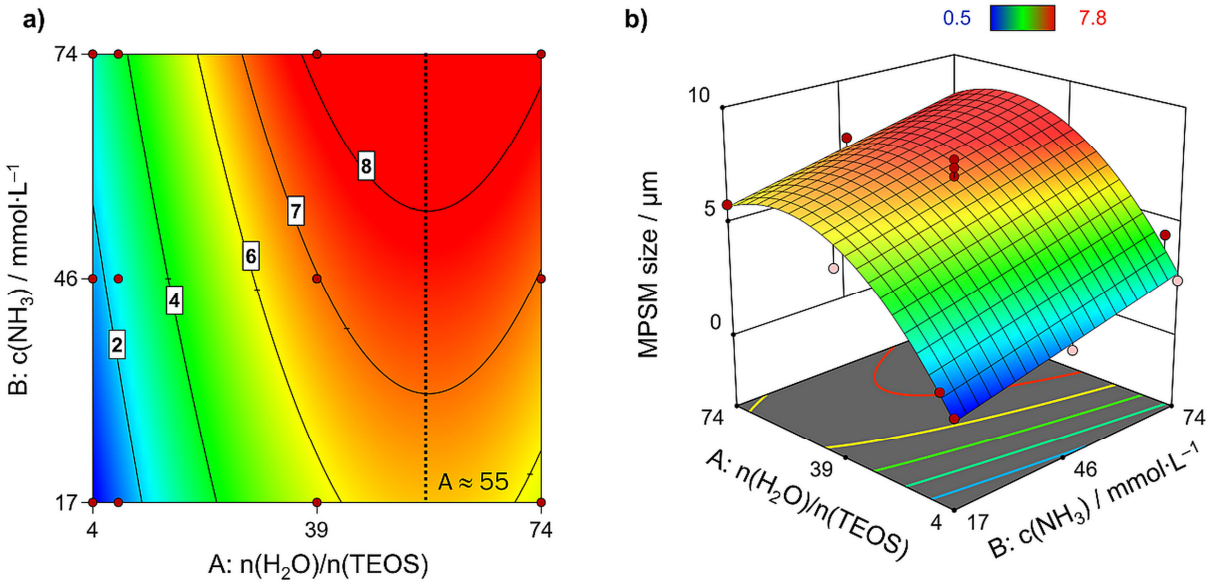


**Figure 7.4 a)** Contour plot with contour lines for different particle sizes in dependence of the process factor levels and **b)** 3D response surface plot of the augmented FCD model regarding the MPSM size. Red areas indicate large particles. Blue areas indicate small particles.

When the ratio of water to TEOS is increased, the resulting MPSMs undergo less shrinkage and thus stay large after calcination. However, larger amounts of water attenuate this effect within the examined experimental design space. This levelling behavior is described by the negative $A^2$ effect term. This is a result of the hydrolysis and condensation rates which exceed the rate of SNP incorporation into the porous template. Consequently, the silica nanoparticles become too large to diffuse into the pores and thus remain in the continuous phase where they form non-porous secondary particles. Thus less silica is incorporated into the templates which leads to smaller silica particles[3].

For the ammonia concentration, a clear trend of size increase can be observed. When the initial ammonia concentration is increased at the start of the synthesis, larger MPSMs result after calcination. On the other hand, at low initial ammonia concentration the SNP production is inefficient. This results in the incorporation of small amounts of SNPs into the polymer beads. After calcination the remaining MPSMs are much smaller than the applied templates. This behavior can be seen clearly in **Figure 7.4**a. For the same molar ratio of water-to-TEOS, the MPSM size increases when the ammonia concentration is increased. This increase varies between two to three micrometers. By applying a low initial ammonia concentration at a low level of $n(H_2O)/n(TEOS)$, MPSMs as small 0.5 µm MPSMs (**MPSM1**) can be prepared, whereas at a high ammonia concentration the particle size increases to 2.5 µm (**MPSM3**) at the same $n(H_2O)/n(TEOS)$ ratio. The slope of the MPSM size increase with increasing ammonia concentration within the investigated design space and is on average $+ 0.04$ µm/mmol·$L^{-1}$.

The final size of the MPSMs is determined by the size and number of incorporated SNPs. Smaller SNPs have a higher volume-to-surface ratio which results in OH-bonding sites between particles[207,208]. Under the elevated temperature during template removal (600 °C), these silanol groups undergo condensation and form Si-O-Si bonds, which results in shrinkage[121]. This reduces the total surface and thus the total free energy[209]. The typical necking was observed (see **Figure S. 7.2**, S. I.). As the calcination conditions were similar for all samples, here the scaling law applies. The larger SNPs require more time at the same temperature to reach a similar sintering degree as samples consisting of smaller SNPs[140,141]. Hence, the larger the SNPs in the HB are, the smaller is the effect of interparticle condensation and thus shrinkage. Moreover, in this polymer/silica system the size of the SNPs and the amount of incorporated silica correlates linearly and in dependence on the sol-gel process conditions[3]. The smaller the SNPs, the less silica is incorporated. This results in even more pronounced shrinkage and explains the strong decrease in MPSM size in the lower region of the design space,

where the factor level settings are low for both factors. Under these conditions sub-2 µm particles were obtained (**MPSM1, 6, 14**).

**Figure 7.3**b displays the morphology of the prepared **MPSM1–12**. The SEM images of the morphology of the particles **MPSM13–15** are given in **Figure S. 7.3** S.I. All MPSMs are formed by interconnected SNPs, which generate pores in the silica network. During template removal via calcination the interconnected SNPs underwent grain growth[140] which is especially pronounced for the settings with less silica incorporation and small SNPs (< 50 nm[3,84], e.g. **MPSM3 Figure 7.3**b). However, surface appearance changes when different regions in the design space are explored. When both, the stoichiometric ratio of water and the ammonia concentration are increased, the larger (≥ 50 nm) and more spherical SNPs are obtained. With increasing ammonia concentration, the interconnection of SNPs is less pronounced and single nanoparticulate structures are visible (**MPSM4, MPSM9 Figure 7.3**b). The size of the SNPs formed during the sol-gel process increases with an increase in n($H_2O$)/n(TEOS) and c($NH_3$), via aggregation within the pores of the polymer template and aggregation and monomer addition growth of the SNPs at the outer surface of the template[3].

### 7.3.2. Effect of incorporated silica content on MPSMs pore volume

As after calcination only the silica part of the HB remains (see **Figure 7.1**), the silica content in the HBs is seen as a critical parameter affecting the properties of the final MPSMs. The pore size, specific surface area and the pore volume of the MPSMs were determined by nitrogen adsorption measurements at 77 K (**Table 7.2**). The pore volumes of the prepared MPSMs were all within the range from 0.32 $cm^3 \cdot g^{-1}$ to 0.92 $cm^3 \cdot g^{-1}$. The smallest pore volumes were observed, when the highest amounts of silica were incorporated into the preceding HB. The statistically significant effects of the process conditions on the pore volume $V_p$ of the MPSMs were identified and were used to derive a statistically significant response surface model. With $R^2 = 0.8373$ and $R^2_{adjusted} = 0.7443$ this model describes the data well. However, the predictive power of the model is comparatively low with $R^2_{predicted} = 0.3806$, which can be attributed to the different types of pores which are formed during calcination in dependence on the amount of incorporated silica (**Figure 7.5**).

The pore volume of the MPSMs in dependence on the determined silica content of the preceding HBs, from which the MPSMs were derived by calcination, is given in **Figure 7.5** and can be fitted by a second order polynomial function with $R^2_{adjusted} = 0.7251$. For high silica contents in the HBs, the pore volume of the MPSMs was found to be lowest and to increase rapidly with decreasing silica contents. For silica contents lower than approximately 11 wt%, the pore volume decreases again.

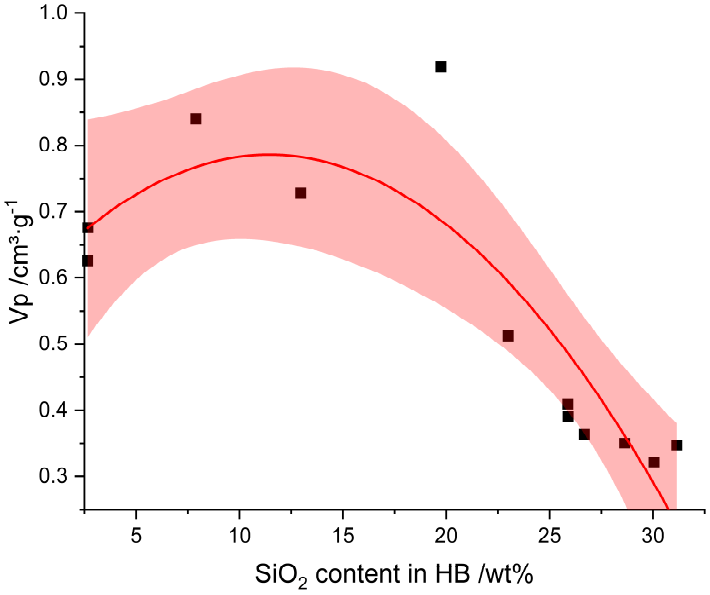


**Figure 7.5** Second-order polynomial fit of $V_P$ and the silica content of the hybrid material. Shaded areas indicate 95 % confidence interval. $R^2_{adjusted} = 0.7251$

Depending on the amount and the size of the SNPs incorporated into the sacrificial template, the morphology of the resulting MPSMs changes. A negative imprint can be formed where the former polymer walls are now pores and the former pores of the polymer template form the new silica pore walls (**Figure 7.6**a).

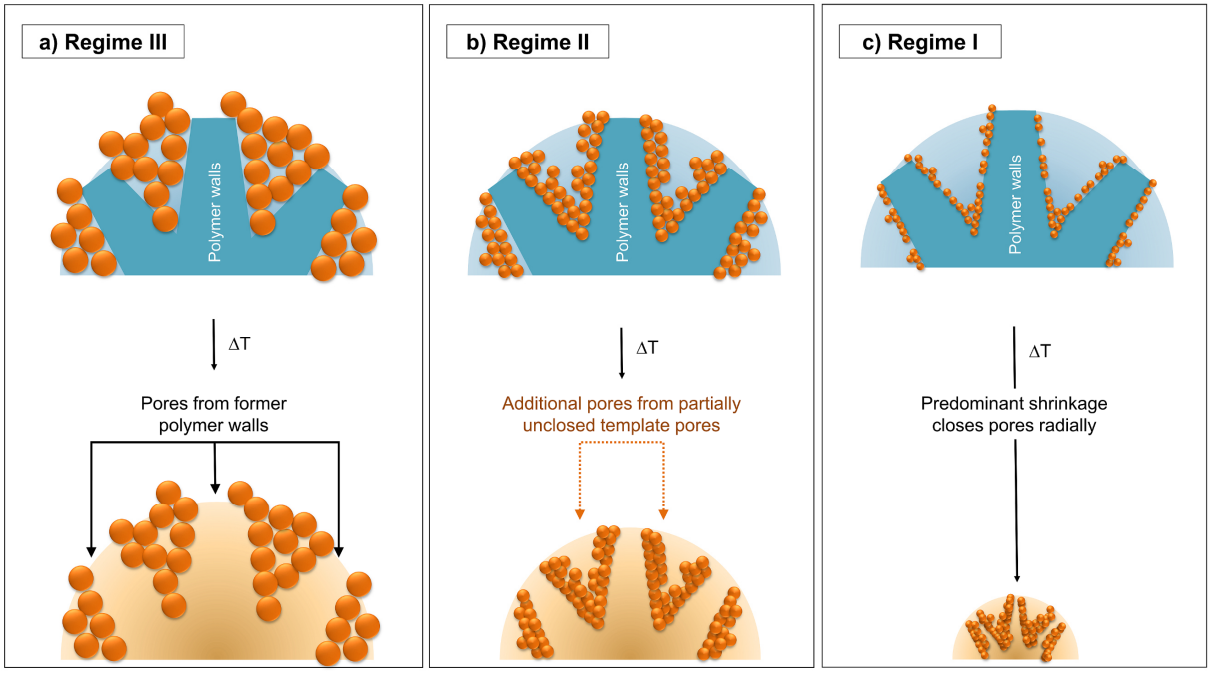


**Figure 7.6** Scheme of pore formation after template removal by calcination for three degrees of silica deposition in the hybrid material according to the defined reaction regimes[3].

If less silica was incorporated into the pores of the template, the polymer walls have been coated only with a silica layer. Compared to the thickness of the walls of the porous polymer matrix, the silica layers are quite thin, only a few nanometers thick, as the SNPs which diffused into the polymer matrix are small (~10–20 nm). During calcination, not only is the template removed, but condensation of adjacent SNPs also occurs. If only thin silica layers are formed, the layers on both sides of the pore wall are too far apart to condense (**Figure 7.6**b). Thus, both new pores are formed by removing the polymer walls and, in addition, former pores are not closed by condensation, so that the porosity of the MPSM and thus the pore volume is increased. For samples with a rather low silica content in the hybrid material, shrinkage is very pronounced, resulting in small MPSMs and partial closure of pores by condensation (**Figure 7.6**c).

This process progresses while some porosity is retained, which is clearly visible for e.g. **MPSM1** in **Figure 7.3**b. However, as the small SNPs are sintered to a greater extent than larger SNPs, the grain growth progresses further[141], leading to closure of pores. Therefore, for samples with low silica content in the HBs, the pore volume is comparatively smaller (**Figure 7.6**c). This change in mechanism of pore formation during calcination in dependence on the silica content in the preceding HBs restricts the predictive power of the pore volume model. Response surface methodology assumes that the system behavior follows the same underlying mechanism throughout the complete studied design space.

### 7.3.3. Pore size

The pore sizes of **MPSM2–5**, **7–13** and **15** varied between 3.2 and 14.8 nm and show mostly broad pore size distributions (see **Figure S. 7.4**, S.I.). The distribution is narrower, for MPSMs with pores below 8.3 nm in median (**MPSM2, 3, 8, 13, 15**). These particles show a bimodal pore size distribution at lower pore sizes, with an increasing amount of micropores with decreasing mean pore size. **MPSM2**, **3**, **8**, **13** and **15** also are the smallest MPSMs in this design space and underwent the most shrinkage (> 30 % decrease in diameter compared to HB). From the FCD a clear dependence of the mean pore size on the effect of both process factors $n(H_2O)/n(TEOS)$ and $c(NH_3)$ was observed. However, the effect of the $n(H_2O)/n(TEOS)$ is non-linear and the factor effects are synergistic as the two-factor interaction effect term AB and the higher-order interaction effect term $A^2B$ are both statistically significant. This means that each of the process factors strongly depends on the factor level setting of the other factor and neither of the two can be separately and independently be discussed. As there is one sample (**MPSM13**) with a leverage value of one, the $R^2_{predicted}$ value cannot be calculated. This sample is located in the lower area of the design space. Moreover, the silica deposition for three samples in this region (**MPSM1**, **MPSM14** and **MPSM6**) was too low

to characterize them by means of nitrogen adsorption after calcination. The position of **MPSM13** in the design space is quite isolated, meaning that this factor level combination strongly influences the model[59]. However, as the $R^2_{adjusted}$ = 0.9941 indicates that an adequate number of terms was used in the mathematical model (meaning that the data were not overfitted), the unusual and hard to physically interpret factor effect term $A^2B$ was included in the model. Moreover, exclusion of the $A^2B$ term leads to a prediction of negative pores size values, which does not make sense and illustrates that the $A^2B$ term is actually real and required for an adequate model. With the $A^2B$ factor interaction term, the predicted pore size of **MPSM1** n($H_2O$)/n(TEOS) and c($NH_3$) at the low factor setting is 1.9 nm, which is a reasonable prediction, since the porous nature of the particles is clearly visible in **Figure 7.3**b. The relative importance of the factors is evident from Equation (7.2), the model equation in terms of coded factors:

$$PD\ /nm = 9.64 + 4.54A + 4.82B + 1.26\ AB - 2.46\ A^2 - 2.83\ A^2B \qquad (7.2)$$

The corresponding interaction plot (**Figure 7.7**a) illustrates the relation between the process factor effects n($H_2O$)/n(TEOS) and c($NH_3$) and the pore size.

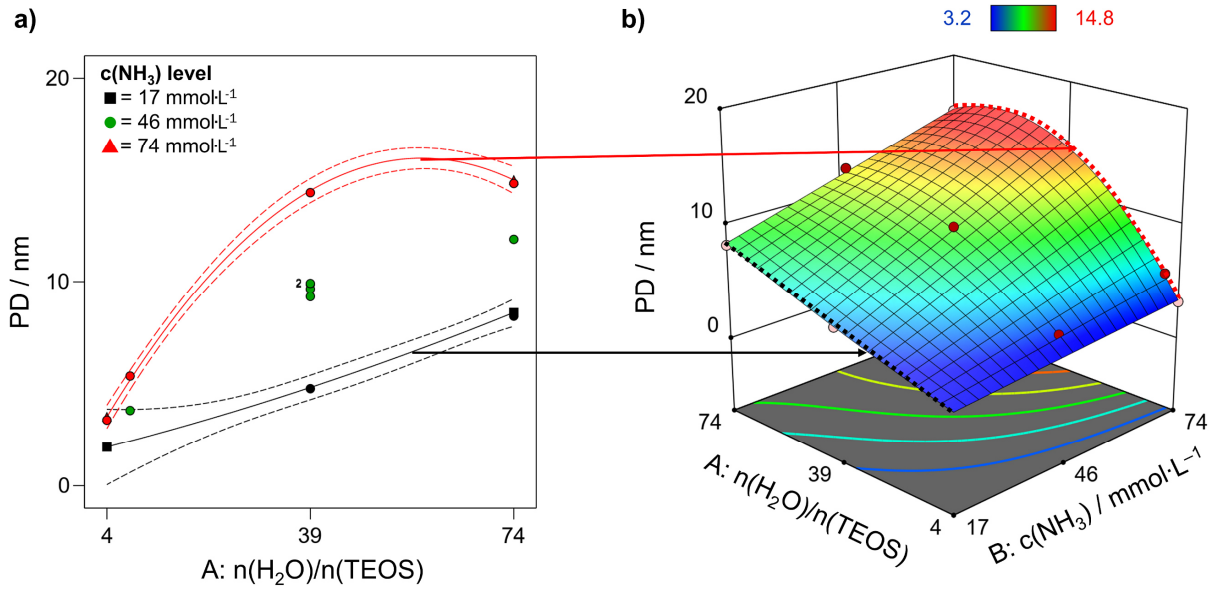


**Figure 7.7 a**) Interaction plot: the black line indicates the effect of higher water levels at low ammonia concentrations while the red line displays the effect of the water-to-TEOS ratio at high levels of ammonia. Dashed lines indicate the 95 % confidence intervals. **b)** 3D response surface plot: Red areas correspond to large pore diameters whereas blue areas indicate small pores. The dashed black and red lines highlight projected the surface edges represented in the interaction plot **a)**.

With increase in ammonia concentration, the pore sizes generally become larger (**Figure 7.7**b), but the steepness of the increase is dependent on the n($H_2O$)/n(TEOS) level.

Under basic reaction conditions, the hydrolysis rate is slower than the condensation rate and thus, it is the rate determining reaction. However, the reaction rates are also dependent on the water-to-TEOS ratio. The addition of water promotes the formation

of silanol groups favoring the hydrolysis[91]. At low ammonia concentrations, the reaction pH for **MPSM1**, **2**, **8**, and **14** lies at 10.5±0.0. Here, the effect of n($H_2O$)/n(TEOS) is linear and the pore size increases linearly with an increase in water-to-TEOS ratio. If the ammonia concentration is increased, the effect of the water-to-TEOS ratio changes gradually from linear to non-linear. For high ammonia concentrations the pH value is 10.9±0.1 (**MPSM3**, **4**, **9**, **15**, **Table S. 7.1**, S. I.). At high water-to-TEOS ratios and higher ammonia concentrations, the dependence of the pore size on the n($H_2O$)/n(TEOS) ratio turns non-linear. In this case, the pore size first increases with increasing water quantity, but from a certain point on, a further increase in pore size becomes the smaller the higher the water quantity is (**Figure 7.7**a, red line). A similar dependence on the process factor settings was observed for the SNP size, which increase in size with increasing ammonia concentration and also exhibit a non-linear behavior with increasing water-to-TEOS ratios[3,106,113]. A clearly linear relation between the size of SNPs incorporated in the porous polymeric template, forming the HBs, and the resulting pore size of the corresponding MPSMs after calcination was observed (see **Figure S. 7.5**, S. I.).

Thus, the pore size of the MPSM is not only dependent on the pore size of the template[2] but also on the size of the SNPs incorporated into the porous network of the polymeric template. As a result, the pore size of the MPSMs can be varied by adjusting the sol-gel process conditions using the process factors n($H_2O$)/n(TEOS) and c($NH_3$).

### 7.3.4. Specific surface area

The specific surface area is an important material characteristic when it comes to separation processes dependent on surface interactions between analyte and stationary phase. The prepared MPSMs showed a range of specific surface area from 164 $m^2 \cdot g^{-1}$ to 772 $m^2 \cdot g^{-1}$, where the lowest SSA occurred at the highest factor level settings for both process factors (the high | high factorial experiment **MPSM4**) and the highest SSA was obtained at the lowest water to precursor ratio and ammonia concentration (the low | low factorial experiment **MPSM3**).

The SSAs of the prepared MPSMs are statistically significantly affected by both process factors n($H_2O$)/n(TEOS) ratio and c($NH_3$), each in a non-linear manner (significant effect terms $A^2$ and $B^2$). The relative process factor strengths are given in model equation (7.3) in coded terms:

$$SSA\ /m^2 \cdot g^{-1} = 237.67 - 291.18A - 172.77B + 229.98A^2 + 126.28B^2 \quad (7.3)$$

Both factors affect the SSA in a similar direction. The factor effect strength of A on the SSA is by far stronger than the factor effect strength B, as can be seen by the model

term coefficients in equation 3. When the factor level of either factor is increased, the SSA decreases (**Figure 7.8**).

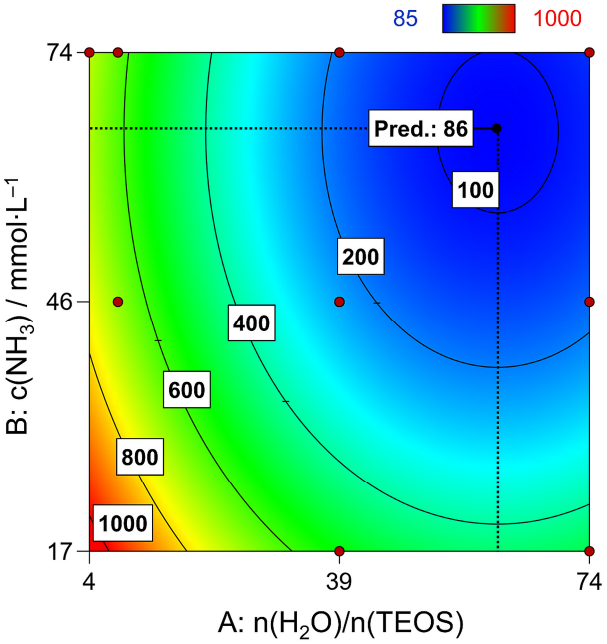


**Figure 7.8** Contour plot for SSA in dependence of $c(NH_3)$ and $n(H_2O)/n(TEOS)$. Contour lines for multiple SSAs are given. Large SSAs are displayed in red. Small SSAs are displayed in blue. Dashed lines indicate the position of predicted minimum of the SSA.

However, the degree of decrease levels off with a further increase in factor level settings. This levelling effect, represented by the second order effect terms (Equation (7.3)), is more pronounced upon changing $n(H_2O)/n(TEOS)$ (**Figure 7.8**). The non-linear behavior for both factors leads to the formation of a region in which a global minimum of SSA is observed within the investigated experimental design space at $n(H_2O)/n(TEOS) \approx 61$ and at $c(NH_3) \approx 65$ mmol·L$^{-1}$. On the other hand, large SSAs were achieved when the starting conditions of the sol-gel process were selected in the low factor level regions of the design space. With $R^2_{predicted} = 0.8991$ the dependence of SSA on the stoichiometric ratio of water-to-precursor and the ammonia concentration can be predicted with good accuracy.

### 7.3.5. HPLC separations of biomolecules

In order to yield enough MPSM material to pack an HPLC column, a new batch of polymeric template was prepared and TEPA functionalized. This template exhibited a slightly higher pore volume, larger specific surface area and larger pore sizes than the template used in the statistical design (see **Table 7.2**). This reflects the low extent of common cause variability of the hard template preparation procedure due to scaling up the process. From this, two batches of MPSMs were prepared (see **MPSM-C$_{18}$-1 Figure 7.9**a and **MPSM-C$_{18}$-2 Figure 7.9**b) with process factor level settings corre-

sponding to **MPSM2** and the **CP**s, respectively. Thus, although the sol-gel parameters were the same for **MPSM-C$_{18}$-1** as **MPSM2** and for **MPSM-C$_{18}$-2** as the **CP**s the materials differ slightly. This is a result from changes in the template characteristics and scale up[2].

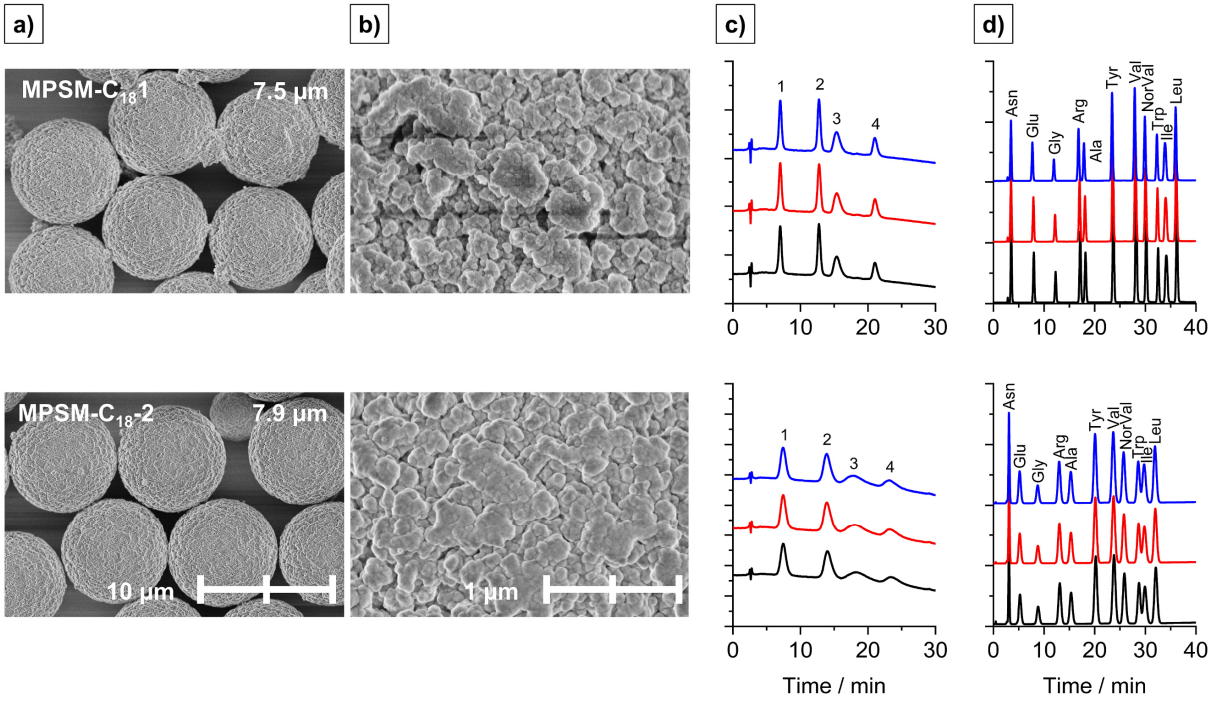


**Figure 7.9** SEM images of MPSMs as packing materials prior to rehydroxylation and C$_{18}$-functionalization with **a)** 5,000 x magnification and **b)** 50,000 x magnification.

Interestingly, the template with the higher pore volume, larger pores and higher SSA resulted in MPSMs with lower pore volumes and lower SSA but enlarged pore sizes. The properties of **MPSM-C$_{18}$-1** and **MPSM-C$_{18}$-2** were also determined by inverse size exclusion chromatography, which exhibited similar trends as the nitrogen sorption characteristics (see **Table S. 7.6,** S.I.). **MPSM-C$_{18}$-1** exhibited smaller pores but a higher SSA than **MPSM-C$_{18}$-2.** This trend fits well with the observations made in the statistical evaluation of the process factor effects n($H_2O$)/n(TEOS) and c($NH_3$). This offers more space within the template pores for aggregation of *in situ* formed highly reactive small silica species und consequently larger SNPs[2]. In combination with the higher template pore volume, more and larger SNPs were incorporated into the template. The sizes of the incorporated SNPs were slightly larger with 25 nm (**MPSM-C$_{18}$-1**, **MPSM2**: 20 nm) and 48 nm (**MPSM-C$_{18}$-2**, **CPs**: 43 nm).

The columns **MPSM-C$_{18}$-1** and **MPSM-C$_{18}$-2** were tested for their separation capability for proteins and amino acids and the corresponding chromatograms are shown in **Figure 7.9**c and d. Both C$_{18}$ functionalized column materials allowed the separation of all four proteins. The retention times were thereby ribonuclease-A < cytochrome c < holo-

transferrin < apomyoglobin. This was consistent for both columns and the reproducibility of the measurement was high (**Figure 7.9**c). However, **MPSM-C$_{18}$-1** exhibited sharper peaks than **MPSM-C$_{18}$-2**, the elution of the last peak was earlier and overall, the resolution was better. All peaks were baseline separated using column **MPSM-C$_{18}$-1** ($R \geq 2.0$), while the resolution between cytochrome c and holo-transferrin was $R_{2\text{-}3} = 1.92$. For **MPSM-C$_{18}$-2**, the resolutions were reduced with $R \geq 1.25$ due to peak broadening. This can be a result of the larger particle size and increased diffusion pathways with larger pores.

The separation of amino acids was successful using both columns. Both columns exhibited a good separation performance. Also, here the peaks of **MPSM-C$_{18}$-2** were generally broader and less intense (**Figure 7.9**d). Interestingly, the elution of the last amino acid leucin was earlier for **MPSM-C$_{18}$-2** than **MPSM-C$_{18}$-1**, which can be attributed to the reduced surface area and thus less retention of the amino acids. However, the separation of arginine and alanine was better using **MPSM-C$_{18}$-2** than **MPSM-C$_{18}$-1**. Column **MPSM-C$_{18}$-1** was able to separate all amino acids in the mixture with a resolution of $R \geq 2.0$ ($R_{ARG\text{-}ALA} = 2.0$). Using **MPSM-C$_{18}$-2** all peaks were separated with a good resolution (> 1.5) except for the pair of TRP and ILE ($R = 1.0$). For **MPSM-C$_{18}$-2** the analysis time was reduced by 11 % compared to **MPSM-C$_{18}$-1**, however, the separation efficiency was decreased. This is a result of the smaller surface area compared to **MPSM-C$_{18}$-1**.

While for the separation of proteins the separation time was increased when using column **MPSM-C$_{18}$-2** the time required for the separation of the amino acids was less than using column **MPSM-C$_{18}$-2.** This can be attributed to the different types of separation. The separation of the proteins is mainly determined by size exclusion. Here, the larger pores allow better mass transfer and increase the retention of proteins with a higher radius of gyration. For the separation of the amino acids, the smaller surface area of **MPSM-C$_{18}$-2** reduces the retention times but also the separation efficiency of the materials. Here, **MPSM-C$_{18}$-1** shows superior separation efficiency allowing a baseline separation of all eleven amino acids.

## 7.4. Conclusions

In this study, it was shown that the hard-template approach can be used as a platform for fabricating a wide range of fully porous monodisperse silica particles. The silica content of the preceding HBs is a critical parameter for the final properties of the silica particles. Thus, the particle size, pore volume, pore size distribution and morphology of the silica particles are determined by the size and number of incorporated SNPs. The installation of the SNPs into the template network is the result of the interaction of the template and the sol-gel process. In this design space the same template was applied. As a result, properties of the MPSMs can be varied by adjusting the sol-gel process conditions using the process factors $n(H_2O)/n(TEOS)$ and $c(NH_3)$.

The tailoring of the property profile was demonstrated with MPSMs. These were successfully applied as column materials for the separation of amino acids and proteins by HPLC.

## 7.5. Supplementary Information

### 7.5.1. Preparation of Hybrid Beads

15 mL of a 2.0 g·L$^{-1}$ SDS solution were prepared and 0.9 g monodisperse polystyrene seeds (1.95 µm, of $d_{90}/d_{10}$ = 1.09) were added. The mixture was sonicated for 10 minutes in. 6.0 mL DBP and 450 mL of a 2.53 g·L$^{-1}$ SDS solution (10 minutes at 5000 rpm) were homogenized and the emulsion was added to the seed particle suspension. The mixture was stirred at 200 rpm for 24 h at room temperature.
The organic phase consisting of 22.5 mL of each cyclohexanol, EDMA, GMA and toluene were homogenized together with 450 mL of SDS (3.33 g·L$^{-1}$), and 1.2 g of the initiator BPO for 10 minutes at 5000 rpm. The emulsion was added and the system stirred at 200 rpm for another 24 h. As stabilizer 450 mL of a PVA solution (23.3 g·L$^{-1}$) was added to the mixture. For polymerization the reaction mixture was stirred at 200 rpm for 24 h at 70 °C. The porous *p*(GMA-*co*-EDMA) particles were washed three times with ethanol and three times with water.

A mixture of 35 g of dried *p*(GMA-*co*-EDMA) particles and 1400 mL deionized water were sonicated for 15 min. Under stirring at 200 rpm, 0.256 mol of TEPA were added dropwise. The mixture was heated to 80 °C for 24 h. The functionalized particles were filtered off and washed three times with ethanol and water. The particles will be further referred to as p@TEPA.

2 g p@TEPA particles were dispersed in a mixture consisting of 2-propanol and water and sonicated for 5 minutes. The amount of added water was calculated in dependence of the stoichiometric ratio of n($H_2O$)/n(TEOS) according to the factor level setting of the FCD. The water content of the ammonia solution is thereby considered. As basic catalyst, a predefined amount of ammonia according to the FCD was added to the mixture under stirring. Then 21.5 mmol of TEOS was added and the mixture was stirred for 24 h at room temperature (550 rpm). The HB particles were separated from the reaction solution and washed three times with ethanol and water. The HBs were then dried at room temperature.

### 7.5.2. pH Values after 24 h

**Table S. 7.1** pH values for the FCD samples 24 h after the start of the synthesis

| | Factor level settings | | |
|---|---|---|---|
| | **A** $n(H_2O)/n(TEOS)$ | **B** $n(NH_3)$ | **pH values** |
| | | /mmol·L-1 | |
| **MPSM1** | 4 | 17.1 | 10.6 |
| **MPSM2** | 74 | 17.1 | 10.2 |
| **MPSM3** | 4 | 74.1 | 11.1 |
| **MPSM4** | 74 | 74.1 | 11.2 |
| **MPSM5** | 39 | 45.6 | 10.8 |
| **MPSM6** | 4 | 45.6 | 10.9 |
| **MPSM7** | 74 | 45.6 | 10.7 |
| **MPSM8** | 39 | 17.1 | 10.4 |
| **MPSM9** | 39 | 74.1 | 10.9 |
| **MPSM10** | 39 | 45.6 | 10.7 |
| **MPSM11** | 39 | 45.6 | 10.7 |
| **MPSM12** | 39 | 45.6 | 10.7 |
| **MPSM13** | 8 | 45.6 | 10.7 |
| **MPSM14** | 8 | 17.1 | 10.5 |
| **MPSM15** | 8 | 74.1 | 11.0 |

### 7.5.3. ANOVA Tables

**Table S. 7.2** Analysis of variance (ANOVA) for the analysis of FCD design of the particle size /μm

| Source | Sum of Squares | df | Mean Square | F-value | p-value | |
|---|---|---|---|---|---|---|
| Model | 101.25 | 3 | 33.75 | 130.54 | < 0.0001 | significant |
| A– $n(H_2O)/n(TEOS)$ | 56.42 | 1 | 56.42 | 218.21 | < 0.0001 | |
| B – $c(NH_3)$ | 11.69 | 1 | 11.69 | 45.21 | < 0.0001 | |
| $A^2$ | 23.14 | 1 | 23.14 | 89.49 | < 0.0001 | |
| Residual | 2.84 | 11 | 0.2585 | | | |
| Lack of Fit | 2.39 | 8 | 0.2993 | 2.00 | 0.3076 | not significant |
| Pure Error | 0.4493 | 3 | 0.1498 | | | |
| Cor Total | 104.10 | 14 | | | | |

**Table S. 7.3** Analysis of variance (ANOVA) for the analysis of FCD design of specific surface area (SSA)

| Source | Sum of Squares | df | Mean Square | F-value | p-value | |
|---|---|---|---|---|---|---|
| Model | $5.141 \cdot 10^5$ | 4 | $1.285 \cdot 10^5$ | 55.95 | < 0.0001 | significant |
| A – n($H_2O$)/n(TEOS) | $3.950 \cdot 10^5$ | 1 | $3.950 \cdot 10^5$ | 171.95 | < 0.0001 | |
| B – c($NH_3$) | $1.329 \cdot 10^5$ | 1 | $1.329E \cdot 10^5$ | 57.88 | 0.0001 | |
| $A^2$ | $1.144 \cdot 10^5$ | 1 | $1.144 \cdot 10^5$ | 49.81 | 0.0002 | |
| $B^2$ | 40445.62 | 1 | 40445.62 | 17.61 | 0.0041 | |
| Residual | 16078.33 | 7 | 2296.90 | | | |
| Lack of Fit | 12137.34 | 4 | 3034.33 | 2.31 | 0.2588 | not significant |
| Pure Error | 3940.99 | 3 | 1313.66 | | | |
| Cor Total | $5.301 \cdot 10^5$ | 11 | | | | |

**Table S. 7.4** Analysis of variance (ANOVA) for the analysis of FCD design of pore diameter (PD)

| Source | Sum of Squares | df | Mean Square | F-value | p-value | |
|---|---|---|---|---|---|---|
| Model | 166.25 | 5 | 33.25 | 368.57 | < 0.0001 | significant |
| A – n($H_2O$)/n(TEOS) | 47.45 | 1 | 47.45 | 525.94 | < 0.0001 | |
| B – c($NH_3$) | 47.19 | 1 | 47.19 | 523.08 | < 0.0001 | |
| AB | 2.53 | 1 | 2.53 | 28.02 | 0.0018 | |
| $A^2$ | 9.12 | 1 | 9.12 | 101.07 | < 0.0001 | |
| $A^2B$ | 6.74 | 1 | 6.74 | 74.74 | 0.0001 | |
| Residual | 0.5413 | 6 | 0.0902 | | | |
| Lack of Fit | 0.2645 | 3 | 0.0882 | 0.9554 | 0.5145 | not significant |
| Pure Error | 0.2768 | 3 | 0.0923 | | | |
| Cor Total | 166.79 | 11 | | | | |

**Table S. 7.5** Analysis of variance (ANOVA) for the analysis of FCD design of the pore volume ($V_p$)

| Source | Sum of Squares | df | Mean Square | F-value | p-value | |
|---|---|---|---|---|---|---|
| Model | 0.4076 | 4 | 0.1019 | 9.01 | 0.0068 | significant |
| A – n($H_2O$)/n(TEOS) | 0.1592 | 1 | 0.1592 | 14.07 | 0.0072 | |
| B – c($NH_3$) | 0.2265 | 1 | 0.2265 | 20.02 | 0.0029 | |
| $A^2$ | 0.0697 | 1 | 0.0697 | 6.16 | 0.0420 | |
| $B^2$ | 0.1065 | 1 | 0.1065 | 9.42 | 0.0181 | |
| Residual | 0.0792 | 7 | 0.0113 | | | |
| Lack of Fit | 0.0664 | 4 | 0.0166 | 3.91 | 0.1459 | not significant |
| Pure Error | 0.0127 | 3 | 0.0042 | | | |
| Cor Total | 0.4868 | 11 | | | | |

## 7.5.4. Appendix Figures

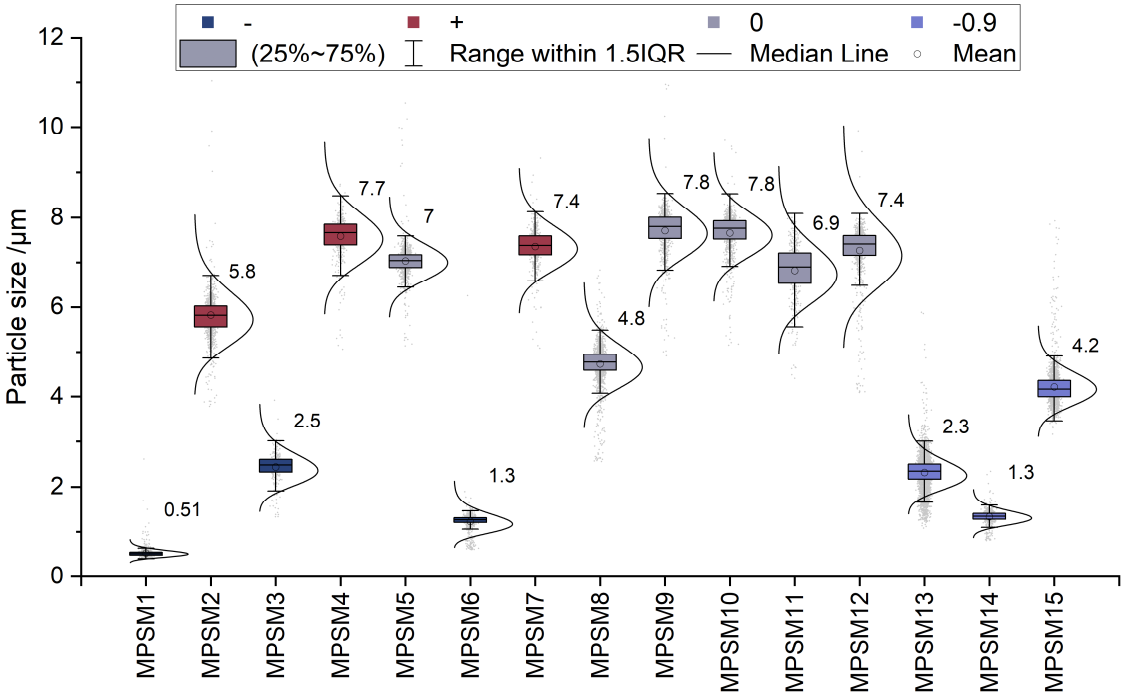


**Figure S. 7.1** Box-Whisker-Plot with lognormal distribution curve of single values (light grey dots) for particle sizes of **MPSM1–15**. Box displays 1. and 3. quartile, whiskers display 1. and 3. quantile + 1.5 · interquartile range. Dark blue box coloration indicates low, red high, grey medium and light blue setting of n($H_2O$)/n(TEOS). Median particle sizes are given for each MPSM.

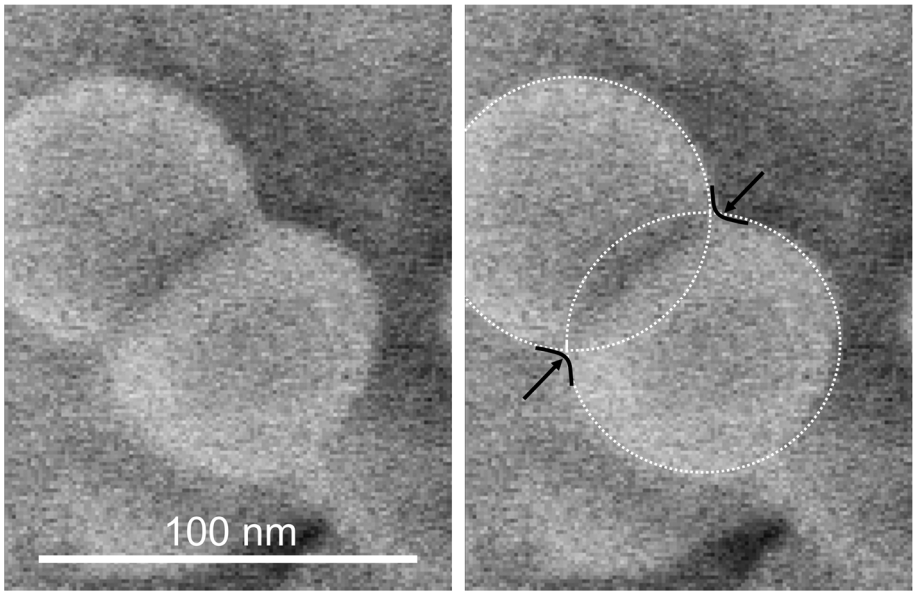


**Figure S. 7.2** Neck formation between two SNPs after calcination. The decrease in radius indicates occurring shrinkage. On the right, the prior SNP outline (dashed white circles) and the neck (solid black lines and black arrows) are highlighted for clarification.

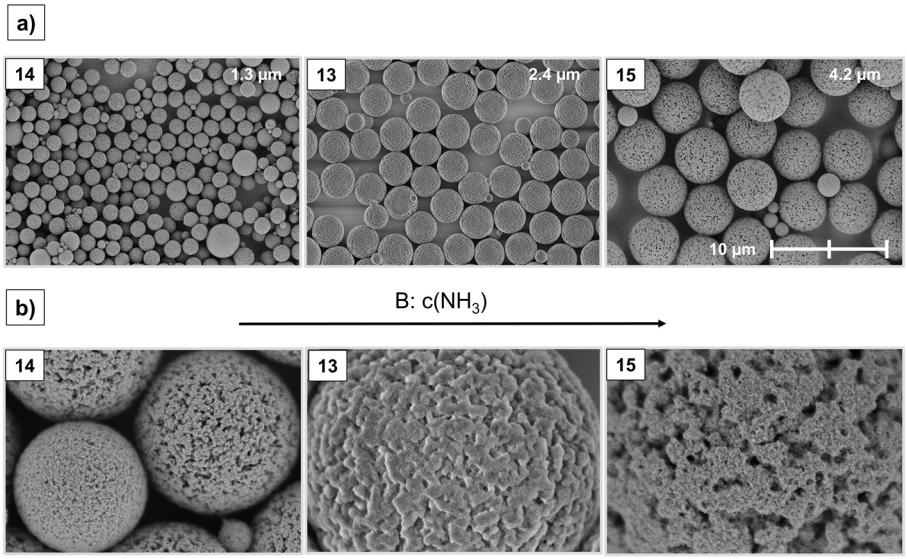


**Figure S. 7.3** SEM image of the additional samples **MPSM13–15** prepared with n($H_2O$)/n(TEOS) = 8 sorted by increasing c($NH_3$) (l.t.r.) at **a)** 5,000× and **b)** 50,000× magnification.

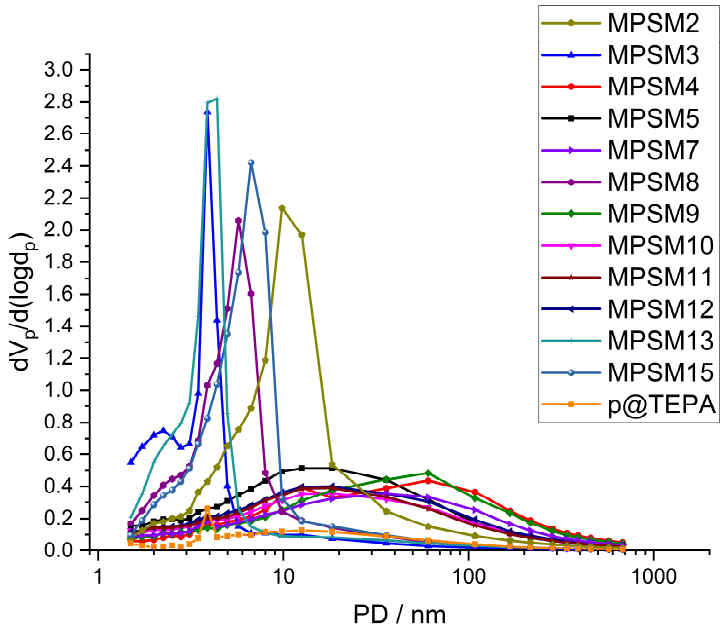


**Figure S. 7.4** Pore size distribution of MPSMs and the corresponding p@TEPA template using the BJH method. The mean pore sizes are given in **Table 7.2**.

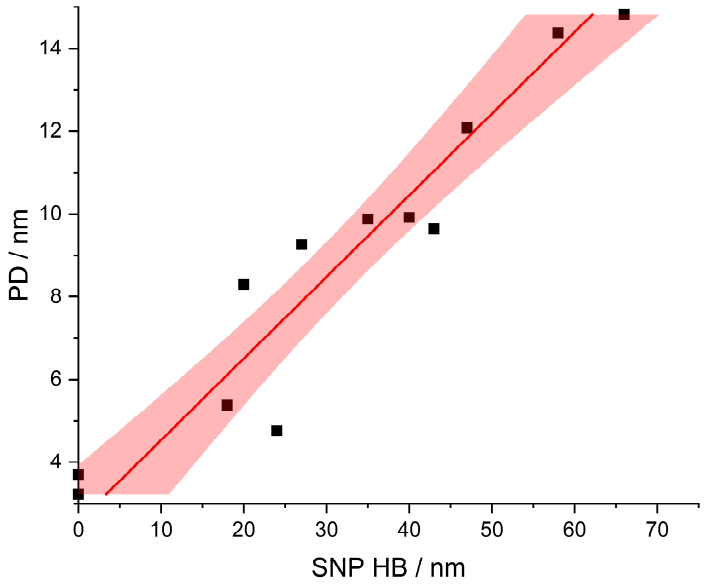


**Figure S. 7.5** Linear regression of PD and the size of SNPs incorporated into the polymeric template. Shaded areas indicate 95 % confidence interval. $R^2$adjusted = 0.8986

### 7.5.5. Inverse Size Exclusion Chromatography Characterization of Columns **MPSM-C$_{18}$-1** and **MPSM-C$_{18}$-2**

**Table S. 7.6** Pore size, pore volume and specific surface area determined by inverse size exclusion[1]

| | **Pore size** | **Pore volume** | **SSA** |
|---|---|---|---|
| | /nm | /cm$^3$·g$^{-1}$ | /m$^2$·g$^{-1}$ |
| **MPSM-C$_{18}$-1** | 23.1 | 0.77 | 134 |
| **MPSM-C$_{18}$-2** | 25.7 | 0.80 | 125 |

**Acknowledgements:** This research was funded the by Bundesministerium für Bildung und Forschung (BMBF, grant number 13FH647IX6). Furthermore, we would like to thank our cooperation partner Dr. Maisch GmbH for their support in packing the columns. We thank Elke Nadler for contributing the SEM measurements.

**Author contributions:** Conceptualization, A.K., and H.A.M.; methodology, J.C.S., F.F., H.A.M. and A.K.; formal analysis, J.C.S.; investigation, J.C.S. and F.F.; resources, H.A.M. and A.K.; data curation, J.C.S.; writing—original draft preparation, J.C.S.; writing—review and editing, F.F., H.A.M. and A.K.; visualization, J.C.S.; supervision, H.A.M. and A.K.; project administration, H.A.M. and A.K.; funding acquisition, A.K. All authors have read and agreed to the published version of the manuscript.

**Declaration of competing interest:** The authors declare that they have no known competing financial interests or personal relationships that could have appeared to influence the work reported in this paper.

**Data availability:** Data will be made available on request.

# 8. Paper V

## Incorporation of Silica Nanoparticles into Porous Templates to Fabricate Mesoporous Silica Microspheres for High Performance Liquid Chromatography Applications

*Fabio Fait[1,2], Julia C. Steinbach[1,2], Andreas Kandelbauer[2,3] and Hermann A. Mayer*[*1]*

[1] Institute of Inorganic Chemistry, University of Tübingen, Auf der Morgenstelle 18, 72076 Tübingen, Germany

[2] Process Analysis and Technology (PA&T), Reutlingen Research Institute, Reutlingen University, Alteburgstrasse 150, 72762 Reutlingen, Germany

[3] Institute of Wood Technology and Renewable Materials, Department of Material Sciences and Process Engineering (MAP), University of Natural Resources and Life Sciences, Gregor-Mendel-Straße 33, 1180 Vienna, Austria

* Correspondence: hermann.mayer@uni-tuebingen.de

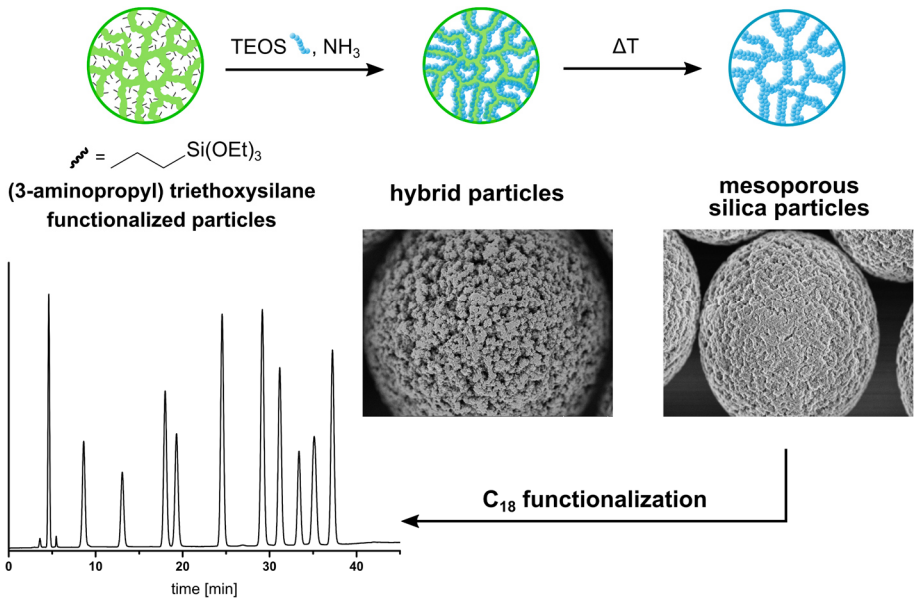


The following chapter is published in a similar form in *Journal of Chromatography A* Volume 1750, Copyright Elsevier (2023) and is reprinted with permission.

Fait, F.; Steinbach, J.C.; Kandelbauer, A.; Mayer, H.A. Incorporation of silica nanoparticles into porous templates to fabricate mesoporous silica microspheres for high performance liquid chromatography applications. *J. Chromatogr. A* **2023**, *1705*, 464190, doi:10.1016/j.chroma.2023.464190.[5]

## Abstract

High performance liquid chromatography is one of the most important analytical tools for the identification and separation of substances. The efficiency of this method is largely determined by the stationary phase of the columns. Although monodisperse mesoporous silica microspheres (MPSM) represent a commonly used material as stationary phase their tailored preparation remains challenging. Here we report on the synthesis of four MPSMs via the hard template method. Silica nanoparticles (SNPs) which form the silica network of the final MPSMs were generated *in situ* from tetraethyl orthosilicate (TEOS) in the presence of (3-aminopropyl) triethoxysilane (APTES) functionalized *p*(GMA-*co*-EDMA) as hard template. Methanol, ethanol, 2-propanol, and 1-butanol were applied as solvents to control the size of the SNPs in hybrid beads (HB). After calcination, MPSMs with different size, morphology and pore properties were obtained and characterized by scanning electron microscopy, nitrogen adsorption measurements, thermogravimetric analysis, solid state NMR and DRIFT IR spectroscopy. Interestingly the $^{29}$Si NMR spectra of the HBs show T and Q group species which suggests that there is no covalent linkage between the SNPs and the template. The MPSMs were functionalized with trimethoxy (octadecyl) silane and used as stationary phases in reversed-phase chromatography to separate a mixture of eleven different amino acids. The separation characteristics of the MPSMs strongly depend on their morphology and pore properties which are controlled by the solvent during the preparation of the MPSMs. Overall, the separation behavior of the best phases is comparable with those of commercially available columns. The phases even achieve faster separation of the amino acids without loss of quality.



## Keywords

polymer template method, mesoporous silica microspheres, $^{29}$Si solid state NMR, high performance liquid chromatography (HPLC).


## 8.1. Introduction

Porous silica particles are widely applied as catalysts and drug carriers, and are used as adsorbents or in separation processes[16,173,175,210,211]. In high performance liquid chromatography (HPLC), totally porous silica particles in the micrometer range with narrow size distributions are of high interest, because they provide high specific surfaces and thus allow best interactions of the analytes between stationary and mobile phases[212].

Industrially, silica particles are produced by emulsion processes or spray drying[104,180,213]. The desired particle diameter is adjusted by the size of the droplet during

emulsification or spraying. Unfortunately, these methods generate broad particle size distributions and require classification of the resulting silica particle batches[181,182]. Therefore sieving, air classification or sedimentation have to be applied to separate the silica particles into fractions with narrow size distributions. This is time-consuming and costly and is also of low productivity, due to waste batches.

Stöber developed a simple method to prepare colloidal nonporous spherical silica particles in a wide range from 10 to 500 nm by ammonia catalyzed hydrolysis and condensation of alkoxy silanes[45]. The size of the silica particles increases up to 800 nm, if in this process the hydrolysis rate of the alkoxy silanes and the siloxane network formation are controlled accordingly. This can be adjusted by critical parameters such as type of alkoxide, $NH_3$ and $H_2O$ concentration, as well as temperature[45,52,84,90,93,214]. Moreover, with increasing chain length of the alcoholic solvent larger silica particles are obtained[94,215]. Seeded growth, semi-batch and the addition of electrolytes are improved techniques which provide access to silica particles in the micrometer range but the particles remain nonporous[183,184,216].

The synthesis of microporous and mesoporous silica particles requires templates[53,123,186]. Soft template methods are based on molecular interaction of silica precursors with non-covalently binding of organic reagents such as cetyltrimethylammonium bromide or triblock copolymers as Pluronic P123. The size of the silica particles is either in the nanometer range or result in polydisperse particles in the micrometer range[123,217–219].

Functionalized poly(glycidyl methacrylate-*co*-ethylene dimethacrylate) (*p*(GMA-*co*-EDMA)) particles have been successfully applied as hard templates in a sol-gel process with tetraethyl orthosilicate (TEOS) to produce porous silica particles in the micrometer range[2,55–57]. Amines such as ethylenediamine, trimethylamine, or tetraethylene pentamine have proven to be useful as functionalization agents, as they provide positive charges on the template surface under the sol-gel conditions. Positively charged amino functions attract the negatively charged silica species, which fill the pores of the template and construct the silica network[55,119].

(3-aminopropyl) triethoxysilane (APTES) is a popular reagent to functionalize silica surfaces[220,221]. The molecule is covalently linked to silica species via the condensation of the triethoxysilane function with surface silanol groups leaving the amino group for further functionalization. In contrast to this, Grama et al. treated *p*(GMA-*co*-EDMA) particles with APTES to bind the molecule via the amino group in an addition reaction with the epoxide to the polymer surface[118]. Here, the triethoxysilane groups enable silica to be deposited in the pores by condensation with silica species generated by a

sol-gel process. This was exploited by Chen et al. in the preparation of micron sized porous silica particles. However, compared to those particles, which were prepared with the TMA functionalized *p*(GMA-*co*-EDMA) polymer, the yield was poor[22].

Mainly, amino functionalized *p*(GMA-*co*-EDMA) templates with different porosity have been investigated for the preparation of MPSMs with comparable settings of the sol-gel process[2,22,119]. In previous studies it was shown that the concentration of ammonia and the molar ratio of $H_2O$ to TEOS have a strong impact on the pore size distribution, the size of the silica particle and the morphology of their surfaces. This is because the conditions of the sol-gel process control the size of the silica nanoparticles (SNPs) which are incorporated into the template[3]. However, the sol-gel process provides multiple other parameters to produce different pore properties and morphologies of the porous silica particles.

The present study aims to demonstrate the control of pore parameters and morphology of mesoporous silica microspheres (MPSMs) prepared via the hard template method using different solvents in the sol-gel process. For this purpose, a base-catalyzed sol-gel process is carried out with the APTES functionalized *p*(GMA-*co*-EDMA) particles **P@APTES** in methanol, ethanol, 2-propanol, and 1-butanol, respectively (**Figure 8.1**). The relevant synthesis steps are analyzed for pore size, pore volume and specific surface area and characterized by NMR and IR spectroscopy. The separation behavior of the silica particles is demonstrated by separating amino acids in high performance liquid chromatography.

## 8.2. Materials and methods

### 8.2.1. Chemicals

Tetraethyl orthosilicate (TEOS) and trimethoxy (octadecyl) silane (ODTMS) were obtained from abcr GmbH (Germany). Acetonitrile (ACN), 1-butanol, tetrahydrofuran, and water (all HPLC grade) were purchased from fisher scientific and ammonia (28–30 % aqueous solution) from Alfa Aesar (Germany). The D,L – amino acids, (3-aminopropyl) triethoxysilane, ethanol), hydrochloric acid, methanol (MeOH), 2-propanol, and triethylamine were bought from Sigma-Aldrich (Germany). Toluene and deionized water were cleaned through a solvent purification system. *ortho*-phthalaldehyde (OPA) reagent for pre-column derivatization of the amino acids was provided by Dr. Maisch HPLC (Germany).

### 8.2.2. Characterization

Scanning electron microscopy images were taken with a Hitachi SU8030 to determine size, dispersity, and morphology of the particles. The size and dispersity of the particles were obtained by measuring at least 400 particles from scanning electron microscopy images. The mean particle diameter is expressed as particle size in μm. The dispersity is given as $d_{90}/d_{10}$ value.

Solid state CP/MAS $^{13}C$ and $^{29}Si$ NMR spectra were recorded on a Bruker AVIIIHD-300WB NMR spectrometer at rotation speeds of 8 kHz ($^{13}C$) and 5 kHz ($^{29}Si$), respectively. The measurement frequencies were 75.47 MHz ($^{13}C$) and 59.63 MHz ($^{29}Si$) and the spectra were referenced to adamantane ($^{13}C$) and octakis (trimethylsiloxy) silsesquioxane ($Q_8M_8$) ($^{29}Si$) as external standards. The contact times of the cross-polarization magic angle spinning (CP/MAS) recordings are 2000 μsec ($^{13}C$) and 5000 μsec ($^{29}Si$) and the relaxation delays are 4 sec ($^{13}C$) and 2 sec ($^{29}Si$), respectively. High pulse decoupling (HPDEC) NMR measurements of $^{29}Si$ has contact times of 9000 μsec and relaxation delays of 30 sec. IR spectra were recorded on a Bruker Vertex 70 FT-IR spectrometer. Particles were pulverized in KBr (20 wt%) and measured using the DRIFT method. Spectra analysis was performed using TopSpin (NMR) and OPUS (IR) software (Bruker).

For the determination of specific surface area, pore size and pore volume the BELSORP MiniX (Microtrac Retsch GmbH) was used. Polymer and hybrid particles were outgassed at 30 °C for 24 h and silica samples at 300 °C for 3 h up to a final vacuum of about $2 \cdot 10^{-2}$ mbar, to eliminate possible physisorbed substances and achieve a reproducible intermediate state[67]. The samples were evacuated using the BELSORP VACII (Microtrac Retsch GmbH). The $N_2$ adsorption and desorption measurements were performed at 77 K. The analysis of adsorption and desorption isotherms was performed using the BELMaster 7 software. Specific surface area was analyzed according to the Brunauer-Emmet-Teller method (BET)[66]. The pore size distributions were determined by using the Barrett-Joyner-Halenda (BJH) method to the desorption isotherms[65]. As previously observed, forced closure of the hysteresis of the desorption isotherm can occur for the organic templates, resulting in a putative pore size distribution at ~ 4 nm[2,188]. This phenomen is also observed for the hybrid beads. Since the BJH method is designed for the desorption isotherm and the median pore size is less affected by this, the pore size distribution of the desorption isotherms are nevertheless shown in this work (**Figure S. 8.4**). Therefore, the data of the median pore sizes of the polymer and hybrid materials in **Table 8.1** are only approximate. The pore volume was obtained from a single point adsorption at $p/p_0$ of 0.95.

Thermogravimetric analysis was performed using the TGA/DSC I from Mettler Toledo. The samples were weight into a 900 µl alumina crucible and were measured under synthetic air (50 mL $min^{-1}$) with a heating rate of 5 K $min^{-1}$. The relative mass of the remaining residue correlates to the amount of $SiO_2$.

Analytical high performance liquid chromatography of amino acids was performed on an Agilent 1100 series system from Agilent Technologies equipped with a quaternary pump with degasser, an auto sampling system, column oven and a fluorescent detector (330 nm extinction, 450 nm emission). Instrument control, data acquisition and automated data analysis was performed by the OpenLAB CDS (Rev. C.01.07 SR3, Agilent Technologies). A sodium phosphate buffer (25 mM, pH = 7.2) was used as eluent buffer. A running gradient from eluent A consisting of buffer and 0.75 vol% THF to eluent B consisting of methanol, acetonitrile, and buffer (35/15/50 vol%) within 50 minutes was used for the separation of the amino acids.

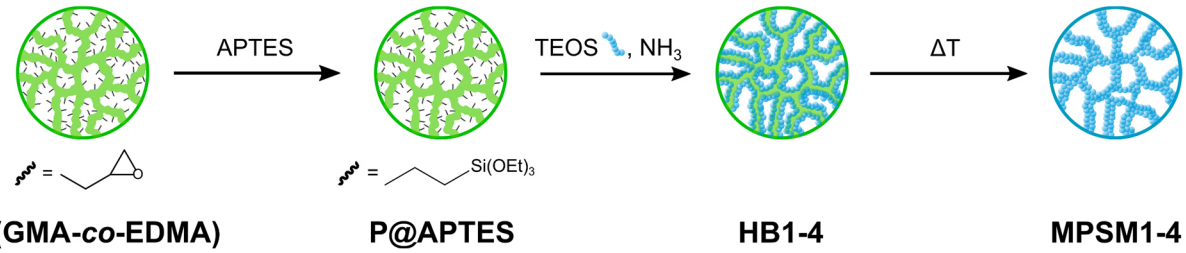


**Figure 8.1** Fabrication of mesoporous silica microspheres using (3-aminopropyl) triethoxysilane functionalized particles as hard template.

## 8.2.3. Synthesis

***p*(GMA-*co*-EDMA)** particles were prepared by a modified procedure which was reported earlier (for details see S.I.)[1,22,56,57,118].

### *8.2.3.1. Preparation of (3-aminopropyl) triethoxysilane functionalized particles* ***P@APTES***

5 g of *p*(GMA-*co*-EDMA) particles were dispersed in 150 mL of methanol, 52.5 mL of (3-aminopropyl) triethoxysilane was added and the mixture was stirred at 60 °C (130 rpm) for 24 h. The particles were separated from the solution, washed three times with $H_2O$ and EtOH, each and dried at 65 °C for 16 h.

### *8.2.3.2. Preparation of particles* ***HB1–4*** *and* ***MPSM1–4***

5 g of APTES functionalized particles (**P@APTES**) were dispersed in 270 mL of methanol (**HB1**), ethanol (**HB2**), 2-propanol (**HB3**) and 1-butanol (**HB4**), respectively, and 30 mL of $H_2O$. Then 12.5 mL of TEOS and 1.25 mL of an ammonia solution were added and stirred at room temperature (130 rpm) for 24 h. The particles were separated from the solution, washed three times with $H_2O$ and EtOH, each and dried at 65 °C for 16 h

to generate **HB1–4**. After calcination at 600 °C for 10 h mesoporous silica microspheres **MPSM1–4** remained.

*8.2.3.3. Octadecyl functionalization of **MPSM1–4** for chromatographic measurements*

5 g of silica particles **MPSM1–4** were dispersed in 600 ml of hydrochloric acid (3.7 %) and stirred for 3 h at 100 °C (130 rpm). The particles were separated from the solution, washed with EtOH and $H_2O$ until neutral and dried at 65 °C for 16 h. The particles were then dispersed in 75 mL of toluene, 25 mL of trimethoxy (octadecyl) silane and 0.5 mL of triethylamine were added, and the mixture was stirred at 100 °C (130 rpm) for 6 h. The particles were separated from the solution, washed three times with toluene, three times with EtOH and twice with MeOH and dried at 65 °C for 16 h.

2 g of functionalized particles were packed with 25 mL of acetone as slurry and MeOH / $H_2O$ (85 vol% / 15 vol%) as pressure medium.

For the analysis of amino acids by reversed-phase chromatography, derivatization of the samples is necessary for detection. In this case, a pre-column derivatization with a mixture of *ortho*-phthalaldehyde and 3-mercaptopropionic acid was used for the primary amines. The derivatized samples were excited with a fluorescence detector at 330 nm and detected at 450 nm. A gradient of 100 % eluent A to 100 % eluent B was run within 50 minutes. A 25 mM sodium phosphate buffer (pH 7.2) containing 0.75 % THF was used as eluent A and a mixture of methanol, acetonitrile, and sodium phosphate buffer (35/15/50 vol%) was used as eluent B. Peaks were assigned by retention times based on single measurements of amino acids in the measurement system.

## 8.3. Results and discussion

Mesoporous micron sized silica particles **MPSM1–4** were prepared from ***p*(GMA-*co*-EDMA**) polymer as starting material in three steps (**Figure 8.1**)[22,119] Monodisperse ***p*(GMA-*co*-EDMA**) polymer microspheres with a size of 7.6 µm are obtained by a seeded swelling polymerization[1,2,57]. The pore properties of the organic polymer are characterized by a median pore size of 16.2 nm, a pore volume of 0.20 mL $g^{-1}$ and a specific surface area of 121 $m^2$ $g^{-1}$ (**Table 8.1**). Functionalization of ***p*(GMA-*co*-EDMA)** with APTES to give **P@APTES** was achieved via nucleophilic attack of the amino group at the epoxide of the polymer, which results in ring opening to form an amino alcohol (**Figure 8.1**). Connecting APTES to the polymer did not change the template in size, dispersity, and morphology. From thermogravimetric measurements and elemental analysis of **P@APTES** a silica content of 6.6 % (**Figure 8.3**) and a nitrogen content of 1.6 % were estimated, which confirmed the successful functionalization of the ***p*(GMA-*co*-EDMA)** particles with APTES[118]. TEOS as precursor was hydrolyzed and condensed to silica nanoparticles (SNPs) in a base-catalyzed sol-gel process in metha-

nol, ethanol, 2-propanol, and 1-butanol, respectively, as solvents. In the presence of **P@APTES** the *in situ* formed SNPs diffuse into the template where they aggregate and built the polymer/silica hybrid beads **HB1–4,** which consist of interpenetrating organic/inorganic networks (**Figure 8.1**, **Table 8.1** and **Figure S. 8.3**). The polymer template was removed by calcination leaving the mesoporous silica microspheres **MPSM1–4** (**Table 8.1**, **Figure 8.2**).

**Table 8.1** Particle properties

| | **particle size** | **dispersity $d_{90}/d_{10}$** | **median pore size** | **pore volume** | **specific surface area** |
|---|---|---|---|---|---|
| | /μm | | /nm | /$cm^3\ g^{-1}$ | /$m^2\ g^{-1}$ |
| ***p*(GMA-*co*-EDMA)** | 7.6 | 1.22 | 16.2 | 0.20 | 121 |
| **P@APTES** | - | - | 15.9 | 0.17 | 94 |
| **HB1** | 8.2 | 1.09 | 20.3 | 0.08 | 42 |
| **HB2** | 8.4 | 1.06 | 27.3 | 0.03 | 15 |
| **HB3** | 8.3 | 1.07 | 29.3 | 0.04 | 13 |
| **HB4** | 8.4 | 1.08 | 29.8 | 0.01 | 5 |
| **MPSM1** | 5.8 | 1.22 | 4.7 | 0.73 | 573 |
| **MPSM2** | 7.4 | 1.14 | 20.3 | 0.46 | 309 |
| **MPSM3** | 7.1 | 1.21 | 20.3 | 0.48 | 317 |
| **MPSM4** | 7.7 | 1.10 | 23.5 | 0.49 | 247 |

The size of the hybrid beads **HB1–4** increases by 600 to 800 nm compared to that of the *p*(GMA-*co*-EDMA) template, while the size distributions of the hybrid particles remained highly monodisperse (**Table 8.1**). When methanol was applied as solvent an edged morphology was obtained (**Figure S. 8.3**). In ethanol and 2-propanol the silica network consisted of nanometer-sized SNPs which enter the pores of the template and agglomerate. As a result, a particulate morphology is obtained. Larger SNPs were formed in 1-butanol which result in a cauliflower-like morphology of the hybrid beads **HB4** (**Figure S. 8.3**). To conclude, with increasing chain length of the alcoholic solvent larger nanometer-sized SNPs are formed, which construct the silica network in the **P@APTES** template.

After the polymer was removed by calcination the silica networks of all particles shrank. Compared to the size of the template the size of the silica particle **MPSM1** is reduced to 5.8 μm while those of the silica particles **MPSM2–4** showed only minor changes and remained comparable to the size of the template (**Table 8.1**). The original morphologies of the hybrid particles were transferred to the final mesoporous silica particles (**Figure 8.2**). Thus, in methanol an edged, in ethanol and 2-propanol a particular and in 1-butanol a cauliflower surface was obtained (**Figure 8.2**).

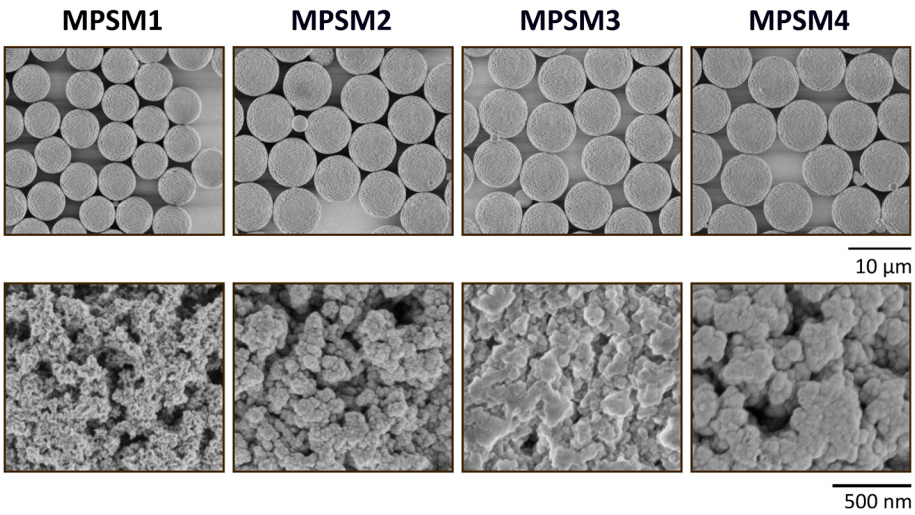


**Figure 8.2** Scanning electron microscopy images (top row: 2,000x, bottom row: 50,000x magnification) from silica particles **MPSM1–4** after calcination at 600 °C for 10 h.

The thermogravimetric curves of the hybrid beads **HB1–4** are composed of the thermal degradation behavior of silica and **P@APTES** (**Figure 8.3**). Roughly three regions of degradation can be identified. The loss of surface water, which is mainly due to the silica, is observed between 30 and 150 °C. Depolymerization and isomerization processes of the polymer template between 200 and 400 °C, as well as degradation of the polymer backbone between 400 and 600 °C lead to the complete decomposition of the template **P@APTES**[222–224]. Moreover, thermogravimetric analysis of the hybrid beads **HB1–4** reveal that different amounts of silica were deposited in the pores of **P@APTES** (**Figure 8.3**).

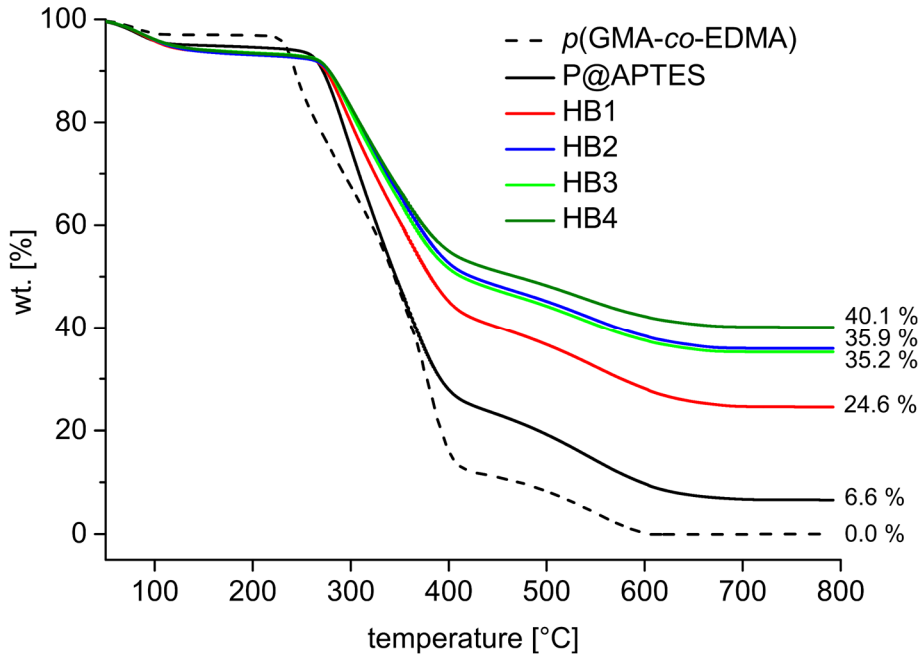


**Figure 8.3** Thermogravimetric analysis curves of the thermal degradation of ***p*(GMA-*co*-EDMA)**, **P@APTES** and **HB1–4** particles.

The smallest quantity of silica was found in the particles **HB1** (24.6 % silica). Hybrid beads **HB2**, **HB3** and **HB4** contain higher amounts of silica (35.9 %, 35.2 % and 40.1 %, respectively). Interestingly, these results indicate that the extent of silica which is incorporated into the polymer network depends on the size of the SNPs that form the silica network.

The silica network that penetrates the polymer template **P@APTES** leads to a decrease of the pore volumes as well as the specific surface areas in the hybrid beads **HB1–4** (**Table 8.1**, **Figure S. 8.4**). Thus, in the hybrid particles **HB1,** which contain the least silica, remain the highest pore volume (0.08 mL $g^{-1}$) and specific surface area of 42 $m^2$ $g^{-1}$ of all hybrid beads. The pore volumes and the specific surface area of **HB2** and **HB3** decreased more (0.03 mL $g^{-1}$ and 0.04 mL $g^{-1}$, as well as 15 $m^2$ $g^{-1}$ and 13 $m^2$ $g^{-1}$). The largest SNPs were formed in 1-butanol, which resulted in the smallest pore volume (0.01 mL $g^{-1}$) and specific surface area (5 $m^2$ $g^{-1}$) for **HB4**. The median pore sizes increase steadily from **HB1** to **HB4** (**Table 8.1**, **Figure S. 8.4**). This is a consequence of the size of the SNPs which are responsible for the pore properties. Larger SNPs lead to a lower specific surface area and higher median pore diameters[3]. With higher chain length of the alcoholic solvent the pore volume of the hybrid beads reduces.

Removing the organic polymer from the hybrid particles by calcination leaves more space in the final MPSMs. Thus, compared to the hybrid materials, the MPSMs possesses considerably larger pore parameters in terms of pore volume and specific surface area (**Table 8.1**, **Figure 8.4**). During calcination of **HB1** the resulting **MPSM1** shrank and the number of pores in the range 20.3 nm in diameter is strongly reduced, while the pores with a size of 4.7 nm remain (**Figure 8.4**). As a consequence of the small pores and the high pore volume (0.73 mL $g^{-1}$), the highest specific surface area of the present experimental series of 573 $m^2$ $g^{-1}$ is obtained. The pore parameters of the particles **MPSM2** and **MPSM3** are very similar. Both MPSMs have a pore volume of ~ 0.5 mL $g^{-1}$, a specific surface area of 305 – 320 $m^2$ $g^{-1}$ and a median pore size of 20.3 nm. The median pore diameter of **MPSM4** is 23.5 nm. Due to larger pores, a lower specific surface area of 247 $m^2$ $g^{-1}$ results.

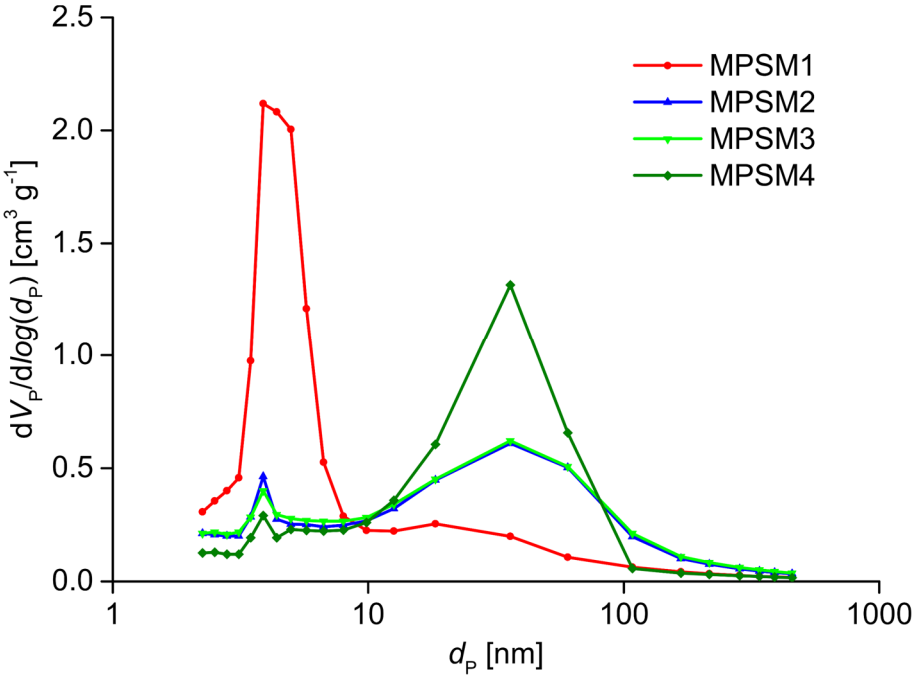


**Figure 8.4** Pore size distributions of silica particles **MPSM1–4**.

The $^{13}$C CP/MAS NMR and DRIFT-IR spectra of the *p*(GMA-*co*-EDMA) particles show the corresponding signals and bands of the copolymer (**Figure S. 8.5** and **Figure S. 8.6**, S.I.)[55,57,150]. Successful functionalization with (3-aminopropyl) triethoxysilane was confirmed by additional characteristic resonances in the $^{13}$C NMR spectrum and absorption bands in the DRIFT IR spectrum of **P@APTES** (**Figure S. 8.5** and **Figure S. 8.7**, S.I.)[225]. The $^{13}$C NMR spectrum of the hybrid particles do not change compared to the previous stage. The resulting characteristic bands of the siloxane network and the silanol groups are also visible in the IR spectra of the polymer/silica hybrid particles (**Figure S. 8.8**, S.I.).

In the $^{29}$Si CP/MAS NMR spectrum of **P@APTES** four resonances are observed between -40 and -80 ppm which are assigned to non-hydrolyzed ($T^0$), partially condensed ($T^1$, $T^2$) and fully condensed ($T^3$) alkoxy silane species (**Figure 8.5**a)[226]. Obviously the trialkoxy silane function hydrolyze and condense to some extent during the functionalization of the templates. In the $^{29}$Si CP/MAS NMR spectrum of the hybrid beads, the $Q^2$, $Q^3$ and $Q^4$ groups at -100 and -110 ppm, respectively, confirm the successful incorporation of silica into the template (**Figure 8.5**b). Interestingly, the signal pattern of the T groups, corresponding to the trialkoxy silane function, in $^{29}$Si CP/MAS NMR spectrum of the hybrids hardly changed compared to that in the spectrum of **P@APTES** (**Figure 8.5**a,b). This indicates that the *in situ* formed SNPs do not condense with the T groups bound to the template, but rather fill the pores. $^{29}$Si HPDEC NMR spectra of the hybrid materials and MPSMs show that the silica network is mainly constructed of fully condensed $Q^4$ groups (**Figure 8.5**b). While after calcination the T groups are completely

converted to Q groups (**Figure 8.5**c), the conversion of $Q^2$ and $Q^3$ to fully condensed $Q^4$ groups require higher temperatures[121].

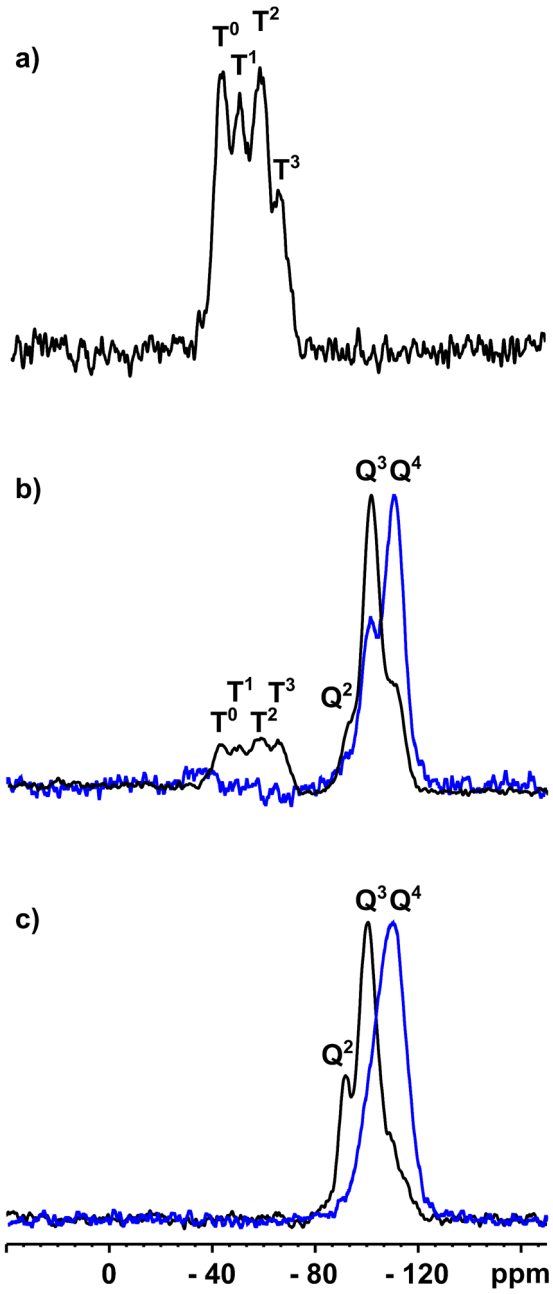


**Figure 8.5** $^{29}$Si CP/MAS NMR spectra (black) and $^{29}$Si HPDEC NMR (blue dashed) of functionalized template **P@APTES** (**a**), hybrid beads **HB** (**b**) and mesoporous silica microspehres **MPSM** (**c**).

The morphology and pore properties of the particles **MPSM1–4** are determined by the size of the nonporous SNPs, which construct the silica network (**Figure 8.2**). The SNPs are generated via a sol-gel process *in situ* and diffuse into the pores of the **P@APTES** template. The size of the SNPs is controlled by the parameters of the sol-gel process and the diffusion rate of the SNPs into the template[3]. Here, under otherwise identical reaction conditions the choice of the solvent controls the *in situ* SNP growth, and thus the property of the final MPSM. Based on the low hydrolysis and condensation rate of

TEOS in methanol a low yield of silica is incorporated into the template (**HB1**), which results in smaller **MPSM1** particles after calcination. The small SNPs condense and the silica network shrinks when the size-forming template is decomposed. The large mesopores, distributed in the template, also disappear, leaving only mesopores of a size of 4.7 nm. In ethanol, 2-propanol, and butanol the SNPs become larger and construct a silica network with larger pores. Due to the introduction of larger amounts of silica into the pores of the template and their larger SNPs, **MPSM2–4** map the template and the void space remains intact after calcination. Consequently, the median pore sizes of the particles **MPSM2–4** hardly decrease.

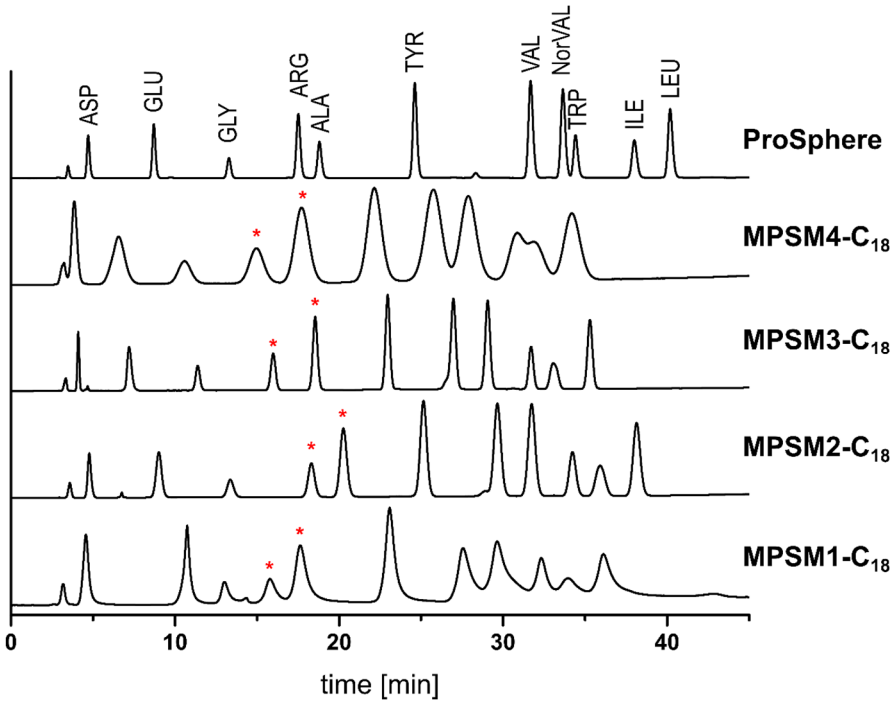


**Figure 8.6** Separation of eleven amino acids on **MPSM1–4-C**$_{18}$. Chromatographic settings: column dimension: 250 x 4.6 mm; mobile phase A: sodium phosphate buffer (25 mM, pH = 7.2) with 0.75 vol% THF, mobile phase B: MeOH/ACN/buffer (35/15/50 vol%); gradient from 0 % B to 100 % B within 50 minutes; injection volume: 20 µl (2.1 µmol µL$^{-1}$ each amino acid); column temperature: 30 °C; fluorescence detection: 330 nm extinction, 450 nm emission. The order of elution (asterisk) of arginine and alanine is reversed for all MPSMs compared to that of the ProSphere column.

Porous silica particles are commonly used as $C_{18}$ functionalized materials in reversed-phase chromatography[37,189]. To determine the separation behavior of the MPSMs as stationary phase, the particles **MPSM1–4** were functionalized with trimethoxy (octadecyl) silane and packed in a 250 x 4.6 mm stainless steel column with acetone as slurry and MeOH / $H_2O$ (85 v.% / 15 v.%) as pressure medium. A linear gradient from 100 % eluent A to 100 % eluent B in 50 minutes was applied to separate the amino acids. The primary amines were derivatized with a mixture of *ortho*-phthalaldehyde and 3-mercaptopropionic acid. Therefore, the analytes were treated with the pre-column derivatization reagent for 90 seconds and then injected. All injections were per-

formed with freshly prepared samples to avoid degradation of the derivatization agent. The derivatized samples were excited with a fluorescence detector at 330 nm and detected at 450 nm. The separation behavior of the four new stationary phases was compared with the commercially available column ProSphere C18 (300 Å, 10 µm, 250 x 4.6 mm).

**Figure 8.6** shows the separation of a mixture of 11 different amino acids consisting of aspartic acid, glutamic acid, glycine, arginine, alanine, tyrosine, valine, norvaline, tryptophan, isoleucine, and leucine. As a result of the high specific surface area of **MPSM1**, the analytes interact longer with the stationary phase, which leads to an incomplete separation. Thus, on **MPSM1-C$_{18}$** just ten of the amino acids can be detected and in addition, the last five amino acids elute into each other. For **MPSM4-C$_{18}$** a few amino acids overlap, so that no complete separation of the components is obtained. This could result from the agglomerated morphology of **MPSM4**, which inhibits the accessibility of pores and thus impedes the diffusion of the analytes into the pores. In contrast to this, baseline separations of all amino acids were achieved with the stationary phases **MPSM2-C$_{18}$** and **MPSM3-C$_{18}$**. Since the particle size and pore parameters of **MPSM2** and **MPSM3** are very similar their chromatographic properties are comparable (**Figure 8.6** and **Table 8.2**). The peak resolution of the separation of arginine and alanine is increased for **MPSM3-C$_{18}$** and all amino acids elute earlier compared to **MPSM3-C$_{18}$** and ProSphere C18. Overall, the separation on both synthesized phases is comparable to the commercially available column. In addition, the phases achieve faster separation of amino acids without loss of quality (**Table 8.2**). Interestingly, the order of elution (asterisk) of arginine and alanine is reversed for all MPSMs compared to that of the ProSphere column (**Figure 8.6**).

**Table 8.2** Column performance for the separation of several amino acids of the MPSM-C$_{18}$ and a commercially available column.

| | $R_{ASP-GLU}$ | $R_{GLU-GLY}$ | $R_{GLY-ARG}$ | $R_{ARG-ALA}$ | $R_{ALA-TYR}$ | $R_{TYR-VAL}$ | $R_{VAL-NorVAL}$ | $R_{Nor-VAL-TRP}$ | $R_{TRP-ILE}$ | $R_{ILE-LEU}$ |
|---|---|---|---|---|---|---|---|---|---|---|
| **MPSM1-C$_{18}$** | 10.07 | 3.20 | 2.81 | 1.55 | 4.86 | 3.68 | 1.35 | 1.88 | 0.95 | 1.16 |
| **MPSM2-C$_{18}$** | 8.06 | 6.24 | 6.53 | 2.49 | 6.25 | 5.63 | 2.51 | 3.04 | 1.76 | 2.27 |
| **MPSM3-C$_{18}$** | 8.55 | 8.37 | 8.73 | 4.64 | 8.25 | 7.14 | 3.55 | 4.68 | 1.84 | 2.95 |
| **MPSM4-C$_{18}$** | 2.56 | 2.71 | 2.75 | 1.62 | 2.63 | 2.00 | 1.12 | 1.55 | 0.53 | 1.29 |
| **ProSphere** | 11.32 | 11.33 | 9.36 | 2.75 | 12.29 | 14.04 | 3.72 | 1.48 | 6.54 | 3.87 |

## 8.4. Conclusion

APTES functionalized *p*(GMA-*co*-EDMA**)** particles provide a good platform to prepare MPSMs and are thus an alternative to amino functionalized *p*(GMA-*co*-EDMA) templates. The particle size, morphology, and pore parameters of MPSMs depend on the settings of the sol-gel process and are thus adjusted at the stage of the hybrid bead syntheses. If the amount of silica deposited in the template and the size of the SNPs are properly tuned the template is mapped accurately. Moreover, larger SNPs also ensure the preservation of the pore structure and the morphology of the MPSMs after calcination.

Interestingly $^{29}$Si NMR spectroscopy of the hybrid beads and MPSMs indicate that the SNPs do not covalently bind to the APTES functions. This agrees with observations made earlier that TEOS is hydrolyzed and condensed in the alcoholic solvent to SNPs before they diffuse into the template[3]. As the SNP growth depends on the solvent, morphology and pore properties of the final MPSM can be adjusted simply by the right choice of the solvent.

## 8.5. Supplementary Information

### 8.5.1. Chemicals

Polyvinyl alcohol (PVA, 87–89 % hydrolyzed, mean average 88000 – 97000 g $mol^{-1}$) and polyvinylpyrrolidone $K_{30}$ (PVP, mean average 40000 g $mol^{-1}$) were aquired from abcr GmbH. Ethyleneglycol dimethacrylate (EDMA) was bought from Acros Organics. Cyclohexanol and sodium dodecyl sulfate (SDS) were purchased from Carl Roth. Styrene was obtained by Fisher Chemicals. Dibenzoyl peroxide (BPO), dibutyl phthalate (DBP) and glycidyl methacrylate (GMA) were purchased from Sigma-Aldrich.

### 8.5.2. Synthesis of polystyrene

Monodisperse polystyrene particles with diameters of 1.9 ± 0.1 µm were prepared as reported earlier[57] (**Figure S. 8.1**).

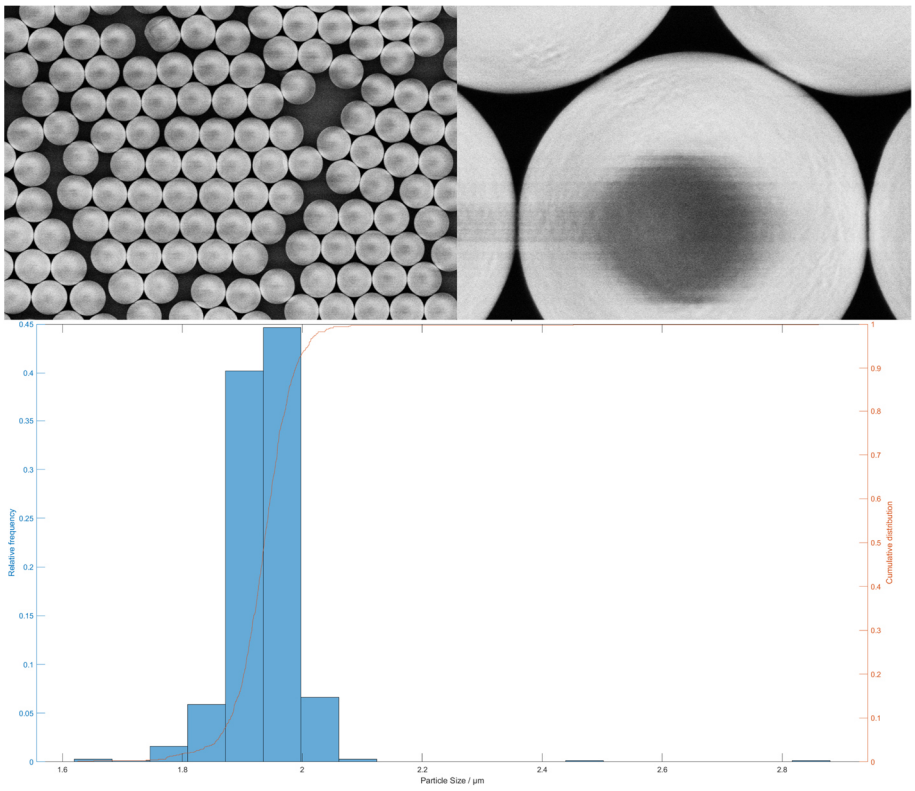


**Figure S. 8.1** Scanning electron microscopy images of applied polystyrene particles (top) and their particle size distribution (bottom).

### 8.5.3. Synthesis of *p*(GMA-*co*-EDMA)

0.3 g of polystyrene particles and 5 mL of an aqueous SDS solution (0.25 wt%) were dispersed in a 250 mL flask. 2 mL DBP were emulsified in 150 mL aqueous SDS solution (0.25 wt%) with a homogenizer at 4500 rpm for 15 min and then added to the polystyrene suspension. The mixture was stirred for 24 h at 200 rpm. 6 mL GMA, 9 mL EDMA, 4 mL cyclohexanol, 11 mL toluene, 0.4 g BPO and 150 mL aqueous SDS solution (0.25 wt%) were emulsified with a homogenizer at 4500 rpm for 15 min. This emulsion, a 150 mL aqueous PVA solution (2.3 wt%) and the activated polystyrene particles were transferred to a 500 mL three-necked flask and stirred for 24 h at 200 rpm. Argon was passed into the reaction mixture for 30 minutes and then heated to 70 °C for 24 hours. The particles were separated from the solution, washed three times with EtOH and three times with $H_2O$ and dried at 65 °C for 16 h. The average particle size of the *p*(GMA-*co*-EDMA) particles is 7.6 ± 0.7 µm (**Figure S. 8.2**).

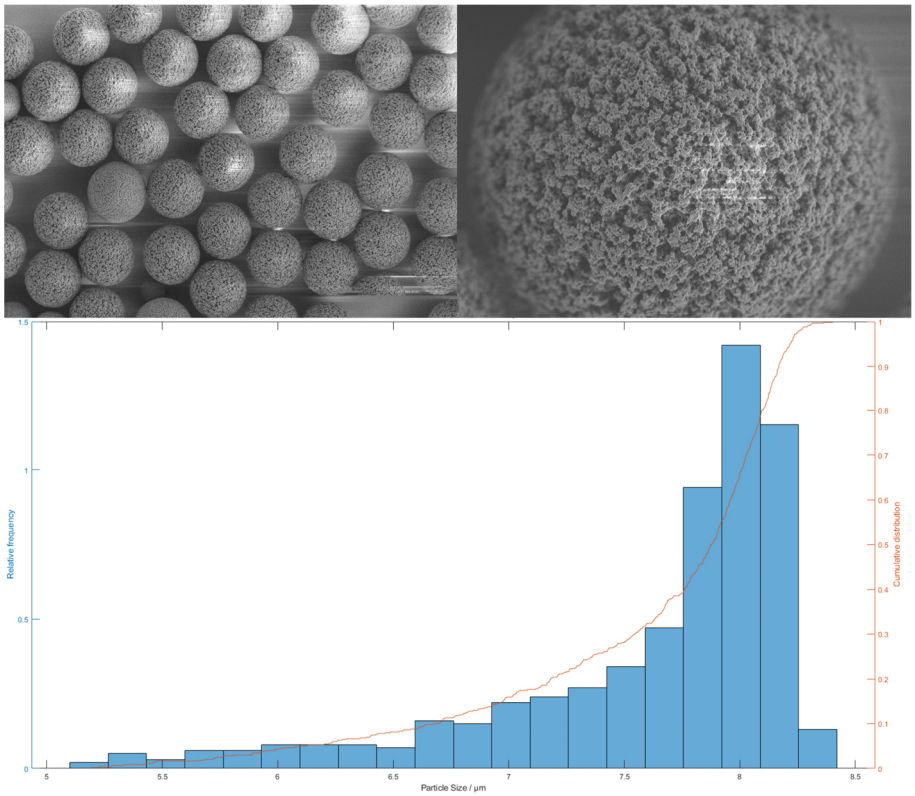


**Figure S. 8.2** Scanning electron microscopy images of the polymer templates *p*(GMA-*co*-EDMA) (7.6 ± 0.7 µm) (top) and the corresponding particle size distribution (bottom).

## 8.5.4. Characterization of HBs

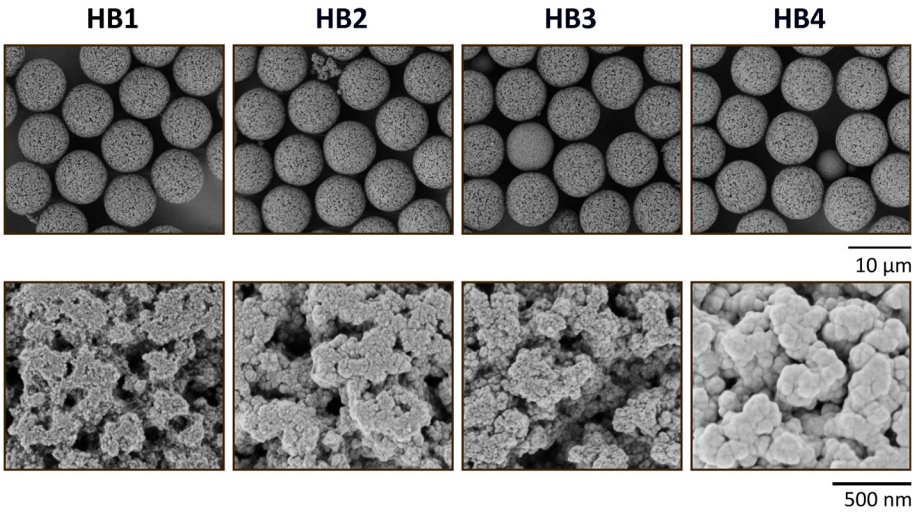


**Figure S. 8.3** Scanning electron microscopy images (top row: 2,000x, bottom row: 50,000x magnification) from hybrid beads after sol-gel process in methanol (**HB1**), ethanol (**HB2**), 2-propanol (**HB3**) and 1-butanol (**HB4**).

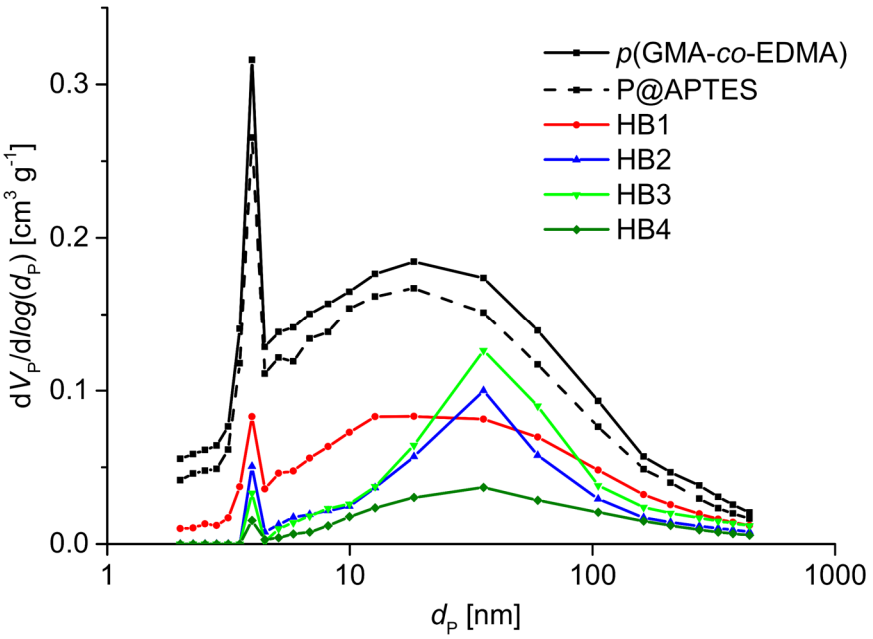


**Figure S. 8.4** Pore size distributions of porous ***p*(GMA-*co*-EDMA)**, functionalized **P@APTES** template and hybrid beads **HB1–4**.

8.5.5. $^{13}C$ CP/MAS solid state NMR spectroscopy of *p*(GMA-*co*-EDMA) and P@APTES

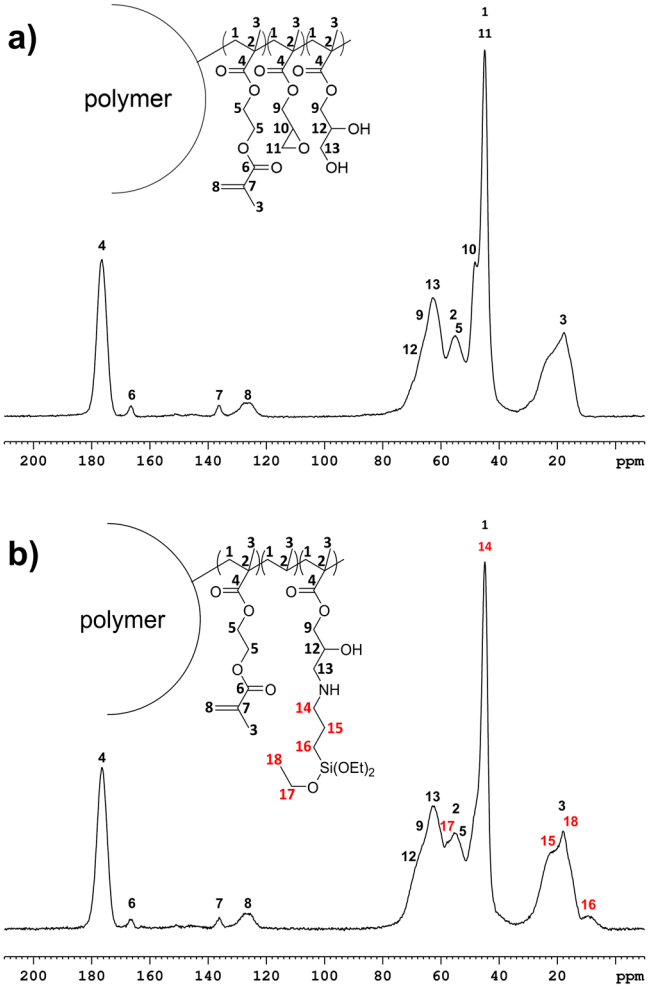


**Figure S. 8.5** $^{13}C$ CP/MAS NMR spectra of **a)** *p*(GMA-*co*-EDMA) and **b)** P@APTES particles.

### 8.5.6. DRIFT IR spectroscopy of *p*(GMA-*co*-EDMA), P@APTES, HBs and MPSMs

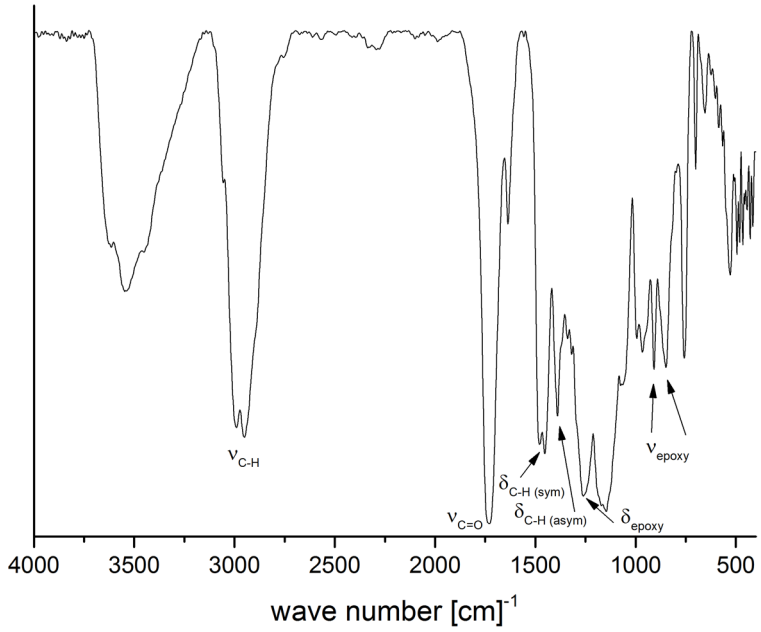


**Figure S. 8.6** DRIFT IR spectra of *p*(GMA-*co*-EDMA) copolymer particles.

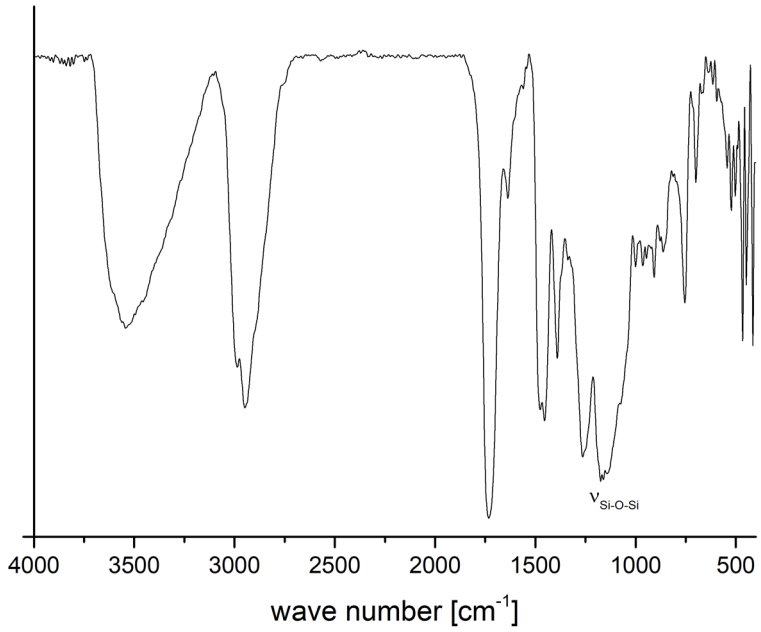


**Figure S. 8.7** DRIFT IR spectra of functionalized P@APTES particles.

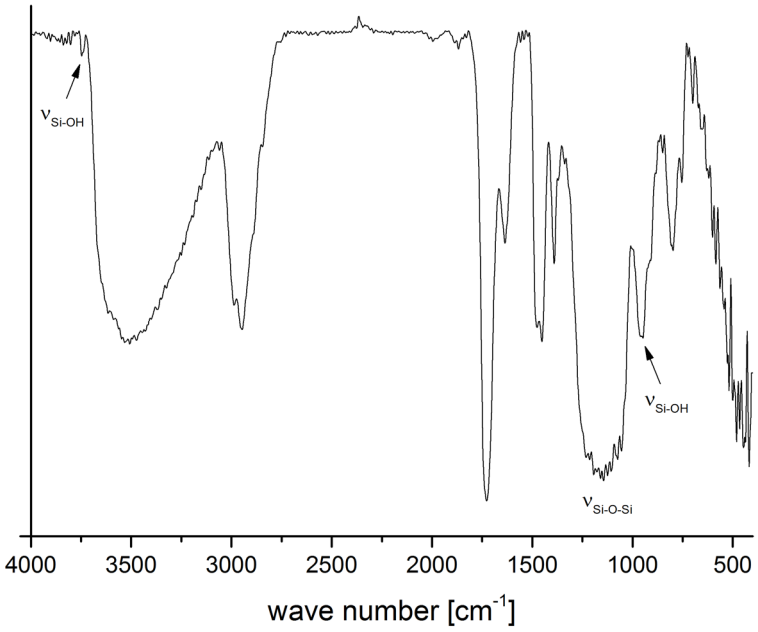


**Figure S. 8.8** DRIFT IR spectra of **HB2** exemplary for hybrid particles.

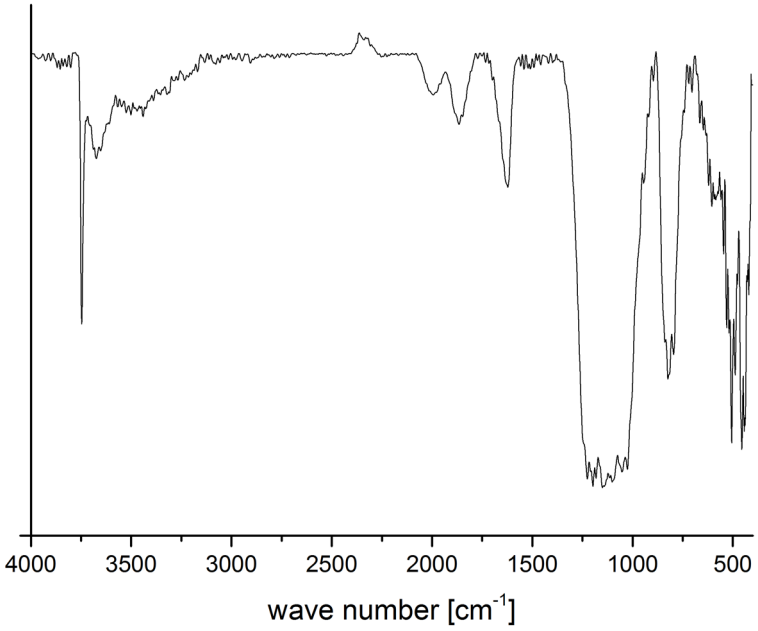


**Figure S. 8.9** DRIFT IR spectra of **MPSM2** exemplary for silica particles.

**Acknowledgments:** This research was funded the by Bundesministerium für Bildung und Forschung (BMBF, grant number 13FH647IX6) and the Bundesministerium für Wirtschaft und Energie (AiF/ZIM, grant number ZF4019203SL8). Furthermore, we would like to thank our cooperation partner Dr. Maisch GmbH for their support in preparing the columns. We thank Elke Nadler for contributing the SEM measurements.

**CRediT authorship contribution statement:** F.F. and J.C.S. conducted the research and investigation processes. F.F. specifically was performing the synthesis of the materials. FF. and J.C.S. were both involved in the analyses of the materials. H.A.M. and A.K. did the project administration, funding acquisition and supervision. All authors have read and agreed to the published version of the manuscript.

# 9. Paper VI

## Tailoring the Morphology of Monodisperse Mesoporous Silica Particles Using Different Alkoxysilanes as Silica Precursors

*Fabio Fait[1,2], Stefanie Wagner[1], Julia C. Steinbach[2], Andreas Kandelbauer[2] and Hermann A. Mayer*[1]*

[1] Institute of Inorganic Chemistry, University of Tübingen, Auf der Morgenstelle 18, 72076 Tübingen, Germany

[2] Process Analysis and Technology (PA&T), Reutlingen Research Institute, Reutlingen University, Alteburgstrasse 150, 72762 Reutlingen, Germany

[3] Institute of Wood Technology and Renewable Materials, Department of Material Sciences and Process Engineering (MAP), University of Natural Resources and Life Sciences, Gregor-Mendel-Straße 33, 1180 Vienna, Austria

* Correspondence: hermann.mayer@uni-tuebingen.de



Fait, F.; Wagner, S.; Steinbach, J.C.; Kandelbauer, A.; Mayer, H.A. Tailoring the Morphology of Monodisperse Mesoporous Silica Particles Using Different Alkoxysilanes as Silica Precursors. *International Journal of Molecular Sciences* **2023**, *24*, 11729, doi:10.3390/ijms241411729.[6]

## Abstract

The use of hard template method for the preparation of monodisperse mesoporous silica particles (MPSM) has been established in recent years. $SiO_2$ is incorporated into functionalized porous *poly*(glycidyl methacrylate-*co*-ethylene glycol dimethacrylate) polymers in form of silica nanoparticles (SNPs). After removal of the template, porous silica materials remain. The size of the deposited SNPs is controlled by the hydrolysis rate of the alkoxysilane. In this article, various precursors with different hydrolysis rates were used and the particle and pore properties of the MPSM were investigated. The properties and morphology of the MPSMs differ according to the SNPs, which are formed in the continuous phase. As an alternative, the sol-gel process was carried out in water only, so that particle formation occurs in the pores of the templated material. The combination of different alkoxysilanes allows the individual design of the morphology of porous silica particles. The use of the particles as stationary phase in high performance liquid chromatography was exemplarily demonstrated with the separation of various water-soluble vitamins.



## Keywords

mesoporous silica microspheres (MPSM), hard template method, high performance liquid chromatography (HPLC)


## 9.1. Introduction

The introduction of high performance liquid chromatography enabled a rapid chemical analysis and separation process of substances and end products. The wide range of applications extends from small molecules[227–229] to pharmaceuticals[230,231], food and environmental analysis[232–234], long-chain polymers[235,236], and biomolecules[237–239]. The most common material in HPLC columns are spherical silica particles because of their mechanically robustness. Moreover, silica particles possess reactive groups on their surface, through which a variety of functionalization are possible[240–242]. Characteristics such as particle size, dispersity, pore structure and surface functionalization influence their chromatographic properties such as selectivity, analysis time, plate number and back pressure. Due to their high specific surface area, fully porous silica particles in the µm range have proven successful in HPLC[243–245].

Probably the best-known representation of spherical silica networks is the Stöber process[45]. Non-porous spherical silica particles in the range of 10 nm to 500 nm can be formed by ammonia-catalyzed hydrolysis and condensation of molecular alkoxysilanes. With semi-batch processes and addition of electrolytes, the particle size can be increased into the µm range[183–185,216].

The hydrolysis rate of the alkoxysilanes is crucial for the size of the siloxane network. The hydrolysis rate is controlled by different parameters like chain length and branching of the alkoxysilane, $NH_3$ and $H_2O$ concentrations, chain length and branching of the alcohol which is used as solvent and temperature[45,90,93,94,215,246]. Under basic conditions an increase in the chain length of the alkyl groups of the alkoxysilane leads to a decrease in the rate of hydrolysis. The increasing steric hindrance and inductive effects of the alkyl groups increase the electron density at the silicon atom and make a nucleophilic attack more difficult. In addition, the decreasing polarity of the alkoxysilanes can lead to phase separation, depending on the solvent applied[89,95,246,247]. The $NH_3$ and $H_2O$ concentrations influence the equilibrium reactions of hydrolysis and condensation. While under basic conditions the condensation of hydrolyzed alkoxysilanes is extremely fast, higher concentrations of $H_2O$ promotes the hydrolysis positively but the condensation negatively[88,90,92,246,247]. Overall, the Stöber process provides non-porous silica nanoparticles with narrow size distributions. The preparation of monodisperse silica particles in the micrometer range are challenging and remain nonporous.

For the synthesis of mesoporous silica microspheres (MPSMs) with narrow size distributions a protocol has been developed that employs functionalized porous *poly* (glycidyl methacrylate-*co*-ethylene glycol dimethacrylate) polymer particles (*p*(GMA-*co*-EDMA)) as hard templates in the presence of the basic hydrolysis and condensation of TEOS[55]. *P*(GMA-*co*-EDMA) functionalized with trimethylamine, (3-amino propyl) triethoxysilane or tetra ethylene pentamine (TEPA) provide excellent environments to deposit silica nanoparticles (SNPs) in the pores of the template where they form a silica network[22,57,119]. Best matches of the templates are achieved if the rate of the growth of the SNPs and their rate of diffusion into the template pores are well balanced. Moreover, the particle and pore properties correlate with the size of the SNPs which depends on the sol gel conditions and the template[2,3].

In this study, we investigated the influence of precursors with different rates of hydrolysis on the particle and pore properties of MPSMs. For this the sol-gel process is carried out under basic conditions in the presence of a tetra ethylene pentamine functionalized *p*(GMA-*co*-EDMA) template (P@TEPA). The size of the silica nanoparticles that accumulate in and on the template depends on the hydrolysis rate of the precursors. The *p*(GMA-*co*-EDMA)/$SiO_2$ hybrid beads (HB) and the MPSMs are characterized for their particles and pore properties by scanning electron microscopy, thermogravimetric analysis, and nitrogen adsorption measurements. Finally, selected MPSMs are functionalized with trimethoxy (octadecyl) silane and used as stationary phases for the separation of different water-soluble vitamins.

## 9.2. Materials and methods

### 9.2.1. Chemicals

Tetraethyl orthosilicate (TEOS), tetramethyl orthosilicate (TMOS) and trimethoxy (octadecyl) silane (ODTMS) were obtained from abcr GmbH. Ammonia (28–30 % aqueous solution), tetrapropyl orthosilicate (TPOS) and tetrabutyl orthosilicate (TBOS) were purchased from Alfa Aesar. Ethanol, hydrochloric acid, 2-propanol, triethylamine and the water-soluble vitamins (Vit. $B_1$, $B_3$, $B_5$, $B_9$, $B_{12}$) were bought from Sigma-Aldrich. Acetonitrile and water (all HPLC grade) were purchased from fisher scientific. Toluene and deionized water were cleaned through a solvent purification system. The test mixture (uracil, phenol, *N*,*N*-diethyl-*m*-toluamide, toluene) for column characterization were provided by Dr. Maisch HPLC, Germany.

### 9.2.2. Characterization

For the evaluation of morphology, particle size and dispersity SEM images were acquired using a Hitachi SU8030. The mean particle diameter was obtained by calculating at least 400 particles from SEM images and is expressed in μm. The pore parameters of the materials are determined by nitrogen adsorption on a BELSORP MiniX from Microtrac Retsch GmbH. The sample preparation was carried out on a BELSORP VACII. For that, the silica materials were heated for 3 h at 300°C and a vacuum of 2 x $10^{-2}$ mbar to remove possible physisorbed residues and to achieve a reproducible equilibrium[67]. Adsorption and desorption isotherms were performed at 77 K. For the determination of the specific surface area, the adsorption isotherms were evaluated by the Brunauer-Emmet-Teller (BET) method, and for the pore volume (single point measurement at $p/p_0 = 0.95$) and pore size distributions, the desorption isotherms were evaluated by the Barrett-Joyner-Halenda (BJH) method using BELMaster 7 software[65,66]. The amount of $SiO_2$ was determined with thermogravimetric measurements on a Mettler Toledo TGA/DSC. Samples were weighed in an aluminum vessel and measured at a heating rate of 5 K $min^{-1}$ and synthetic air (50 mL $min^{1}$).

Analytical high performance liquid chromatography of water-soluble vitamins was performed on an Agilent 1100 series system from Agilent Technologies consisted of a quaternary pump with degasser, an auto sampling system, column oven and a diode array detector. Instrument control, data acquisition and automated data analysis was performed by the OpenLAB CDS software (Rev. C.01.07 SR3, Agilent Technologies). A running gradient of eluent A consisting of water and 0.025 vol% TFA to eluent B consisting of acetonitrile was used according to Heudi et al.[248]. The vitamins $B_1$, $B_5$ and $B_{12}$ (1 mg $mL^{-1}$), $B_3$ (0.5 mg $mL^{-1}$) and $B_9$ (2 mg $mL^{-1}$) were solved in water.

### 9.2.3. Synthesis

Monodisperse porous *p*(GMA-*co*-EDMA) particles were prepared by a seed suspension polymerization of glycidyl methacrylate and ethylene glycol dimethacrylate in the presence monodisperse polystyrene particles (1.5 µm ± 0.1 µm, **Figure S. 9.1**, S.I.)[1,55,57]. Then, the *p*(GMA-*co*-EDMA) particles were functionalized with TEPA according to previous reports (for Details see Supporting Information, **Figure S. 9.1**–**Figure S. 9.3** S.I. [3,57,119]) to generate P@TEPA template particles. A nitrogen content of 2.4 % and spectroscopic analysis indicates the successful functionalization.

#### *9.2.3.1. Preparation of monodisperse porous hybrid beads (**HB1a–f**, **HB2a–d**) and mesoporous silica microspheres (**MPSM1a–f**, **MPSM2a–d**)*

**Method 1:** 1 g of P@TEPA particles were dispersed in a mixture of 60 mL of 2-propanol and 7.5 mL of $H_2O$. Then 2.4 mL of TMOS (**a**), TEOS (**b**), TPOS (**c**) and TBOS (**d**), respectively, and 0.2 mL of an aqueous ammonia solution (28–30 %) were added and the mixture was stirred at 200 rpm for 24 h to produce hybrid beads **HB1a–d** (Table 1).

The hybrids **HB1e–f** were produced after 2.4 mL of TEOS and 1.5 mL of TMOS (**e**) or TPOS (**f**), respectively, and 0.2 mL of an aqueous ammonia solution (28–30 %) were added to a dispersion of 1 g P@TEPA particles in 60 mL of 2-propanol and 7.5 mL of $H_2O$. The mixture was stirred at 200 rpm for 24 h (**Table 9.1**).

**Method 2**: 1 g of P@TEPA particles were dispersed in 67.5 mL of $H_2O$. Then 2.4 mL of the corresponding alkoxysilane were added and the mixture was stirred at 200 rpm. After 24 h, 0.2 mL of an aqueous ammonia solution (28–30 %) was added and the reaction was stirred for further 24 h at 200 rpm to produce hybrid beads **HB2a–d** (**Table 9.1**).

All hybrid beads were separated from their solutions, washed three times with EtOH and three times with $H_2O$ and dried at 65 °C for 16 h. The resulting hybrid beads were calcinated at 600 °C for 10 h to provide the corresponding mesoporous silica microspheres **MPSMs** (**Table 9.1**).

#### *9.2.3.2. Octadecyl functionalization of mesoporous silica microspheres for chromatographic measurements*

5 g of silica particles **MPSM1b** were dispersed in 600 mL of hydrochloric acid (3.7 %) and stirred for 3 h at 100 °C (200 rpm). The particles were separated from the solution, washed with EtOH and $H_2O$ until neutral and dried at 65 °C for 16 h. The particles were then dispersed in 75 mL toluene, 25 mL of ODTMS and 0.5 mL of triethylamine were added, and the mixture was stirred at 100 °C (200 rpm) for 6 h. The particles were separated from the solution, washed three times with toluene, three times with EtOH and twice with MeOH and dried at 65 °C for 16 h.

The functionalized particles were packed with acetone as slurry and MeOH / $H_2O$ (85 vol% / 15 vol%) as pressure medium.

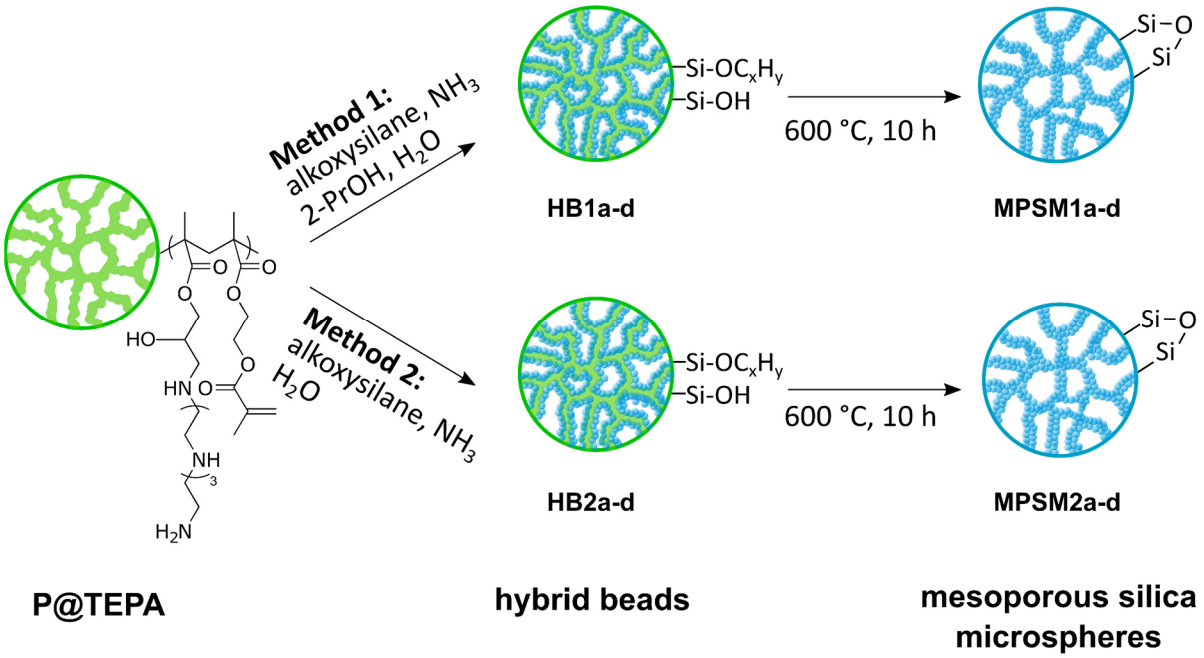


**Scheme 9.1** Synthesis of mesoporous silica microspheres with the alkoxysilanes TMOS (**a**), TEOS (**b**), TPOS (**c**) and TBOS (**d**) as precursors.

## 9.3. Results and discussion

**Table 9.1** Particle properties of hybrid beads and corresponding mesoporous silica microspheres.

| | particle size | $SiO_2$ content | | particle size | median pore size | pore volume | specific surface area |
|---|---|---|---|---|---|---|---|
| | /µm | /% | | /µm | /nm | /mL $g^{-1}$ | /$m^2$ $g^{-1}$ |
| **HB1a** | 6.3 | 37.8 | **MPSM1a** | 6.0 | 23.6 | 0.50 | 271 |
| **HB1b** | 6.3 | 29.9 | **MPSM1b** | 5.5 | 11.3 | 0.84 | 389 |
| **HB1c** | 6.3 | 17.7 | **MPSM1c** | 3.6 | 8.8 | 0.62 | 339 |
| **HB1d** | 6.3 | 6.6 | **MPSM1d** | 2.2 | 4.0 | 0.68 | 637 |
| **HB2a** | 6.7 | 32.7 | **MPSM2a** | 5.9 | 15.7 | 0.87 | 390 |
| **HB2b** | 6.2 | 35.8 | **MPSM2b** | 6.0 | 24.9 | 0.69 | 346 |
| **HB2c** | 6.0 | 0.01 | **MPSM2c** | 0.8 | a) | a) | a) |
| **HB2d** | 6.0 | 0.01 | **MPSM2d** | 0.5 | a) | a) | a) |
| **HB1e** | 7.1 | 43.0 | **MPSM1e** | 7.3 | 16.6 | 0.79 | 247 |
| **HB1f** | 8.6 | 33.8 | **MPSM1f** | 6.6 | 15.6 | 1.06 | 311 |

a) The poor yield did not allow adsorption measurements.

### 9.3.1. Preparation and characterization of **MPSM1a–d** and **MPSM2a–d**

Monodisperse tetra ethylene pentamine (TEPA) functionalized *p*(GMA-*co*-EDMA) served as template in the preparation of all MPSMs discussed here. The characteristic features of this P@TEPA template are a diameter of 6.0 ± 0.5 µm, a median pore diameter of 14.4 nm and a pore volume of 0.24 mL $g^{-1}$ (**Figure S. 9.2** and **Figure S. 9.3**, S.I.).

In the presence of the P@TEPA template a basic sol-gel process was performed with the four different alkoxysilanes TMOS (**a**), TEOS (**b**), TPOS (**c**) and TBOS (**d**), respectively, in 2-propanol and $H_2O$ as solvents (Methods 1 and 2, Scheme 1). In Method 1 all reactants except the template are soluble in 2-propanol. Under these conditions silica nanoparticles (SNP) are formed in the continuous phase, which diffuse into the template and accumulate in the pores and on the surface[2,3,22,119]. The size of the SNPs depends on the hydrolysis and condensation rates of the precursors. With the fastest rate of hydrolysis, TMOS forms the largest SNPs which accumulate in the pores (**Figure S. 9.4**, **HB1a**). Moreover, the hydrolysis and condensation rates of TMOS is so high that the SNPs become too large (~ 60 nm) to enter the template network. These secondary particles remain in the continuous phase and are mostly removed from the template during the purification process, while some of them are left at the template surface (**Figure S. 9.4**, **HB1a**). With TEOS as precursor, particle formation is already four times slower than for TMOS[89], resulting in smaller SNPs which easily penetrate the porous network of the template and form **HB1b** (**Figure S. 9.4**). With increasing chain length of the TPOS and TBOS alkoxides, the hydrolysis rate further decreases. Thus, less silica species is available for condensation to build SNPs. The accumulation of SNPs in the template is now difficult to observed (**Figure S. 9.4**, **HB1c** and **HB1d**). Overall, the size of the SNPs decreases with the rates of hydrolysis in the TMOS > TEOS > TPOS > TBOS series (**Figure S. 9.4**).

In Method 2 the sol-gel process is carried out in $H_2O$ which reduces the differences of the kinetic effects of hydrolysis and condensation of the four different alkoxysilanes (Method 2, **Scheme 9.1**). Ammonia as catalyst is added after 24 h of stirring to enable the nonpolar precursors to diffuse into the template network. Condensation does not start until $NH_3$ is added. After another 24 h, the hybrid particles **HB2a–d** were obtained (**Figure S. 9.5** and **Table 9.1**). Interestingly, because the rate of hydrolysis of TMOS is strongly reduced, no secondary particles are observed. The particles **HB2a** grow by 0.7 µm and **HB2b** by 0.3 µm compared to the template and are thus larger than **HB1a–d**. In contrast to particles prepared by Method 1, a more edgy morphology of the hybrid materials is achieved. For TPOS (**HB2c**) and TBOS (**HB2d**) as precursors, there are no changes in size and morphology compared to the template.

The amount of incorporated silica was determined for **HB1a–d** and **HB2a–d** via thermogravimetric analysis of the hybrid beads and are compared in **Figure 9.1**. Here hybrid particles **HB1a** show the highest silica content (37.8 %). The amount of silica of **HB1b** (29.9 %), **HB1c** (17.7 %) and **HB1d** (6.6 %) also decreases according to the decreasing hydrolysis rate.

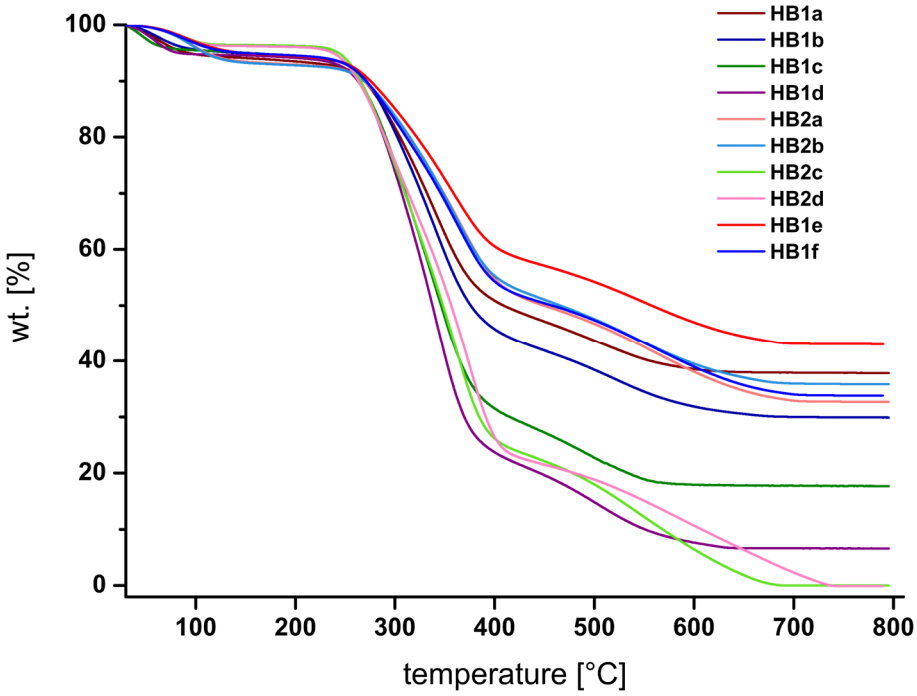


**Figure 9.1** TGA measurements of hybrid beads **HB1a–f** and **HB2a–d**.

The amount of $SiO_2$ in **HB2a** and **HB2b** is 32.7 % and 35.8 %, respectively, and differs little (**Figure 9.1**). Due to the suppressed hydrolysis in $H_2O$, the hydrolysis rates of TMOS and TEOS are comparable. Thus, a similar amount of $SiO_2$ is deposited. The percentage of incorporated silica in the hybrid particles correlates well with the particle size of the resulting MPSM (**Table 9.1**). Thermogravimetric analysis of **HB2c** and **HB2d** result in only very small amounts of $SiO_2$.

Calcination of the hybrid beads **HB1a–d** and **HB2a–d** for 10 h at 600 °C removed the organic polymer template and releases the monodisperse mesoporous silica microspheres **MPSM1a–d** (**Figure 9.2**) and **MPSM2a–d** (**Figure 9.3**). The nanoparticulate morphology of the MPSMs is comparable to those of their corresponding hybrid beads. The particle size of the MPSMs decreases with decreasing hydrolysis rate of the precursors. Thus, while **MPSM1a** (6.0 µm) and **MPSM1b** (5.5 µm) represent the size of the template quite well the sizes of **MPSM1c** (3.6 µm) and **MPSM1d** (2.2 µm) are strongly reduced. Consequently, only TMOS and TEOS map the template to 100 % and

92 %, respectively, while for TPOS and TBOS the template is mapped to only 60 % and 37 %, respectively.

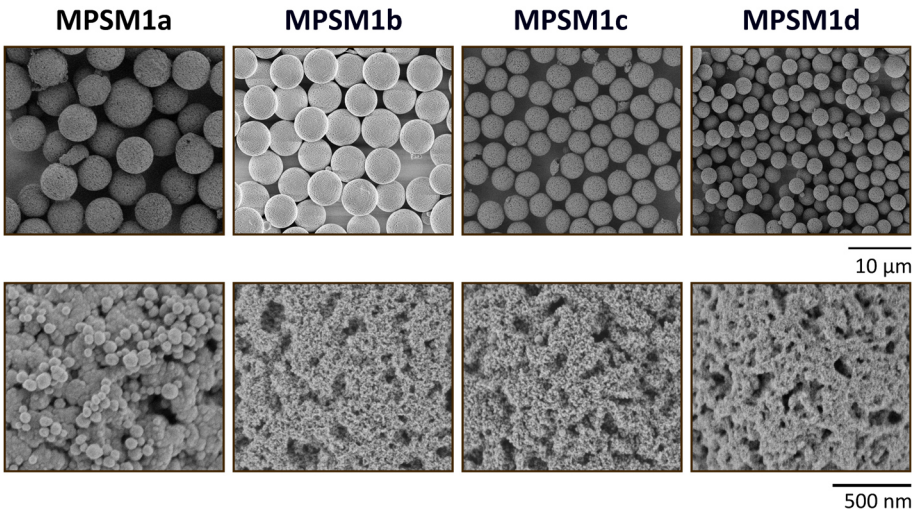


**Figure 9.2** SEM images of mesoporous silica microspheres **MPSM1a–d** with 2,000 x magnification (top row) and 50,000 x magnification (bottom row).

The particle size of **MPSM2a** and **MPSM2b** are 5.9 µm and 6.0 µm, respectively, and completely replicate the template. For **MPSM2c** and **MPSM2d**, 800 nm and 500 nm polydisperse porous silica particles are generated. Only the hydrolysis rates of TMOS and TEOS are fast enough to form sufficient SNPs to reproduce the template. Particle formation takes place inside the template, resulting in an edged morphology of **MPSM2a** and **MPSM2b**. For TPOS and TBOS, the hydrolysis rate in $H_2O$ is very slow. After 24 h, only a small percentage of precursors are reacted, resulting in a smaller amount of silica. Consequently, the particles **MPSM2c** and **MPSM2d** shrink very much, and their yield is low.

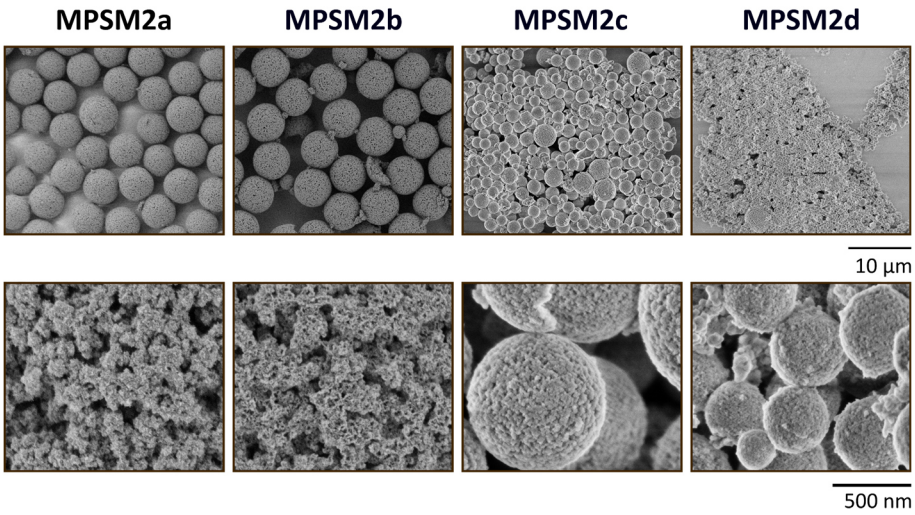


**Figure 9.3** SEM images of mesoporous silica microspheres **MPSM2a–d** with 2,000x magnification (top row) and 50,000x magnification (bottom row).

The pore properties of the MPSMs were determined via nitrogen adsorption measurements and listed in **Table 9.1**. The corresponding pore size distributions are shown in **Figure 9.4**.

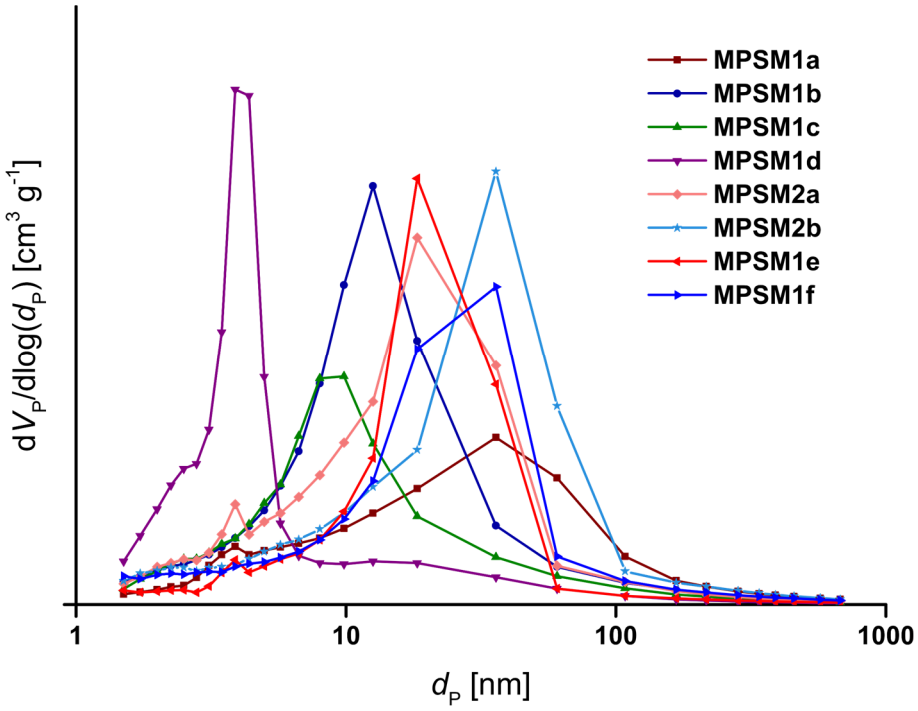


**Figure 9.4** Pore size distributions of **MPSM1a–f** and **MPSM2a–b**.

Here, the median pore size of the MPSM decreases and the specific surface area increases with decreasing hydrolysis rate of the precursor. This result correlates with the size of the SNPs which form the silica network. Large SNPs result in large pores of MPSMs while small SNPs result in smaller pores[2,119].Thus, **MPSM1a** has a median pore size of 23.6 nm, **MPSM1b** 11.3 nm, **MPSM1c** 8.8 nm, and **MPSM1d** 4.0 nm. Smaller pores result in a larger specific surface area. Consequently, **MPSM1d** has the highest specific surface area and **MPSM1a** has the lowest specific surface area. The sol-gel process according to Method 2 leads to an edgier morphology for **MPSM2a** and **MPSM2b** resulting in a larger surface area compared to **MPSM1a** and **MPSM1b**. The pore volume of the MPSMs differs between 0.5 mL $g^{-1}$ and 0.9 mL $g^{-1}$.

### 9.3.2. Preparation and characterization of **MPSM1e** and **MPSM1f**

The properties of the MPSMs are controlled by the hydrolysis rate of the precursors and the solvent medium. TMOS produces non-porous secondary particles while TPOS does not fully map the size of the template if the sol-gel process is carried out in 2-propanol and $H_2O$, to avoid the unwanted properties of the two precursors, combinations of TMOS and TPOS with TEOS (**MPSM1e**: TMOS+TEOS; **MPSM1f**: TPOS+TEOS) were applied in a sol-gel process in the presence of a P@TEPA template with a diameter of 7.2 µm. The synthesized HBs and MPSMs are shown in **Figure 9.5**. Interestingly,

no secondary particles are observed for **HB1e** and **MPSM1e**. The corresponding silica microspheres have a nanoparticulate surface and exhibit a size of 7.3 µm. Thus, they completely map the template without the negative effects of the high hydrolysis rate of TMOS.

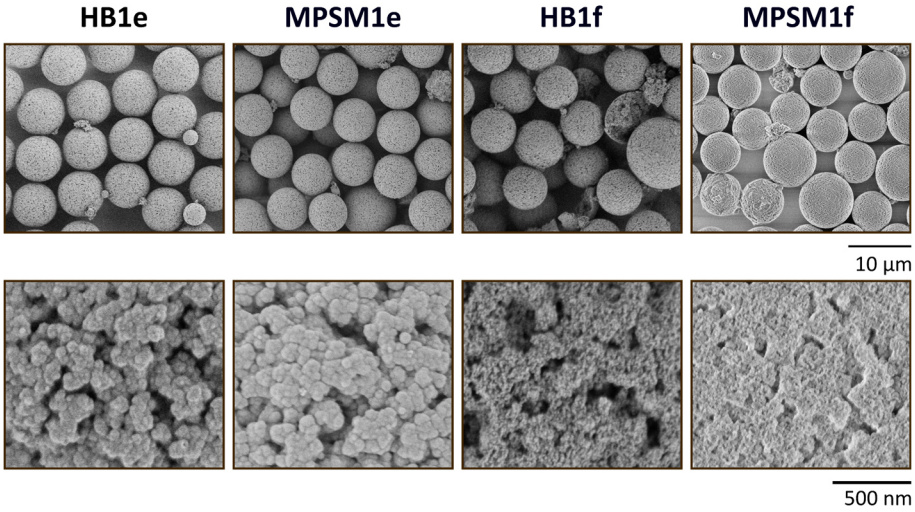


**Figure 9.5** SEM images of hybrid beads **HB1e** and **HB1f** and corresponding **MPSM1e** and **MPSM1f** with 2,000x magnification (top row) and 50,000x magnification (bottom row).

With a median pore size of 16.6 nm, this is in between those of **MPSM1a** and **MPSM1b**. This results in SNPs in the continuous phase that are smaller than those of **MPSM1a** and larger than those of **MPSM1b**. The combination of TEOS and TPOS leads to the particles **HB1f** and **MPSM1f**. The resulting silica materials have a size of 6.6 µm, representing 92 % of the template. Interestingly, the median pore size of 15.6 nm and the pore volume of 1.06 mL $g^{-1}$ are larger than the pore properties of **MPSM1b** where only TEOS was used. Compared with **MPSM1c**, the template is better replicated in **MPSM1f**.

### 9.3.3. Chromatographic measurements of **MPSM1b**

For the use of particles as stationary phase in high performance liquid chromatography, they need high monodispersity to achieve efficient separation. Particles **MPSM1b** were chosen based on their particle size and dispersity to investigate as stationary phase in HPLC. The synthesized particles **MPSM1b** were functionalized with trimethoxy (octadecyl)silane and packed in a 250 mm x 4.6 mm stainless steel column with acetone as slurry and methanol/water (85 vol% / 15 vol%) as pressure medium.

The reproducibility of the synthesis of **MPSM1b** in its chromatographic properties is shown in **Figure 9.6**. Three different batches with the same reaction conditions were packed in 250 mm x 4.6 mm stainless steel columns and examined for their chromato-

graphic properties. As can be seen in **Figure 9.6**, all three batches show the same retention behavior for the test mixture.

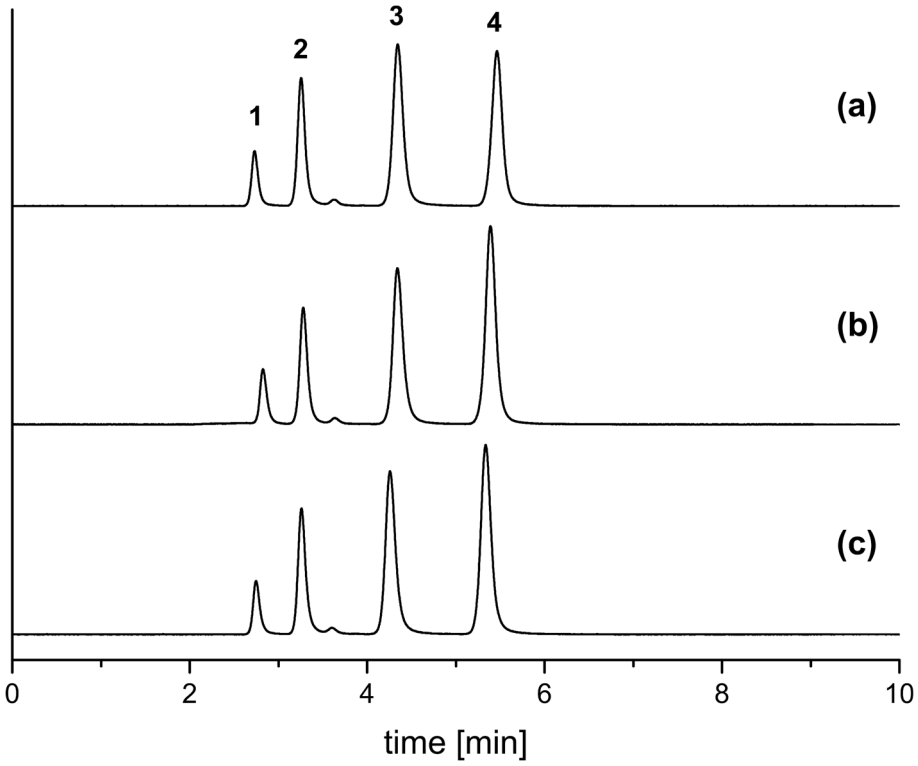


**Figure 9.6** Reproducibility of chromatographic properties from three different batches of **MPSM1b-C$_{18}$** synthesized according to Method 1. Chromatographic settings: column dimension: 250 x 4.6 mm; mobile phase: MeOH/$H_2O$ (85 wt% / 15 wt%); analytes: uracil (**1**), phenol (**2**), *N*,*N*-diethyl-*m*-toluamide (**3**), toluene (**4**); flow: 1 mL min$^{-1}$; inject volume: 5 µl; UV-detection: 254 nm.

The successful separation of five water-soluble vitamins is shown in **Figure 9.7**. A gradient from eluent A, consisting of water containing 0.025 % TFA, to eluent B, consisting of ACN, was used for the separation. An initial isocratic step for 5 min with eluent A is followed by an increase from eluent B to eluent A to 25/75 (v./v.) in 6 min according to Heudi et al.

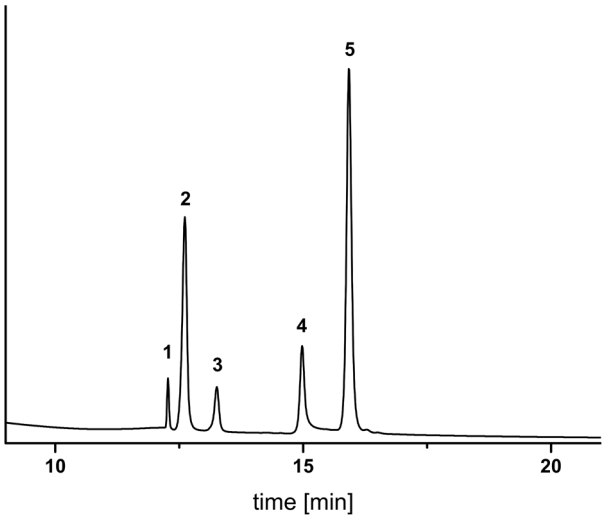


**Figure 9.7** Separation of five water-soluble vitamins. Chromatographic settings: column dimension: 250 x 4.6 mm; eluent A: $H_2O$ with 0.025 vol% TFA, eluent phase B: ACN; gradient (A/B): 5. min (100/0), 11. min (75/25), 19. min (60/40), 20. min (60/40), 21. min (100/0), 25. min (100/0); injection volume: 20 µl; column temperature: 30 °C; UV detection: 210 nm.

This is followed by a second gradient on Eluent B to Eluent A 40/60 (v./v.) in 8 min, holding this for an additional minute. Then the initial conditions are restored in 1 minute and equilibrated for 4 minutes. The vitamins were baseline separated and assigned based on single measurements of the analytes. The elution order is vitamin $B_1$ < $B_3$ < $B_5$ < $B_9$ < $B_{12}$ detected by 210 nm.

## 9.4. Conclusions

The synthesis of monodisperse mesoporous silica microspheres (MPSM) with different morphologies and pore properties using functionalized *p*(GMA-*co*-EDMA) particles as hard template was successfully demonstrated. Depending on the hydrolysis rate of the precursors, the properties of the MPSMs vary. When 2-propanol and $H_2O$ are used as continuous phase, silica nanoparticles form outside of the template and diffuse into the pores. In the pores and on the surface of the template, these aggregate and form a nanoparticulate morphology. Depending on the hydrolysis rate of the precursors, the size of the SNP is affected which control the properties of the MPSM. This was demonstrated by scanning electron microscopy, thermogravimetric analysis, and nitrogen adsorption measurements. Tetraethyl orthosilicate completely maps the polymer template, exhibiting pores with a size of 11.3 nm. Faster hydrolysis rates result in SNPs that are too large to diffuse into the template. In contrast, at slower hydrolysis rates, the template is not completely mapped. It became apparent that the size of the SNP has a crucial role on the pore size of the MPSM. The larger the SNP the larger the pores of the MPSM. The nanoparticle formation in the continuous phase could be suppressed by performing the sol-gel process in $H_2O$ only. Tetramethyl and tetraethyl orthosilicates fully displayed the template in this process and have an edged morphology.

The combination of TMOS and TPOS with TEOS leads to the suppression of their unwanted side effects and the mapping of the template with different morphologies.

The silica particles synthesized with TEOS according to Method 1 were functionalized with trimethoxy (octadecyl) silane and used as stationary phase in HPLC. Complete baseline separation of five water-soluble vitamins was achieved with these microspheres. The robustness of the synthesis of MPSMs in its chromatographic properties was demonstrated via HPLC using three different batches with a reversed-phase test mixture.

## 9.5. Supplementary Information

### 9.5.1. Chemicals

Polyvinyl alcohol (PVA, 87–89 % hydrolyzed, mean average 88000 – 97000 g $mol^{-1}$), polyvinylpyrrolidone $K_{30}$ (PVP, mean average 40000 g $mol^{-1}$) and $K_{90}$ (mean average 360000 g $mol^{-1}$) from abcr GmbH. Ethyleneglycol dimethacrylate (EDMA) was bought from Acros Organics. Cyclohexanol and sodium dodecyl sulfate (SDS) were purchased from Carl Roth. Styrene was obtained by Fisher Chemicals. Dibenzoyl peroxide (BPO), dibutyl phthalate (DBP), glycidyl methacrylate (GMA) and tetraethylene pentamine (TEPA) were purchased from Sigma-Aldrich.

### 9.5.2. Synthesis of polystyrene

Monodisperse polystyrene particles with diameters of 1.5 ± 0.1 were prepared as reported earlier (**Figure S. 9.1**)

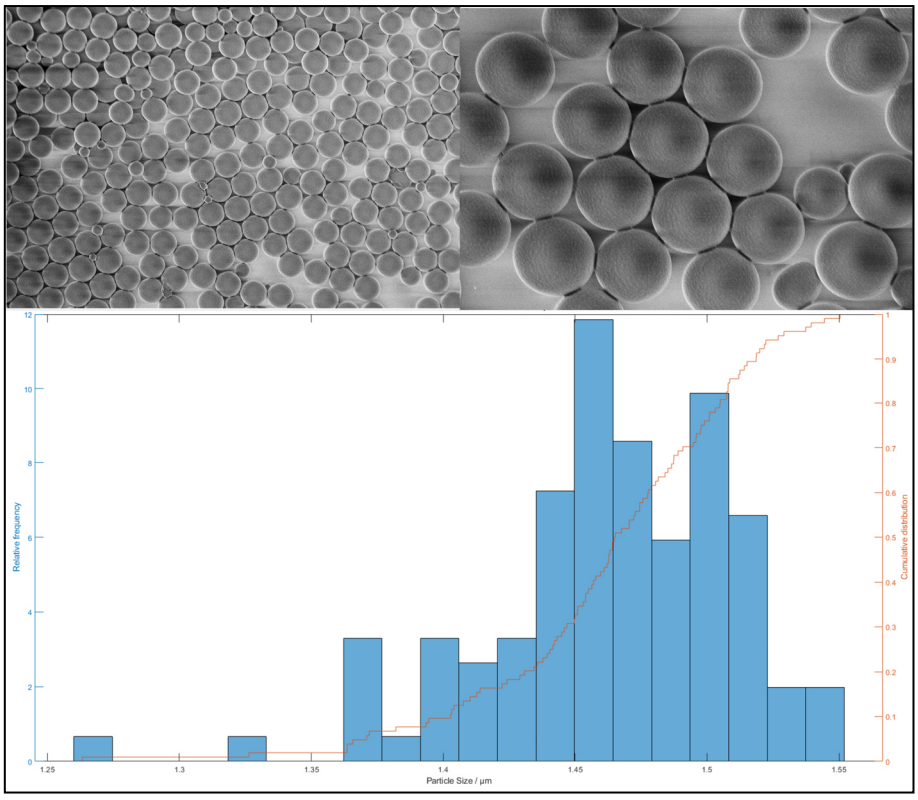


**Figure S. 9.1** SEM images of applied polystyrene particles (top) and their particle size distribution (bottom).

### 9.5.3. Synthesis of P@TEPA

0.3 g of polystyrene particles and 5 mL of an aqueous SDS solution (0.25 wt%) were dispersed in a 250 mL flask. 2 mL DBP were emulsified in 150 mL aqueous SDS solution (0.25 wt%) with a homogenizer at 4500 rpm for 15 min and then added to the polystyrene suspension. The mixture was stirred for 24 h at 200 rpm. 6 mL GMA, 9 mL

EDMA, 6 mL cyclohexanol, 16.5 mL toluene, 0.4 g BPO and 150 mL aqueous SDS solution (0.25 wt%) were emulsified with a homogenizer at 4500 rpm for 15 min. This emulsion, a 150 mL aqueous PVA solution (2.3 wt%) and the activated polystyrene particles were transferred to a 500 mL three-necked flask and stirred for 24 h at 200 rpm. Argon was passed into the reaction mixture for 30 minutes and then heated to 70 °C for 24 hours. The particles were separated from the solution, washed three times with EtOH and three times with $H_2O$ and dried at 65 °C for 16 h. The average particle size of the *p*(GMA-*co*-EDMA) particles were 6.0 ± 0.5 µm (**Figure S2**).

5 g of *p*(GMA-*co*-EDMA) particles and 200 mL of $H_2O$ were dispersed in a 500 mL flask. 7.5 of mL TEPA were added while stirring the suspension at 200 rpm. The reaction mixture was heated to 80 °C for 24 h. The particles were separated from the solution, washed three times with EtOH and three times with $H_2O$ and dried at 65 °C for 16 h.

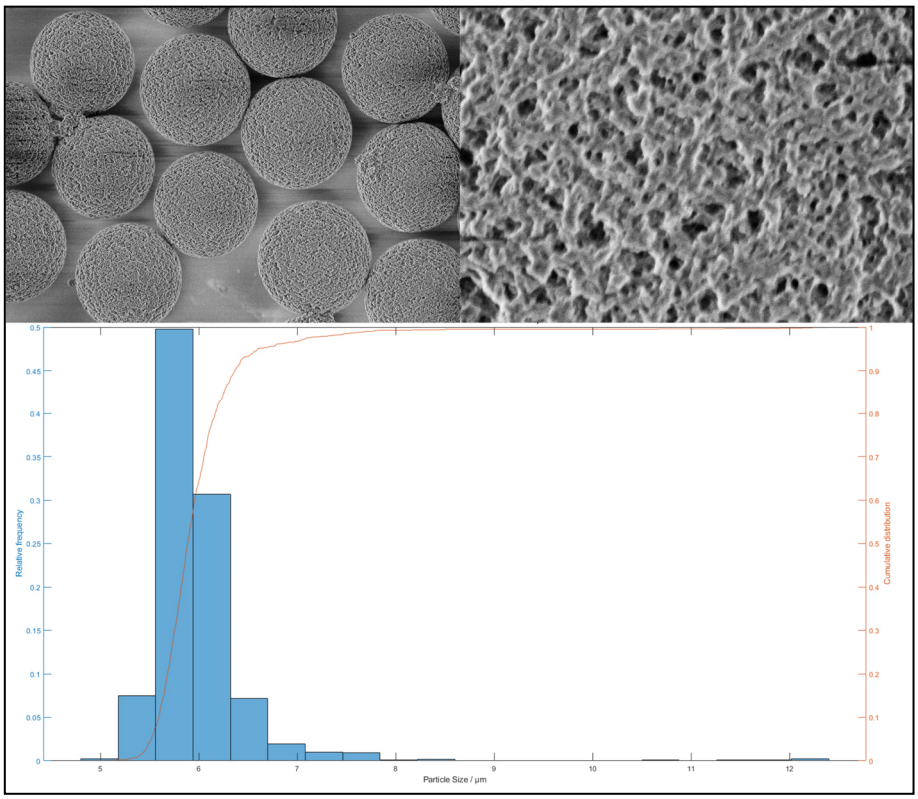


**Figure S. 9.2** SEM images of the polymer templates *p*(GMA-*co*-EDMA) (top) and corresponding particle size distribution (bottom).

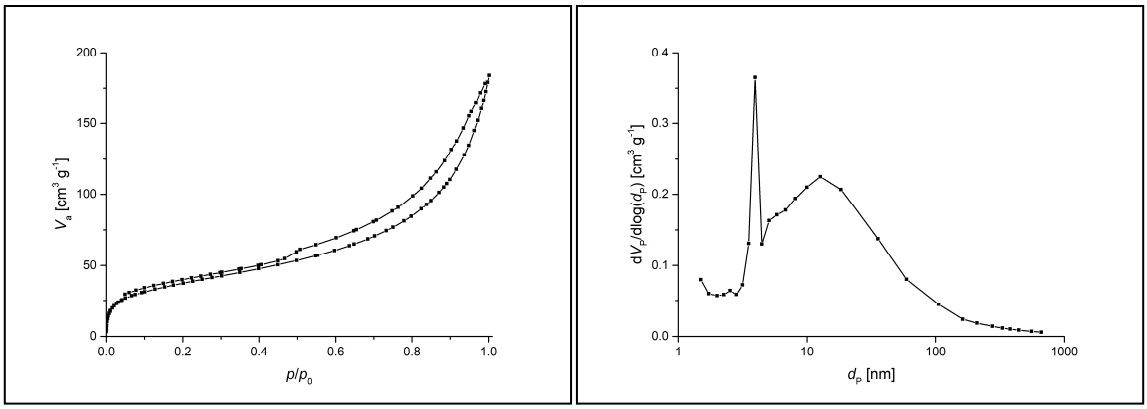


**Figure S. 9.3** Isotherms (left) and pore size distribution (right) of *p*(GMA-*co*-EDMA).

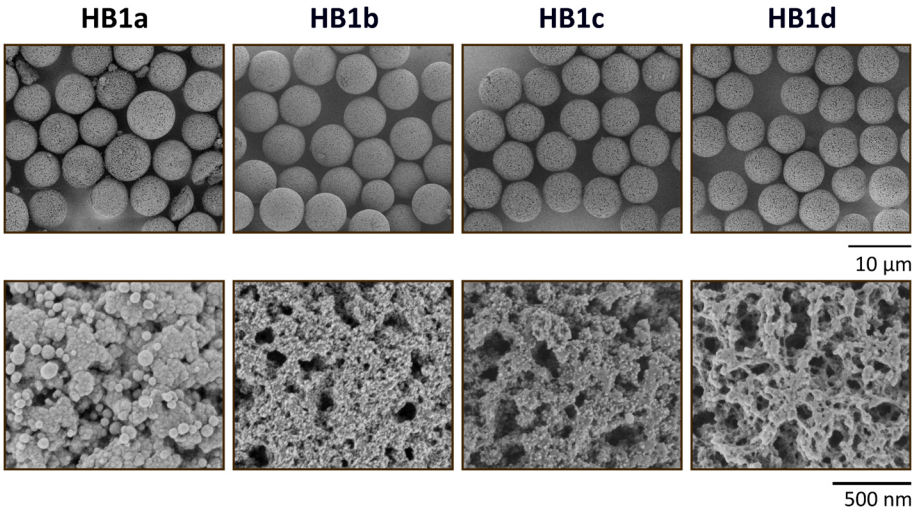


**Figure S. 9.4** SEM images of hybrid beads **HB1a – HB1d** with 2,000x magnification (top row) and 50,000x magnification (bottom row).

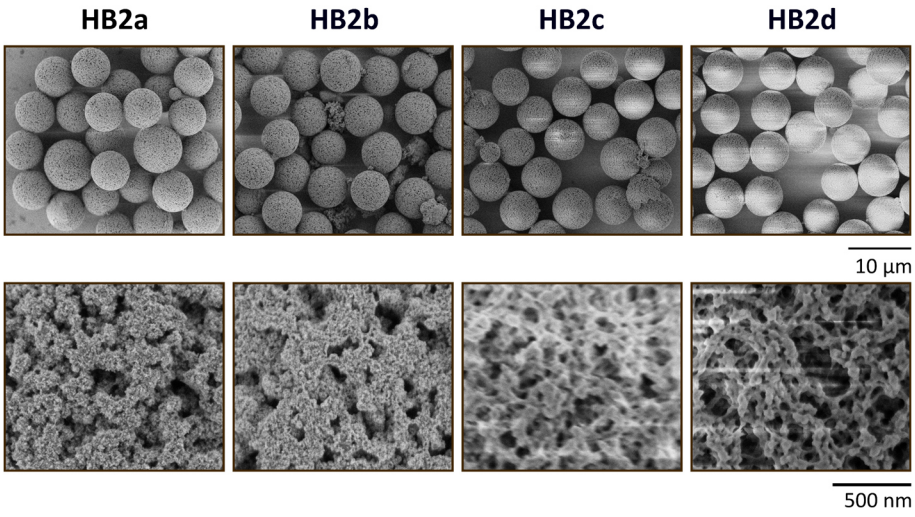


**Figure S. 9.5** SEM images of hybrid beads **HB2a – HB2d** with 2,000x magnification (top row) and 50,000x magnification (bottom row).

**Acknowledgments**

This research was funded the by Bundesministerium für Bildung und Forschung (BMBF, grant number 13FH647IX6) and the Bundesministerium für Wirtschaft und Energie (AiF/ZIM, grant number ZF4019203SL8). Furthermore, we would like to thank our cooperation partner Dr. Maisch GmbH for their support in preparing the columns. We thank Elke Nadler for contributing the SEM measurements and Julia C. Steinbach for providing the MATLAB script.

# 10. Unpublished Results

## 10.1. Polystyrene – Effects of syntheses conditions on size, dispersity and yield

Polymeric latex particles on a nano- to microscale are used in many applications[249] such as coatings[250], biotechnology[251–253], nanomedicine[254] or as seed particles for the production of porous materials[1,9]. In this thesis, the synthesized polystyrene seed particles find application as seed-particle for the seed-swelling synthesis of the porous polymer particles. Highly monodisperse polystyrene particles of various sizes are required for this purpose, as they are critical to the shape and dispersity of the resulting porous polymer. The size dependency of the porous polymer onto the size of the polystyrene particle is described by the equation (10.1) presented by Hosoya and Fréchet (1993)[82] in an adaptation by Gong et al. (2006)[125]:

$$\log D = \log d + \frac{1}{3} log \frac{M+m}{m} \tag{10.1}$$

Where D is the expected diameter of the porous polymer, d is the diameter of the polystyrene seed, M is the mass of the organic phase consisting of monomers and inert porogens used in the seed swelling process and m is the mass of seed particles[125].

### 10.1.1. Material and methods

#### *10.1.1.1. Chemicals*

Ethanol (HPLC grade, EtOH), methanol (HPLC grade, MeOH) and styrene (99 %) purchased from Fisher Scientific GmbH (Schwerte, Germany). Polyvinylpyrrolidone K30 (PVP) and benzoyl peroxide (BPO, 75 %) were purchased from Sigma-Aldrich Chemie GmbH (Traufkirchen, Germany). All chemicals were used as delivered.

#### *10.1.1.2. Preparation of PS seeds*

PS seed particles were synthesized by dispersion polymerization in alcoholic media. Styrene (99 %), alcohol and water were added to a three-neck flask (100 mL) with amounts according to the process factor settings of the RSM (**Table S. 10.1**). After the addition of stabilizer and BPO as initiator, the suspension was sonicated for 10 min. The suspension was stirred at 120 rpm for 30 min with a magnetic stirrer at room temperature. The mixture was purged with argon for 20 minutes. Then, the temperature was raised to 70 °C for 24 h under reflux. The PS seed particles were centrifuged at 7500 rpm for 2 min and washed three times with ethanol and three times with deionized water to remove the reaction solution. The particles were freeze-dried in vacuo for 72 h. The goal is to achieve a set of highly monodisperse polystyrene particles in various sizes. Thus, an RSM with variation of following process parameters was per-

formed including solvent type, monomer amount, initiator ratio, stabilizer ratio and solvent ratio (**Table S. 10.1**).

**Table S. 10.1** Factor level settings for the RSM

| | **Low Setting (-)** | **Medium Setting (0)** | **High Setting (+)** |
|---|---|---|---|
| **A** – solvent type (categoric) | MeOH | - | EtOH |
| **B** – monomer wt% | 12 | 26 | 40 |
| **C** – initiator wt% (relative to monomer) | 0.2 | 2.2 | 4.2 |
| **D** – stabilizer wt% (relative to monomer) | 4 | 12 | 20 |
| **E** – solvent ratio (alcohol/$H_2O$ wt% per solvent) | 70 | 85 | 100 |

## 10.1.2. Results and discussion

Overall 69 syntheses were prepared with a wide range of particle size distributions (monodisperse, polydisperse and bimodal) and particle sizes (see **Table S. 10.2**). Using ethanol resulted in generally bigger particles than particles prepared in methanol and the addition of water lead to smaller particles but massively increases dispersity. The type of solvent had no significant effect on the dispersity. With increasing monomer concentration and initiator concentration, the particle size increased. These factors showed a significant two-factor interaction, which means that the effect of one factor is dependent on the factor level setting of another factor. These process factors, can thus, not be considered separately. The increase in particle size increased with higher levels of monomer. This effect was massively enhanced if simultaneously, the level of initiator was elevated. At high initiator and monomer concentrations, as well as high water content, the particle size distributions become highly polydisperse. The stabilizer showed no significant effect onto the dispersity, but lead to a decrease in particle size with increasing levels of stabilizer. However, this effect was attenuated for higher levels of stabilizer (> 12 wt%) reflected by a statistically significant quadratic factor effect term.

**Table S. 10.2** Factor level settings and their corresponding particle properties particle size, dispersity, and yield. Outlier are marked italic. n.a. = no or too little precipitation for analysis

| | **Factors** | | | | | **Responses** | | |
|---|---|---|---|---|---|---|---|---|
| | **A** | **B** | **C** | **D** | **E** | | | |
| **Std** | **Solvent Type** | **Monomer** | **Initiator** | **Stabilisator** | **Solvent ratio** | **$d_{50}$** | **$d_{90}/d_{10}$** | **Yield** |
| | | /wt% per mixture | /wt% per monomer | /wt% per monomer | /wt% per solvent | /nm | | /% |
| **PS-1.1** | MeOH | 12 | 0.2 | 4 | 70 | n.a. | n.a. | 0.0 |
| **PS-1.2** | MeOH | 40 | 0.2 | 4 | 70 | 5530 | 2.53 | 0.0 |
| ***PS-1.3*** | *MeOH* | *12* | *4.2* | *4* | *70* | *830* | *1.91* | *59.3* |
| ***PS-1.4*** | *MeOH* | *40* | *4.2* | *4* | *70* | *330* | *1.21* | *1.9* |
| **PS-1.5** | MeOH | 12 | 0.2 | 20 | 70 | n.a. | n.a. | 0.0 |
| **PS-1.6** | MeOH | 40 | 0.2 | 20 | 70 | 340 | 1.46 | 5.2 |

| | | | | | | | | |
|---|---|---|---|---|---|---|---|---|
| **PS-1.7** | MeOH | 12 | 4.2 | 20 | 70 | 500 | 1.48 | 25.3 |
| ***PS-1.8*** | *MeOH* | *40* | *4.2* | *20* | *70* | *440* | *1.41* | *29.8* |
| **PS-1.9** | MeOH | 12 | 0.2 | 4 | 100 | 420 | 2.03 | 0.0 |
| **PS-1.10** | MeOH | 40 | 0.2 | 4 | 100 | 1100 | 2.35 | 4.4 |
| **PS-1.11** | MeOH | 12 | 4.2 | 4 | 100 | 1630 | 1.58 | 71.2 |
| **PS-1.12** | MeOH | 40 | 4.2 | 4 | 100 | 3520 | 1.06 | 63.9 |
| **PS-1.13** | MeOH | 12 | 0.2 | 20 | 100 | 520 | 1.7 | 33.8 |
| **PS-1.14** | MeOH | 40 | 0.2 | 20 | 100 | 840 | 2.36 | 6.5 |
| **PS-1.15** | MeOH | 12 | 4.2 | 20 | 100 | 480 | 1.11 | 1.2 |
| ***PS-1.16*** | *MeOH* | *40* | *4.2* | *20* | *100* | *720* | *6.18* | *93.9* |
| **PS-1.17** | MeOH | 26 | 2.2 | 12 | 85 | 560 | 2.17 | 55.8 |
| **PS-1.18** | MeOH | 26 | 2.2 | 12 | 85 | 690 | 1.85 | 31.8 |
| **PS-1.19** | MeOH | 26 | 2.2 | 12 | 85 | 430 | 1.48 | 34.3 |
| **PS-1.20** | MeOH | 26 | 2.2 | 12 | 85 | 800 | 1.83 | 27.7 |
| **PS-1.21** | MeOH | 26 | 2.2 | 12 | 85 | 380 | 2.51 | 32.2 |
| **PS-1.22** | MeOH | 12 | 2.2 | 12 | 85 | 230 | 1.42 | 0.2 |
| **PS-1.23** | MeOH | 40 | 2.2 | 12 | 85 | 460 | 2.71 | 69.2 |
| **PS-1.24** | MeOH | 26 | 0.2 | 12 | 85 | 330 | 1.4 | 0.0 |
| **PS-1.25** | MeOH | 26 | 4.2 | 12 | 85 | 440 | 3.95 | 72.0 |
| **PS-1.26** | MeOH | 26 | 2.2 | 4 | 85 | 650 | 2.54 | 66.9 |
| **PS-1.27** | MeOH | 26 | 2.2 | 20 | 85 | 520 | 2.21 | 37.2 |
| **PS-1.28** | MeOH | 26 | 2.2 | 12 | 70 | 840 | 1.96 | 20.1 |
| **PS-1.29** | MeOH | 26 | 2.2 | 12 | 100 | 620 | 3.06 | 59.2 |
| **PS-1.30** | EtOH | 12 | 0.2 | 4 | 70 | n.a. | n.a. | 0.0 |
| **PS-1.31** | EtOH | 40 | 0.2 | 4 | 70 | 730 | 2.27 | 11.0 |
| **PS-1.32** | EtOH | 12 | 4.2 | 4 | 70 | 920 | 1.82 | 29.0 |
| ***PS-1.33*** | *EtOH* | *40* | *4.2* | *4* | *70* | *680* | *3.04* | *40.1* |
| **PS-1.34** | EtOH | 12 | 0.2 | 20 | 70 | n.a. | n.a. | 0.0 |
| **PS-1.35** | EtOH | 40 | 0.2 | 20 | 70 | 470 | 1.44 | 11.0 |
| **PS-1.36** | EtOH | 12 | 4.2 | 20 | 70 | 530 | 1.58 | 57.5 |
| **PS-1.37** | EtOH | 40 | 4.2 | 20 | 70 | 410 | 2.78 | 66.3 |
| **PS-1.38** | EtOH | 12 | 0.2 | 4 | 100 | n.a. | n.a. | 0.0 |
| **PS-1.39** | EtOH | 40 | 0.2 | 4 | 100 | n.a. | n.a. | 0.0 |
| ***PS-1.40*** | *EtOH* | *12* | *4.2* | *4* | *100* | *460* | *1.44* | *0.0* |
| **PS-1.41** | EtOH | 40 | 4.2 | 4 | 100 | 8100 | 1.05 | 99.7 |
| **PS-1.42** | EtOH | 12 | 0.2 | 20 | 100 | 240 | 1.25 | 1.7 |
| **PS-1.43** | EtOH | 40 | 0.2 | 20 | 100 | 970 | 2.41 | 16.8 |
| **PS-1.44** | EtOH | 12 | 4.2 | 20 | 100 | 1460 | 1.76 | 18.0 |
| **PS-1.45** | EtOH | 40 | 4.2 | 20 | 100 | 2240 | 1.11 | 74.5 |
| **PS-1.46** | EtOH | 26 | 2.2 | 12 | 85 | 650 | 2.14 | 10.7 |
| **PS-1.47** | EtOH | 26 | 2.2 | 12 | 85 | 490 | 1.94 | 45.1 |
| **PS-1.48** | EtOH | 26 | 2.2 | 12 | 85 | 610 | 2.65 | 67.0 |
| **PS-1.49** | EtOH | 26 | 2.2 | 12 | 85 | 390 | 4.14 | 74.6 |
| **PS-1.50** | EtOH | 26 | 2.2 | 12 | 85 | 630 | 2.78 | 55.7 |
| **PS-1.51** | EtOH | 12 | 2.2 | 12 | 85 | n.a. | n.a. | 0.0 |
| **PS-1.52** | EtOH | 40 | 2.2 | 12 | 85 | 730 | 1.77 | 45.6 |
| **PS-1.53** | EtOH | 26 | 0.2 | 12 | 85 | n.a. | n.a. | 0.0 |
| **PS-1.54** | EtOH | 26 | 4.2 | 12 | 85 | 1370 | 2.5 | 87.9 |
| **PS-1.55** | EtOH | 26 | 2.2 | 4 | 85 | 1640 | 2.7 | 89.2 |
| **PS-1.56** | EtOH | 26 | 2.2 | 20 | 85 | 830 | 1.91 | 16.5 |
| **PS-1.57** | EtOH | 26 | 2.2 | 12 | 70 | 1000 | 2.16 | 28.4 |
| **PS-1.58** | EtOH | 26 | 2.2 | 12 | 100 | 1340 | 3.28 | 57.6 |
| **PS-1.59** | EtOH | 40 | 4.2 | 4 | 100 | 7780 | 1.04 | 93.1 |
| **PS-1.60** | EtOH | 12 | 4.2 | 12 | 100 | 180 | 1.85 | 0.8 |
| **PS-1.61** | EtOH | 26 | 4.2 | 20 | 100 | 1410 | 1.09 | 65.5 |
| **PS-1.62** | EtOH | 26 | 4.2 | 4 | 100 | 3340 | 1.05 | 66.0 |
| **PS-1.63** | EtOH | 26 | 4.2 | 12 | 100 | 640 | 1.92 | 98.0 |
| **PS-1.64** | EtOH | 12 | 2.2 | 20 | 100 | n.a. | n.a. | 0.0 |

| | | | | | | | | |
|---|---|---|---|---|---|---|---|---|
| **PS-1.65** | MeOH | 26 | 4.2 | 20 | 100 | 650 | 2.07 | 98.5 |
| **PS-1.66** | MeOH | 12 | 4.2 | 12 | 100 | 1060 | 1.10 | 13.7 |
| **PS-1.67** | MeOH | 12 | 2.2 | 20 | 100 | 660 | 1.95 | 24.1 |
| **PS-1.68** | MeOH | 26 | 4.2 | 12 | 100 | 560 | 2.21 | 54.5 |
| **PS-1.69** | MeOH | 40 | 2.2 | 20 | 100 | 530 | 1.99 | 70.8 |

Due to the extremely high variance in this dataset a smaller RSM was set up, which eliminated the factors of solvent type and solvent ratio. Although methanol lead to smaller particles, ethanol was chosen as solvent due to its lower toxicity and because there is an interference with methanol at high monomer levels resulting in extremely high dispersity (see exemplarily **Figure 10.1**).

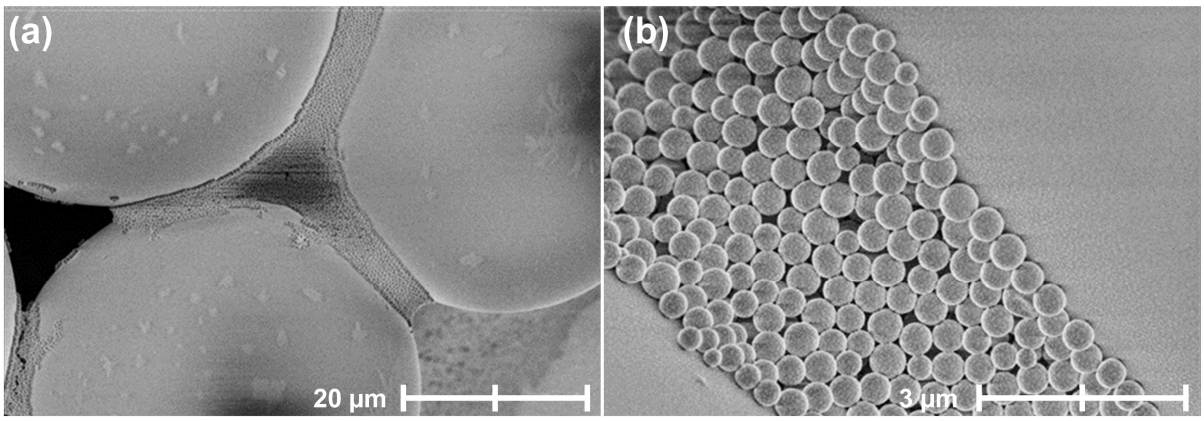


**Figure 10.1 a)** SEM images of experiment **PS-1.8** showing the different dimensions of the particle sizes. The largest particle measured under SEM has a size of ~75 µm, other bigger particles exhibit sizes between 35–50 µm. However, even larger polystyrene spheres up to an estimated size of 1000 µm diameter were formed, which were observed with the bare eye. **b)** The part of smaller particles (~ 0.4 µm) is close to a monodisperse distribution after evaluation with $d_{90}/d_{10}$ = 1.41.

The reduced factor settings and the corresponding response results are given in **Table S. 10.3**. The monomer was varied between 19 wt% and 33 wt%, the initiator between 2.2 wt% and 4.2 wt% per monomer and the stabilizer was varied between 8 wt% and 16 wt% per monomer. As the point **PS-2.1**, with all factor level settings on low (-/-/-), did not result in precipitation of PS particles, three additional points were added. Here, all factor levels were set to low but for one setting the coded level was –0.5 instead of –1 to avoid the extreme point[12]. These particles are given as **PS-2.14** to **PS-2.16**. **PS-2.13** was identified as an outlier according to the Grubbs's test[255] at an α-level of 0.05 and was thus not included in model evaluation.

**Table S. 10.3** Reduced factor level settings with corresponding response values for median particle size, $d_{90/10}$ and the yield. **PS-2.14–PS2.16** were added to compensate for the missing values of **PS-2.1**. n.a. = no or too little precipitation for analysis

| | Factors | | | Responses | | |
|---|---|---|---|---|---|---|
| Sample | A Monomer | B Initiator | C Stabilizer | $d_{50}$ | $d_{90/10}$ | Yield |
| | /wt% | /wt% | /wt% | /nm | | /% |
| **PS-2.1** | 19.0 | 2.2 | 8 | n.a. | n.a. | 0.0 |
| **PS-2.2** | 33.0 | 2.2 | 8 | 780 | 5.73 | 43.6 |
| **PS-2.3** | 19.0 | 4.2 | 8 | 1880 | 1.73 | 16.7 |
| **PS-2.4** | 33.0 | 4.2 | 8 | 2600 | 1.08 | 83.2 |
| **PS-2.5** | 19.0 | 2.2 | 16 | 340 | 1.44 | < 0.1 |
| **PS-2.6** | 33.0 | 2.2 | 16 | 660 | 4.90 | 62.9 |
| **PS-2.7** | 19.0 | 4.2 | 16 | 1140 | 3.35 | 45.6 |
| **PS-2.8** | 33.0 | 4.2 | 16 | 1880 | 1.17 | 85.6 |
| **PS-2.9** | 26.0 | 3.2 | 12 | 820 | 4.05 | 40.7 |
| **PS-2.10** | 26.0 | 3.2 | 12 | 560 | 3.14 | 36.0 |
| **PS-2.11** | 26.0 | 3.2 | 12 | 720 | 4.88 | 69.9 |
| **PS-2.12** | 26.0 | 3.2 | 12 | 650 | 4.66 | 58.0 |
| **PS-2.13** | 26.0 | 3.2 | 12 | 1640 | 1.18 | 51.8 |
| **PS-2.14** | 22.5 | 2.2 | 8 | 1120 | 3.94 | 30.2 |
| **PS-2.15** | 19.0 | 2.7 | 12 | 890 | 1.18 | 1.5 |
| **PS-2.16** | 19.0 | 2.2 | 10 | 540 | 1.11 | 0.3 |

*10.1.2.1. Particle size*

For the particle size $d_{50}$ a statistically significant model ($p = 0.0003$) with the statistically significant ($p < 0.05$) terms B – initiator, C – stabilizer, the two-factor interaction AB and the non-linear term $C^2$ was established. To fulfill the rule of hierarchy the factor term A – monomer was also added[59]. The model showed a good data fit and predictive power with $R^2 = 0.9218$ and $R^2_{predicted} = 0.7181$. The relative strength of the factor effects is given as coded equation (10.2):

$$d_{50} = 781.65 + 131.62\ A + 550.32\ B - 26.86\ C + 207.67\ AB + 521.65\ C^2 \quad (10.2)$$

The two-factor interaction between monomer and initiator is similar, as already described in the large scale RSM. Here also, the increase in particle size is enhanced when both factors level settings are increased and more monomer and initiator are introduced into the synthesis (**Figure 10.2**a).

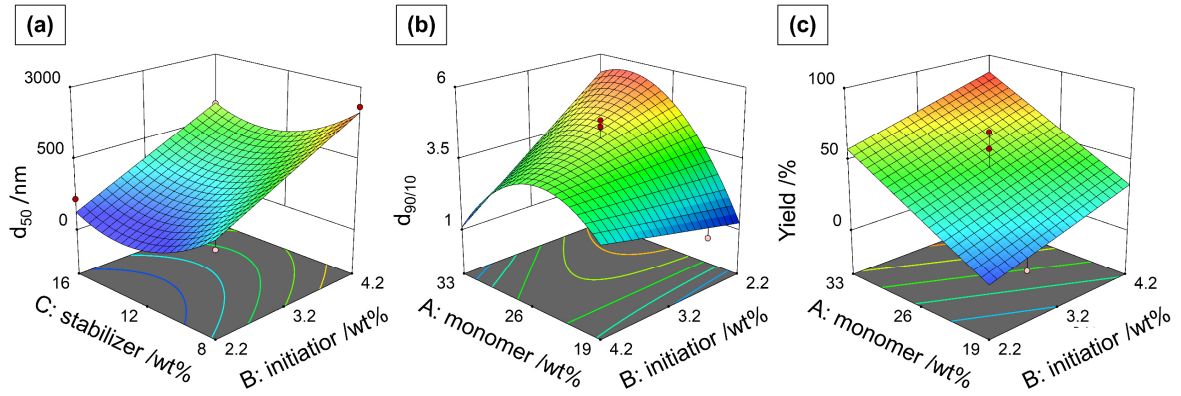


**Figure 10.2** Response surface plots showing the values for the responses predicted by the response surface model across the design space for each combination of process factor settings for **a)** the median particle size at high levels of monomer, **b)** dispersity and **c)** yield both at medium factor level settings of the stabilizer. Blue color corresponds to low and red to high response values. Note that for **b)** the axis of the initiator is inversed for better visibility.

If the amount of initiator is increased, the proportion of free radical chains in the reaction solution increases. With increased levels of monomer, the solubility of PS in the continuous phase is improved. As a result, the critical chain length also increases. Nucleation nuclei form more rapidly and the coagulation of oligomeric radicals is accelerated. The increased coagulation rates resulting from both, increased level of monomer and initiator, favor larger particle diameters[71,72,126].

The effect of the stabilizer is negative but combined with a positive $C^2$ factor effect term. Generally, the more stabilizer is within the system the higher relative surface-to-volume ratio of smaller monomer droplets can be better stabilized and coalescence is inhibited. However, the effect is attenuating as the stabilizer content is further increased over approximately 12 wt%. Below this stabilizer content no further significant reduction in particle size is observed.

### *10.1.2.2. Dispersity*

The dispersity is critical for PS seed batches which are used as seeds in the following seed-swelling polymerization, as the shape and size distribution is determined by the seed.

A statistically significant model for the dispersity could be established with a predictive power of the model $R^2_{predicted} = 0.7347$ ($R^2 = 0.8971$). For the dispersity, the factor effect terms A – monomer, B – initiator and their two-factor interaction AB and the non-linear effect terms $A^2$ were found to be statistically significant at an α-level of 0.05. The impact of the factors on the dispersity is given in coded terms in equation (10.3)

$$d_{\frac{90}{10}} = 4.25 + 0.6784\ A - 0.7560\ B - 1.36\ AB - 1.72\ A^2 \qquad (10.3)$$

As a two-factor interaction is present, the isolated discussion of factor effects is not sensible. The interaction in combination with the non-linear $A^2$ term is visible in **Figure 10.2**b as shift of maximum in the dispersity in dependence of A and B. For high initiator concentrations, the dispersity is highest when the monomer concertation is around 24 wt% but for low initiator concentrations the maximum shifts towards higher monomer concentration (30 wt%). Monodisperse particle distributions with a $d_{90}/d_{10} < 1.4$ are either achieved with high monomer and high initiator concentrations or at low monomer concentrations with low initiator settings.

*10.1.2.3. Yield*

The yield of the synthesis was modeled with a predictive power of $R^2_{predicted} = 0.7749$ ($R^2 = 0.8544$) and was only statistically significantly affected by the linear effects of monomer and initiator concentration. Their relative effect strength in coded terms is shown in equation (10.4):

$$\text{Yield } /\% = 45.30 + 27.29\ A + 14.38\ B \tag{10.4}$$

As the initiator and monomer levels are increased, also the yield is increased. This results from more initiator radicals present with increased levels of initiator and thus more oligomeric chains forming. Thus, the rate of particle formation is increased[126]. As the monomer concentration rises, more monomer can be attached to formed reaction seeds as the critical chain length is prolonged with higher styrene concentrations[71]. As a result, the yield can be increased by using higher levels of monomer and initiator.

*10.1.2.4. Optimized settings to achieve monodisperse PS seeds*

Monodisperse particles of various sizes with a sufficient yield are favorable. Hence, a numerical optimization was performed with following criteria: 1) minimization of dispersion (within $d_{90}/d_{10}$ of 1.08 – 1.40), as this is a very critical property and 2) maximize yield (at least 50 %). Using these criteria, following particles predictions of synthesis setting to attain differently sized monodisperse PS seeds are predicted (**Table S. 10.4**).

**Table S. 10.4** Prediction of syntheses settings and resulting PS seed properties fulfilling the optimization criteria: 1) minimization of dispersion (within $d_{90/10}$ of 1.08 – 1.40) and 2) maximize yield (at least 50%).

| Syntheses | Monomer | Initiator | Stabilizer | $d_{50}$ | $d_{90/10}$ | Yield | Desirability |
|---|---|---|---|---|---|---|---|
| | /wt% | /wt% | | /nm | | /% | |
| **1** | 33.0 | 4.2 | 8.0 | 2490 | 1.09 | 87.4 | 0.985 |
| **2** | 33.0 | 4.2 | 16.0 | 1900 | 1.09 | 87.4 | 0.985 |
| **3** | 33.0 | 4.2 | 12.2 | 1660 | 1.09 | 87.4 | 0.985 |

A range of particle sizes between 1660 nm up to 2490 nm can be achieved. The only factor changing to steer the particle size is the amount of stabilizer, as it affects particle size but not dispersity or yield.

### 10.1.3. Conclusion

For the preparation of monodisperse PS seeds, the monomer and initiator concentration have to be in a suitable range, which is found at high settings for both factors (33.0 wt% monomer and 4.2 wt% initiator). Under these conditions, a narrow size distribution can be achieved. As the dispersity is not affected by the stabilizer concentration (for stabilizing concentrations between 8 wt% and 16 wt% to monomer), the particle size can be steered by variation of the concentration of the stabilizer.

## 10.2. Optimization of the separation method for reversed-phase HPLC protein separation

The efficiency of a HPLC separation is not only based on the column properties, but can be further adapted by optimizing the applied method.

In order to attain a good separation method for the reversed-phase separation of a protein mixture using a commercially available Prosphere 300 column, a systematic analysis was performed. The investigated factors were A – starting condition of the gradient (eluent B%), B – end conditions of the gradient (eluent B%) and C – duration of gradient (min). The aim was to achieve a good resolution between all four signals ($R \geq 2$) while minimizing the analysis time to minimize resource expenditure (solvents and time).

### 10.2.1. Materials and methods

#### *10.2.1.1. Chemicals*

Acetonitrile (ACN, HPLC grade) and HPLC grade water were purchased from Fisher Scientific. Trifluoracetic acid (TFA) and the protein standard H2899 were obtained from Sigma Aldrich. The column Prosphere 300 column (4.6 x 250 mm, C-18, 300 Å) was kindly provided by Dr. Maisch GmbH.

#### *10.2.1.2. Separation procedure*

Eluent A consisted of HPLC water with 0.1 % of TFA. Eluent B consisted of ACN with 0.08 % TFA. The proteins (ribonuclease A, cytochrome c, holo-transferrin and apomyoglobin each 1 mg) of the standard were solubilized in 1 mL A:B 90:10. For each measurement 5 µL of the sample were injected.

The factor setting for optimization of the separation were varied according to an FCD within the factor level ranges given in **Table S. 10.5**. Although the factors can also be described as steepness of the gradient with $B\%\cdot min^{-1}$, this cannot be applied as factor, as the retention is also dependent on the overall ratio of B%. This affects the equilibrium of the analyte and is decisive for whether the analyte is adsorbed onto the surface or elutes with the eluent.

**Table S. 10.5** Factor level settings of starting and ending condition as well as the duration of the gradient.

| | **Low (-)** | **Medium (0)** | **High (+)** |
|---|---|---|---|
| **A** – Starting conditions of gradient /%B | 10 | 20 | 30 |
| **B** – End conditions of gradient /%B | 70 | 85 | 100 |
| **C** – Duration of gradient /min | 10 | 25 | 40 |

### *10.2.1.3. Set-up*

All measurements were performed on an Agilent 1100 system (Agilent Technologies, Waldbronn, Germany) equipped with a quaternary pump and degasser, an auto sampling system, column oven and a DAD detector (215 nm). The Chem-Station software (B.04.03, Agilent Technologies, Waldbronn, Germany) was used for instrument control, data acquisition and automated data analysis. The conception and analysis of the FCD was performed using the Design-Expert 12 (12.0.12.0 64-bit, Stat-Ease Inc.).

## 10.2.2. Results and discussion

The resolution between peak a and peak b (**Figure 10.3**), which corresponds to the separation of ribonuclease A and cytochrome c, varied from 1.60 to 8.38. Thus, the separation of these substances is not critical, but a resolution of ≥ 2.00 is favorable as it reflects a complete baseline separation.

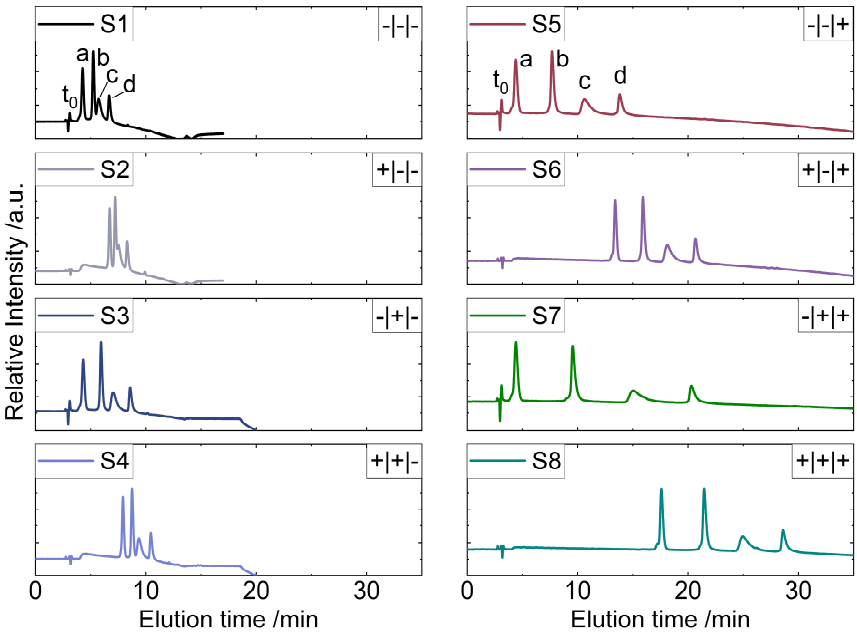


**Figure 10.3** Chromatograms of the protein separation for the factorial points of the FCD. Elution sequence is the same for all measurements: a) ribonuclease A b) cytochrome c c) holo-transferrin and d) apomyoglobin (exemplarily indicated in **S1** and **S5**). Detection wavelength was 215 nm, injection was 5 µL with 1 mg·mL$^{-1}$ of each protein. The factor level settings for each separation according to **Table S. 10.6** is indicated in the upper right corner of the respective chromatogram.

Most critical is the separation between peeks b and c (**Figure 10.3**), which correspond to cytochrome c and holo-transferrin, respectively. The resolution varied between 0.67 and 4.22, thus for some methods, no baseline separation was achieved. The resolution of the separation of holo-transferrin and apomyoglobin varied between 1.31 and 3.77. Here, some separations did not result in a baseline separation. The required analysis time until the elution of apomyoglobin (elution time of signal d, $t_d$) took from 6.68 to

28.62 minutes. To minimize analysis time and resources, this response should be minimized. All results are summarized in **Table S. 10.6**.

General trends in the chromatogram can be seen in **Figure 10.3**, which show the chromatograms of the factorial points **S1–8** (separations 1–8). As the starting condition (factor A) is risen from 10 % to 30% of eluent B, the peaks elute earlier and the peaks are further apart. As the end condition (factor B) increases from 70 % to 100% of eluent B (e.g. from **S5** to **S7** and **S1** to **S3**) all analytes elute earlier but the resolution is worse, especially between peaks c and c (cytochrome c and holo-transferrin, respectively). For the duration of the gradient (factor C), the resolution between peaks is improved but the elution is retarded and the general analysis time is massively increased. However, as shown in **Table S. 10.7**, highly complex models with two-factor interactions and quadratic effects are needed to describe the dependencies of the resolutions of the factor settings.

**Table S. 10.6** Factor level settings and their corresponding responses resolutions between peak pairs and the elution time of apomyoglobin (d). The table is separation order is listed in Yates standard order.

| Separation | A Starting conditions | B End conditions | C Duration of gradient | $R_{ab}$ | $R_{abc}$ | $R_{cd}$ | $T_d$ |
|---|---|---|---|---|---|---|---|
| | /B% | /B% | /min | | | | /min |
| **S1** | 10 | 70 | 10 | 2.31 | 0.94 | 1.63 | 10.45 |
| **S2** | 30 | 70 | 10 | 3.49 | 1.18 | 1.65 | 8.57 |
| **S3** | 10 | 100 | 10 | 1.60 | 0.68 | 1.66 | 8.30 |
| **S4** | 30 | 100 | 10 | 2.45 | 0.67 | 1.31 | 6.68 |
| **S5** | 10 | 70 | 40 | 8.09 | 3.42 | 3.29 | 28.62 |
| **S6** | 30 | 70 | 40 | 8.38 | 4.22 | 3.77 | 20.31 |
| **S7** | 10 | 100 | 40 | 5.95 | 2.68 | 2.88 | 20.68 |
| **S8** | 30 | 100 | 40 | 6.21 | 3.17 | 3.13 | 13.82 |
| **S9** | 10 | 85 | 25 | 4.74 | 2.16 | 2.45 | 16.68 |
| **S10** | 30 | 85 | 25 | 6.10 | 3.06 | 3.33 | 12.11 |
| **S11** | 20 | 70 | 25 | 7.16 | 3.06 | 3.74 | 17.64 |
| **S12** | 20 | 100 | 25 | 4.91 | 2.18 | 3.16 | 12.72 |
| **S13** | 20 | 85 | 10 | 2.06 | 0.77 | 1.39 | 8.43 |
| **S14** | 20 | 85 | 40 | 7.49 | 3.23 | 3.10 | 20.68 |
| **S15** | 20 | 85 | 25 | 5.88 | 2.51 | 3.26 | 14.65 |
| **S16** | 20 | 85 | 25 | 5.38 | 2.43 | 2.70 | 14.70 |
| **S17** | 20 | 85 | 25 | 5.85 | 2.49 | 3.30 | 14.61 |
| **S18** | 20 | 85 | 25 | 5.84 | 2.46 | 3.23 | 14.60 |
| **S19** | 20 | 85 | 25 | 5.82 | 2.49 | 3.27 | 14.61 |

All models for the resolutions $R_{ab}$, $R_{bc}$, $R_{cd}$ and elution time of apomyoglobin $t_d$, statistically significant models with a high predictive power ($R^2_{predicted} \geq 0.80$) were established. An overview over selected statistical model parameters is given in **Table S. 10.7**. Highly complex models with multiple non-linear factor effects and two-factor interactions are needed to describe the effects on the resolutions and elution time of apomyoglobin. The corresponsing coded equations are given in **Table S. 10.8**

**Table S. 10.7** Selected statistical parameters from the ANOVA tables for the models of the peak resolutions and the elution time of apomyoblobin.

| Statistical parameter | Model term | $R_{ab}$ | $R_{bc}$ | $R_{cd}$ | $t_d$ |
|---|---|---|---|---|---|
| p-values | Model | < 0.0001 | < 0.0001 | < 0.0001 | < 0.0001 |
| | **A** – starting condition | 0.0039 | 0.0003 | n.s. | < 0.0001 |
| | **B** – end condition | < 0.0001 | < 0.0001 | n.s. | < 0.0001 |
| | **C** – gradient time | < 0.0001 | < 0.0001 | < 0.0001 | < 0.0001 |
| | AB | n.s. | 0.0037 | n.s. | 0.0069 |
| | AC | n.s. | 0.0280 | n.s. | < 0.0001 |
| | BC | 0.0236 | 0.0332 | n.s. | < 0.0001 |
| | $A^2$ | n.s. | n.s. | n.s. | 0.0094 |
| | $B^2$ | n.s. | n.s. | n.s. | 0.0015 |
| | $C^2$ | 0.0002 | 0.0001 | n.s. | n.s. |
| | Lack of fit | 0.1622 | 0.0126 | 0.2762 | 0.0013 |
| $R^2$ | | 0.9799 | 0.9870 | 0.8692 | 0.9995 |
| $R^2_{adjusted}$ | | 0.9715 | 0.9799 | 0.8447 | 0.9990 |
| $R^2_{predicted}$ | | 0.9466 | 0.9505 | 0.8028 | 0.9910 |

To obtain a baseline separation for all four analytes while minimizing the analysis time, the models were combined by numerical optimization. The optimization parameters were chosen to aim for a resolution between all analytes of ≥ 2.00 and a minimization of the elution time $t_d$ (in range: 2.00 – max, $t_d$: minimize).

**Table S. 10.8** Coded equations for the models of the peak resolutions and the elution time of apomyoblobin.

| Model term | $R_{ab}$ | $R_{bc}$ | $R_{cd}$ | $t_d$ |
|---|---|---|---|---|
| | +5.7600 | +2.5400 | +3.1900 | +14.6200 |
| **A** – starting condition | +0.3940 | +0.2420 | - | -2.3200 |
| **B** – end condition | -0.8310 | -0.3440 | - | -2.3400 |
| **C** – gradient time | +2.4200 | +1.2500 | +0.8530 | +6.1700 |
| AB | -0.3200 | - | - | +0.2129 |
| AC | - | +0.1325 | - | -1.4600 |
| BC | - | -0.1275 | - | -1.3000 |
| $A^2$ | - | - | - | -0.3327 |
| $B^2$ | - | - | - | +0.4553 |
| $C^2$ | -0.9832 | -0.4442 | -0.8557 | - |

With a desirability of 0.884 a good setting for an optimized method could be achieved. **Figure 10.4** shows the numerical optimization as ramp graph. All resolutions are predicted to be R ≥ 2.00 and apomyoglobin is predicted to elute after 9.22 min after injection. The optimized method settings are A – starting condition 30 %B, B – end condition 100 %B and a C – gradient duration of 20.30 min.

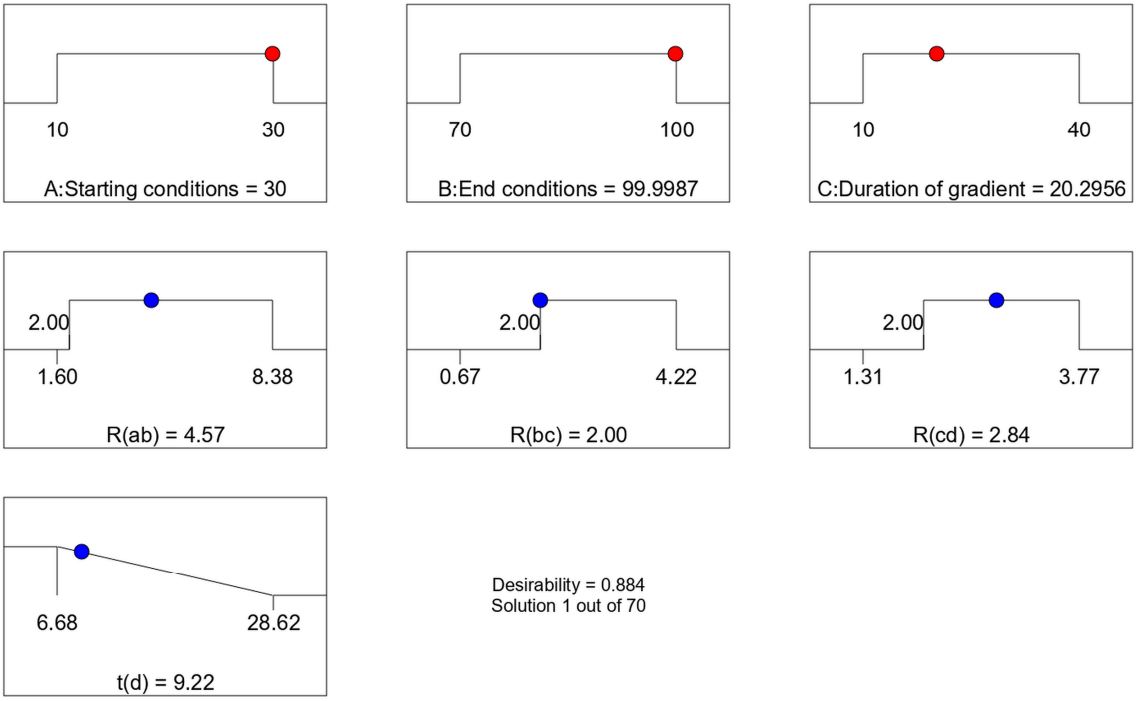


**Figure 10.4** Numerical optimization graph as ramps. Optimization criteria were resolutions ≥ 2 and a minimization of elution time of d ($t_d$). A desirability of 0.884 was reached. R(ab) = resolution between peaks a and b, R(bc) = resolution between peaks b and c, R(cd) = resolution between peaks c and d. The red dots mark the process factor settings needed to attain the optimized results. The blue dots mark the respective value of each response at the optimized factor level settings.

To test the optimized method and validate the prediction, the separation of the protein mixture was conducted three times using the optimized method. The chromatograms are shown in **Figure 10.5**. A good separation of all signals was achieved with the last analyte eluting in less than ten minutes.

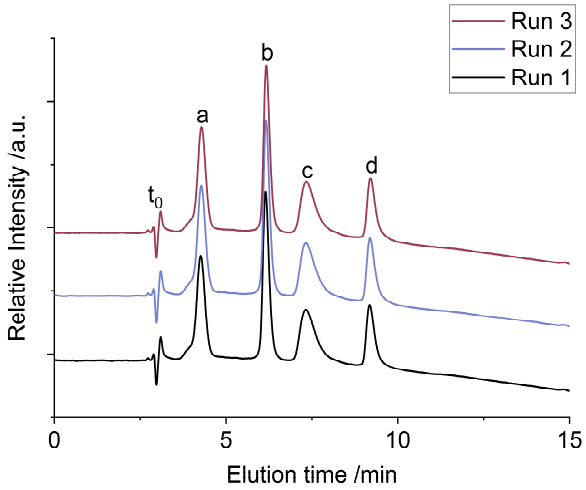


**Figure 10.5** Chromatograms of validation runs of the protein separation with the optimized method. Elution sequence is the same for all measurements: **a)** ribonuclease A **b)** cytochrome c **c)** holo-transferrin and d) apomyoglobin.

**Table S. 10.9** shows the prediction versus actual table for the protein separation with the optimized gradient settings. The actual values are given as mean ± standard deviation. The predicted and actual values match quite well and the actual values lie within the 95 % confidence interval of the prediction. This confirms the validity of the models. Although all analytes already eluted after ten minutes, the overall analysis time is 20.30 minutes. However, as the overall change in eluent composition within this time is known, the gradient steepness of 3.45 B%·min$^{-1}$ can be determined (see equation (10.5)).

$$\text{Gradient steepness } [\text{B\%} \cdot \text{min}^{-1}] = \frac{(\text{end condition [B \%]} - \text{starting condition [B\%]})}{Duration\ of\ gradient\ [min]} \qquad (10.5)$$

**Table S. 10.9** Actual versus prediction table for the response values under application of the optimized gradient conditions for the separation of the protein mixture H2899. CI = confidence interval of 95 % for low (-) and high (+) boundary.

| **Predicted / Actual / Residual** | **$R_{ab}$** | **$R_{bc}$** | **$R_{cd}$** | **$t_d$** /min |
|---|---|---|---|---|
| Predicted Value | 4.57 | 2.00 | 2.84 | 9.22 |
| (±95 % CI) | (4.14–4.99) | (1.81–2.19) | (2.61–3.06) | (9.8.94-9.50) |
| Actual Value | 4.83±0.04 | 1.98±0.01 | 2.87±0.02 | 9.19±0.02 |
| Residual | 0.26 | -0.02 | 0.03 | -0.03 |

Using this information, the analysis time can be reduced without effecting the separation. The method parameters are starting condition: 30.0 B%, end condition: 64.5 B% with a gradient duration of ten minutes.

### 10.2.3. Conclusion

The resolution of peaks is dependent in a complex way on the gradient conditions starting condition, end condition and the duration of the gradient for the separation of ribonuclease A, cytochrome c, holo-transferrin and apomyoglobin. The approach of RSM allowed a precise prediction of the optimal gradient for a baseline separation of all analytes with minimal time and thus resource expenditure, when using the Prosphere 300 column as stationary phase. An optimal separation method for this set-up was established with the elution of all four analytes in under ten minutes. Moreover, this approach can be transferred to self-prepared separation columns to efficiently optimize the separation method to achieve the best separation efficiency.

## 10.3. Thermogravimetric analysis of template removal

The preparation of porous silica materials using a template requires a subsequent removal step of the sacrificial template[46,47,51]. Thereby, the removal procedure is dependent on the type of template. For polymeric hard-templates, here *p*(GMA-*co*-EDMA), the thermoset has to be removed by calcination at high temperatures. Temperatures of up to 500 °C are required to fully remove the template from the hybrid material to prepare the MPSMs[223,224]. However, due to condensation of residual silanol groups, silica can undergo shrinkage as a result of elevated temperatures[121]. This behavior can affect the structure of the silica and its pores and can be used to modify these[120,256]. Consequently, the conditions of calcination have to be chosen carefully to avoid sintering of the residual silica, and thus closure of pores, which occurs at temperatures above 400 °C[121].
Thermogravimetry (TGA) measures the change in mass as function of the temperature[257] and allows to assess the decomposition processes of materials, and to determine the residual mass of non-decomposable sample components, e.g. silica. Moreover, the kinetics of mass loss due to processes like sublimation, decomposition, vaporization or oxidation can be assessed by thermal analysis[150,258]. Model free kinetics or iso-conversional methods are a way to determine the activation energy of a reaction without the assumption of a kinetic model. The processes need to fulfill the assumption that the reaction rate at a certain conversion depends solely on the temperature[258].

In this section, the thermal decomposition steps of the *p*(GMA-*co*-EDMA) part of the hybrid material and evaporation of adsorbed and/or water released by condensation of silanol groups are investigated to improve process understanding of calcination. It is to be investigated whether a mild calcination is possible which completely burns out the polymer without affecting the pore structure of the silica by condensation.

### 10.3.1. Material and methods

The thermogravimetric measurements were performed with a TGA/DSC I (Mettler Toledo) under synthetic air (50 mL·min$^{-1}$) and with varying heating rates. Samples were measured in a 900 µL alumina crucible with sample masses of ~230 mg.

For the iso-conversional method a set of different heating rates (0.5, 0.7, 1.0, 1.3, 1.6, 1.8, 2.0, 3.0, 4.0, 5.0, 6.0, 7.5, 10.0 K·min$^{-1}$) from 30 – 800 °C and 1 K·min$^{-1}$ to 850 °C were used. To simulate the conditions of the calcination oven measurements were conducted with a heating rate of 3 K·min$^{-1}$ from 30 – 600°C with a subsequent isothermal section of 10 h at 600°C.

The polymer template was prepared with 40/60 v./v. GMA to EDMA, 50/50 v./v. monomer to porogen ratio with the porogen mixture consisting of 73.3/26.7 v./v. toluene/cyclohexanol. After amino-functionalization with TEPA, 15 g of the p@TEPA particles were dispersed in 900.0 mL IPA with 112.5 mL $H_2O$ and were sonicated for 15 minutes. Subsequently, 36.0 mL TEOS and 3.6 mL of 25 % $NH_4OH$ were added and stirred at room temperature for 24 h (130 rpm, mechanic stirrer). Thereafter, the HBs were washed with ethanol and water for three times and then dried. The silica reference material was prepared similar to the hybrid beads (HBs) but without the presence of p@TEPA and in smaller scale (× 0.4).

Conversion rate and model fitting was performed using the Kinetics Neo Software (Netzsch Gerätebau GmbH). The models were fitted by minimizing the difference between the measured and the calculated values.

### 10.3.2. Results and discussion

In order to be able to assign the stages of the mass change to the individual materials p@TEPA, HB and silica were calcinated individually at 1.0 $K \cdot min^{-1}$. **Figure 10.6** shows the thermogram and the conversion rate for all three materials. While the p@TEPA is completely decomposed, the silica material has a weight loss of 15.1 %, the HB has a weight loss of 69.0 % and thus consists of 31.0 % silica.

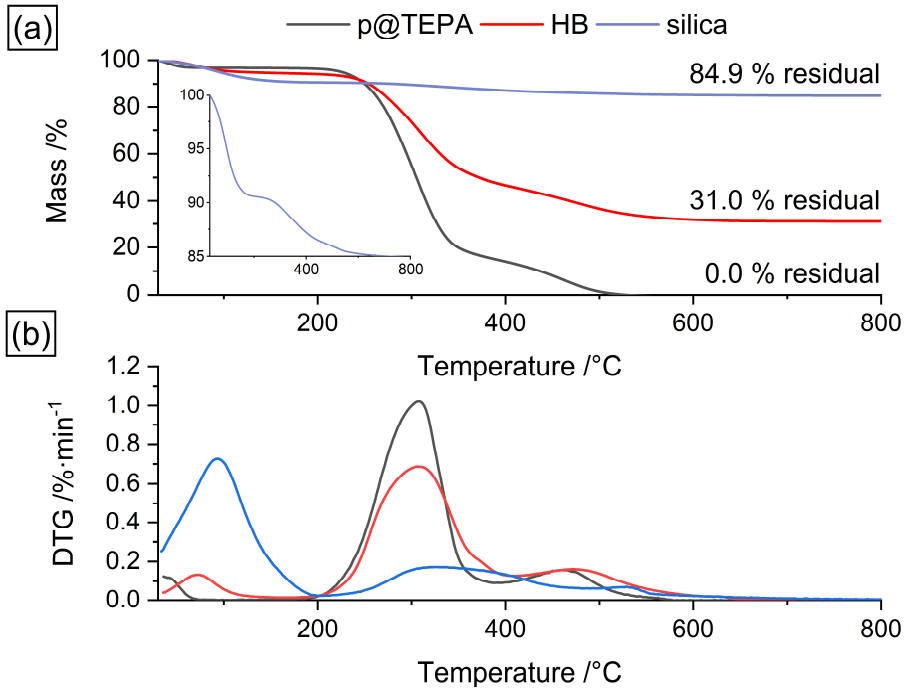


**Figure 10.6 a)** TGA thermogram with rescaled thermogram for silica and **b)** conversion rate of p@TEPA, HB and silica in comparison.

It can be clearly seen that the HB is made up of the p@TEPA and silica, as the mass loss stages of both materials are present. The first weight loss in the thermograms results from desorption of water and is most pronounced for the silica. Here, the desorption of surface adsorbed water takes place from 0 to 170 min, which equals a temperature between 30 °C and 200 °C. Thereafter, the silica surface is still fully hydroxylated and no water is adsorbed at the surface. From 200 to ~ 450 min (230 – 480 °C) a second mass loss stage of silica can be seen. This mass loss can be attributed to condensation of silanol groups[121]. A third, very small increase in conversion rate can be observed between 465 and 530 min, which corresponds to a temperature between 495 °C and 560°C. Here, further condensation of silanol groups occurs (temperature of maximum weight loss, $T_{max}$ = 529 °C). Raman et al. observed sintering above 550 °C, which lead to a reduction of porosity[123]. For p@TEPA, three main steps of mass loss are observed. First, from desorption of water at low temperatures up to 70°C. The second (195°C – 385 °C, $T_{max}$ = 307 °C) and third (385 – 580 °C, $T_{max}$ = 465°C) are attributed to the decomposition of the polymeric backbone. The peak form of the second peak indicates that here two processes are overlapping. From literature and measurements at higher temperature gradients, this can be confirmed and can be attributed to the depolymerization and following isomerization of the epoxy group[222–224].The polymer is completely decomposed at ca. 580 °C.
The HB material shows properties from both components, silica and p@TEPA and exhibits mass losses from both parts. Interestingly, the third polymeric decomposition step is shifted to higher temperatures with $T_{max}$ = 473 °C. This is a result from the addition of silica as inorganic filler into the p@TEPA, which acts as a thermal insulator and thus shifts the decompositions to higher temperatures.

The $T_{max}$ of the last condensation step in the silica material lies above the $T_{max}$ of the last decomposition step within the HB. Thus, the activation energy of the decomposition of the HB was analyzed using model free kinetics to assess, if a full removal of the polymer from the HB material is possible without complete condensation of silanol groups of the silica part. Therefore, measurements with multiple heating rates were conducted. **Figure 10.7** show the thermograms and conversion rate diagrams for the decomposition of the HB for multiple heating rates. Thereby, a shift in processes occurs at ca. 2 – 3 K·min$^{-1}$. For slow heating rates up to 2.0 K·min$^{-1}$ no overlap of curves is visible and the conversion rate is solely dependent on the temperature (**Figure 10.7**a and c). Here, the prerequisite for the application of model-free kinetics is given. The curves of the heating rates of 1.8 K·min$^{-1}$ and 2.0 K·min$^{-1}$ already start to differ from even slower heating rates, but are similar enough to be still included. For the higher heating rates 3.0 K·min$^{-1}$ to 10.0 K·min$^{-1}$, the curves start to overlap (**Figure 10.7**b and d). This indicates that the thermogravimetric measurement is strongly dependent on

the heating rate and thus the prerequisite for model free kinetics is not given. Here, probably a change in reaction path occurs or the process is diffusion controlled[259]. At temperatures around 300 – 400 °C, the second stage of the polymer decomposition takes place. As already mentioned above, at higher heating rates this stages is spitted into two processes – the depolymerization and isomerization of the epoxy groups[222–224]. As the heating rate is increased, the isomerization rate outpaces the depolymerization rate and thus, it is probably a diffusion-controlled process and cannot be described using model free kinetics.

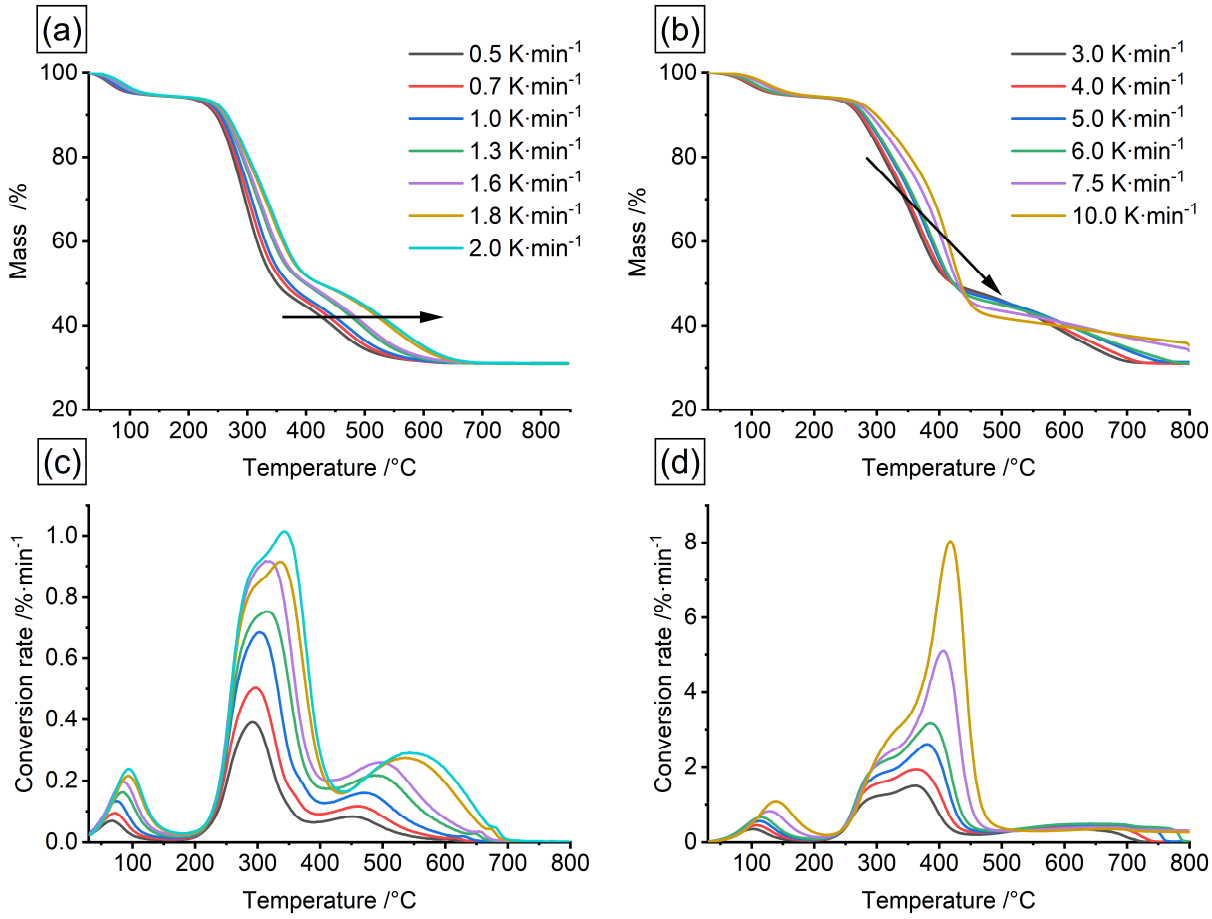


**Figure 10.7** Thermograms for heat rate ranges from **a)** 0.5 to 2.0 K·min$^{-1}$ and **b)** 3.0 to 10.0 K·min$^{-1}$ and corresponding conversion rate diagrams for **c)** 0.5 to 2.0 K·min$^{-1}$ and **d)** 3.0 to 10.0 K·min$^{-1}$.

Using the Vyazovkin algorithm with the data from the heating rates of 0.5 K·min$^{-1}$ to 2.0 K·min$^{-1}$, the data could be fitted very well with $R^2 = 0.9997$ and the activation energy over the progression of the decomposition could be predicted (**Figure 10.8**). At a conversion of approximately 0.7, the activation energy drops to 20 kJ·mol$^{-1}$ (e.g. at ca. 500 °C for a heating rate of 1.3 K·min$^{-1}$). This indicates that it might be possible to change from a dynamic heating rate to an isothermal setting at e.g. 500 °C following a heating rate of 1.3 K·min$^{-1}$ and thus, allow a complete decomposition of the polymer without inducing vicious condensation of silanol groups in the silica part of the HB. However, as can be seen in **Figure 10.8**b, small changes in the heating rate result in shifts in the

temperature at which a certain conversion is reached. This limits the applicability with common laboratory calcination ovens and this approach cannot be transferred to the laboratory scale needed to calcinate larger amounts of HBs to attain enough MPSM material to pack a HPLC column. Furthermore, at heating rates > 3.0 K·min$^{-1}$ a constant mass could only be obtained at temperatures of ≥ 700 °C, which automatically means that inevitably the condensation of silica occurs (**Figure 10.7**). For the 3.0 K·min$^{-1}$, which equals the heating rate of the calcination oven, the $T_{max\text{-}silanol}$ is 580 °C und thus the temperature of silanol condensation is exceeded.

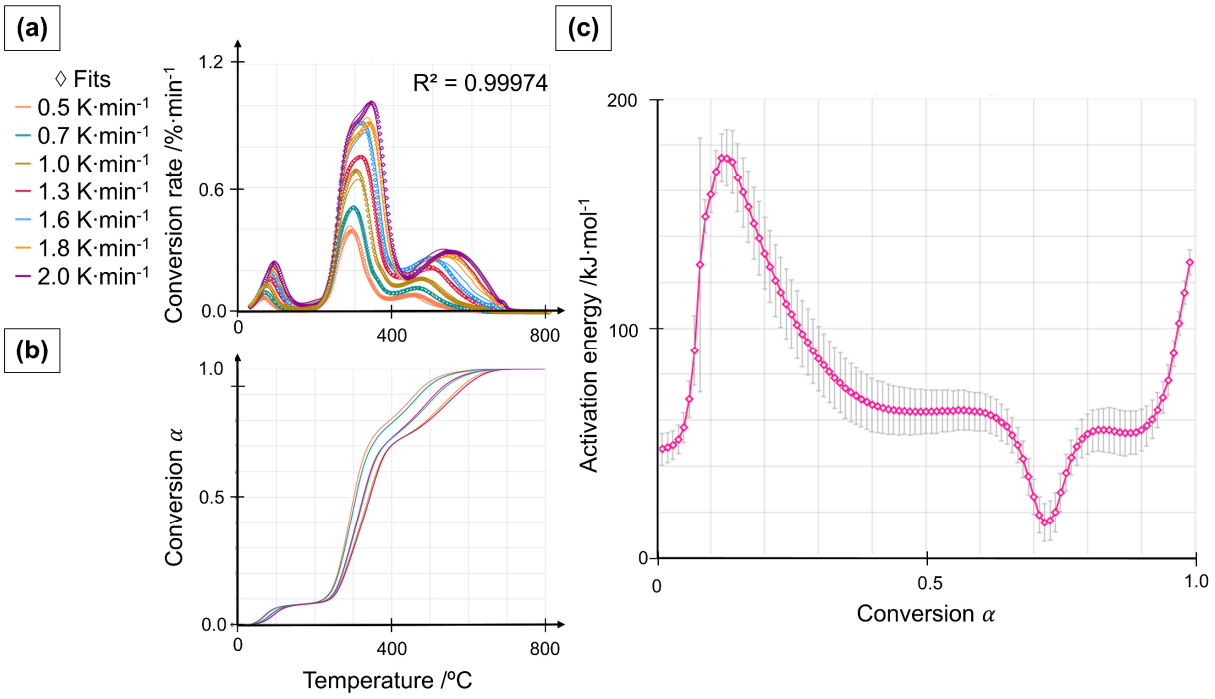


**Figure 10.8** TGA evaluation of the thermal decomposition of HBs at heating rates between 0.5 to 2.0 K·min$^{-1}$ using the Vyazovkin algorithm. **a)** Conversion rate fit over temperature **b)** degree of conversion $\alpha$ over temperature and **c)** calculated activation energy over degree of conversion $\alpha$.

## 10.3.3. Conclusion

The decomposition of HBs can be categorized into two heating rate regions: < 2.0 K·min$^{-1}$, where the process can be described using model free kinetics and > 2.0 K·min$^{-1}$ in which diffusion-controlled processes occur, which make a prediction of the activation energy using model free kinetics not feasible. Although the model free kinetics indicate that in theory a mild calcination method should theoretically be possible, the high demands (very small heating rates that must be adjusted very precisely) cannot be realized on a laboratory scale. Thus, the calcination procedure was carried out in a standardized manner at 600 °C for 10 h with an initial heating rate of 3.0 K·min$^{-1}$ for all calcination procedures.

# References


1. Steinbach, J.C.; Fait, F.; Wagner, S.; Wagner, A.; Brecht, M.; Mayer, H.A.; Kandelbauer, A. Rational Design of Pore Parameters in Monodisperse Porous Poly(glycidyl methacrylate-co-ethylene glycol dimethacrylate) Particles Based on Response Surface Methodology. *Polymers (Basel)* **2022**, *14*, 382, doi:10.3390/polym14030382.
2. Fait, F.; Steinbach, J.C.; Kandelbauer, A.; Mayer, H.A. Impact of porosity and surface functionalization of hard templates on the preparation of mesoporous silica microspheres. *Microporous Mesoporous Mat.* **2023**, *351*, 112482, doi:10.1016/j.micromeso.2023.112482.
3. Steinbach, J.C.; Fait, F.; Mayer, H.A.; Kandelbauer, A. Monodisperse Porous Silica/Polymer Nanocomposite Microspheres with Tunable Silica Loading, Morphology and Porosity. *Int. J. Mol. Sci.* **2022**, *23*, 14977, doi:10.3390/ijms232314977.
4. Steinbach, J.C.; Fait, F.; Mayer, H.A.; Kandelbauer, A. Sol-Gel-Controlled Size and Morphology of Mesoporous Silica Microspheres Using Hard Templates. *ACS Omega* **2023**, *8*, 30273–30284, doi:10.1021/acsomega.3c03098.
5. Fait, F.; Steinbach, J.C.; Kandelbauer, A.; Mayer, H.A. Incorporation of silica nanoparticles into porous templates to fabricate mesoporous silica microspheres for high performance liquid chromatography applications. *J. Chromatogr. A* **2023**, *1705*, 464190, doi:10.1016/j.chroma.2023.464190.
6. Fait, F.; Wagner, S.; Steinbach, J.C.; Kandelbauer, A.; Mayer, H.A. Tailoring the Morphology of Monodisperse Mesoporous Silica Particles Using Different Alkoxysilanes as Silica Precursors. *Int. J. Mol. Sci.* **2023**, *24*, 11729, doi:10.3390/ijms241411729.
7. Steinbach, J.; Goedicke-Fritz, S.; Tutdibi, E.; Stutz, R.; Kaiser, E.; Meyer, S.; Baumbach, J.I.; Zemlin, M. Bedside Measurement of Volatile Organic Compounds in the Atmosphere of Neonatal Incubators Using Ion Mobility Spectrometry. *Front. Pediatr.* **2019**, *7*, 248, doi:10.3389/fped.2019.00248.
8. Steinbach, J.C.; Schneider, M.; Hauler, O.; Lorenz, G.; Rebner, K.; Kandelbauer, A. A Process Analytical Concept for In-Line FTIR Monitoring of Polysiloxane Formation. *Polymers (Basel)* **2020**, *12*, 2473, doi:10.3390/polym12112473.
9. Wagner, A.; Wagner, S.; Bredfeldt, J.-E.; Steinbach, J.C.; Mukherjee, A.; Kronenberger, S.; Braun, K.; Kandelbauer, A.; Mayer, H.A.; Brecht, M. Chemical Imaging of Single Anisotropic Polystyrene/Poly (Methacrylate) Microspheres with Complex Hierarchical Architecture. *Polymers (Basel)* **2021**, *13*, 1438, doi:10.3390/polym13091438.
10. Wahrendorff, P.; Stefanakis, M.; Steinbach, J.C.; Allnoch, D.; Zuber, R.; Kapfhammer, R.; Brecht, M.; Kandelbauer, A.; Rebner, K. Simultaneous Determination of Droplet Size, pH Value and Concentration to Evaluate the Aging Behavior of Metalworking Fluids. *Sensors* **2021**, *21*, 8299, doi:10.3390/s21248299.
11. Steinbach, J.C.; Golovko, D.S.; Kandelbauer, A.; Rebner, K. Real-Time Quantification of Meat Paste Constituents Displaying Nonlinear Blending Behavior Including Salt Using an In-Line NIR MEMS Sensor. *ACS Food Sci. Technol.* **2023**, *3*, 1288–1299, doi:10.1021/acsfoodscitech.3c00163.
12. Nölle, L.; Schietinger, C.; Loritz, L.; Virtaci, M. Effektbestimmung der Synthesefaktoren mittels statistischer Versuchsplanung zur Herstellung monodisperser Polystyrol- Partikel. Abschlussbericht POL WS2021/2022; Reutlingen University, Hochschule Reutlingen.
13. Markus, K.; Wahrendorff, P.; Wolf, M. Steuerung der Morphologie poröser Poly(GMA-co- EDMA) Partikel mittels statistischer Versuchsplanung; Hochschule Reutlingen, Reutlingen, 2021.
14. Manzano, M.; Vallet-Regí, M. Mesoporous Silica Nanoparticles for Drug Delivery. *Adv. Funct. Mater.* **2020**, *30*, 1902634, doi:10.1002/adfm.201902634.
15. Siavashani, A.Z.; Nazarpak, M.H.; Bakhsh, F.F.; Toliyat, T.; Solati-Hashjin, M. Preparation of Mesoporous Silica Nanoparticles for Insulin Drug Delivery. *AMR* **2013**, *829*, 251–257, doi:10.4028/www.scientific.net/AMR.829.251.
16. Dohare, A.; Sudhakar, S.; Brodbeck, B.; Mukherjee, A.; Brecht, M.; Kandelbauer, A.; Schäffer, E.; Mayer, H.A. Anisotropic and Amphiphilic Mesoporous Core-Shell Silica Microparticles Provide

Chemically Selective Environments for Simultaneous Delivery of Curcumin and Quercetin. *Langmuir* **2021**, *37*, 13460–13470, doi:10.1021/acs.langmuir.1c02210.
17. Giraldo, L.F.; López, B.L.; Pérez, L.; Urrego, S.; Sierra, L.; Mesa, M. Mesoporous Silica Applications. *Macromol. Symp.* **2007**, *258*, 129–141, doi:10.1002/masy.200751215.
18. Hartmann, M. Ordered Mesoporous Materials for Bioadsorption and Biocatalysis. *Chem. Mater.* **2005**, *17*, 4577–4593, doi:10.1021/cm0485658.
19. Slowing, I.I.; Trewyn, B.G.; Giri, S.; Lin, V.S.-Y. Mesoporous Silica Nanoparticles for Drug Delivery and Biosensing Applications. *Adv. Funct. Mater.* **2007**, *17*, 1225–1236, doi:10.1002/adfm.200601191.
20. Cheong, W.J. Porous Silica Particles As Chromatographic Separation Media: A Review. *Bull Korean Chem Soc* **2014**, *35*, 3465–3474, doi:10.5012/bkcs.2014.35.12.3465.
21. Unsal, E.; Elmas, B.; Çamlı, S.T.; Tuncel, M.; Şenel, S.; Tuncel, A. Monodisperse-porous poly(styrene-co-divinylbenzene) beads providing high column efficiency in reversed phase HPLC. *J. Appl. Polym. Sci.* **2005**, *95*, 1430–1438, doi:10.1002/app.21368.
22. Chen, J.; Zhu, L.; Ren, L.; Teng, C.; Wang, Y.; Jiang, B.; He, J. Fabrication of Monodisperse Porous Silica Microspheres with a Tunable Particle Size and Pore Size for Protein Separation. *ACS Appl. Bio Mater.* **2018**, *1*, 604–612, doi:10.1021/acsabm.8b00088.
23. Unger, K.K.; Skudas, R.; Schulte, M.M. Particle packed columns and monolithic columns in high-performance liquid chromatography-comparison and critical appraisal. *J. Chromatogr. A* **2008**, *1184*, 393–415, doi:10.1016/j.chroma.2007.11.118.
24. Rosa, S.S.; Prazeres, D.M.F.; Azevedo, A.M.; Marques, M.P.C. mRNA vaccines manufacturing: Challenges and bottlenecks. *Vaccine* **2021**, *39*, 2190–2200, doi:10.1016/j.vaccine.2021.03.038.
25. Boysen, R.I.; Hearn, M.T. HPLC of Peptides and Proteins. *Curr Protoc Protein Sci* **2001**, *23*, doi:10.1002/0471140864.ps0807s23.
26. Siddiqui, M.R.; AlOthman, Z.A.; Rahman, N. Analytical techniques in pharmaceutical analysis: A review. *Arabian Journal of Chemistry* **2017**, *10*, S1409-S1421, doi:10.1016/j.arabjc.2013.04.016.
27. Frank, M.P.; Powers, R.W. Simple and rapid quantitative high-performance liquid chromatographic analysis of plasma amino acids. *J. Chromatogr. B Analyt. Technol. Biomed. Life Sci.* **2007**, *852*, 646–649, doi:10.1016/j.jchromb.2007.01.002.
28. Mant, C.T.; Chen, Y.; Yan, Z.; Popa, T.V.; Kovacs, J.M.; Mills, J.B.; Tripet, B.P.; Hodges, R.S. HPLC analysis and purification of peptides. *Peptide Characterization and Application Protocols*; Humana Press, 2007; pp 3–55.
29. Lorbetskie, B.; White, T.; Creskey, M.; Zhang, X.; Girard, M.; Tam, R.Y.; Sauvé, S.; Lu, H. Selective reversed-phase high-performance liquid chromatography method for the determination of intact SARS-CoV-2 spike protein. *J. Chromatogr. A* **2022**, *1680*, 463424, doi:10.1016/j.chroma.2022.463424.
30. Liu, L.; Guo, S.; Che, C.; Su, Q.; Zhu, D.; Hai, X. Improved HPLC method for the determination of ribavirin concentration in red blood cells and its application in patients with COVID-19. *Biomed. Chromatogr.* **2022**, *36*, e5370, doi:10.1002/bmc.5370.
31. Da Ruos, J.; Baldo, M.A.; Daniele, S. Analytical Methods for the Determination of Major Drugs Used for the Treatment of COVID-19. A Review. *Crit. Rev. Anal. Chem.* **2022**, 1–35, doi:10.1080/10408347.2022.2039094.
32. Bilgin, Z.D.; Evcil, I.; Yazgi, D.; Binay, G.; Okuyucu Genc, C.; Gulsen, B.; Huseynova, A.; Ozdemir, A.Z.; Ozmen, E.; Usta, Y.; et al. Liquid Chromatographic Methods for COVID-19 Drugs, Hydroxychloroquine and Chloroquine. *J. Chromatogr. Sci.* **2021**, *59*, 748–757, doi:10.1093/chromsci/bmaa110.
33. Ketterer, T.; Mulbe, F. von der; Reidel, L.; Mutzke, T. Method for purifying RNA on a preparativescale by means of HPLC. 12/520,172, 05-Oct-20.
34. Gjerde, D.T.; Hoang, L.; Hornby, D. *RNA Purification and Analysis*, 4., completely rev. und enl. ed.; Wiley: Weinheim, 2009.
35. Visvikis-Siest, S.; Theodoridou, D.; Kontoe, M.-S.; Kumar, S.; Marschler, M. Milestones in Personalized Medicine: From the Ancient Time to Nowadays-the Provocation of COVID-19. *Front. Genet.* **2020**, *11*, 569175, doi:10.3389/fgene.2020.569175.

36. Romagnuolo, I.; Mariut, C.; Mazzoni, A.; Santis, G. de; Moltzen, E.; Ballensiefen, W.; Lange, C.; Frosini, A.; D'Errico, G. Sino-European science and technology collaboration on personalized medicine: overview, trends and future perspectives. *Per. Med.* **2021**, *18*, 455–470, doi:10.2217/pme-2021-0030.
37. Hayes, R.; Ahmed, A.; Edge, T.; Zhang, H. Core–shell particles: Preparation, fundamentals and applications in high performance liquid chromatography. *J. Chromatogr. A* **2014**, *1357*, 36–52, doi:10.1016/j.chroma.2014.05.010.
38. Wei, J.-X.; Shi, Z.-G.; Chen, F.; Feng, Y.-Q.; Guo, Q.-Z. Synthesis of penetrable macroporous silica spheres for high-performance liquid chromatography. *J. Chromatogr. A* **2009**, *1216*, 7388–7393, doi:10.1016/j.chroma.2009.04.066.
39. Huber, J.F.K. Stofftransport und Stoffverteilung bei chromatographischen Prozessen. *Ber. Bunsenges. Phys. Chem.* **1973**, *77*, 179–184, doi:10.1002/bbpc.19730770308.
40. Ma, Y.; Qi, L.; Ma, J.; Wu, Y.; Liu, O.; Cheng, H. Large-pore mesoporous silica spheres: synthesis and application in HPLC. *Colloids Surf. A: Physicochem. Eng. Asp.* **2003**, *229*, 1–8, doi:10.1016/j.colsurfa.2003.08.010.
41. Josic, D.; Kovac, S. Reversed-phase High Performance Liquid Chromatography of proteins. *Curr Protoc Protein Sci* **2010**, *Chapter 8*, Unit 8.7, doi:10.1002/0471140864.ps0807s61.
42. Galarneau, A.; Iapichella, J.; Brunel, D.; Fajula, F.; Bayram-Hahn, Z.; Unger, K.; Puy, G.; Demesmay, C.; Rocca, J.-L. Spherical ordered mesoporous silicas and silica monoliths as stationary phases for liquid chromatography. *J. Sep. Sci.* **2006**, *29*, 844–855, doi:10.1002/jssc.200500511.
43. Xu, W.; Zhang, K.; Zhang, Y.; Jiang, J. Packing Fraction, Tortuosity, and Permeability of Granular-Porous Media With Densely Packed Spheroidal Particles: Monodisperse and Polydisperse Systems. *Water Resour. Res.* **2022**, *58*, doi:10.1029/2021WR031433.
44. Nawrocki, J.; Dunlap, C.; McCormick, A.; Carr, P.W. Part I. Chromatography using ultra-stable metal oxide-based stationary phases for HPLC. *J. Chromatogr. A* **2004**, *1028*, 1–30, doi:10.1016/j.chroma.2003.11.052.
45. Stöber, W.; Fink, A.; Bohn, E. Controlled growth of monodisperse silica spheres in the micron size range. *J. Colloid Interface Sci.* **1968**, *26*, 62–69, doi:10.1016/0021-9797(68)90272-5.
46. Yiding, L.; James, G.; Yadong, Y. Templated synthesis of nanostructured materials. *Chem. Soc. Rev.* **2013**, *42*, 2610–2653, doi:10.1039/C2CS35369E.
47. Bao, Y.; Shi, C.; Wang, T.; Li, X.; Ma, J. Recent progress in hollow silica: Template synthesis, morphologies and applications. *Microporous Mesoporous Mat.* **2016**, *227*, 121–136, doi:10.1016/j.micromeso.2016.02.040.
48. Petkovich, N.D.; Stein, A. Controlling macro- and mesostructures with hierarchical porosity through combined hard and soft templating. *Chem. Soc. Rev.* **2013**, *42*, 3721–3739, doi:10.1039/c2cs35308c.
49. Yuan, Z.-Y.; Su, B.-L. Insights into hierarchically meso–macroporous structured materials. *J. Mater. Chem. UR* **2006**, *16*, 663–677, doi:10.1039/B512304F.
50. Deng, Y.; Wei, J.; Sun, Z.; Zhao, D. Large-pore ordered mesoporous materials templated from non-Pluronic amphiphilic block copolymers. *Chem. Soc. Rev.* **2013**, *42*, 4054–4070, doi:10.1039/c2cs35426h.
51. Wu, S.-H.; Mou, C.-Y.; Lin, H.-P. Synthesis of mesoporous silica nanoparticles. *Chem. Soc. Rev.* **2013**, *42*, 3862–3875, doi:10.1039/C3CS35405A.
52. Singh, L.P.; Bhattacharyya, S.K.; Kumar, R.; Mishra, G.; Sharma, U.; Singh, G.; Ahalawat, S. Sol-Gel processing of silica nanoparticles and their applications. *Adv. Colloid Interface Sci.* **2014**, *214*, 17–37, doi:10.1016/j.cis.2014.10.007.
53. Zhang, L.; Jin, L.; Liu, B.; He, J. Templated Growth of Crystalline Mesoporous Materials: From Soft/Hard Templates to Colloidal Templates. *Front. Chem.* **2019**, *7*, 22, doi:10.3389/fchem.2019.00022.
54. Shiba, K.; Shimura, N.; Ogawa, M. Mesoporous silica spherical particles. *J. Nanosci. Nanotechnol.* **2013**, *13*, 2483–2494, doi:10.1166/jnn.2013.7423.

55. He, J.; Yang, C.; Xiong, X.; Jiang, B. Preparation and characterization of monodisperse porous silica microspheres with controllable morphology and structure. *J. Polym. Sci. A Polym. Chem.* **2012**, *50*, 2889–2897, doi:10.1002/pola.26066.
56. Xia, H.; Wan, G.; Yang, F.; Wang, J.; Bai, Q. Preparation of monodisperse large-porous silica microspheres with polymer microspheres as the templates for protein separation. *Mater. Lett.* **2016**, *180*, 19–22, doi:10.1016/j.matlet.2016.05.044.
57. Xia, H.; Wan, G.; Zhao, J.; Liu, J.; Bai, Q. Preparation and characterization of monodisperse large-porous silica microspheres as the matrix for protein separation. *J. Chromatogr. A* **2016**, *1471*, 138–144, doi:10.1016/j.chroma.2016.10.025.
58. Muzammil, E.M.; Khan, A.; Stuparu, M.C. Post-polymerization modification reactions of poly(glycidyl methacrylate)s. *RSC Adv.* **2017**, *7*, 55874–55884, doi:10.1039/C7RA11093F.
59. Myers, R.H.; Montgomery, D.C.; Anderson-Cook, C.M. *Response surface methodology*: *Process and product optimization using designed experiments*, Fourth edition; Wiley: Hoboken, New Jersey, 2016, ISBN 9781118916025.
60. Box, G.E.P.; Hunter, J.S.; Hunter, W.G. *Statistics for experimenters*: *Design, innovation, and discovery*, 2. ed.; Wiley-Interscience: Hoboken, NJ, 2005, ISBN 0471718130.
61. Ryan, T.P. *Modern experimental design;* Wiley-Interscience: Hoboken, New Jersey, 2007, ISBN 978-0-471-21077-1.
62. Seidl, R.; Weiss, S.; Zikulnig-Rusch, E.M.; Kandelbauer, A. Response surface optimization for improving the processing behavior of melamine formaldehyde impregnation resins. *J Appl Polym Sci* **2021**, *138*, 50181, doi:10.1002/app.50181.
63. Esbensen, K.H.; Swarbrick, B.; Westad, F.; Whitcombe, P.; Andersen, M. *Multivariate data analysis*: *An introduction to multivariate analysis, process analytical technology and quality by design*, 6th edition; CAMO: Oslo, Magnolia, TX, 2018, ISBN 978-82-691104-0-1.
64. Sing, K.S.W. Reporting physisorption data for gas/solid systems with special reference to the determination of surface area and porosity (Recommendations 1984). *Pure Appl. Chem.* **1985**, *57*, 603–619, doi:10.1351/pac198557040603.
65. Thommes, M.; Kaneko, K.; Neimark, A.V.; Olivier, J.P.; Rodriguez-Reinoso, F.; Rouquerol, J.; Sing, K.S. Physisorption of gases, with special reference to the evaluation of surface area and pore size distribution (IUPAC Technical Report). *Pure Appl. Chem.* **2015**, *87*, 1051–1069, doi:10.1515/pac-2014-1117.
66. Lowell, S.; Shields, J.E.; Thomas, M.A.; Thommes, M. *Characterization of Porous Solids and Powders: Surface Area, Pore Size and Density;* Springer Netherlands: Dordrecht, 2004, ISBN 978-1-4020-2303-3.
67. Rouquerol, F.; Rouquerol, J.; Sing, K.S.W.; Llewellyn, P.L.; Maurin, G. *Adsorption by powders and porous solids*: *Principles, methodology and applications*, Second edition; Elsevier/AP: Amsterdam, 2014.
68. Wagner, S. Templatgestützte Synthese monodisperser, poröser Silicapartikel mit maßgeschneiderten Morphologien als Trennphasen für die HPLC. Dissertation; Eberhard-Karls-Universität Tübingen, Tübingen, 2021.
69. Piaopiao, W.; Zihui, M. Progress in polystyrene microspheres. *IOP Conf. Ser.: Mater. Sci. Eng.* **2019**, *563*, 22001, doi:10.1088/1757-899X/563/2/022001.
70. Gokmen, M.T.; Du Prez, F.E. Porous polymer particles—A comprehensive guide to synthesis, characterization, functionalization and applications. *Prog. Polym. Sci.* **2012**, *37*, 365–405, doi:10.1016/j.progpolymsci.2011.07.006.
71. Paine, A.J. Dispersion polymerization of styrene in polar solvents. 7. A simple mechanistic model to predict particle size. *Macromolecules* **1990**, *23*, 3109–3117, doi:10.1021/ma00214a013.
72. Paine, A.J.; Luymes, W.; McNulty, J. Dispersion polymerization of styrene in polar solvents. 6. Influence of reaction parameters on particle size and molecular weight in poly(N-vinylpyrrolidone)-stabilized reactions. *Macromolecules* **1990**, *23*, 3104–3109, doi:10.1021/ma00214a012.
73. Arshady, R. Suspension, emulsion, and dispersion polymerization: A methodological survey. *Colloid Polym Sci* **1992**, *270*, 717–732, doi:10.1007/BF00776142.

74. Chaudhary, V.; Sharma, S. Suspension polymerization technique: parameters affecting polymer properties and application in oxidation reactions. *J Polym Res* **2019**, *26*, doi:10.1007/s10965-019-1767-8.
75. Šmigol, V.; Švec, F. Synthesis and properties of uniform beads based on macroporous copolymer glycidyl methacrylate–ethylene dimethacrylate: A way to improve separation media for HPLC. *Journal of Applied Polymer Science* **1992**, *46*, 1439–1448, doi:10.1002/app.1992.070460814.
76. Seidl, J.; Malinský, J.; Dušek, K.; Heitz, W. Makroporöse Styrol-Divinylbenzol-Copolymere und ihre Verwendung in der Chromatographie und zur Darstellung von Ionenaustauschern. *Adv. Polymer Sci.* **1967**, *5*, 113–213, doi:10.1007/BFb0051281.
77. Ugelstad, J.; Mórk, P.C.; Kaggerud, K.; Ellingsen, T.; Berge, A. Swelling of oligomer-polymer particles. New methods of preparation. *Adv. Colloid Interface Sci.* **1980**, *13*, 101–140, doi:10.1016/0001-8686(80)87003-5.
78. Ugelstad, J.; Kaggerud, K.H.; Hansen, F.K.; Berge, A. Absorption of low molecular weight compounds in aqueous dispersions of polymer-oligomer particles, 2. A two step swelling process of polymer particles giving an enormous increase in absorption capacity. *Makromol. Chem.* **1979**, *180*, 737–744, doi:10.1002/macp.1979.021800317.
79. Benes, M.J.; Horák, D.; Svec, F. Methacrylate-based chromatographic media. *J. Sep. Sci.* **2005**, *28*, 1855–1875, doi:10.1002/jssc.200500186.
80. Ellingsen, T.; Aune, O.; Ugelstad, J.; Hagen, S. Monosized stationary phases for chromatography. *J. Chromatogr. A* **1990**, *535*, 147–161, doi:10.1016/S0021-9673(01)88940-8.
81. Ugelstad, J.; Mfutakamba, H.R.; Mørk, P.C.; Ellingsen, T.; Berge, A.; Schmid, R.; Holm, L.; Jørgedal, A.; Hansen, F.K.; Nustad, K. Preparation and application of monodisperse polymer particles. *J. polym. sci., C Polym. symp.* **1985**, *72*, 225–240, doi:10.1002/polc.5070720125.
82. Hosoya, K.; Fréchet, J.M.J. Influence of the seed polymer on the chromatographic properties of size monodisperse polymeric separation media prepared by a multi-step swelling and polymerization method. *J. Polym. Sci. A Polym. Chem.* **1993**, *31*, 2129–2141, doi:10.1002/pola.1993.080310819.
83. Okay, O. Macroporous copolymer networks. *Prog. Polym. Sci.* **2000**, *25*, 711–779, doi:10.1016/S0079-6700(00)00015-0.
84. Plumeré, N.; Ruff, A.; Speiser, B.; Feldmann, V.; Mayer, H.A. Stöber silica particles as basis for redox modifications: particle shape, size, polydispersity, and porosity. *J. Colloid Interface Sci.* **2012**, *368*, 208–219, doi:10.1016/j.jcis.2011.10.070.
85. Brinker, C.J.; Scherer, G.W. *Sol-gel science*: *The physics and chemistry of sol-gel processing;* Acad. Press: Boston, 1990, ISBN 9780121349707.
86. Keefer, K.D. The Effect of Hydrolysis Conditions on the Structure and Growth of Silicate Polymers. *Mat. Res. Soc. Symp. Proc.* **1984**, *32*, doi:10.1557/PROC-32-15.
87. Brinker, C.J. Hydrolysis and condensation of silicates: Effects on structure. *J. Non-Cryst. Solids* **1988**, *100*, 31–50, doi:10.1016/0022-3093(88)90005-1.
88. Han, Y.; Lu, Z.; Teng, Z.; Liang, J.; Guo, Z.; Wang, D.; Han, M.-Y.; Yang, W. Unraveling the Growth Mechanism of Silica Particles in the Stöber Method: In Situ Seeded Growth Model. *Langmuir* **2017**, *33*, 5879–5890, doi:10.1021/acs.langmuir.7b01140.
89. Chen, K.C.; Tsuchiya, T.; Mackenzie, J.D. Sol-gel processing of silica. *J. Non-Cryst. Solids* **1986**, *81*, 227–237, doi:10.1016/0022-3093(86)90272-3.
90. van Blaaderen, A.; van Geest, J.; Vrij, A. Monodisperse colloidal silica spheres from tetraalkoxysilanes: Particle formation and growth mechanism. *J. Colloid Interface Sci.* **1992**, *154*, 481–501, doi:10.1016/0021-9797(92)90163-G.
91. Levy, D.; Zayat, M. *The sol-gel handbook*: *Volume 1: Synthesis and Processing : Volume 2: Characterization and Properties of Sol-Gel Materials : Volume 3: Application of Sol-Gel Materials;* Wiley-VCH: Weinheim, Germany, 2015, ISBN 3527670823.
92. Matsoukas, T.; Gulari, E. Dynamics of growth of silica particles from ammonia-catalyzed hydrolysis of tetra-ethyl-orthosilicate. *J. Colloid Interface Sci.* **1988**, *124*, 252–261, doi:10.1016/0021-9797(88)90346-3.

93. Harris, M.T.; Brunson, R.R.; Byers, C.H. The base-catalyzed hydrolysis and condensation reactions of dilute and concentrated TEOS solutions. *J. Non-Cryst. Solids* **1990**, *121*, 397–403, doi:10.1016/0022-3093(90)90165-I.
94. Sadasivan, S.; Dubey, A.K.; Li, Y.; Rasmussen, D.H. Alcoholic Solvent Effect on Silica Synthesis—NMR and DLS Investigation. *J. Solgel. Sci. Technol.* **1998**, *12*, 5–14, doi:10.1023/A:1008659708390.
95. Bogush, G.H.; Tracy, M.A.; Zukoski, C.F. Preparation of monodisperse silica particles: Control of size and mass fraction. *J. Non-Cryst. Solids* **1988**, *104*, 95–106, doi:10.1016/0022-3093(88)90187-1.
96. Arantes, T.M.; Pinto, A.H.; Leite, E.R.; Longo, E.; Camargo, E.R. Synthesis and optimization of colloidal silica nanoparticles and their functionalization with methacrylic acid. *Colloids Surf. A: Physicochem. Eng. Asp.* **2012**, *415*, 209–217, doi:10.1016/j.colsurfa.2012.09.041.
97. González-Álvarez, R.J.; Naranjo-Rodríguez, I.; Hernández-Artiga, M.P.; Palacios-Santander, J.M.; Cubillana-Aguilera, L.; Bellido-Milla, D. Experimental design applied to optimisation of silica nanoparticles size obtained by sonosynthesis. *J Sol-Gel Sci Technol* **2016**, *80*, 378–388, doi:10.1007/s10971-016-4129-6.
98. Brodbeck, B. Maßgeschneiderte Silicapartikel mit komplexen 3D-Strukturen; Eberhard-Karls-Universität Tübingen, Tübingen, 2020.
99. Lindberg, R.; Sjöblom, J.; Sundholm, G. Preparation of silica particles utilizing the sol-gel and the emulsion-gel processes. *Colloids Surf. A: Physicochem. Eng. Asp.* **1995**, *99*, 79–88, doi:10.1016/0927-7757(95)03117-V.
100. Davies, G.-L.; Barry, A.; Gun'ko, Y.K. Preparation and size optimisation of silica nanoparticles using statistical analyses. *Chem. Phys. Lett.* **2009**, *468*, 239–244, doi:10.1016/j.cplett.2008.12.031.
101. Luo, L.; Liang, Y.; Erichsen, E.S.; Anwander, R. Monodisperse mesoporous silica nanoparticles of distinct topology. *J. Colloid Interface Sci.* **2017**, *495*, 84–93, doi:10.1016/j.jcis.2017.01.107.
102. Greasley, S.L.; Page, S.J.; Sirovica, S.; Chen, S.; Martin, R.A.; Riveiro, A.; Hanna, J.V.; Porter, A.E.; Jones, J.R. Controlling particle size in the Stöber process and incorporation of calcium. *J. Colloid Interface Sci.* **2016**, *469*, 213–223, doi:10.1016/j.jcis.2016.01.065.
103. Bourebrab, M.A.; Oben, D.T.; Durand, G.G.; Taylor, P.G.; Bruce, J.I.; Bassindale, A.R.; Taylor, A. Influence of the initial chemical conditions on the rational design of silica particles. *J. Solgel. Sci. Technol.* **2018**, *88*, 430–441, doi:10.1007/s10971-018-4821-9.
104. Hyde, E.D.E.R.; Seyfaee, A.; Neville, F.; Moreno-Atanasio, R. Colloidal Silica Particle Synthesis and Future Industrial Manufacturing Pathways: A Review. *Ind. Eng. Chem. Res.* **2016**, *55*, 8891–8913, doi:10.1021/acs.iecr.6b01839.
105. LaMer, V.K.; Dinegar, R.H. Theory, Production and Mechanism of Formation of Monodispersed Hydrosols. *J. Am. Chem. Soc.* **1950**, *72*, 4847–4854, doi:10.1021/ja01167a001.
106. Park, S.K.; Kim, K.D.; Kim, H.T. Preparation of silica nanoparticles: determination of the optimal synthesis conditions for small and uniform particles. *Colloids Surf. A: Physicochem. Eng. Asp.* **2002**, *197*, 7–17, doi:10.1016/S0927-7757(01)00683-5.
107. Green, D.; Lin, J.; Lam, Y.-F.; Hu, M.-C.; Schaefer, D.W.; Harris, M. Size, volume fraction, and nucleation of Stober silica nanoparticles. *J. Colloid Interface Sci.* **2003**, *266*, 346–358, doi:10.1016/S0021-9797(03)00610-6.
108. Bailey, J.K.; Mecartney, M.L. Formation of colloidal silica particles from alkoxides. *Colloids Surf.* **1992**, *63*, 151–161, doi:10.1016/0166-6622(92)80081-C.
109. Matsoukas, T.; Gulari, E. Monomer-addition growth with a slow initiation step: A growth model for silica particles from alkoxides. *J. Colloid Interface Sci.* **1989**, *132*, 13–21, doi:10.1016/0021-9797(89)90210-5.
110. Matsoukas, T.; Gulari, E. Self-sharpening distributions revisited—polydispersity in growth by monomer addition. *J. Colloid Interface Sci.* **1991**, *145*, 557–562, doi:10.1016/0021-9797(91)90385-L.
111. Neville, F.; Seyfaee, A. Real-time monitoring of in situ polyethyleneimine-silica particle formation. *Langmuir* **2013**, *29*, 14681–14690, doi:10.1021/la403040u.
112. Bogush, G.; Zukoski, C. Uniform silica particle precipitation: An aggregative growth model. *J. Colloid Interface Sci.* **1991**, *142*, 19–34, doi:10.1016/0021-9797(91)90030-C.

113. Bogush, G.; Zukoski, C. Studies of the kinetics of the precipitation of uniform silica particles through the hydrolysis and condensation of silicon alkoxides. *J. Colloid Interface Sci.* **1991**, *142*, 1–18, doi:10.1016/0021-9797(91)90029-8.
114. Carcouët, C.C.M.C.; van de Put, M.W.P.; Mezari, B.; Magusin, P.C.M.M.; Laven, J.; Bomans, P.H.H.; Friedrich, H.; Esteves, A.C.C.; Sommerdijk, N.A.J.M.; van Benthem, R.A.T.M.; et al. Nucleation and growth of monodisperse silica nanoparticles. *Nano Lett.* **2014**, *14*, 1433–1438, doi:10.1021/nl404550d.
115. Stein, A.; Rudisill, S.G.; Petkovich, N.D. Perspective on the Influence of Interactions Between Hard and Soft Templates and Precursors on Morphology of Hierarchically Structured Porous Materials. *Chem. Mater.* **2014**, *26*, 259–276, doi:10.1021/cm402184h.
116. Yongsheng, L.; Jianlin, S. Hollow-Structured Mesoporous Materials: Chemical Synthesis, Functionalization and Applications. *Adv Mater* **2014**, *26*, 3176–3205, doi:10.1002/adma.201305319.
117. Caruso, R.A. Nanocasting and Nanocoating. *Colloid Chemistry I*; Springer, Berlin, Heidelberg, 2003; pp 91–118.
118. Grama, S.; Plichta, Z.; Trchová, M.; Kovářová, J.; Beneš, M.; Horák, D. Monodisperse macroporous poly(glycidyl methacrylate) microspheres coated with silica: Design, preparation and characterization. *React Funct Polym* **2014**, *77*, 11–17, doi:10.1016/j.reactfunctpolym.2014.01.010.
119. Bai, J.; Zhu, Q.; Tang, C.; Liu, J.; Yi, Y.; Bai, Q. Synthesis and application of 5 μm monodisperse porous silica microspheres with controllable pore size using polymeric microspheres as templates for the separation of small solutes and proteins by high-performance liquid chromatography. *J. Chromatogr. A* **2022**, *1675*, 463165, doi:10.1016/j.chroma.2022.463165.
120. Basso, A.M.; Nicola, B.P.; Bernardo-Gusmão, K.; Pergher, S.B.C. Tunable Effect of the Calcination of the Silanol Groups of KIT-6 and SBA-15 Mesoporous Materials. *Appl. Sci.* **2020**, *10*, 970, doi:10.3390/app10030970.
121. Zhuravlev, L.T. The surface chemistry of amorphous silica. Zhuravlev model. *Colloids Surf. A* **2000**, *173*, 1–38, doi:10.1016/S0927-7757(00)00556-2.
122. Zhuravlev, L.T. Characterization of amorphous silica surface. *React Kinet Catal Lett* **1993**, *50*, 15–25, doi:10.1007/BF02062184.
123. Raman, N.K.; Anderson, M.T.; Brinker, C.J. Template-Based Approaches to the Preparation of Amorphous, Nanoporous Silicas. *Chem. Mater.* **1996**, *8*, 1682–1701, doi:10.1021/cm960138.
124. Krol, D.M.; Mulder, C.; van Lierop, J.G. Raman investigation of autoclave-prepared, monolithic silica gels. *J. Non-Cryst. Solids* **1986**, *86*, 241–250, doi:10.1016/0022-3093(86)90492-8.
125. Gong, B.; Zhu, J.; Li, L.; Qiang, K.; Ren, L. Synthesis of non-porous poly(glycidylmethacrylate-co-ethylenedimethacrylate) beads and their application in separation of biopolymers. *Talanta* **2006**, *68*, 666–672, doi:10.1016/j.talanta.2005.05.003.
126. Iordache, T.-V.; Banu, N.D.; Giol, E.D.; Vuluga, D.M.; Jerca, F.A.; Jerca, V.V. Factorial design optimization of polystyrene microspheres obtained by aqueous dispersion polymerization in the presence of poly(2-ethyl-2-oxazoline) reactive stabilizer. *Polym. Int.* **2020**, *47*, 141, doi:10.1002/pi.5974.
127. Sáenz, J.M.; Asua, J.M. Dispersion copolymerization of styrene and butyl acrylate in polar solvents. *J. Polym. Sci., Part A: Polym. Chem.* **1996**, *34*, 1977–1992, doi:10.1002/(SICI)1099-0518(19960730)34:10<1977:AID-POLA16>3.0.CO;2-F.
128. Socrates, G. *Infrared and Raman characteristic group frequencies*: *Tables and charts*, 3. ed., repr. as paperback; Wiley: Chichester, 2010, ISBN 9780470093078.
129. Halász, I.; Martin, K. Pore Sizes of Solids. *Angew. Chem. Int. Ed. Engl.* **1978**, *17*, 901–908, doi:10.1002/anie.197809011.
130. Roy, R. Nanocomposites: Retrospecr and Prospect. *Mat. Res. Soc. Symp. Proc.* **1992**, *286*, 241–250, doi:10.1557/PROC-286-241.
131. Kiasat, A.R.; Nazari, S.; Davarpanah, J. Facile synthesis of an organic–inorganic nanocomposite, PEG–silica, by sol–gel method; its characterization and application as an efficient catalyst in regioselective nucleophilic ring opening of epoxides: Preparation of β-azido alcohols and β-cyanohydrins. *C. R. Chim.* **2014**, *17*, 124–130, doi:10.1016/j.crci.2013.07.008.

132. Tumnantong, D.; Rempel, G.L.; Prasassarakich, P. Preparation of poly(methyl methacrylate)-Silica nanoparticles via differential microemulsion polymerization and physical properties of NR/PMMA-SiO 2 hybrid membranes. *Polym Eng Sci* **2018**, *58*, 759–766, doi:10.1002/pen.24611.
133. Guo, J.; Mattos, B.D.; Tardy, B.L.; Moody, V.M.; Xiao, G.; Ejima, H.; Cui, J.; Liang, K.; Richardson, J.J. Porous Inorganic and Hybrid Systems for Drug Delivery: Future Promise in Combatting Drug Resistance and Translation to Botanical Applications. *Curr. Med. Chem.* **2019**, *26*, 6107–6131, doi:10.2174/0929867325666180706111909.
134. Rahman, I.A.; Padavettan, V. Synthesis of Silica Nanoparticles by Sol-Gel: Size-Dependent Properties, Surface Modification, and Applications in Silica-Polymer Nanocomposites—A Review. *J. Nanomater.* **2012**, *2012*, 1–15, doi:10.1155/2012/132424.
135. Meer, S.; Kausar, A.; Iqbal, T. Attributes of Polymer and Silica Nanoparticle Composites: A Review. *Polym.-Plast. Technol. Mater* **2016**, *55*, 826–861, doi:10.1080/03602559.2015.1103267.
136. Zou, H.; Wu, S.; Shen, J. Polymer/silica nanocomposites: preparation, characterization, properties, and applications. *Chem. Rev.* **2008**, *108*, 3893–3957, doi:10.1021/cr068035q.
137. Zhao, S.; Xu, D.; Ma, H.; Sun, Z.; Guan, J. Controllable preparation and formation mechanism of monodispersed silica particles with binary sizes. *J. Colloid Interface Sci.* **2012**, *388*, 40–46, doi:10.1016/j.jcis.2012.08.012.
138. Putz, F.; Waag, A.; Balzer, C.; Braxmeier, S.; Elsaesser, M.S.; Ludescher, L.; Paris, O.; Malfait, W.J.; Reichenauer, G.; Hüsing, N. The influence of drying and calcination on surface chemistry, pore structure and mechanical properties of hierarchically organized porous silica monoliths. *Microporous Mesoporous Mat.* **2019**, *288*, 109578, doi:10.1016/j.micromeso.2019.109578.
139. Qiu, M.; Feng, J.; Fan, Y.; Xu, N. Pore evolution model of ceramic membrane during constrained sintering. *J Mater Sci* **2009**, *44*, 689–699, doi:10.1007/s10853-008-3202-0.
140. Rahaman, M.N. *Ceramic Processing and Sintering*, Second edition; CRC Press: Boca Raton, 2017, ISBN 9781315274126.
141. Kang, S.-J.L. *Sintering*: *Densification, Grain Growth, and Microstructure*, 1st ed.; Elsevier Butterworth-Heinemann; Elsevier Science & Technology: Amsterdam, Boston, London, 2005, ISBN 9780080493077.
142. Reymond, F.; Vollet, C.; Plichta, Z.; Horák, D. Fabrication and characterization of tosyl-activated magnetic and nonmagnetic monodisperse microspheres for use in microfluic-based ferritin immunoassay. *Biotechnol Progress* **2013**, *29*, 532–542, doi:10.1002/btpr.1683.
143. Miletić, N.; Vuković, Z.; Nastasović, A.; Loos, K. Macroporous poly(glycidyl methacrylate-co-ethylene glycol dimethacrylate) resins—Versatile immobilization supports for biocatalysts. *J. Mol. Catal. B Enzym.* **2009**, *56*, 196–201, doi:10.1016/j.molcatb.2008.04.012.
144. Xu, S.; Wang, Y.; Tang, Y.; Ji, Y. A protein-based mixed selector chiral monolithic stationary phase in capillary electrochromatography. *New J. Chem.* **2018**, *42*, 13520–13528, doi:10.1039/C8NJ02309C.
145. Roberts, M.W.H.; Ongkudon, C.M.; Forde, G.M.; Danquah, M.K. Versatility of polymethacrylate monoliths for chromatographic purification of biomolecules. *J. Sep. Sci.* **2009**, *32*, 2485–2494, doi:10.1002/jssc.200900309.
146. Ming-Yu, D.; Rui, Z.; Hong, P. Preparation of Weak Cation Exchange Monolithic Capillary Column and Its Application for Protein Separation. *Chinese J. Anal. Chem.* **2009**, *37*, 395–398, doi:10.1016/S1872-2040(08)60091-2.
147. Wang, X.; Liu, H.; Sun, Z.; Zhao, S.; Zhou, Y.; Li, J.; Cai, T.; Gong, B. Monodisperse restricted access material with molecularly imprinted surface for selective solid-phase extraction of 17β-estradiol from milk. *J. Sep. Sci.* **2020**, doi:10.1002/jssc.202000449.
148. Golub, D.; Krajnc, P. Emulsion templated hydrophilic polymethacrylates. Morphological features, water and dye absorption. *React. Funct. Polym.* **2020**, *149*, 104515, doi:10.1016/j.reactfunctpolym.2020.104515.
149. Hérault, D.; Saluzzo, C.; Lemaire, M. Preparation of monodisperse enantiomerically pure glycidyl methacrylate–ethylene glycol dimethacrylate copolymers in dispersion copolymerization: Functionalization. *React. Funct. Polym.* **2006**, *66*, 567–577, doi:10.1016/j.reactfunctpolym.2005.10.010.

150. Stefanović, I.S.; Ekmeščić, B.M.; Maksin, D.D.; Nastasović, A.B.; Miladinović, Z.P.; Vuković, Z.M.; Micić, D.M.; Pergal, M.V. Structure, Thermal, and Morphological Properties of Novel Macroporous Amino-Functionalized Glycidyl Methacrylate Based Copolymers. *Ind. Eng. Chem. Res.* **2015**, *54*, 6902–6911, doi:10.1021/acs.iecr.5b01285.
151. Xiao, J.; Lu, Q.; Cong, H.; Shen, Y.; Yu, B. Microporous poly(glycidyl methacrylate- co -ethylene glycol dimethyl acrylate) microspheres: synthesis, functionalization and applications. *Polym. Chem.* **2021**, *12*, 6050–6070, doi:10.1039/D1PY00834J.
152. Srisopa, A. Preparation of monodisperse porous poly(glycidylmethacrylate-co-ethylenedimethacrylate) microspheres and their application as stationary phase for superheated water HPLC. *Talanta* **2016**, *147*, 358–363, doi:10.1016/j.talanta.2015.10.014.
153. Flores-Rojas, G.G.; Pino-Ramos, V.H.; López-Saucedo, F.; Concheiro, A.; Alvarez-Lorenzo, C.; Bucio, E. Improved covalent immobilization of lysozyme on silicone rubber-films grafted with poly(ethylene glycol dimethacrylate-co-glycidylmethacrylate). *Eur. Polym. J.* **2017**, *95*, 27–40, doi:10.1016/j.eurpolymj.2017.07.040.
154. Ugelstad, J.; Söderberg, L.; Berge, A.; Bergström, J. Monodisperse polymer particles — a step forward for chromatography. *Nature* **1983**, *303*, 95–96, doi:10.1038/303095a0.
155. Dubinsky, S.; Park, J.I.; Gourevich, I.; Chan, C.; Deetz, M.; Kumacheva, E. Toward Controlling the Surface Morphology of Macroporous Copolymer Particles. *Macromolecules* **2009**, *42*, 1990–1994, doi:10.1021/ma802813v.
156. Pączkowski, P.; Gawdzik, B. Studies on Preparation, Characterization and Application of Porous Functionalized Glycidyl Methacrylate-Based Microspheres. *Materials (Basel)* **2021**, *14*, doi:10.3390/ma14061438.
157. Costa, L.C.; Monteiro, R.C.; Castro, H.M.A.; Ribeiro, T.S.; Oliveira, M.A.; Torquato, E.C.C.; Arcanjo, M.E.; Marques, M.R.C. Glycidyl Methacrylate-ethylene Glycol Dimethacrylate Copolymers with Varied Pore Structures Prepared with Different Reaction Parameters. *Mat. Res.* **2020**, *23*, doi:10.1590/1980-5373-mr-2019-0550.
158. Yu, B.; Xue, T.; Pang, L.; Zhang, X.; Shen, Y.; Cong, H. The Effect of Different Porogens on Porous PMMA Microspheres by Seed Swelling Polymerization and Its Application in High-Performance Liquid Chromatography. *Materials (Basel)* **2018**, *11*, doi:10.3390/ma11050705.
159. Yu, S.; Ng, F.L.; Ma, K.C.C.; Mon, A.A.; Ng, F.L.; Ng, Y.Y. Effect of porogenic solvent on the porous properties of polymer monoliths. *J. Appl. Polym. Sci.* **2013**, *127*, 2641–2647, doi:10.1002/app.37514.
160. Ferreira, A.; Bigan, M.; Blondeau, D. Optimization of a polymeric HPLC phase: poly(glycidyl methacrylate–co-ethylene dimethacrylate). *React. Funct. Polym.* **2003**, *56*, 123–136, doi:10.1016/S1381-5148(03)00049-X.
161. Smigol, V.; Svec, F. Preparation and properties of uniform beads based on macroporous glycidyl methacrylate–ethylene dimethacrylate copolymer: Use of chain transfer agent for control of pore-size distribution. *J. Appl. Polym. Sci.* **1993**, *48*, 2033–2039, doi:10.1002/app.1993.070481116.
162. Pączkowski, P.; Grochowicz, M.; Chabros, A.; Gawdzik, B.; Ryczkowski, J. Infrared photoacoustic spectroscopy as an alternative tool for the analysis of surface-modified glycidyl-based polymeric microspheres. *Polym. Test.* **2019**, *76*, 173–180, doi:10.1016/j.polymertesting.2019.03.022.
163. Kessler, W. *Multivariate Datenanalyse für die Pharma-, Bio- und Prozessanalytik*: *Ein Lehrbuch*. Ein Lehrbuch, 1. Aufl., 1. Nachdr; Wiley-VCH: Weinheim, 2008, ISBN 978-3-527-31262-7.
164. Ulitzsch, S.; Bäuerle, T.; Chassé, T.; Lorenz, G.; Kandelbauer, A. Optimizing the Process Efficiency of Reactive Extrusion in the Synthesis of Vinyltrimethoxysilane-Grafted Ethylene-Octene-Copolymer (EOC-g-VTMS) by Response Surface Methodology. *Polymers (Basel)* **2020**, *12*, doi:10.3390/polym12122798.
165. Bäuerle, T.; Ulitzsch, S.; Lorenz, A.; Rebner, K.; Chassé, T.; Kandelbauer, A.; Lorenz, G. Effects of process parameters on silane grafting of liquid ethylene-propylene copolymer by reactive extrusion as quantified by response surface methodology. *Polymer* **2020**, *202*, 122601, doi:10.1016/j.polymer.2020.122601.
166. Kim, J.-W.; Suh, K.-D. Monodisperse polymer particles synthesized by seeded polymerization techniques. *J. Ind. Eng. Chem.* **2008**, *14*, 1–9, doi:10.1016/j.jiec.2007.06.001.

167. Xu, M.; Peterson, D.S.; Rohr, T.; Svec, F.; Fréchet, J.M.J. Polar polymeric stationary phases for normal-phase HPLC based on monodisperse macroporous poly(2,3-dihydroxypropyl methacrylate-co-ethylene dimethacrylate) beads. *Anal. Chem.* **2003**, *75*, 1011–1021, doi:10.1021/ac026216w.
168. Hansen, C.M. *Hansen Solubility Parameters*: *A user's handbook*, 2nd ed.; CRC Press: Boca Raton, 2007.
169. Rahman, M.A.; Mutalib, M.A.; Li, K.; Othman, M. Pore Size Measurements and Distribution for Ceramic Membranes, 183–198.
170. Dubinsky, S.; Zhang, H.; Nie, Z.; Gourevich, I.; Voicu, D.; Deetz, M.; Kumacheva, E. Microfluidic Synthesis of Macroporous Copolymer Particles. *Macromolecules* **2008**, *41*, 3555–3561, doi:10.1021/ma800300d.
171. Wang, D.; Bierwagen, G.P. Sol–gel coatings on metals for corrosion protection. *Prog. Org. Coat.* **2009**, *64*, 327–338, doi:10.1016/j.porgcoat.2008.08.010.
172. Chruściel, J.J.; Leśniak, E. Modification of epoxy resins with functional silanes, polysiloxanes, silsesquioxanes, silica and silicates. *Prog. Polym. Sci.* **2015**, *41*, 67–121, doi:10.1016/j.progpolymsci.2014.08.001.
173. Crudden, C.M.; Sateesh, M.; Lewis, R. Mercaptopropyl-modified mesoporous silica: a remarkable support for the preparation of a reusable, heterogeneous palladium catalyst for coupling reactions. *J. Am. Chem. Soc.* **2005**, *127*, 10045–10050, doi:10.1021/ja0430954.
174. Wei, J.; Sun, Z.; Luo, W.; Li, Y.; Elzatahry, A.A.; Al-Enizi, A.M.; Deng, Y.; Zhao, D. New Insight into the Synthesis of Large-Pore Ordered Mesoporous Materials. *J. Am. Chem. Soc.* **2017**, *139*, 1706–1713, doi:10.1021/jacs.6b11411.
175. Gallis, K.W.; Araujo, J.T.; Duff, K.J.; Moore, J.G.; Landry, C.C. The Use of Mesoporous Silica in Liquid Chromatography. *Adv. Mater.* **1999**, *11*, 1452–1455, doi:10.1002/(SICI)1521-4095(199912)11:17<1452:AID-ADMA1452>3.0.CO;2-R.
176. Wagner, B.M.; Schuster, S.A.; Boyes, B.E.; Kirkland, J.J. Superficially porous silica particles with wide pores for biomacromolecular separations. *J. Chromatogr. A* **2012**, *1264*, 22–30, doi:10.1016/j.chroma.2012.09.052.
177. Kirkland, J.J.; Truszkowski, F.A.; Dilks, C.H.; Engel, G.S. Superficially porous silica microspheres for fast high-performance liquid chromatography of macromolecules. *J. Chromatogr. A* **2000**, *890*, 3–13, doi:10.1016/S0021-9673(00)00392-7.
178. Ide, M.; Wallaert, E.; van Driessche, I.; Lynen, F.; Sandra, P.; van der Voort, P. Spherical mesoporous silica particles by spray drying: Doubling the retention factor of HPLC columns. *Microporous Mesoporous Mat.* **2011**, *142*, 282–291, doi:10.1016/j.micromeso.2010.12.013.
179. Kimling, M.C.; Caruso, R.A. Sol–gel synthesis of hierarchically porous TiO2 beads using calcium alginate beads as sacrificial templates. *J. Mater. Chem.* **2012**, *22*, 4073–4082, doi:10.1039/C2JM15720A.
180. Liu, W.; Wu, W.; Selomulya, C.; Chen, X.D. A single step assembly of uniform microparticles for controlled release applications. *Soft Matter* **2011**, *7*, 3323, doi:10.1039/c0sm01371d.
181. Melnyk, I.V.; Zub, Y.L.; Véron, E.; Massiot, D.; Cacciaguerra, T.; Alonso, B. Spray-dried mesoporous silica microspheres with adjustable textures and pore surfaces homogenously covered by accessible thiol functions. *J. Mater. Chem.* **2008**, *18*, 1368, doi:10.1039/b717133a.
182. Waldron, K.; Wu, Z.; Wu, W.D.; Liu, W.; Zhao, D.; Chen, X.D.; Selomulya, C. Formation of uniform large SBA-15 microspheres via spray drying. *J. Mater. Chem. A* **2014**, *2*, 19500–19508, doi:10.1039/C4TA05002A.
183. Chen, S.-L.; Dong, P.; Yang, G.-H.; Yang, J.-J. Characteristic Aspects of Formation of New Particles during the Growth of Monosize Silica Seeds. *J. Colloid Interface Sci.* **1996**, *180*, 237–241, doi:10.1006/jcis.1996.0295.
184. Nozawa, K.; Gailhanou, H.; Raison, L.; Panizza, P.; Ushiki, H.; Sellier, E.; Delville, J.P.; Delville, M.H. Smart control of monodisperse Stöber silica particles: effect of reactant addition rate on growth process. *Langmuir* **2005**, *21*, 1516–1523, doi:10.1021/la048569r.

185. Nakabayashi, H.; Yamada, A.; Noba, M.; Kobayashi, Y.; Konno, M.; Nagao, D. Electrolyte-added one-pot synthesis for producing monodisperse, micrometer-sized silica particles up to 7 microm. *Langmuir* **2010**, *26*, 7512–7515, doi:10.1021/la904316f.
186. Kresge, C.T.; Leonowicz, M.E.; Roth, W.J.; Vartuli, J.C.; Beck, J.S. Ordered mesoporous molecular sieves synthesized by a liquid-crystal template mechanism. *Nature* **1992**, *359*, 710–712, doi:10.1038/359710a0.
187. Grama, S.; Horák, D. Preparation of monodisperse porous silica particles using poly(glycidyl methacrylate) microspheres as a template. *Physiol. Res.* **2015**, *64*, S11-7, doi:10.33549/physiolres.933135.
188. Groen, J.C.; Peffer, L.A.; Pérez-Ramírez, J. Pore size determination in modified micro- and mesoporous materials. Pitfalls and limitations in gas adsorption data analysis. *Microporous Mesoporous Mat.* **2003**, *60*, 1–17, doi:10.1016/S1387-1811(03)00339-1.
189. Claessens, H.A.; van Straten, M.A. Review on the chemical and thermal stability of stationary phases for reversed-phase liquid chromatography. *J. Chromatogr. A* **2004**, *1060*, 23–41, doi:10.1016/j.chroma.2004.08.098.
190. Lee, K.; Sathyagal, A.N.; McCormick, A.V. A closer look at an aggregation model of the Stöber process. *Colloids Surf. A: Physicochem. Eng. Asp.* **1998**, *144*, 115–125, doi:10.1016/S0927-7757(98)00566-4.
191. Krasucka, P.; Stefaniak, W.; Kierys, A.; Goworek, J. Polymer–silica composites and silicas produced by high-temperature degradation of organic component. *Thermochimica Acta* **2015**, *615*, 43–50, doi:10.1016/j.tca.2015.07.004.
192. Kwon, S.-C.; Adachi, T.; Araki, W.; Yamaji, A. Thermo-viscoelastic properties of silica particulate-reinforced epoxy composites: Considered in terms of the particle packing model. *Acta Materialia* **2006**, *54*, 3369–3374, doi:10.1016/j.actamat.2006.03.026.
193. Qingyuan, L.; Xiangxu, L.; Ryong, C.U. Mechanical Properties of Styrene-Butadiene Rubber Reinforced with Silica by in situ Tetraethoxysilane Hydrolysis over Acid Catalyst. *Elastomers and Composites* **2018**, *53*, 57–66, doi:10.7473/EC.2018.53.2.57.
194. Kelly, T.L.; Che, S.P.Y.; Yamada, Y.; Yano, K.; Wolf, M.O. Influence of surface morphology on the colloidal and electronic behavior of conjugated polymer-silica microspheres. *Langmuir* **2008**, *24*, 9809–9815, doi:10.1021/la8013688.
195. McInnes, S.J.P.; Voelcker, N.H. Silicon-polymer hybrid materials for drug delivery. *Future Med. Chem.* **2009**, *1*, 1051–1074, doi:10.4155/fmc.09.90.
196. Ciriminna, R.; Fidalgo, A.; Pandarus, V.; Béland, F.; Ilharco, L.M.; Pagliaro, M. The sol-gel route to advanced silica-based materials and recent applications. *Chem. Rev.* **2013**, *113*, 6592–6620, doi:10.1021/cr300399c.
197. Thébault M.; Kutuzova L.; Jury S.; Eicher I.; Zikulnig-Rusch E.-M.; Kandelbauer A. Effect of Phenolation, Lignin-Type and Degree of Substitution on the Properties of Lignin-Modified Phenol-Formaldehyde Impregnation Resins: Molecular Weight Distribution, Wetting Behavior, Rheological Properties and Thermal Curing Profiles. *J. Renew. Mater.* **2020**, *8*, 603–630, doi:10.32604/jrm.2020.09616.
198. Chiang, Y.-D.; Lian, H.-Y.; Leo, S.-Y.; Wang, S.-G.; Yamauchi, Y.; Wu, K.C.-W. Controlling Particle Size and Structural Properties of Mesoporous Silica Nanoparticles Using the Taguchi Method. *J. Phys. Chem. C* **2011**, *115*, 13158–13165, doi:10.1021/jp201017e.
199. Wang, H.-C.; Wu, C.-Y.; Chung, C.-C.; Lai, M.-H.; Chung, T.-W. Analysis of Parameters and Interaction between Parameters in Preparation of Uniform Silicon Dioxide Nanoparticles Using Response Surface Methodology. *Ind. Eng. Chem. Res.* **2006**, *45*, 8043–8048, doi:10.1021/ie060299f.
200. Xu, P.; Wang, H.; Tong, R.; Du, Q.; Zhong, W. Preparation and morphology of SiO2/PMMA nanohybrids by microemulsion polymerization. *Colloid Polym Sci* **2006**, *284*, 755–762, doi:10.1007/s00396-005-1428-9.
201. Brunauer, S.; Emmett, P.H.; Teller, E. Adsorption of Gases in Multimolecular Layers. *J. Am. Chem. Soc.* **1938**, *60*, 309–319, doi:10.1021/ja01269a023.

202. Galarneau, A.; Iapichella, J.; Bonhomme, K.; Di Renzo, F.; Kooyman, P.; Terasaki, O.; Fajula, F. Controlling the Morphology of Mesostructured Silicas by Pseudomorphic Transformation: a Route Towards Applications. *Adv. Funct. Mater.* **2006**, *16*, 1657–1667, doi:10.1002/adfm.200500825.
203. Makarov, A.; LoBrutto, R.; Karpinski, P. Effect of pressure on secondary structure of proteins under ultra high pressure liquid chromatographic conditions. *J. Chromatogr. A* **2013**, *1318*, 112–121, doi:10.1016/j.chroma.2013.09.067.
204. Galabova, B.B. Mesoporous silica nanoparticles: Synthesis, functionalization, drug loading and release - A review. *Trop. J. Pharm Res* **2022**, *20*, 1091–1100, doi:10.4314/tjpr.v20i5.30.
205. Kleitz, F.; Schmidt, W.; Schüth, F. Evolution of mesoporous materials during the calcination process: structural and chemical behavior. *Microporous Mesoporous Mat.* **2001**, *44-45*, 95–109, doi:10.1016/S1387-1811(01)00173-1.
206. Dewaele, C.; Verzele, M. Influence of the particle size distribution of the packing material in reversed-phase high-performance liquid chromatography. *J. Chromatogr. A* **1983**, *260*, 13–21, doi:10.1016/0021-9673(83)80002-8.
207. Kamiya, H.; Mitsui, M.; Takano, H.; Miyazawa, S. Influence of Particle Diameter on Surface Silanol Structure, Hydration Forces, and Aggregation Behavior of Alkoxide-Derived Silica Particles. *J Am Ceram Soc.* **2000**, *83*, 287–293, doi:10.1111/j.1151-2916.2000.tb01187.x.
208. Wang, R.; Wunder, S.L. Effects of Silanol Density, Distribution, and Hydration State of Fumed Silica on the Formation of Self-Assembled Monolayers of n -Octadecyltrichlorosilane. *Langmuir* **2000**, *16*, 5008–5016, doi:10.1021/la991635i.
209. Poppe, T. Sintering of highly porous silica-particle samples: analogues of early Solar-System aggregates. *Icarus* **2003**, *164*, 139–148, doi:10.1016/S0019-1035(03)00137-4.
210. Ditzinger, F.; Price, D.J.; Ilie, A.-R.; Köhl, N.J.; Jankovic, S.; Tsakiridou, G.; Aleandri, S.; Kalantzi, L.; Holm, R.; Nair, A.; et al. Lipophilicity and hydrophobicity considerations in bio-enabling oral formulations approaches - a PEARRL review. *J. Pharm. Pharmacol.* **2019**, *71*, 464–482, doi:10.1111/jphp.12984.
211. He, Q.; Shi, J.; Chen, F.; Zhu, M.; Zhang, L. An anticancer drug delivery system based on surfactant-templated mesoporous silica nanoparticles. *Biomaterials* **2010**, *31*, 3335–3346, doi:10.1016/j.biomaterials.2010.01.015.
212. Kirkland, J.J.; Dilks, C.H.; DeStefano, J.J. Normal-phase high-performance liquid chromatography with highly purified porous silica microspheres. *J. Chromatogr. A* **1993**, *635*, 19–30, doi:10.1016/0021-9673(93)83111-5.
213. Arshady, R. Beaded polymer supports and gels. *J. Chromatogr. A* **1991**, *586*, 181–197, doi:10.1016/0021-9673(91)85124-X.
214. Tan, C.G.; Bowen, B.D.; Epstein, N. Production of monodisperse colloidal silica spheres: Effect of temperature. *J. Colloid Interface Sci.* **1987**, *118*, 290–293, doi:10.1016/0021-9797(87)90458-9.
215. Malay, O.; Yilgor, I.; Menceloglu, Y.Z. Effects of solvent on TEOS hydrolysis kinetics and silica particle size under basic conditions. *J Sol-Gel Sci Technol* **2013**, *67*, 351–361, doi:10.1007/s10971-013-3088-4.
216. Zhang, J.H.; Zhan, P.; Wang, Z.L.; Zhang, W.Y.; Ming, N.B. Preparation of monodisperse silica particles with controllable size and shape. *J. Mater. Res.* **2003**, *18*, 649–653, doi:10.1557/JMR.2003.0085.
217. Mesa, M.; Sierra, L.; López, B.; Ramirez, A.; Guth, J.-L. Preparation of micron-sized spherical particles of mesoporous silica from a triblock copolymer surfactant, usable as a stationary phase for liquid chromatography. *Solid State Sci.* **2003**, *5*, 1303–1308, doi:10.1016/S1293-2558(03)00185-7.
218. Hanrahan, J.P.; Donovan, A.; Morris, M.A.; Holmes, J.D. Synthesis and swelling of large pore diameter mesoporous silica spheres. *J. Mater. Chem.* **2007**, *17*, 3881, doi:10.1039/b705023b.
219. Ahmed, A.; Clowes, R.; Willneff, E.; Ritchie, H.; Myers, P.; Zhang, H. Synthesis of Uniform Porous Silica Microspheres with Hydrophilic Polymer as Stabilizing Agent. *Ind. Eng. Chem. Res.* **2010**, *49*, 602–608, doi:10.1021/ie901213v.

220. Gartmann, N.; Schütze, C.; Ritter, H.; Brühwiler, D. The Effect of Water on the Functionalization of Mesoporous Silica with 3-Aminopropyltriethoxysilane. *J. Phys. Chem. Lett.* **2010**, *1*, 379–382, doi:10.1021/jz9002795.
221. Lee, H.W.; Cho, H.J.; Yim, J.-H.; Kim, J.M.; Jeon, J.-K.; Sohn, J.M.; Yoo, K.-S.; Kim, S.-S.; Park, Y.-K. Removal of Cu(II)-ion over amine-functionalized mesoporous silica materials. *Ind. Eng. Chem. Res.* **2011**, *17*, 504–509, doi:10.1016/j.jiec.2010.09.022.
222. Macan, J.; Brnardić, I.; Orlić, S.; Ivanković, H.; Ivanković, M. Thermal degradation of epoxy–silica organic–inorganic hybrid materials. *Polym. Degrad. Stab.* **2006**, *91*, 122–127, doi:10.1016/j.polymdegradstab.2005.04.024.
223. Acquah, C.; Danquah, M.K.; Moy, C.K.S.; Anwar, M.; Ongkudon, C.M. Thermogravimetric characterization of ex situ polymethacrylate (EDMA-co-GMA) monoliths. *Can. J. Chem. Eng.* **2017**, *95*, 1345–1351, doi:10.1002/cjce.22781.
224. Grochowicz, M.; Pączkowski, P.; Gawdzik, B. Investigation of the thermal properties of glycidyl methacrylate–ethylene glycol dimethacrylate copolymeric microspheres modified by Diels–Alder reaction. *J Therm Anal Calorim* **2018**, *133*, 499–508, doi:10.1007/s10973-017-6785-3.
225. Caravajal, G.S.; Leyden, D.E.; Quinting, G.R.; Maciel, G.E. Structural characterization of (3-aminopropyl)triethoxysilane-modified silicas by silicon-29 and carbon-13 nuclear magnetic resonance. *Anal. Chem.* **1988**, *60*, 1776–1786, doi:10.1021/ac00168a027.
226. Lippmaa, E.; Maegi, M.; Samoson, A.; Engelhardt, G.; Grimmer, A.R. Structural studies of silicates by solid-state high-resolution silicon-29 NMR. *J. Am. Chem. Soc.* **1980**, *102*, 4889–4893, doi:10.1021/ja00535a008.
227. Wang, Q.C.; Svec, F.; Fréchet, J.M. Reversed-phase chromatography of small molecules and peptides on a continuous rod of macroporous poly(styrene-co-divinylbenzene). *J. Chromatogr. A* **1994**, *669*, 230–235, doi:10.1016/0021-9673(94)80352-8.
228. DeStefano, J.J.; Langlois, T.J.; Kirkland, J.J. Characteristics of superficially-porous silica particles for fast HPLC: some performance comparisons with sub-2-microm particles. *J Chromatogr Sci* **2008**, *46*, 254–260, doi:10.1093/chromsci/46.3.254.
229. DeStefano, J.J.; Boyes, B.E.; Schuster, S.A.; Miles, W.L.; Kirkland, J.J. Are sub-2 μm particles best for separating small molecules? An alternative. *J. Chromatogr. A* **2014**, *1368*, 163–172, doi:10.1016/j.chroma.2014.09.078.
230. Peysson, W.; Vulliet, E. Determination of 136 pharmaceuticals and hormones in sewage sludge using quick, easy, cheap, effective, rugged and safe extraction followed by analysis with liquid chromatography-time-of-flight-mass spectrometry. *J. Chromatogr. A* **2013**, *1290*, 46–61, doi:10.1016/j.chroma.2013.03.057.
231. Bayen, S.; Yi, X.; Segovia, E.; Zhou, Z.; Kelly, B.C. Analysis of selected antibiotics in surface freshwater and seawater using direct injection in liquid chromatography electrospray ionization tandem mass spectrometry. *J. Chromatogr. A* **2014**, *1338*, 38–43, doi:10.1016/j.chroma.2014.02.034.
232. Lu, Y.; Shen, Q.; Dai, Z.; Zhang, H. Multi-walled carbon nanotubes as solid-phase extraction adsorbent for the ultra-fast determination of chloramphenicol in egg, honey, and milk by fused-core C18-based high-performance liquid chromatography-tandem mass spectrometry. *Anal Bioanal Chem* **2010**, *398*, 1819–1826, doi:10.1007/s00216-010-4095-8.
233. Tölgyesi, A.; Sharma, V.K.; Fekete, J. Development and validation of a method for determination of corticosteroids in pig fat using liquid chromatography-tandem mass spectrometry. *J. Chromatogr. B* **2011**, *879*, 403–410, doi:10.1016/j.jchromb.2010.12.027.
234. Šatínský, D.; Jägerová, K.; Havlíková, L.; Solich, P. A New and Fast HPLC Method for Determination of Rutin, Troxerutin, Diosmin and Hesperidin in Food Supplements Using Fused-Core Column Technology. *Food Anal. Methods* **2013**, *6*, 1353–1360, doi:10.1007/s12161-012-9551-y.
235. Gaborieau, M.; Castignolles, P. Size-exclusion chromatography (SEC) of branched polymers and polysaccharides. *Anal Bioanal Chem* **2011**, *399*, 1413–1423, doi:10.1007/s00216-010-4221-7.
236. Schoenmakers, P.; Aarnoutse, P. Multi-dimensional separations of polymers. *Anal. Chem.* **2014**, *86*, 6172–6179, doi:10.1021/ac301162b.

237. Kirkland, J.J.; Schuster, S.A.; Johnson, W.L.; Boyes, B.E. Fused-core particle technology in high-performance liquid chromatography: An overview. *J. Pharm. Anal* **2013**, *3*, 303–312, doi:10.1016/j.jpha.2013.02.005.
238. Staub, A.; Zurlino, D.; Rudaz, S.; Veuthey, J.-L.; Guillarme, D. Analysis of peptides and proteins using sub-2 μm fully porous and sub 3-μm shell particles. *J. Chromatogr. A* **2011**, *1218*, 8903–8914, doi:10.1016/j.chroma.2011.07.051.
239. Wagner, B.M.; Schuster, S.A.; Boyes, B.E.; Kirkland, J.J. Superficially porous silica particles with wide pores for biomacromolecular separations. *J. Chromatogr. A* **2012**, *1264*, 22–30, doi:10.1016/j.chroma.2012.09.052.
240. Badley, R.D.; Ford, W.T.; McEnroe, F.J.; Assink, R.A. Surface modification of colloidal silica. *Langmuir* **1990**, *6*, 792–801, doi:10.1021/la00094a013.
241. Albert, K.; Brindle, R.; Martin, P.; Wilson, I.D. Characterisation of C18-bonded silicas for solid-phase extraction by solid-state NMR spectroscopy. *J. Chromatogr. A* **1994**, *665*, 253–258, doi:10.1016/0021-9673(94)85055-0.
242. Vrancken, K.; Possemiers, K.; van der Voort, P.; Vansant, E. Surface modification of silica gels with aminoorganosilanes. *Colloids Surf. A: Physicochem. Eng. Asp.* **1995**, *98*, 235–241, doi:10.1016/0927-7757(95)03119-X.
243. Gritti, F.; Guiochon, G. Comparative study of the performance of columns packed with several new fine silica particles. Would the external roughness of the particles affect column properties? *J. Chromatogr. A* **2007**, *1166*, 30–46, doi:10.1016/j.chroma.2007.06.064.
244. Baker, J.S.; Vinci, J.C.; Moore, A.D.; Colón, L.A. Physical characterization and evaluation of HPLC columns packed with superficially porous particles. *J. Sep. Sci.* **2010**, *33*, 2547–2557, doi:10.1002/jssc.201000251.
245. Cabooter, D.; Fanigliulo, A.; Bellazzi, G.; Allieri, B.; Rottigni, A.; Desmet, G. Relationship between the particle size distribution of commercial fully porous and superficially porous high-performance liquid chromatography column packings and their chromatographic performance. *J. Chromatogr. A* **2010**, *1217*, 7074–7081, doi:10.1016/j.chroma.2010.09.008.
246. van Helden, A.K.; Jansen, J.W.; Vrij, A. Preparation and characterization of spherical monodisperse silica dispersions in nonaqueous solvents. *J. Colloid Interface Sci.* **1981**, *81*, 354–368, doi:10.1016/0021-9797(81)90417-3.
247. Giesche, H. Synthesis of monodispersed silica powders I. Particle properties and reaction kinetics. *J. Eur. Ceram. Soc.* **1994**, *14*, 189–204, doi:10.1016/0955-2219(94)90087-6.
248. Heudi, O.; Kilinç, T.; Fontannaz, P. Separation of water-soluble vitamins by reversed-phase high performance liquid chromatography with ultra-violet detection: application to polyvitaminated premixes. *J. Chromatogr. A* **2005**, *1070*, 49–56, doi:10.1016/j.chroma.2005.02.033.
249. Moulay, S. Functionalized Polystyrene and Polystyrene-Containing Material Platforms for Various Applications. *Polym.-Plast. Technol. Mater.* **2018**, *57*, 1045–1092, doi:10.1080/03602559.2017.1370109.
250. Okudan, A.; Sinan, F. Fractionation effects of polystyrene on acylation reaction and their adhesive and corrosive properties. *J Coat Technol Res* **2013**, *10*, 631–640, doi:10.1007/s11998-013-9479-1.
251. Holzapfel, V.; Musyanovych, A.; Landfester, K.; Lorenz, M.R.; Mailänder, V. Preparation of Fluorescent Carboxyl and Amino Functionalized Polystyrene Particles by Miniemulsion Polymerization as Markers for Cells. *Macromol. Chem. Phys.* **2005**, *206*, 2440–2449, doi:10.1002/macp.200500372.
252. Grafmueller, S.; Manser, P.; Diener, L.; Diener, P.-A.; Maeder-Althaus, X.; Maurizi, L.; Jochum, W.; Krug, H.F.; Buerki-Thurnherr, T.; Mandach, U. von; et al. Bidirectional Transfer Study of Polystyrene Nanoparticles across the Placental Barrier in an ex Vivo Human Placental Perfusion Model. *Environ. Health Perspect.* **2015**, *123*, 1280–1286, doi:10.1289/ehp.1409271.
253. Loos, C.; Syrovets, T.; Musyanovych, A.; Mailänder, V.; Landfester, K.; Nienhaus, G.U.; Simmet, T. Functionalized polystyrene nanoparticles as a platform for studying bio-nano interactions. *Beilstein J. Nanotechnol.* **2014**, *5*, 2403–2412, doi:10.3762/bjnano.5.250.
254. Gulka, C.P.; Swartz, J.D.; Trantum, J.R.; Davis, K.M.; Peak, C.M.; Denton, A.J.; Haselton, F.R.; Wright, D.W. Coffee rings as low-resource diagnostics: detection of the malaria biomarker

Plasmodium falciparum histidine-rich protein-II using a surface-coupled ring of Ni(II)NTA gold-plated polystyrene particles. *ACS Appl. Mater. Interfaces.* **2014**, *6*, 6257–6263, doi:10.1021/am501452k.

255. DIN Deutsches Institut für Normung e. V. *Accuracy (trueness and precision) of measurement methods and results - Part 2: Basic method for the determination of repeatability and reproducibility of a standard measurement method (ISO 5725-2:2019)*: *Text in German and English, DIN ISO 5725-2* (DIN ISO 5725-2) (accessed on 9 December 2022).
256. Rashid, R.; Afroze, F.; Ahmed, S.; Shah Miran, M.; Bin, A.; Susan, H. Control of the Porosity and Morphology of Ordered Mesoporous Silica by Varying Calcination Conditions. *Mater. Today: Proc.* **2019**, *15*, 546–554, doi:10.1016/j.matpr.2019.04.119.
257. Ehrenstein, G.W.; Trawiel, P.; Riedel, G. *Thermal Analysis of Plastics*: *Theory and Practice;* Hanser Verlag: München, 2004, ISBN 9783446434141.
258. Vyazovkin, S. *Isoconversional Kinetics of Thermally Stimulated Processes;* Springer: Cham, 2015, ISBN 9783319141756.
259. Opfermann, J.R.; Kaisersberger, E.; Flammersheim, H.J. Model-free analysis of thermoanalytical data-advantages and limitations. *Thermochimica Acta* **2002**, *391*, 119–127, doi:10.1016/S0040-6031(02)00169-7.